



Domes and Crosses: Exploiting synergies in two methodologies for biaxial tensile testing of membrane tissues

Daniel Jonathan Pons

*Submitted to the University of Cape Town
in partial fulfilment of the degree of
MSc in Mechanical Engineering*

April 2022



The copyright of this thesis vests in the author. No quotation from it or information derived from it is to be published without full acknowledgement of the source. The thesis is to be used for private study or non-commercial research purposes only.

Published by the University of Cape Town (UCT) in terms of the non-exclusive license granted to UCT by the author.

Declaration

I, Daniel Jonathan Pons, hereby:

- (a) grant the University of Cape Town free license to reproduce the above thesis in whole or in part, for the purpose of research;
- (b) declare that:
 - i. the above thesis is my own unaided work, both in concept and execution, and that apart from the normal guidance from my supervisor, I have received no assistance apart from that explicitly stated in the Acknowledgements.
 - ii. neither the substance nor any part of the above thesis has been submitted in the past, or is being, or is to be submitted for a degree at this University or at any other university.

I know the meaning of plagiarism and declare that all the work in the document, save for that which is properly acknowledged, is my own. This thesis/dissertation has been submitted to the Turnitin module (or equivalent similarity and originality checking software) and I confirm that my supervisor has seen my report and any concerns revealed by such have been resolved with my supervisor.

I am now presenting the report for examination for the degree of M.Sc Eng (Mechanical) .

D.J Pons

July 25, 2022

Abstract

Biaxial tensile testing is the preferred method for mechanically testing membranous tissue as it can capture the tissue load response more holistically than uniaxial methods. There are two dominant approaches within the field of biaxial tensile testing: planar and bulge. Both methods can induce a state of biaxial tension within a specimen and both have their advantages and disadvantages. Bulge testing has the benefit of imposing a simple boundary condition on the tissue, making it quick and easy to set up. Planar Biaxial Tensile (PBT) testing is very sensitive to specimen preparation and requires non-trivial gripping systems. Some knowledge of the direction of maximum stiffness, prior to specimen mounting, is necessary for PBT to yield useful data. However, literature suggests that PBT is the more rigorous of the methods when it comes to collecting data to fully characterise a material model for membrane tissues. This study used the ease of bulge testing to determine the mean fibre axis of the tissue which informed the angle of PBT specimen excision. This was a rapid, non-destructive and creative method to avoid otherwise highly expensive imaging approaches to determine mean fibre direction. Further work was also done to develop a method of accurately determining specimen thickness for very thin tissues using a creative histological technique. By using a block of cutting medium to shape the membrane during processing steps, all four of the loaded edges of the tissue could be sectioned simultaneously for thickness measurement. Finally, the study served to develop a membrane tissue test protocol for further research using the in-house built biaxial tensile machines.

Acknowledgements

My sincere gratitude goes to:

My Supervisor, Dr Reuben Govender, who helped me navigate the completion of this endeavour despite severely challenging circumstances.

BISRU staff and my postgraduate colleagues (Jono, Andrew, Claire, Muhsin and Vinay) who took time away from their work and studies to help me with various challenges I faced.

The NRF, Reino Stegen, UCT, David and Veronica Smith whom all valued this research and my education enough to fund me the whole way through.

Marianne, Dirk and Alec for their continued interest, input and advice.

Parents Jonathan & Helen as well as dear friends Marcel, Ed and John who emotionally supported me through many difficult patches on this journey.

Most of all, my God who gave me life and breath in my lungs, allowing me to complete this great endeavour.

Contents

Chapter 1 Introduction.....	1
1.1 Background & Motivation.....	1
1.2 Objectives	2
1.3 Scope.....	2
1.4 Research Overview	2
Chapter 2 Literature Review	5
2.1 Mammalian Small Intestinal Submucosa	5
2.1.1 Related anatomy	5
2.1.2 Overview of Mechanical Properties	7
2.1.3 Some uses for SIS.....	7
2.1.4 Production of SIS.....	8
2.2 Methods in Mechanical Testing of MT	8
2.2.1 Load, Displacement and Geometric Measurement	9
2.2.2 Optical Displacement Tracking	11
2.2.3 Environmental Control.....	14
2.2.4 Tissue Preconditioning	15
2.3 Bulge Testing Methods	17
2.3.1 Clamping	17
2.3.2 Inflation	17
2.3.3 Stress Calculation	17
2.4 PBT Testing Methods.....	18
2.4.1 Mean Fibre Axis identification.....	18
2.4.2 Mounting and Specimen Design	21
2.4.3 Pre-load	22
2.4.4 Tension ratios	22
2.5 The State of Local Research.....	24
2.5.1 Research objectives	24
2.5.2 Bulge Testing.....	24
2.5.3 PBT.....	26
2.5.4 Research Gaps to Explore	27

Chapter 3 Experimental Apparatus.....	29
3.1 Digital Image Correlation.....	29
3.1.1 Dantec Dynamics Istra4D	29
3.1.2 Speckling Method.....	29
3.1.3 Typical Procedure and Evaluation Settings.....	30
3.2 Bulge Test Rig.....	31
3.2.1 System overview.....	31
3.2.2 Syringe Pump	31
3.3 Planar Biaxial Tensile Tester.....	33
3.3.1 System overview.....	33
Chapter 4 Methodology.....	35
4.1 Requirement Driven Methodology	35
4.2 Displacement Measurement.....	37
4.2.1 Speckling.....	37
4.2.2 Optics and lighting.....	39
4.3 PBT Specimen Preparation.....	40
4.3.1 Pre-Bulge Test Preparations	40
4.3.2 Inflation chamber	42
4.3.3 Bulge testing.....	43
4.3.4 MFA Identification Algorithm	44
4.3.5 Goniometric Cutter.....	46
4.3.6 Alignment Preservation and Specimen Excision	49
4.4 Planar Bi-axial Tensile Testing.....	52
4.4.1 Specimen Transfer and Gripping.....	52
4.4.2 Moisture control.....	54
4.4.3 Extension control and force measurement	54
4.4.4 Post-Testing Procedure.....	55
4.5 Tissue Thickness Measurement	55
4.5.1 Evaluation of available methods.....	55
4.5.2 Development of histological methods.....	57
4.5.3 Final method.....	59
4.6 Data Processing & Calculations	61
4.6.1 Engineering Stress Calculation	61
4.6.2 Curve Fitting.....	62

Chapter 5 Results and Discussion.....	63
5.1 Design and Process Performance	63
5.1.1 Tissue Clamping System	63
5.1.2 Chain of alignment preservation.....	66
5.1.2.1 Fixation of the BTR	66
5.1.2.2 DIC Calibration	67
5.1.3 Goniometric Cruciform Specimen Cutter.....	67
5.1.3.1 Cut quality	67
5.1.3.2 Process issues	67
5.1.4 Moisture preservation measures	69
5.1.5 Planar-biaxial MT Grips	70
5.1.6 Uncertainty and Error Propagation.....	71
5.2 DIC Data Quality Evaluation	72
5.2.1 Mechanical Effects of Speckling.....	72
5.2.2 Evaluation Parameters	73
5.2.3 Impact of Speckling on DIC Noise.....	74
5.3 MFA Identification	75
5.3.1 Test pressure cycle	75
5.3.2 DIC Facet Size Optimisation	76
5.3.3 Parameter Selection Dependence.....	78
5.3.4 Process Performance	81
5.4 Specimen Geometric Measurement	83
5.4.1 Through Section Thickness Variation.....	83
5.4.2 Width measurement	84
5.5 MFA Verification Through PBT Testing	86
5.5.1 Extent Dataset Selection.....	86
5.5.2 PBT Stress-Strain Overview	88
5.5.3 Curve Fitting	89
5.6 Requirement Metric Performance.....	94
Chapter 6 Conclusions & Recommendations	97
6.1 A Promising Methodology	97
6.1.1 An Alternative Use for a BTR	97
6.1.2 A Robust Algorithm was Developed.....	98
6.1.3 Effective Specimen Transfer	98

6.1.4	A Stress Confounding Specimen Design	98
6.1.5	A Requirement Satisfying Method.....	98
6.2	Recommendations	99
6.2.1	Load Control for the Planar Biaxial Tester	99
6.2.2	BTR Specimen Humidification	99
6.2.3	MFA ID Parameter Optimisation	99
6.2.4	Computational Investigation	99
References		101
Appendices		107
Appendix A: Detailed Experimental Methods.....		108
A.1	Specimen Preparation	108
A.2	Digital Image Correlation	109
A.2.1	Setup and Calibration.....	109
A.2.2	Correlation	110
A.2.3	Evaluation and Data Export	110
A.3	Chromotrope Aniline Blue Stain.....	112
A.3.1	Method:	112
A.3.2	Reagents.....	112
A.3.3	Results.....	112
A.4	Safety Datasheets	113
A.5	Micrograph Calibration.....	113
A.6	Testing Procedure Overview	113
A.7	Continuum Material Modelling Method.....	114
A.7.1	Stress Calculations.....	115
A.7.2	Material Modelling	117
Appendix B: Detailed Experimental Results.....		119
B.1	Sealing.....	119
B.2	Displacement Data Quality.....	119
B.2.1	DIC Speckle Quality	119
B.3	Bulge Summary	122
B.4	Additional Algorithm Check Specimens	123
B.5	Full Stress-Strain Data	124
B.6	Excluded Curve Fits	140
B.7	Uncertainty Budgeting	142

Appendix C: Drawings and Design.....	143
C.1 Clamping Assembly	143
C.1.1 Gasket	143
C.1.2 Cover Plate and Base Plate	146
C.2 Pressure Chamber Stand	149
C.3 Calibration Target Guide	153
C.4 Goniometric Cutting Jig	155
C.4.1 Full Cutting Jig Assembly	155
C.4.2 Cutting Block Assembly	158
C.5 Planar Biaxial Tensile Grip Card	161
C.6 Wax Mould.....	163
Appendix D: Python Code	167
D.1 Data Processing.....	167
D.1.1 BTR	167
D.1.2 PBT	167
D.2 Data Analysis	168
D.2.1 Basic MFA-ID Algorithm	168
D.2.2 Multiprocessing MFA-ID Module	168
D.2.3 PBT Stress-Strain analysis	168
D.3 Additional Libraries.....	169
D.4 Databases	169
D.4.1 Bulge DIC Data.....	169
D.4.2 Measured Values	170
D.4.3 PBT DIC Data.....	170
Appendix E: Modifications to Arduino Code.....	171
E.1 Max & Min Pressure Triggering	171
E.2 Pressure Profile Control Logic	172
E.3 Additional Button Logic	172
Appendix F: Ethics Clearance.....	173

List of Tables

Table 2.1: <i>Summary of Giorgio's Findings</i>	6
Table 2.2: <i>Comparison of measurement approaches</i>	10
Table 3.3: <i>Typical DIC evaluation parameters used</i>	30
Table 4.4: <i>Methodology Requirements Summary</i>	36
Table 4.5: <i>Typical MFA identification algorithm parameters used</i>	46
Table 5.6: <i>Summary of the impact of speckle statistics on NSR.</i>	74
Table 5.7: <i>Requirement achievement analysis</i>	94
Table B.3.8: <i>A summary of all the bulge testing MFA-ID parameters and results</i>	122
Table B.7.9: <i>Uncertainty budget with typical BTR DIC values for different facet sizes</i>	142
Table B.7.10: <i>Uncertainty budget with typical PBT DIC values for different facet sizes</i>	142
Table B.7.11: <i>Uncertainty budget for a typical PBT specimen width measurement</i>	142
Table B.7.12: <i>Specimen eight uncertainty budget for PBT specimen thickness</i>	142
Table B.7.13: <i>Uncertainty budget for PBT load measurement</i>	142

List of Figures

Figure 1.1: Overview of the key processes in the steps to measure MFA aligned PBT data...	3
Figure 2.1: Schematic of the small intestine wall.	6
Figure 2.2: Phase contrast microscopy of rat small intestinal submucosa.	6
Figure 2.3: Schematic cross-section of a bulge specimen under load P_g	8
Figure 2.4: Schematic of a planar biaxial tensile specimen under load.....	9
Figure 2.5: (a) Discrete marking strategy by Bellini et al.	12
Figure 2.6: (a) A control volume set up by Tonge et al.	14
Figure 2.7: (a) A controlled environment created for uniaxial testing of breast skin.....	15
Figure 2.8: A typical stress-stretch response before and after pre-conditioning.....	16
Figure 2.9: Langer's lines generally depicting the MFA of human skin.....	19
Figure 2.10: Tissue stretching method applied by Choi and Vito to determine MFA	20
Figure 2.11: Induced PBT deformation using grips, sutures and rakes,	21
Figure 2.12: Variations on the cruciform specimen (undeformed)	22
Figure 2.13: A colour map linking the(a) plane of invariants to (b)a PBT test	23
Figure 2.14: Schematic of Curry's bulge test rig	24
Figure 2.15: Bulge test setup developed by Fischer	25
Figure 2.16: A schematic of Graham's high strain rate BTR.....	25
Figure 2.17: Schematic of Caine's PBT tester.....	26
Figure 3.1: Bulge testing set-up schematic.....	31
Figure 3.2: a) Original BTR control system.....	32
Figure 3.3: (a) Original BTR wiring.	33
Figure 3.4: Planar biaxial testing set-up schematic.....	34
Figure 3.5: Planar biaxial tensile tester designed by Caine,	34
Figure 4.1: A representation of the "fall-out" speckling method.....	37
Figure 4.2: Poor speckle pattern performance.....	38
Figure 4.3: Good speckle pattern performance.....	38
Figure 4.4: Solutions to optical problems encountered in DIC testing.....	40
Figure 4.5: (a) Opening tube of tissue into flat rectangular form. (b) Spreading tissue.....	41
Figure 4.6: (a) Bulged membrane from placing the plate down on a surface.....	41
Figure 4.7: Tissue clamping assembly.....	42
Figure 4.8: A typical bulge-test pressure profile using the BTR.	43
Figure 4.9: (a) Bulge-testing setup. (b) Hot water-filled syringe	44
Figure 4.10: MFA identification algorithm output graph.....	45
Figure 4.11: Section-view of the first cutting block with unsupported \mathcal{E} untrimmed blades. ..	47
Figure 4.12: Improved cutting block with the internal blade support \mathcal{E} trimming.....	47
Figure 4.13: Cutting block blade preparation using disposable razorblades.	48
Figure 4.14: Razor blade preparation:.....	49
Figure 4.15: Partially sectioned goniometric cutting jig.....	49
Figure 4.16: (a) Alignment triangle jig ensured a consistent frame of reference.....	51
Figure 4.17: (a) 10 mm gauge-width cutter.....	51

Figure 4.18: <i>PBT specimen gripping and transfer card</i>	52
Figure 4.19: <i>(a)PBT tester arms positioned to align DIC axes to the MFA</i>	53
Figure 4.20: <i>Planar biaxial tensile specimen under load on a saline bath.</i>	54
Figure 4.21: <i>(a) Visual tissue thickness measurement</i>	56
Figure 4.22: <i>(a)Poor quality in-house tissue section.</i>	57
Figure 4.23: <i>(a) View of sectioned pipe normal to cutting plane</i>	58
Figure 4.24: <i>Circular cross-section of the SIS</i>	59
Figure 4.25: <i>(a) Specimen preparation process (b) Results after twelve-hour processing</i>	59
Figure 4.26: <i>(a) Micrograph showing each arm used for thickness measurement</i>	60
Figure 5.1: <i>(a) Coconut oil inflation of a rudimentary steel on steel clamping</i>	64
Figure 5.2: <i>The difficult release of tissue from the clamping mechanism</i>	65
Figure 5.3: <i>Design issues found with the clamp assembly</i>	65
Figure 5.4: <i>BTR DIC (a)alignment and (b)calibration steps</i>	66
Figure 5.5: <i>Progression of specimen excision quality assessment</i>	67
Figure 5.6: <i>(a) MT & cutting surface adhesion, (b) cutting surface not fully located</i>	68
Figure 5.7: <i>Saline bath used to maintain specimen hydration during PBT tests.</i>	69
Figure 5.8: <i>Grip performance with two specimen installations</i>	70
Figure 5.9: <i>Spray paint speckling shown to little influence specimen pressure history</i>	72
Figure 5.10: <i>HE specimen peak strain NSR</i>	73
Figure 5.11: <i>ImageJ speckle pattern histogram analysis comparison</i>	75
Figure 5.12: <i>Angular error calculation for a single datapoint.</i>	76
Figure 5.13: <i>DIC facet size optimisation findings</i>	77
Figure 5.14: <i>Examples of (a) reference, (b) apex and (c) POI time-steps of the bulge test.</i> ..	78
Figure 5.15: <i>MFA angle statistics using a range of MFA ID algorithm inputs</i>	79
Figure 5.16: <i>Isotropy statistics using a range of MFA ID algorithm inputs.</i>	80
Figure 5.17: <i>Comparison of (a) angles calculated vs angles cut across all specimens</i>	81
Figure 5.18: <i>Mean cruciform specimen thickness along the edges of the ROI.</i>	83
Figure 5.19: <i>Varied separation between specimens due to wax histological method</i>	84
Figure 5.20: <i>Specimen 11 shape change</i>	85
Figure 5.21: <i>Mean arm width along each axis for all specimens.</i>	85
Figure 5.22: <i>Equibiaxial engineering stress-strain curves for low NSR specimens</i>	86
Figure 5.23: <i>Shifted MFA equibiaxial engineering stress-strain curves</i>	87
Figure 5.24: <i>Shifted CFA equibiaxial engineering stress-strain curves</i>	88
Figure 5.25: <i>MFA and CFA stress-strain curve-fits featuring a range of isotropy values</i>	89
Figure 5.26: <i>Imperfect curve fitting to stress-strain datasets with exponential functions</i>	90
Figure 5.27: <i>Exponential curves fitted to equibiaxial extension data.</i>	91
Figure 5.28: <i>(S9) A highly anisotropic specimen and (S10) a mis-identified MFA</i>	91
Figure 5.29: <i>Swapped extension ratios showed MFA & CFA curvature differences.</i>	92
Figure 5.30: <i>Exponential curves fitted to equibiaxial extension data.</i>	93
Figure 5.31: <i>A comparison of the two isotropy measures for the curve-fitted specimens</i>	94
Figure A.1.1: <i>Process flow diagram describing the specimen preparation procedure</i>	108
Figure A.2.2: <i>DIC setup and calibration procedure</i>	109
Figure A.2.3: <i>DIC evaluation and data export protocol.</i>	110
Figure A.2.4: <i>DIC evaluation start-point selection</i>	111
Figure A.5.5: <i>1 mm optical calibration graticule</i>	113

Figure B.1.6: <i>(a) Rudimentary simple steel on steel clamping system with rupture.....</i>	119
Figure B.2.7: <i>ImageJ analysis of speckle patterns in the ROI.....</i>	120
Figure B.2.8: <i>ImageJ analysis of speckle patterns in the ROI.....</i>	121
Figure B.4.9: <i>MFA angle statistics for specimens 2 and 16.....</i>	123
Figure B.4.10: <i>Specimen 2 and 16 isotropy statistics given a range of MFA-ID inputs.....</i>	123
Figure B.6.11: <i>Specimen 3 excluded on the grounds of load discontinuity.....</i>	140
Figure B.6.12: <i>Specimen 15 excluded on the grounds of low load.....</i>	140
Figure B.6.13: <i>Specimen 12,13,14 excluded on the grounds of load noise</i>	141
Figure C.1.14: <i>Gasket assembly.....</i>	143
Figure C.1.15: <i>Simplified gasket deformation.....</i>	143
Figure C.2.16: <i>Failed point of pressure chamber stand arm.....</i>	149
Figure D.2.17: <i>An overview of the algorithm inputs and outputs.....</i>	168
Figure E.1.18: <i>Code block for additional max and min pressure triggers</i>	171
Figure E.2.19: <i>Code block for controlling the inflation profile.....</i>	172
Figure E.3.20: <i>Logic to ensure all circumstances were considered.....</i>	172

Nomenclature

Acronym	Explanation
2D-DIC	Two-Dimensional Digital Image Correlation
3D	Three Dimensional
3D DIC	Three-Dimensional Digital Image Correlation
BISRU	The Blast and Impact Survivability Unit
BT	Bulge Test
BTR	Bulge Test Rig
CFA	Cross Fibre Axis
CNC	Computer Numerically Controlled
DAQ	Data Acquisition
DIC	Digital Image Correlation
FDM	Fusion Deposition Modelling
FEA	Finite Element Analysis
FHS	Faculty of Health Sciences
GAG	Glycosaminoglycan
GIT	Gastro-Intestinal Tract
HDPE	High Density Polyethylene
HE	High Extension
LE	Low Extension
ME	Medium Extension
MFA	Mean Fibre Axis
MFA-ID	Mean Fibre Axis Identification
MT	Membranous Tissue
NSR	Noise to Signal Ratio
ODM	Optical Displacement Measurement
PBT	Planar Biaxial Tensile
PPE	Personal Protective Equipment
ROI	Region of Interest
SALS	Small Angle Light Scattering
SIS	Small Intestinal Submucosa
UCT	The University of Cape Town
UTS	Ultimate Tensile Strength
UTT	Uniaxial Tensile Test

Chapter 1

Introduction

1.1 Background & Motivation

The mechanical properties of membranous tissue (MT) can be useful information to have in a wide range of applications. Be it skin, pericardium, aortic tissue or even intestinal tissue, there are safety measures, medical devices or surgical procedures whose development has been aided by this information [1]–[3].

Within the Blast Impact and Survivability Research Unit (BISRU), the mechanical properties of biological tissue have been studied with the objective of simulating human body response to accidents and extreme loads. The skin, lungs and eardrums can all suffer non-fatal damage for victims of an explosion. Hence improved mechanical response data and constitutive models for these tissues would help BISRU develop better injury criteria. In South Africa (from communications with local skin researchers) the absence of MT data has been due to the lack of local mechanical testing facilities. Local researchers were forced to use data from international collaborators.

While uniaxial studies of MT might abound due to ease of testing, a review of the literature showed that planar biaxial tensile (PBT) testing could best replicate *in vivo* load scenarios and provide sufficient different scenarios to fully populate an anisotropic, nonlinear material model.

At BISRU, Curry [4] and Caine [5] made efforts to develop bulge and planar biaxial testing equipment respectively. These studies used silicone elastomers as surrogate material during commissioning, instead of biological MT. Further development of the gripping mechanisms of both the bulge test rig (BTR) and PBT tester was needed to accommodate more delicate and anisotropic MT specimens.

The problem with PBT testing was that results have been shown to be highly dependent on specimen alignment to the mean tissue fibre axis (MFA) [6]. Yet PBT testing holds the greatest versatility in being able to easily mimic particular *in vivo* load cases by varying tension ratios. Researchers have employed advanced imaging equipment to identify the MFA [7]. The time involved in imaging can lead to tissue degradation, while some methods use chemical treatment which changes the tissue stiffness.

Bulge testing is the alternative to PBT testing, which does not face the same alignment problems, as the specimen is typically gripped in a circular aperture. However, bulge testing requires a low specimen thickness and even tissue distribution for the calculated stresses to be representative[8]. Typically, bulge testers are only used for equibiaxial testing of MT (equal tension ratios) due to the difficulties in testing with non-circular bulge apertures [9].

While considering the benefits and shortcomings of PBT and bulge testing described in the literature, the lack of side-by-side comparison of the two approaches became apparent to this researcher. It also became apparent that in some areas, synergies between the two approaches could be exploited to make up for the shortfalls of the other. These synergies presented themselves as opportunities for development of new approaches in this study.

1.2 Objectives

The primary objective of this work was to develop a methodology such that it would be possible to obtain stress and strain data for MT under the constraint that specimens should be aligned consistently with respect to the mean fibre axis (MFA). This methodology could make use of the existing PBT and bulge test equipment. Any microscopy would be reserved for post-mortem investigation rather than prior to mechanical testing and would ideally exclude the use of highly specialised microscopy. The preparation and mounting of specimens should not overtly rely on human dexterity (such as suturing).

1.3 Scope

To avoid the complications of working with (bio-hazardous) human tissue, or the logistical difficulties around recently slaughtered animals, this study used ovine intestinal submucosa (sheep intestines) as being broadly representative of MT. Sheep intestines are easily sourced in ample quantities as sausage casing and are easily stored and handled according to food hygiene practices.

Only quasi-static testing was to be performed and the use of testing equipment for the study was limited to the Bulge Test Rig (BTR) developed in [4] and the PBT tester developed in [5].

This dissertation focused on laboratory methodological development and qualitative evaluation of various techniques. Simulation of the experiments using Finite Element Analysis, and rigorous fitting and validation of material models, was left for future research.

1.4 Research Overview

Review of the available literature was conducted with the focus of teasing out the potential for a relatively low cost and simple approach to improve PBT specimen preparation and mounting, while providing a backdrop to contextualise the reader in this niche of research.

Figure 1.1 shows a highly simplified diagram of the key steps to produce high quality PBT stress-strain data for MT using this method and has been provided.

An overview of existing equipment was given before walking the reader through the methodology required to use bulge testing as a non-destructive means to determine MFA for PBT specimen preparation. A low-pressure bulge test was sufficient to determine preferential fibre behaviour, using three dimensional (3D) digital image correlation (DIC) and a python MFA identification algorithm. Specimen preparation & transfer using disposable and alignment preserving cards was showcased and PBT testing performed.

The results of this study showed that the BTR could be used to extract information about a specimen without damaging or straining it beyond what the specimen would be pre-conditioned to (in normal PBT testing procedures). The mean fibre axis identification (MFA-ID) algorithm was capable of reliably identifying the angle to excise the PBT specimen and a confidence level based on DIC data quality as well as specimen isotropy. Once excised, the ratio of stiffness between MFA and CFA identified in the MFA-ID algorithm closely matched that of the approximated ratio of stiffness of the PBT stress-strain curves.

The methodology developed in this project holds great potential for use in more complete studies of MT. The simplicity of MFA-ID using a BTR meant that PBT testing can be done on tissues with comparatively short turn-around times without specific knowledge as to the exact orientation at which the specimen was excised from the parent tissue.

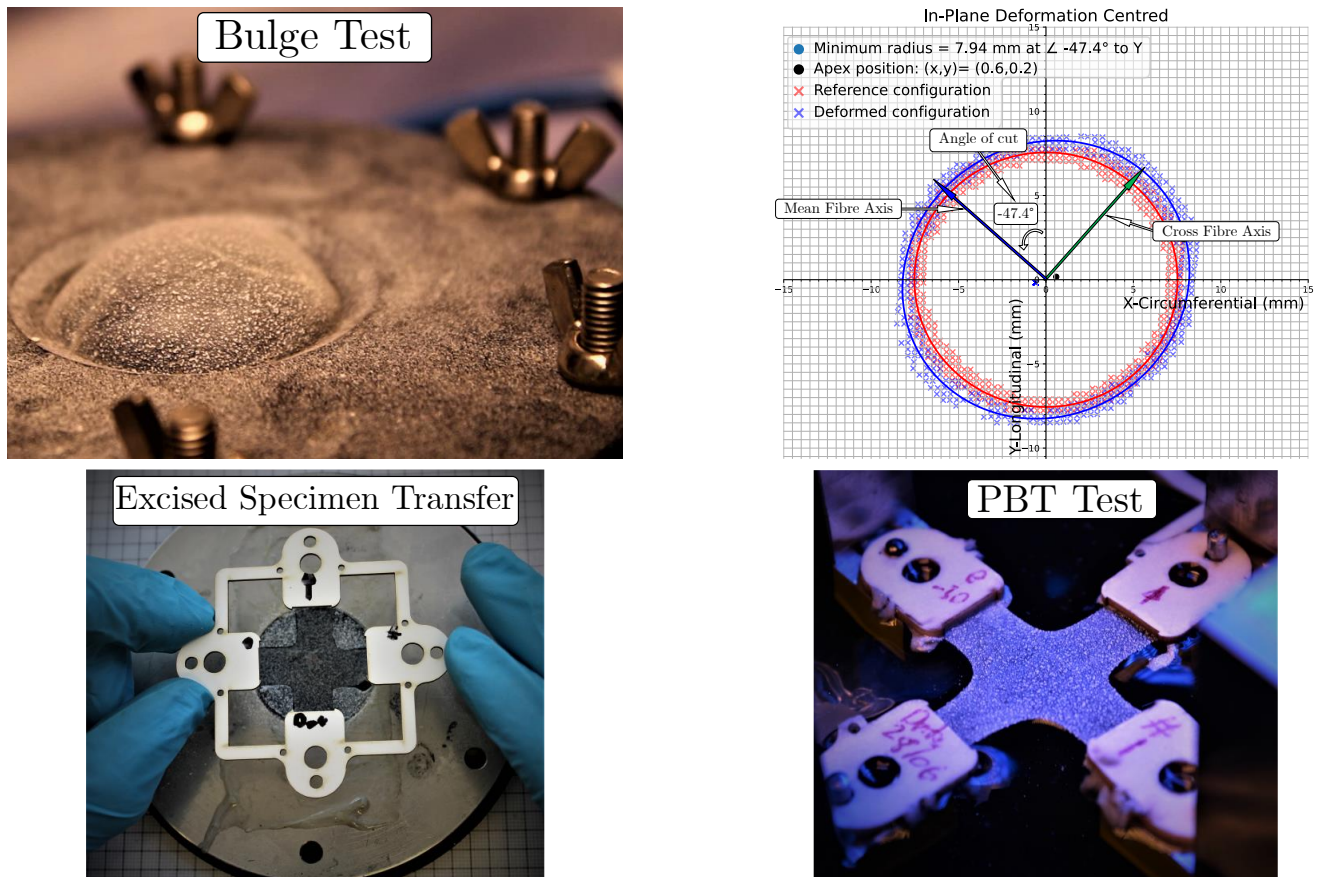


Figure 1.1: Overview of the key processes in the steps to measure MFA aligned PBT data

Chapter 2

Literature Review

This chapter discusses the ongoing study of membranous tissue (MT) mechanical properties and offers an introduction to the specimen material used in this study. Some information was provided regarding the dominant methods of mechanical testing of MT (bulge and planar biaxial tensile testing). This offers context to the design work done to incorporate both methods into one study.

2.1 Mammalian Small Intestinal Submucosa

The small intestinal submucosa (SIS) is a thin membrane located in the small intestine primarily made up of collagen and small amounts of elastin. The collagen fibres of SIS are the driving constituent for its anisotropic qualities [1]. Readily available as a meat by-product, ovine SIS was used exclusively as the specimen material in this study. Understanding this material (its uses, production, anatomy and histology) helped inform the testing regimen developed and the interpretation of results.

2.1.1 Related anatomy

As shown in Figure 2.1, the SIS is located between the mucosa and the circular muscle layers in the small intestinal wall. It performs a purely structural role and has been likened to a skeleton for the small intestine [2].

SIS has been known to contain important growth factors for tissue engineering (several types of collagen, glycosaminoglycans and glycoproteins) [3]–[5]. Other elements found in the submucosal layer are: fibroblasts, blood vessels, nerves, lymphatic vessels, mast cells, plasma cells, eosinophils and other blood-born cells [2]. The main constituents of SIS are collagen and elastin. Collagen presents itself in the form of large fibre networks and bundles within the SIS [2], [6]. Both skin and SIS depend on their high collagen content (70%) for load bearing [7].

The bi-helical lay of collagen fibres in the SIS represented in Figure 2.1 exhibits two main fibre directions of approximately $\pm 50^\circ$ to the longitudinal axis of the intestinal tract. These fibres help SIS limit intestinal distension while supporting the directional motion of peristalsis [2].

Phase contrast microscopy has been used to quantify the lay of SIS collagen fibres [2], [6]. Figure 2.2 shows such a micrograph from which general fibre angles can be quantified. Giorgio

found that the angle of this lattice arrangement changed to accommodate the load direction applied to the SIS [2].

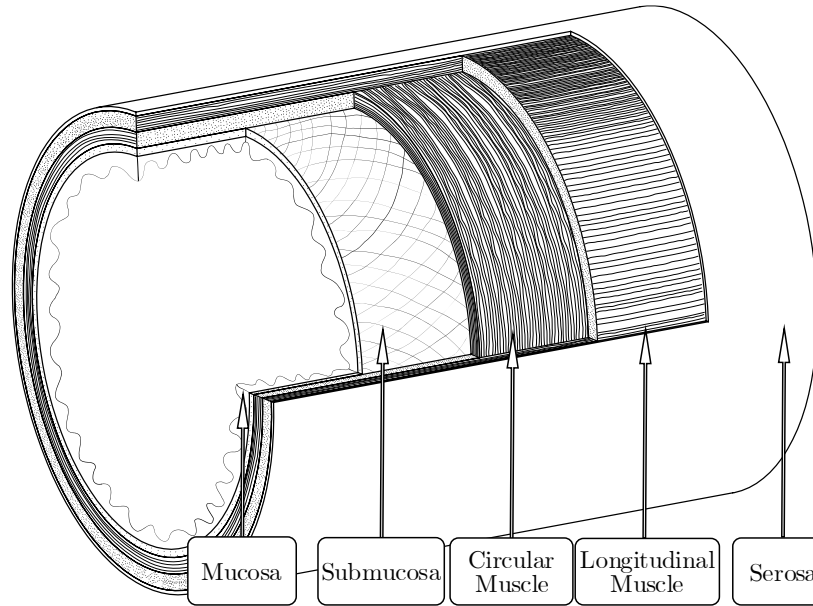


Figure 2.1: *Schematic of the small intestine wall. Texturing indicates fibre direction. Adapted from[2]*

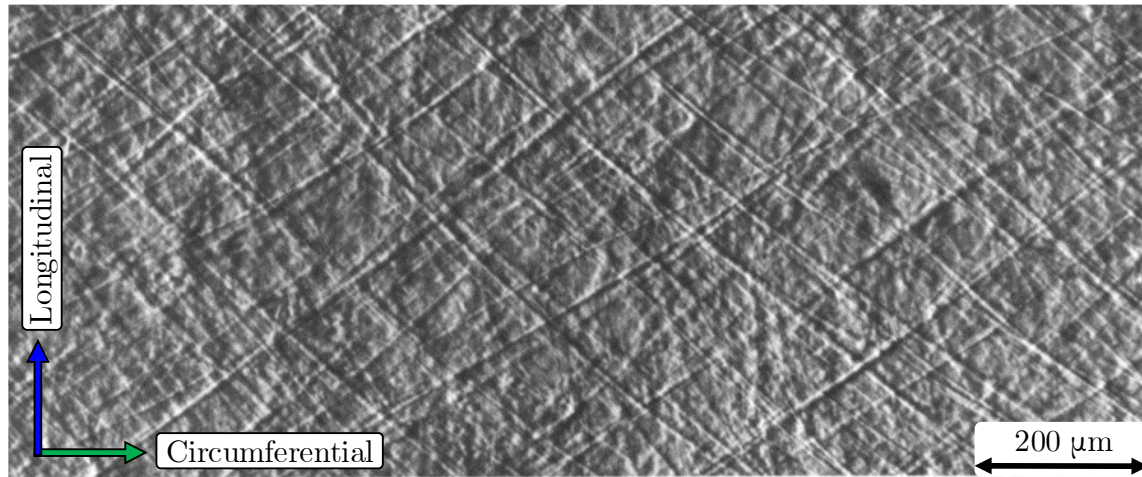


Figure 2.2: *Phase contrast microscopy of rat small intestinal submucosa. Sourced with permission[2].*

Giorgio's findings regarding lattice angle and load direction have been summarised in Table 2.1 and show that the SIS is an anisotropic material. Furthermore, due to blood vessel coupling, SIS has also been shown to be heterogenous. [2], [6]

Table 2.1: *Summary of Giorgio's Findings [2]*

Distension Direction	Angles wrt. Longitudinal Axis
Longitudinal	$\pm 30^\circ$
Radial	$\pm 60^\circ$
No Distension	$\pm 50^\circ$

2.1.2 Overview of Mechanical Properties

Giorgio did not quantify the loads placed on the tissue, but rather applied tension manually without measurement, to induce two general states of loading of the cylindrical tissue (longitudinal and radial)[2].

However, other studies measured the fibre behaviour under quantified loading [6]. Here, Sacks occasionally found two distinct fibre populations oriented at $\pm 28^\circ$ with respect to the longitudinal axis of porcine SIS [6]. He used a Small Angle Light Scattering (SALS) method to determine the preferred fibre orientation [6], [8]. This required equipment not available to the present study. While both Giorgio and Sacks reported similar fibre lay, Sacks' measurements of load response showed SIS to be anisotropic and non-linear.

Non-linearity was explained by the polymeric entanglement of the collagen fibre bundles. By means of biaxial loading, Sacks established that “*the circumferential stress-strain response was strongly affected by the maximum longitudinal strain level, but the maximum circumferential strain level only weakly affected the longitudinal stress-strain response*”. This suggested that such asymmetric mechanical coupling is linked to strong fibrous mechanical interactions. Sacks highlighted that the angular distribution is not consistent and is often highly localised.

These findings motivated for development of faster and more cost-effective methods of establishing localised preferred fibre directions. Furthermore, the full field multi-axial load-response was found necessary to better understand the mechanical properties of SIS.

2.1.3 Some uses for SIS

Sausage casings are the main use for the intestinal submucosa in the food industry [9]. By varying animal type and/or position along the gastrointestinal tract (GIT), sufficient variation in membrane thickness and diameter can be used to make the wide range of sausages produced in the world today [9].

Historically, SIS was the main component of the cord known as “catgut”. Catgut was used in musical instruments extensively before the transition to steel and nylon stringed instruments [10]. Later, it was used in tennis racquets, but sutures are what it is most known for. These sutures are still used today for specific procedures and in developing countries with poor access to synthetic alternatives [10]. Catgut is made up of multiple SIS strands twisted together, where cord diameter depends on the number of strands, be it two or three for sutures or well over twenty for a double bass string.

Mammalian SIS grafts are used as a natural scaffold in tissue engineering. Porcine SIS is commercially available as a proven medical device for genitourinary system applications [3]. This use of SIS has provoked study into its mechanical properties (both uniaxial and biaxial) [6]. Sacks explained in his study that knowledge of these mechanical properties would serve to improve grafting practices when seeking to repair Achilles’ tendons, cranial dura mater, abdominal walls as well as the vascular regions [6].

In this study, SIS was most useful as a surrogate material for skin, as it exhibited anisotropy, heterogeneity and moisture dependent elasticity.

2.1.4 Production of SIS

Ovine intestinal tissue is readily found in sausage casings, which are a single layer of the intestine (the SIS). This is isolated by means of mechanical processing [9].

The large supply of salt-cured SIS, its low cost and the fact that it is a by-product of the meat industry made it an ideal specimen material for this MSc, within the context of a broader research project into MT mechanical response. Ethically, the use of this material is not dissimilar to the ethics of meat eating as the use of this material would not require any test animals to be sacrificed. A synthetic alternative would be manufactured casings. These are largely made of collagen to mimic the texture and consistency of natural casings without the natural variation issues that come with using them.

2.2 Methods in Mechanical Testing of MT

Skin is the largest organ of the human body and is capable of a vast array of functions. This example of MT was yet to be mechanically understood to the same extent as synthetic materials. As medical devices often interact with it, an improved understanding of MT holds great potential for innovation [11]. Endoscopes for example need to interact with the GIT wall. Poor understanding of this membrane's mechanical characteristics could result in wasteful testing, over-engineering or even injury. MT material model assistance in design has already proven useful [11].

MT characterisation has mainly been done for low strain-rates or under uniaxial loading [12]. Due to the limitations of uniaxial tensile (UT) testing, biaxial testing has long been recognised as an important test in fully characterising MT [13]. Dynamic biaxial characteristics of MT would be useful in body-impact simulations, which would aid development of personal protective equipment (PPE) in industrial/defence applications or of medical treatment methods.

Figure 2.3 depicts the inflation of a clamped membrane aka. a bulge test (BT). This is a very simple way to induce biaxial stress at the bulge apex. The apparatus to perform such a test will here be called a bulge test rig (BTR). Biaxial stress can also be induced using a planar biaxial tensile (PBT) test rig. Figure 2.4 shows how this device applies and measures tension on perpendicular axes in the plane of the membrane.

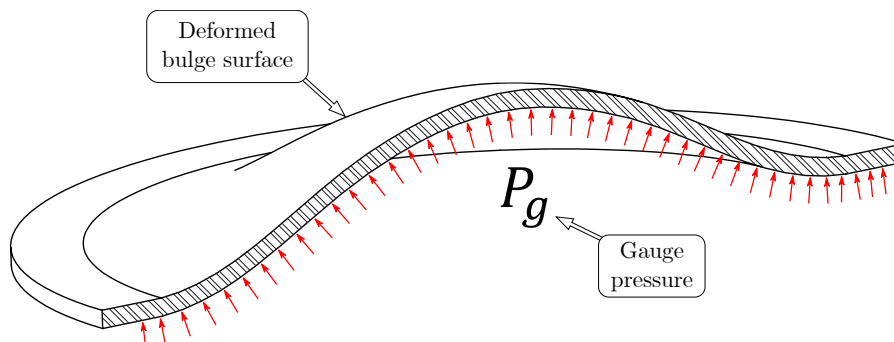


Figure 2.3: *Schematic cross-section of a bulge specimen under load P_g*

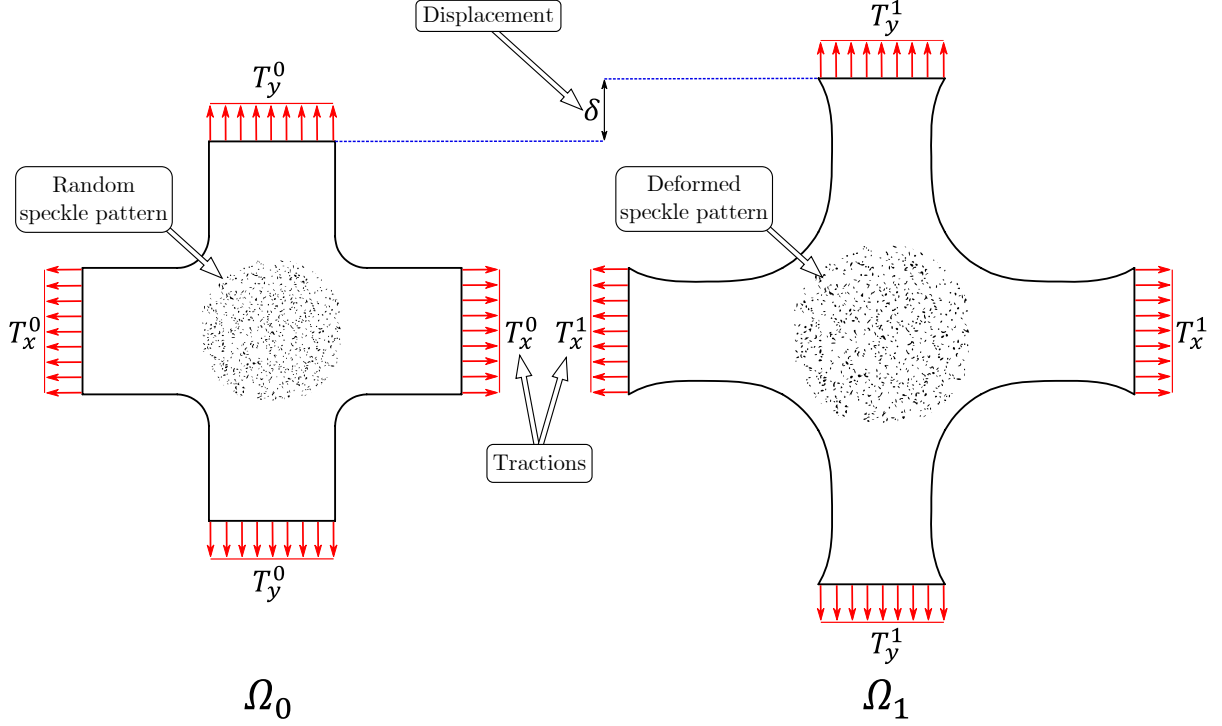


Figure 2.4: *Schematic of a planar biaxial tensile specimen under load*

Uniaxial tensile testing of MT was the forerunner of mechanical testing of soft tissues. Uniaxial testing was the most ubiquitous method for obtaining mechanical properties of engineering materials. While uniaxial tensile studies of MT are still current [7], [14], they have limited capacity in capturing anisotropic load response [15].

2.2.1 Load, Displacement and Geometric Measurement

UT, PBT and bulge testing were the only types of mechanical tensile tests for MT considered in this study. *In vivo* bulge tests and others such as torsion and indentation tests were out of the scope of investigation.

Tensile tests required force measurement on each axis of interest. Bulge tests required measurement of the pressure difference over the membrane. Unlike conventional engineering materials, MT did not allow fine control of thickness or specimen geometry due to its anatomy. Combined with the variation and heterogeneity in biological materials, this meant that a varied load response was expected from specimen to specimen.

Loadcells with a very high resolution and low noise to signal ratio (NSR) were needed to accurately measure the PBT load-response. Table 2.2 shows how these requirements were the same for BT pressure transducers. For example, a loadcell used to test skin may be inappropriate for pericardium or SIS. This was due to the differing MT elasticity, maximum available thickness and specimen size.

Apex and crosshead displacement are not adequate measures of displacement for MT bulge and tensile tests respectively. This is because the strain in the region of interest cannot be approximated analytically by using these measures. For anisotropic materials, optical methods of determining strain are preferred. These have been discussed in more detail in section 2.2.2.

Table 2.2: *Comparison of measurement approaches and uncertainties pertaining to load and thickness measurement among some researchers of MT*

STUDY (Author 1 [ref])	TEST TYPE	LOAD RESOLUTION	DISPLACEMENT METHOD	THICKNESS MEASUREMENT METHOD	TISSUE TESTED	MEAN THICKNESS (μm)	THICKNESS UNCERTAINTY (μm)	THICKNESS NOISE TO SIGNAL RATIO (%)
Sacks [6]	PBT	1 mN	Four-point optical feature tracking	Dial calliper	Porcine SIS	125	25	20
Bellini [11]	PBT	0.6 mN	Four-point optical feature tracking	Micrometre	Porcine small intestine	875	210	24
Meador [21]	PBT	50 mN	Optical shape tracking	Optical: freeze-cut tissue	Murine skin	705	275	39
Choi [26]	PBT	9.8 mN	Five-point optical feature tracking	Resistivity micrometre	Canine pericardium	55	22	40
Vastmans [31]	PBT	70 mN	Five-point optical feature tracking	Optical: fresh tissue	Ovine artery	1150	230	20
Amini [53]	PBT	4.91 mN	Four-point optical feature tracking	Dial micrometre	Porcine small bowl mesentery	1206	531	44
Lakhani [17]	Bulge	1 mBar	Full field speckle DIC	Digital micrometre	Porcine skin	3650	73	2
Tonge [16]	Bulge	0.1 mBar	Full field speckle DIC	Dial calliper	Human skin	3390	339	10
Diab [28]	Bulge	0.72 mBar	Full field speckle DIC	Vernier calliper	Human breast skin	2632	100	3.8
Bose [14]	Uniaxial	500 mN	Crosshead	Not stated	Collagen film	71	10	14
Pissarenko [7]	Uniaxial	-	Full field speckle DIC	Optical: fresh tissue	Porcine dermis	147	1.47	1

Cross-sectional geometry was the final piece of information required to calculate the load stress. Gauge-width and thickness measurement of engineering specimen materials can usually be done with a vernier calliper or micrometer. Measuring the thickness of soft and thin materials was not a simple task and Table 2.2 showed that it has been approached in a variety of ways.

Due to brevity or omission by researchers, not all approaches could be evaluated. The stated uncertainties by researchers only reflected repeatability of a single measurement at a point. None of these researchers accounted for thickness variation along the cross-section.

It is extremely difficult to determine the difference between touching the surface of MT and deforming it when measuring thickness with a contact method. Thus, the validity of some very low uncertainties in thickness reported by Sacks [6], Tonge [16] and Lakhani [17] came into question. The specific techniques they used possibly led to the elevated confidence in their values. Unfortunately, these methods are not reported in enough detail to critique further.

Comparison of thickness NSR values across the approaches showed that non-contact optical methods were promising. Non-contact methods were often better documented and did not have the confounding factor of deformation during measurement.

Table 2.2 showed that it was possible to measure tissue thickness accurately with limited equipment. Thickness could also be measured poorly with advanced equipment, i.e., technique was key. Optical techniques offered the least dependence on operator skill when measuring and thus reduced the opportunity for human error.

Optical methods were used as a control for evaluating thickness measurement techniques in a study by Lee and Langdon [18]. They did however identify one other method which was both simple to use and not statistically different to the control. This was a Mitutoyo non-rotating thickness gauge. Lastly they noted that for such contact measurement techniques, the contact force used to close the device on the tissue should be cited [18]. This force may not be practical to measure, but destructive testing in optical methods may not always be an option.

An alternative method for measuring thickness has been described in the work of Cavinato *et al* [19]. Here, two blue light lasers were used to map the thickness of a bulge specimen without disturbing the membrane [19]. As the novel apparatus developed by Cavinato *et al* was not accessible to the researcher, nor was it within the scope of this project to replicate, this method of thickness determination has been left for future consideration.

2.2.2 Optical Displacement Tracking

An alternative to crosshead displacement measurement was optical displacement measurement (ODM) [20]. ODM has the edge over other techniques in that it has capacity to capture full-field displacements with a non-contact approach. Both of these characteristics were key for capturing the displacement of low-stiffness anisotropic materials like MT [20].

ODM has a few different styles that depend on the equipment available to the researcher. The simplest form of ODM is discrete feature tracking on the specimen's surface. This style typically uses four or five dots placed in a square shape with the optional fifth dot being used to mark the centre of this square. Bellini *et al.*'s implementation of such a method was shown

in Figure 2.5(a). Table 2.2 showed how this approach was used by many researchers. This was likely due to there being easily accessible *Matlab* modules that accommodated this approach.

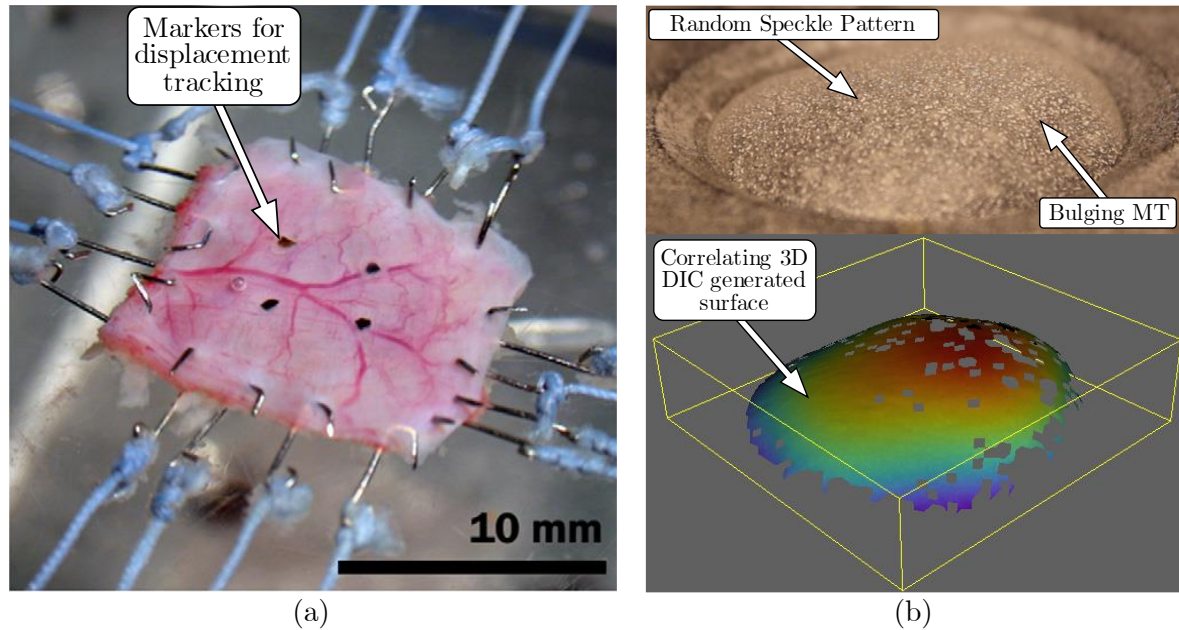


Figure 2.5: (a) *Discrete marking strategy by Bellini et al. adapted from [11] with permission*, (b) *Speckle and measured displacement field produced using DIC*

A similar approach taken by Meador *et al.* [21] was to use an asymmetrical shape to track distortion. The shape was used to capture residual strains *in vivo* to offset the applied strains *in vitro*. This did not differ significantly from the discrete point feature tracking methods. Likewise, both approaches only required one camera to view the specimen from above to avoid parallax errors.

It is impossible to measure three dimensional displacements in this way. Bulge surface like Figure 2.5(b) can't be measured without the use of mirrors to achieve stereoscopic "vision" seen in Figure 2.6(b). This stereoscopic limitation is inconsequential when loads and specimens share one plane. Unfortunately, PBT testing was not always fully planar. Out of plane displacement of the membrane cannot be determined adequately using monoscopic image capture.

Bulge testing required three-dimensional displacement measurement using stereoscopic image capture like that of Tonge *et al.* in Figure 2.6(a). This was possible to do with discrete markers on the specimen surface, however it may have misrepresented the curved surface of the bulge profile. This was because such grid-based methods of marking relied heavily on accurate mark placement.

The initial grid spacing formed the calibration for all further conversion between pixel position and true spatial position [22]. This calibration can also be done using a calibration target (a checker pattern with known dimensions and markings for orientation) to convert pixel location to spatial position.

For 3D calibration, simultaneous stereoscopic image capture of a target in multiple orientations was needed. This ensured that the ODM algorithm could track spatial position using the perspective difference of the two viewpoints. However, even with accurate calibration, strains

computed from a grid method were fundamentally limited by grid spacing. This method was challenging enough to use with a rigid material like steel. To follow this method with MT would prove highly ineffective and inefficient.

The alternative approach to evenly marking out a dense grid of points is to use a random speckle pattern of points upon which a virtual grid of points can be overlayed to track. This approach is otherwise known as digital image correlation (DIC)

Once calibrated, the algorithm creates a virtual grid pattern of points to track from images of a speckle pattern. Each grid point is tracked by creating an identifier of grey values in a facet of pixels around it. This facet was compared between images and moved with the speckles; thus, the displacement of a virtual grid point was determined by the correct identification of the facet in each image and comparison to its initial position. A useful reference on DIC in the context of bulge tests and soft materials was Machado *et al.* [23].

As Machado *et al.* discussed, DIC has its shortcomings and relies on uniqueness of each facet to prevent poor correlation and thus increased uncertainty in displacement [23]. It is hampered by brightness differences between images taken by each camera and the number of pixels available to determine grey values in a facet, ie camera resolution [23]. Other factors might include uneven lens or aperture effects between cameras that are too large to be corrected for. Limitations were sometimes software related, however with commercial systems, it was more often operator error that causes such problems. All the above problems are avoidable and can be managed with due diligence.

Speckle quality was (like in all ODM) a very important aspect of DIC and quality of results depended on the level of uniqueness and contrast in the speckle pattern. This marking strategy was far more forgiving than any of the prior methods in that it was random and did not require exact placement, which made it ideal for MT.

From Table 2.2 we saw that the use of optical feature tracking was prevalent among PBT researchers. This was not as effective at estimating strain within the square of points as DIC. This was because the markers were used to linearly interpolate the strain behaviour of an anisotropic (and possibly heterogenous) material.

Consider a heterogeneous sample containing a small, vascularised region, where deformation is only tracked with two markers on either side. The localised strains around the vascular region will not be apparent, as the strain calculation is averaged between the two markers. By contrast, with DIC, the random speckle allows displacement measurement at smaller intervals and hence finer resolution of localised strains. Any heterogeneity would be easy to identify in the displacement field and addressed appropriately.

3D DIC offered the best method to capture full field displacement of the MT. As a commercial DIC solution was available for use with this project and all other methods seemed to require far greater effort to get right, it was decided to proceed with the available method.

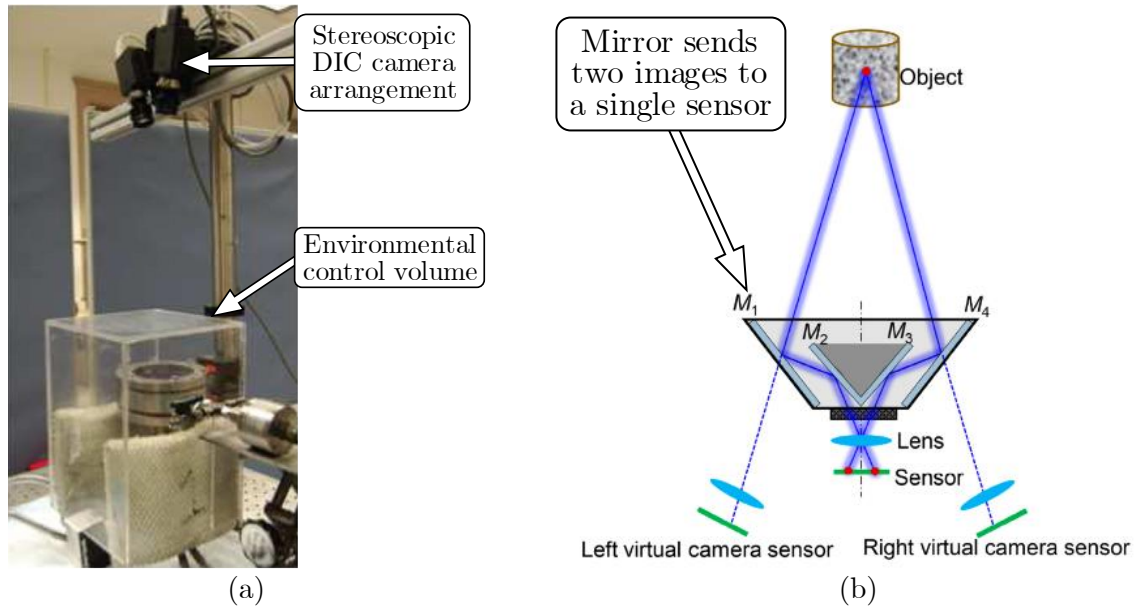


Figure 2.6: (a) A control volume set up by Tonge *et al.* [16] adapted with permission, (b) Mirror based stereoscopic DIC adapted with permission from [24]

2.2.3 Environmental Control

Temperature has significant effect on the load response of MT. Ambient temperature in the relevant literature was either at room temperature (25°C), or close to human body temperature (37°C). Human myocardium and murine skin were tested at 37°C to ensure that the tissue would give representative mechanical data for *in vivo* tissue [21], [25]. Room temperature was used by Sacks and Choi to test porcine SIS and canine pericardium respectively [6], [26].

Humidity influences evaporation rate, which in turn effects tissue moisture levels. In the work of Bose *et al.*, collagen films tested in submerged conditions featured a 10.2% reduction in ultimate tensile strength (UTS) with respect to a specimen exposed to ambient air [14]. Failure strain increased by as much as 16% for submerged film tests in the same comparison [14]. These changes between dry and pre-hydrated samples were substantial. The UTS of hydrated collagen was a mere 3.5% of the dry. Wet strains were greater than the dry by at least 22%. Thin, collagenous SIS would react similarly, thus tissue hydration was a key factor to control.

Sacks and Gloekner also tested SIS and performed PBT tests with the specimen floating on a saline bath, this both hydrated the MT and slowed the process of decomposition [6]. Bulge tests conducted by Tonge *et al.* & Lakhani *et al.* were inside control volumes [16], [17] seen in Figure 2.6. This prevented rapid changes in mechanical properties caused by leaving the tissue open to atmosphere. They also used a phosphate-buffered saline (PBS) solution as their inflation medium, which served to prevent both tissue dehydration and degradation.

Tonge *et al.* did not observe statistically significant differences between high and low humidity test environments. This they attributed to the fact that the dermis dominated the mechanical behaviour of the tissue [16]. Here, the dermis remained exposed to the PBS which helped retain moisture content of the MT [16]. While this may be true, it was more likely that dehydration was prevented by skin's natural keratinisation and intracellular lipids [27]

Figure 2.7(b) shows how Diab *et al.* [28] bulge tested fresh human breast and abdominal skin exposed to atmosphere. This approach was appropriate to the tissue used and the method of testing as the natural keratinisation of the epidermis prevented escape of moisture. Figure 2.7(a) shows how Kumaraswamy *et al.* used moisture control for the same tissue when uniaxial testing in [29]. This was necessary to prevent the unkeratinised parts of the skin from releasing moisture to atmosphere. This specialised uniaxial tensile test (UTT) arrangement used by Kumaraswamy *et al.* was not commonplace. Other researchers such as Pissarenko *et al.* manually moistened the cut tissue surfaces during testing to avoid dehydration. [7].

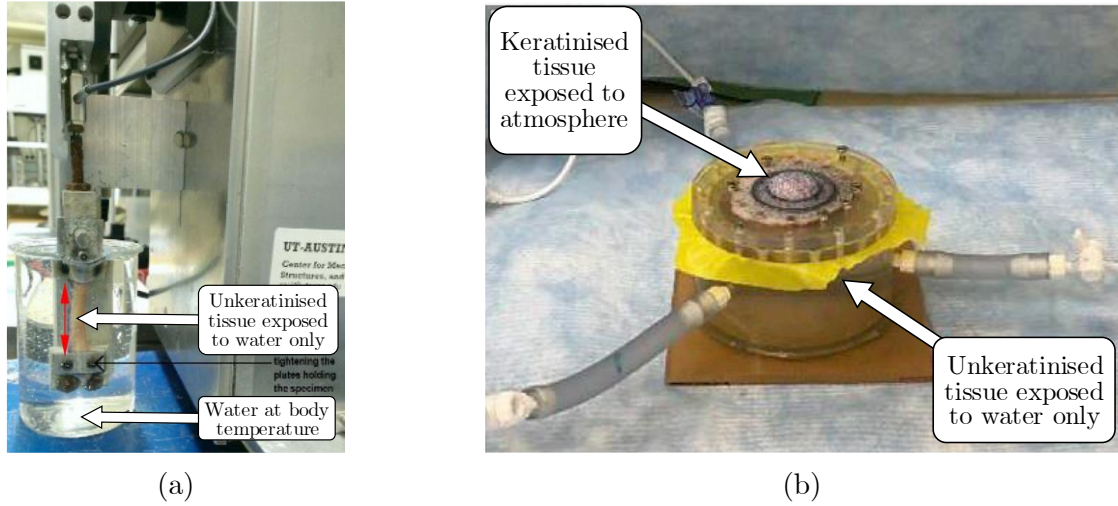


Figure 2.7: (a) A controlled environment created for uniaxial testing of breast skin adapted with permission from [29], (b) Bulge specimen exposed to atmosphere on external keratinised surface adapted with permission from [28]

The SIS is a single layer of a thicker MT. This meant it did not possess any dehydration prevention measures like skin does. MT moisture content held great significance, as a single quasistatic test could exceed an hour as in the case of Tonge *et al.* [16]. This study aimed to test one specimen on two devices which meant longer exposure to the environment.

The effects of speckling methods on the load response of the MT seemed unclear in the literature. Some speckles or de-shining dustings could have significant effect on the moisture content of the outermost layer of the MT specimen.

As the objective of this study was not to fully characterise the material, it was unnecessary to reproduce *in vivo* temperatures. Tests therefore took place at room temperature and with moisture control.

2.2.4 Tissue Preconditioning

MT is a viscoelastic material [30]. Literature shows that it exhibits a logarithmically decreasing peak load for a repeated fixed displacement. Thus, MT only behaves elastically after preconditioning [31],[32]. Wong *et al.* [33] agreed with Hukins [34] that preconditioning tissue probably changes its behaviour due to displacement of tissue fluids such as water and glycosaminoglycans (GAGs).

To achieve results that can be repeated by others, researchers have typically reported their results after preconditioning. There was, however, variation in the preconditioning parameters

between studies. Some preconditioned their specimens below the test load, then incrementally increased the peak load for a set of tests until failure [31]. Others preconditioned at the peak load of the test and only reported the values from the fifth or sixth cycle and thereafter proceeded to increase loading [11], [32]. Sacks' findings for biaxial response of MT agreed with Kumaraswamy *et al.* who generalised the response to create the plot in Figure 2.8 [29]. Sacks did not observe much change in response between the 2nd and 12th cycles[32].

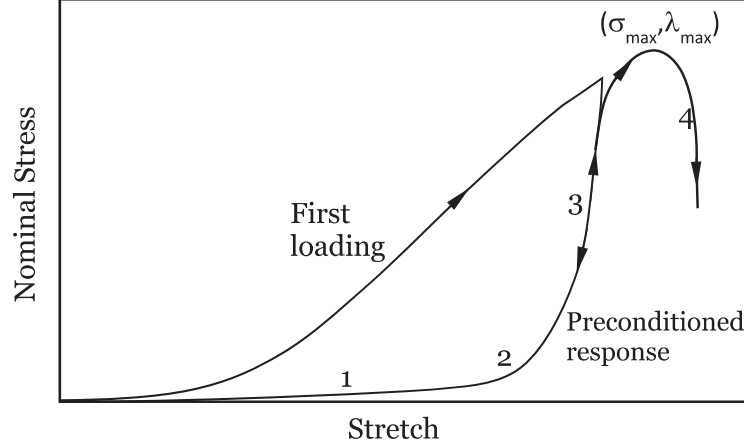


Figure 2.8: A typical stress-stretch response before and after pre-conditioning, used with permission [29]

In tensile testing of MT, preconditioned specimens have a characteristic behaviour of an initial low modulus in zone one of Figure 2.8. After this, there is an observed “knee-point” in the curve (zone two). Here, modulus rapidly increases until a third zone of a consistently high modulus followed by softening and failure in zone four. The first loading of the tissue has a much higher modulus that increases initially and then steadies to a more gradual slope.

Kumaraswamy *et al.* explained zone one of the curve as the stretching of an elastin network rather than of the elastin itself until stage two features uncrimping of collagen networks that straighten to align with the load, resulting in the much larger stiffness of zone three [29].

Pissarenko *et al.* found preconditioning inappropriate when the risk of tissue damage was unacceptable [7]. Tonge *et al.* were among the few who found the impact of preconditioning in their human skin bulge tests to be negligible. This finding was partly agreed upon by Diab, Kumaraswamy and Reece *et al.* when they tested human breast tissue [28]. They differed in that they found preconditioning useful for higher pressure tests. Kumaraswamy *et al.* [29] explained that preconditioning can help capture the *intrinsic elastic response* of the tissue described by Fung [35]. Thus, before reaching a preconditioned steady-state, specimen behaviour was indicative of the viscoelastic behaviour of the tissue [29].

It was clear from the literature that preconditioning is necessary if attempting to compare MT tensile test results. It was also clear that the capture of some of the preconditioning cycle behaviour would be useful in characterising the viscoelastic behaviour of the tissue. The findings of Sacks [32] regarding the number of preconditioning cycles per test were used extensively in the experiment design of this project.

2.3 Bulge Testing Methods

The simplicity and limited number of boundary conditions on a BTR make it the easiest biaxial tensile test to perform. Despite this, it produced the most complex data to analyse.

2.3.1 Clamping

Before inflation, the MT must be firmly sealed along the circumference of the bulge aperture. Clamping and sealing methods in the literature varied. Tonge *et al.* used glue to seal human skin tissue against a Plexiglass plate [16]. Diab *et al.* used an O-ring to seal the rim of the cover plate and made rounded edges on this plate to prevent stress concentration [28]. Lakhani *et al.* used a combination of the above; using glue to secure human skin tissue to a plate and an O-ring to seal around it [17].

None of the studies attempted to impose different strain ratios on the tissue with elliptical clamp apertures. Such apertures have successfully imposed different extension ratios on specimens, thereby facilitating improved material characterisation [12]. This required changing the clamp plate to achieve these different ratios. Clamping changes like this would be problematic when performing multiple tests on the same piece of delicate tissue. Clamp plates would also need to be sized to the available tissue dimensions.

More practical extension ratio variation with PBT testing is discussed in section 2.4.4.

2.3.2 Inflation

Syringe pumps were used almost exclusively in bulge testing research of MT [16], [17], [28]. These could best provide quasistatic flow rates at the pressures required for MT testing.

The mechanics of bulge testing prescribed a highly unstable initial MT position with very little restorative force until significant displacement was achieved. This led to highly non-linear strain-rates during a test if a constant inflation rate was applied [36]. This problem was addressed by Lakhani *et al.* who applied an increasing inflation rate using a syringe pump to achieve near-constant strain rate [17].

With water commonly chosen as a medium for inflation, the pressure increase during inflation needed to be offset by the head between the pressure transducer and the membrane apex [36]. These pressures were then used to calculate the stresses on the membrane.

2.3.3 Stress Calculation

The calculation of membrane stresses in bulge testing of MT could not be based on spherical pressure vessel formulas due to the non-spherical deformations observed in anisotropic materials [23]. Machado *et al.* applied a curvature tensor field approach that was populated using 3D DIC data from bulge testing to determine the stresses in non-axisymmetric bulge tests [23]. Their approach has been used extensively in MT bulge testing [16], [28].

The above assumed a uniform specimen thickness, which is not necessarily true for MT. For very thin membranous tissues, like SIS, large variations in specimen thicknesses had been observed and deformations were significantly non-axisymmetric. Regions with small or large

curvatures could not be identified as being due either to modulus variation or to tissue thickness variation. The only remedy to this problem would be to take positional measurements of the membrane thickness to help accurately define the membrane mesh in a finite element analysis (FEA) approach.

Numerical approaches were a common alternative or concurrent method of calculating stresses in MT membranes[37]. FEA was typically used inversely to determine the parameters of the selected material model [23], [28], [37]. This approach would use the recorded pressure history as a load on the membrane's lower surface and, usually, a fully fixed edge boundary condition on the membrane [37]. Diab *et al.* used a model of the clamping plate for the membrane to interact with during the simulated inflation.

As this study only made use of bulge tests to identify preferential fibre orientation, the details of the bulge test stress calculations have been omitted for brevity.

2.4 PBT Testing Methods

Planar biaxial tensile (PBT) testing was the most practical way to rigorously quantify the full load response of MT. This was due to its ability to easily test the wide range of tension ratios required to best characterise MT behaviour [38]. A BTR could only impose an extension ratio boundary condition and not control the tension ratio close to the ROI.

Being able to work with very small samples, PBT testers were highly economical in their use of tissue. They also did not require changes in mounting to test different tension ratios. All loads and strains occur in one plane as opposed to a three-dimensional bulge which allowed for simpler results analysis.

There were unfortunately more variables to control in PBT than in bulge testing, for example, specimen shape and gripping methods.

2.4.1 Mean Fibre Axis identification

PBT tests typically pull in orthogonal directions (x & y) which require square or cruciform specimens. Significant variation was observed in PBT tests on the same MT with different specimen orientation. Therefore, methods of regulating specimen orientation wrt. the tissue were used by researchers.

MT has been shown to contain fibres which arrange themselves into a cross-linked network like that of Figure 2.2. This network usually exhibited preferential direction(s) which were linked to localised movement or the constraint requirements of the surrounding tissue.

Wood has a highly preferential fibre lay, predominantly related to withstanding bending loads on the tree branches and trunk. Cellulose fibres arranged longitudinally and held together by lignin and hemicellulose are highly optimised for dealing with this loading. Humans have exploited this aspect of wood which makes it easy to cut but very strong when used in tension or bending.

It would not make sense to cut tensile specimens out of wood in random orientations and expect to see similar UTS results. A similar principle has been applied with MT. However, it was not possible to assess its “grain” with the naked eye. Even with special optical techniques such as those used to produce Figure 2.2, it can be very difficult to identify a mean fibre axis (MFA) and a cross fibre axis (CFA).

Some methods of assessing the MFA are polarised light microscopy [39], phase contrast microscopy [2] and small angle light scattering (SALS) [6], [8].

Sacks, using SALS, and checking with polarised light microscopy [6] identified the MFA of each specimen by selecting only minimally vascularised regions of the SIS. Vascularised tissue was too arduous to analyse given that blood vessels obstructed measurement. Furthermore, regions between blood-vessels exhibited similar MFA to the minimally vascularised SIS [6]. Thus, the effect of heterogeneous tissue zones on the bulk deformation response was not quantified and may have resulted in misleading measurements.

Assessing fibre microstructure in this way required optical clearing of the tissue which would influence its load-response. These lengthy processes would further hamper the rapid testing required to measure fresh MT before degradation onset.

A less common approach was to perform histological analysis. This produced insight into tissue composition and structure at the scale of the sample which was seldom of the same scale as the specimen. Histology is an inherently destructive process taking at least 24 hr to process samples. True tissue behaviour can also be misrepresented when cutting sections due to variations in alignment and tissue flatness.

Researchers commonly assumed MFA orientation based on generalisations like Langer’s [40] shown in Figure 2.9. These MFA orientation maps were not always very detailed and required the assumption that generalisation was appropriate to the specimen. These simplistic approaches did not remedy the problem of widely varying MT tensile data.

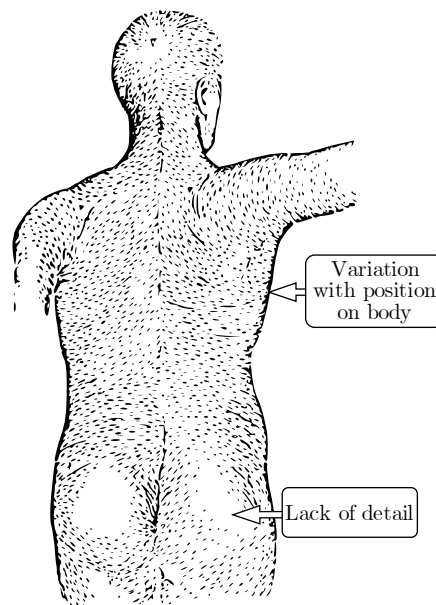


Figure 2.9: *Langer’s lines generally depicting the MFA of human skin adapted from [40]*

In the case of MT excised from tubular structures like arteries or intestines, such generalised approaches may be valid. Bellini *et al.* excised square specimens from porcine GIT noting its position and orientation wrt. its coordinate frame [11]. This made sense given the MT only had two main directions, along the GIT or around its circumference.

Parent organ/body geometry has guided MT specimen preparation in various studies[21], [41]. Defining the test axes for a biaxial test in this way, while commonplace, is questionable. This highly tissue-specific approach also relied heavily on human skill to accurately prepare samples. Furthermore, it required detailed documentation of specimen orientation wrt. parent organs to avoid confusion of MFA and CFA results.

Figure 2.10 shows how Choi and Vito used a method of extension and marking to identify the MFA [26]. This was a manual process which had multiple opportunities for bias and operator error. Despite this, the concept of this method held great promise for improved applications.

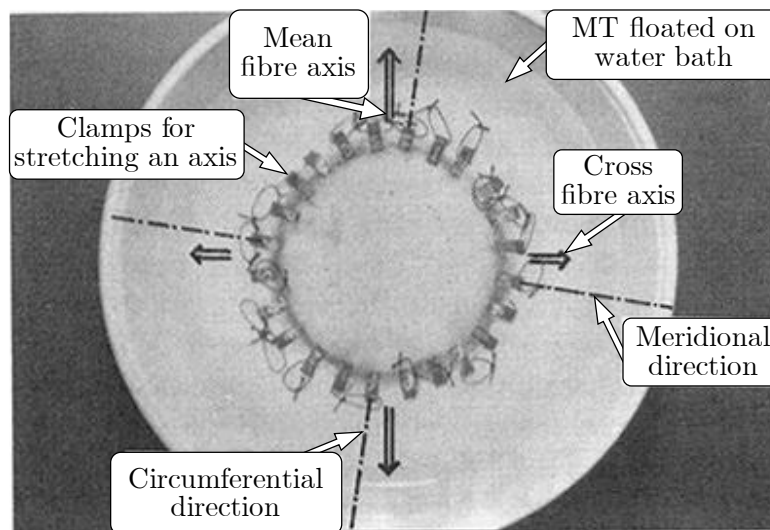


Figure 2.10: *Tissue stretching method applied by Choi and Vito to determine MFA, adapted from [26]*

Choi and Vito made two equidistant marks from the centre of the specimen along the line of a uniaxial preload. These were repeated at 15° intervals around a circular specimen. When the tissue relaxed, these points formed an ellipse. The shortest radius of which was the axis of lowest deformation (also the MFA).

This method was used to orient specimen preparation and held potential to be emulated using a BTR. A bulge test would produce a continuous version of Choi and Vito's discretised deformation. Such an approach was not found by this researcher in the available MT literature.

Correct MFA identification was a confounding factor in testing MT PBT specimens and has led to meaningless model parameter fitting once outside a material-dependent threshold of misalignment [42].

This was the key reason to develop better MFA identification methods in this study. Correct MFA identification however can be rendered useless if specimens are not mounted correctly.

2.4.2 Mounting and Specimen Design

PBT specimens have been gripped and shaped in many ways. The rigorously standardised methods of PBT testing engineering materials can only be loosely applied to MT. Specimen design and gripping standards for MT have not been resolved as yet[43], [44].

Figure 2.5(a) and Figure 2.11 show specimen shapes and mounting methods unique to low stiffness materials such as MT. MT specimens were typically cruciform shaped like Figure 2.13(b) or square like in Figure 2.11. Square specimens made economical use of tissue, while cruciform specimens keep mounting stresses well away from the ROI.

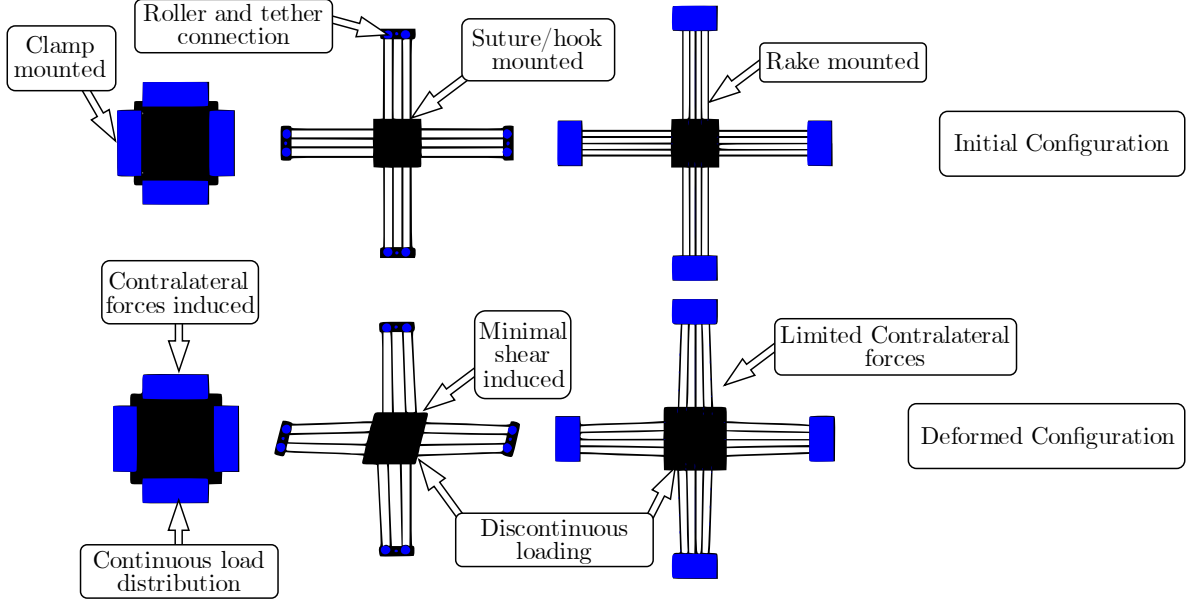


Figure 2.11: *Induced PBT deformation using grips, sutures and rakes, adapted from [44]*

Figure 2.11 showed that square specimens facilitate a variety of gripping methods however, none of these resulted in a homogeneous stress state. It was observed by Fehervary *et al.* that all mounting methods strike a balance between the following [44]:

1. Highly discontinuous loading: Minimal shear & contralateral force transmission
2. Smooth load distribution: Unmeasured contralateral forces.

Fehervary *et al.* used an argument of compromise to settle on square specimens with rakes[44].

The cruciform specimen was usually only clamp mounted as the arms served to minimise contralateral forces. Some cruciform standards for steels stipulated slits in the arms to give results like that of the rakes in Figure 2.11.

These alternative methods were discussed extensively by Avanzini and Battini [45]. Using a hyperelastic material, they found that the cruciform with slits (pictured in Figure 2.12) resulted in efficient load transfer to the centre of the specimen.

At higher loads, tapered arms resulted in high stress & strain in the ROI, however load uniformity decayed significantly. It was noted that adding a radius to the cruciform specimen improved loading efficiency and decreased stress concentration.

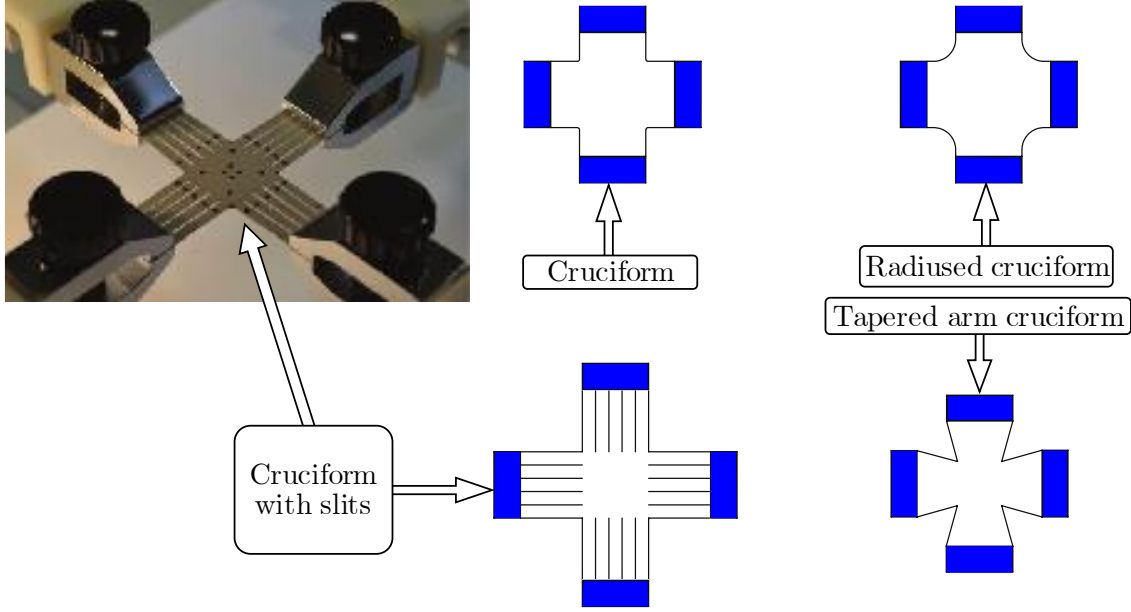


Figure 2.12: *Variations on the cruciform specimen (undeformed), adapted from [45].*

Though not pictured in Figure 2.12, Avanzini and Battini tested a square specimen with hooks, which proved to be effective although prone to misalignment [45]. This may be worsened for MT which exhibits more anisotropy than an elastomer. They also noted that some of these approaches would load MT unfavourably by imposing stress concentrations.

In this study, a radiused cruciform was used to mitigate stress concentration. Furthermore, time constraints, unreliable lab-access and delays in equipment manufacture during the COVID-19 pandemic made this a logical choice.

2.4.3 Pre-load

Pre-loading of MT specimens was common to many studies. Meador *et al.* used the lowest recordable value of their loadcell (50 mN) as a preload. This established a standardised reference configuration for their data analysis however, the effects of neglecting this step were not investigated[21]. Bellini *et al.* used a 10 mN preload and assumed that the tissue was sufficiently planar at this tension [11]. It is supposed that this was done, here and in other studies [6], in the absence of 3D DIC data. Such data could have been used to define the initial configuration based on measured specimen flatness.

PBT testing under load control was not possible in this project. Preloading was replaced with careful alignment, tissue transfer and 3D-DIC strain measurement.

2.4.4 Tension ratios

Seibert *et al.* offered a useful summary of the necessity of imposing different biaxial stress states that help to characterise a material model that can predict the response of a hyperelastic material under load states other than uniaxial or equibiaxial tension[38]. The plane of the invariants listed in the equations below was consulted to make this need clear. This approach only worked if the material was assumed incompressible, which was true for most MT.

The plane is spanned by the first and second principal invariants ($I_{\mathbf{B}}$ and $II_{\mathbf{B}}$) of the left Cauchy-Green deformation tensor \mathbf{B} from equation 2.1 and 2.2 [38]. The result of the third invariant shows the material's incompressibility and stipulates volume conservation.

$$I_{\mathbf{B}} = \text{tr}\mathbf{B} = \mathbf{B}:\mathbf{I} \quad 2.1$$

$$II_{\mathbf{B}} = \frac{1}{2}[(\mathbf{B}:\mathbf{I})^2 - \mathbf{B}^T:\mathbf{B}] \quad 2.2$$

$$III_{\mathbf{B}} = \det\mathbf{B} = 1 \quad 2.3$$

Seibert *et al.* [38] applied numerical values for uniaxial tension and equibiaxial tension to plot a very similar curve to that of Sasso *et al.* in [46], which is depicted in Figure 2.13(a). The colour map applied to both components of Figure 2.13 shows the stress states at play within a single PBT test.

Seibert *et al.* explained that all possible tensile stress states lie between the curves of equibiaxial tension and uniaxial tension [38]. Therefore, testing a material at different tension ratios would help to produce invariants that can be used to characterise the material model better for load cases between these two profiles.

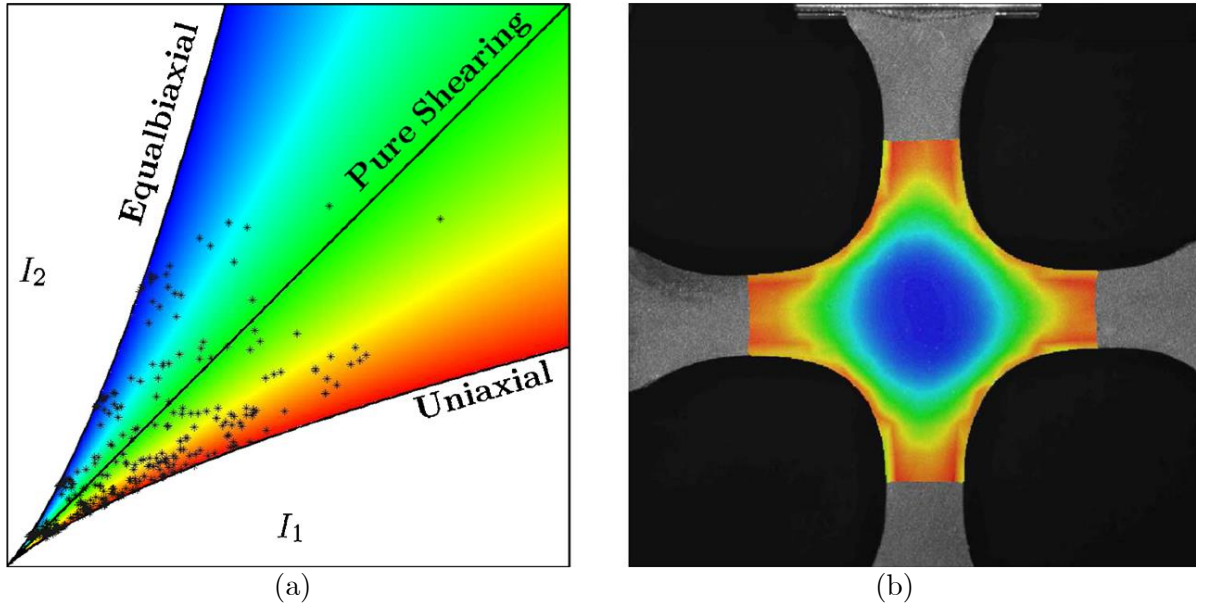


Figure 2.13: A colour map linking the (a) plane of invariants to (b) a PBT test, sourced with permission from [46]

PBT research appeared to use very similar tension ratios with following five tension/extension ratios 1:1, 1:0.75, 1:0.5, 0.75:1 and 0.5:1 [11], [25] being the most common.

Fehervary *et al.* used three of these and added a fourth that represented the physiological strain of the load case they were modelling [44]. Researchers were not always clear on their use of tension ratios vs extension ratios. Tension ratios were prevalent if their PBT testers facilitated load control. Due to the equipment limitations in this project and similar studies on SIS using extension control [6], [21], testing was done under displacement control.

2.5 The State of Local Research

BISRU at UCT has only recently reached the maturity in facilities to undertake testing of MT. Due to the absence of local facilities capable of testing very soft membranes, all of the studies up to this point have been in development of mechanisms to eventually test the mechanical properties of MT [12], [36], [47], [48]. These studies used elastomeric materials as MT surrogates to commission the equipment that had been developed.

Within BISRU, Pillay investigated DIC marking strategies for membranous tissues but didn't perform controlled mechanical loading and measurement of his specimens [49]. This project was therefore the first within BISRU to work with MT.

2.5.1 Research objectives

There has been an ongoing project within BISRU to quantify the mechanical properties of human tissue and bone. Computational models using these properties would improve the understanding of human body response to blast or impact loading. The skin is a human's first point of contact with blast and impact. This fact was a driving force in developing equipment that could biaxially test MT with the end objective of characterising human skin tissue [12], [36], [47]–[49].

Beyond BISRU laboratories and within the locality of South Africa, facilities to mechanically test MT are extremely limited. It is supposed that little mechanical study of human skin is being done in Southern Africa and perhaps all Africa. This motivated continuation of this study as the representation of African skin and other MT mechanical properties in publications would otherwise remain limited.

2.5.2 Bulge Testing

Curry developed a quasi-static bulge tester to capture low strain rate behaviour that could lead to higher rate tests [36]. He designed, built and tested a BTR using silicone rubber as a MT surrogate [36]. Figure 2.14 shows Curry's BTR which had application limits on bulge aperture, maximum pressure, and strain-rate [36]. The quasi-static BTR featured a stepper motor operated syringe pump with a leadscrew to improve gear reduction. This was used to reach a maximum strain rate of 0.03 s^{-1} with the aperture he selected [36]. This BTR was selected for use in this project as it was best suited for quasistatic testing.

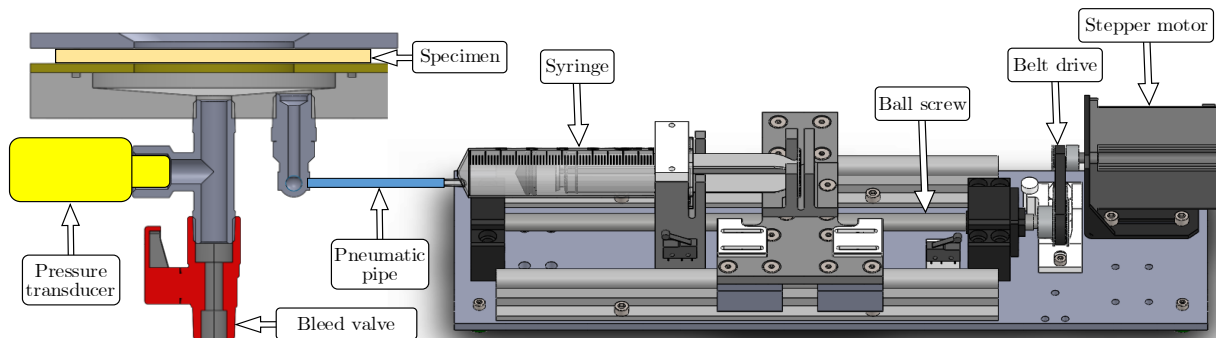


Figure 2.14: *Schematic of Curry's bulge test rig, adapted from [36].*

Quasistatic equipment was developed as a validation method for high strain-rate models. Earlier studies by Graham and later Fischer worked to develop bulge test apparatus higher strain-rates [48], [50].

Figure 2.15 pictures Fischer's work on a pneumatically actuated BTR. He aimed to develop a testing device that could work for a wide range of pressures, and hence a wider range of materials, owing to a reconfigurable piston system [48]. This BTR could test at intermediate strain rates, furthermore it featured proportional integral closed loop load control [48].

Bulge apex displacement was used to calculate the stress based on an analytical model [48]. As Fischer couldn't access 3D DIC measurements, his capacity to measure strains & strain-rate were limited. He also used silicon rubber for commissioning tests however, the system was less readily adaptable to MT testing than Curry's BTR [48].

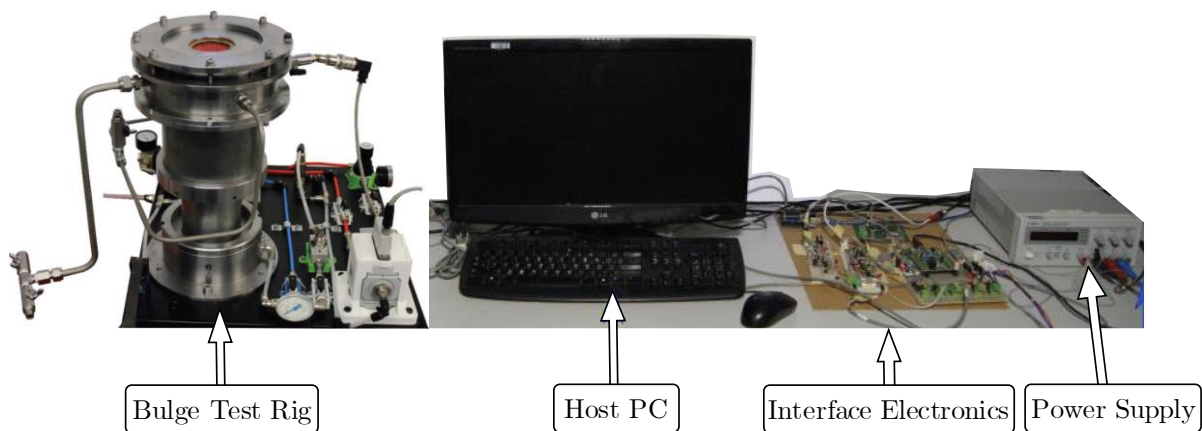


Figure 2.15: *Bulge test setup developed by Fischer adapted from [48].*

Figure 2.16 schematically shows Graham's high strain-rate BTR. He used a pressure transducer to capture the load history and a high speed DIC system to capture displacement [12]. Silicone rubber was tested at strain rates ranging from 0.26 s^{-1} to 827 s^{-1} [12]. The high-speed camera system was the limitation on increased strain-rate. Graham also used ellipsoidal bulge apertures to induce differing strain ratios on the specimens [12].

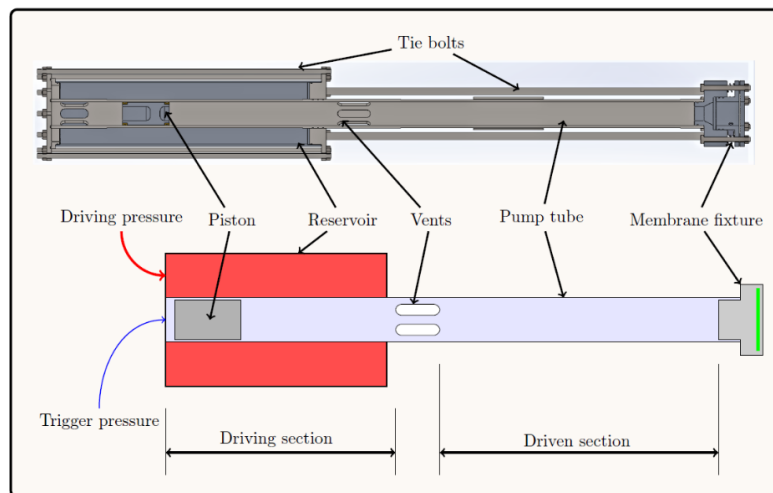


Figure 2.16: *A schematic of Graham's high strain rate BTR from [12].*

The lessons learned from Fischer and Graham's work were applied in using Curry's BTR. Here, MT testing under quasistatic biaxial tensile load formed a basis for future dynamic study.

2.5.3 PBT

Caine built a low strain rate PBT test platform for MT and commissioned it using silicone rubber specimens up to maximum strain rates of $0.8/s$ [47]. Figure 2.17 shows how Caine used individual stepper motors on each axis that could facilitate extension ratio variation in testing. The system used *GRBL* and *Arduino* motor controls. This facilitated G-Code programming of the PBT tester [47].

Caine built the PBT tester in a displacement control configuration. This meant that initial positioning and alignment of the arms was very important to do before testing. Fischer's difficulties in implementing load control motivated its exclusion in Caine's design.

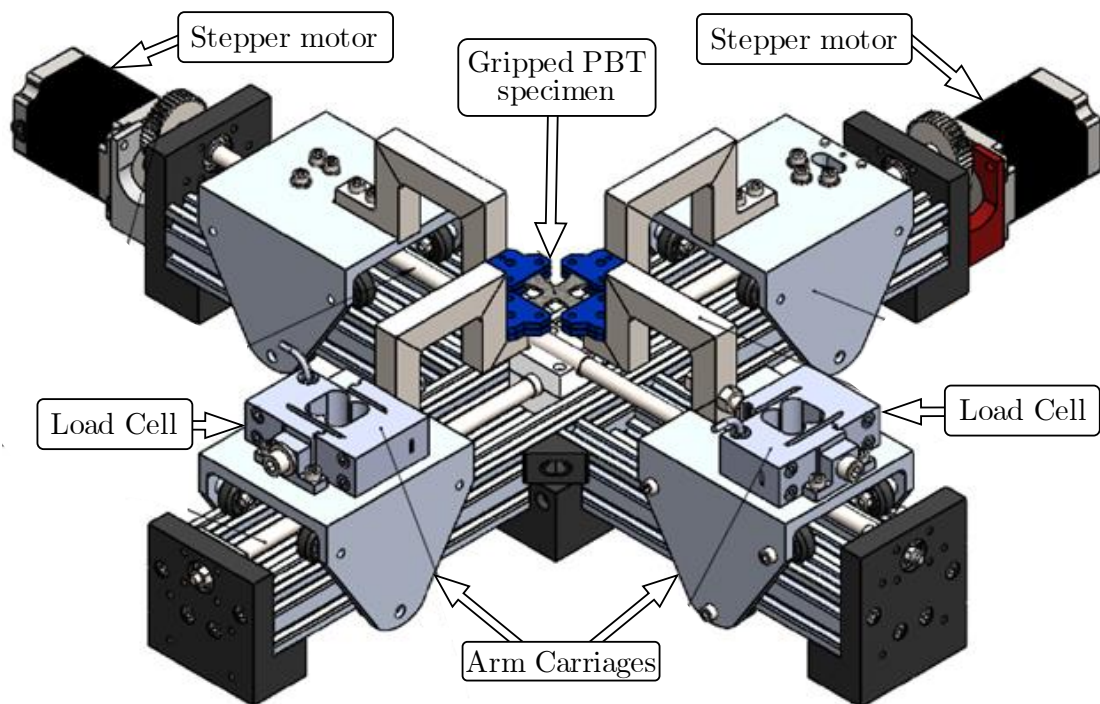


Figure 2.17: *Schematic of Caine's PBT tester, adapted from [47].*

2.5.4 Research Gaps to Explore

BISRU's MT biaxial tensile testing capacity was less mature than that of many researchers cited in this chapter. Many of these better-established researchers have also already found niches in the MT research field such as PBT or bulge testing. It is noteworthy that the first BISRU research grant exploring MT was applied for in 2015 and this has supported the development of all the test equipment discussed in sections 2.5.2-2.5.3

It has been observed that there was room for a commissioning trial on MT. This trial would not only consist of the mechanical testing of tissue on the BTR and PBT tester. It was observed that there was need for a simple, low-cost and non-destructive method of determining specimen MFA before a PBT specimen excision. This was motivated by the large variation in MT PBT test results due to specimen excision orientation.

Methods applied by Sacks [6] and others [51], [52] to determine MFA were not suitable for the style of testing of MT planned within BISRU. Given BISRU's strong ties with a local tertiary research hospital, it is planned that skin tissues be tested almost immediately after excision to determine the most accurate *in vivo* properties. Tissue processing delays from advanced microscopic or histological methods of MFA identification would necessitate freezing of tissue. Secondly, following Langer lines and other generalised MFA knowledge was excluded based on its reliance on too many assumptions and, further, relies on exact documentation of the tissue location and orientation *in vivo*. This would also be impractical as it relies on the rigor of health-care workers in following a procedure unrelated to the purpose of excision such as a plastic surgery procedure.

These methods were not ideal and thus a gap was identified: there was need for a method to rapidly estimate the MFA of MT before PBT specimen excision. The approach taken was to exploit the ease of specimen preparation and testing of MT on a BTR which required no prior knowledge of MFA.

Using a very low strain bulge, it was hypothesised that the MFA could be determined for a specimen rapidly without prior knowledge of the parent tissue. This method relied on 3D DIC to determine the major and minor axes of an elliptical deformation contour.

In summary, this method offered to commission both PBT tester and BTR for MT research and further investigate a method of improving the speed, quality and cost-effectiveness of biaxially testing membranous tissues.

Chapter 3

Experimental Apparatus

This chapter explains the makeup and the use of equipment that was not developed in this study. These were the bulge test rig (BTR), the planar biaxial tensile (PBT) test rig and the commercial digital image correlation (DIC) system. Detailed descriptions of the development and commissioning of the BTR and PBT rigs can be found in the respective works of Curry [4] and Caine [5]. The same DIC system was used in both works to measure full-field displacements of membranes tested on the rigs. Pillay [50] was responsible for the development of DIC speckling methods that were utilised in this study.

3.1 Digital Image Correlation

3.1.1 Dantec Dynamics Istra4D

The methods used in this study were limited to optical non-contact measurements. Commercial DIC software, namely *Dantec Dynamics Istra4D*, was used for 3D displacement measurements in this study. It has been shown that DIC was superior to other motion tracking solutions as resolution was controlled in the software and is only limited by speckle pattern quality. Thus, it was an appropriate solution for both bulge and PBT tests.

3.1.2 Speckling Method

DIC requires a randomised speckle pattern, with sufficient contrast and speckle size. Methods of speckling had seen some development over the course of the commissioning trials. When silicone was first used as a MT substitute, dyed liquid silicone was centripetally spattered onto the specimens during the casting stage, prior to full cure of the substrate.

This produced large variation in DIC speckle pattern quality. More recent work used an airbrush to speckle using silicone-specific paint. This proved to be the most successful method of speckling for silicone. In the work of Pillay [50], black or white aerosol spray-paint was found to be the most effective marking strategy for the ovine SIS used in this project.

3.1.3 Typical Procedure and Evaluation Settings

The overall procedure used for gathering DIC data for a test was modelled on the descriptions of [54], which were as follows:

1. Hardware and Software Initialising
2. Camera Setup
3. Calibration
4. Image acquisition
5. Evaluation
6. Data Visualisation

The DIC cameras were transferred freely between the PBT and BTR machines to capture displacement data. Frequency of the DIC data acquisition was kept below 2 Hz to reduce the size of the data-files produced in the tests and to facilitate faster evaluation of data. DIC data was initially evaluated using the fastest possible settings combination, which sacrificed some accuracy, but allowed for rapid verification that images were of sufficient quality. The resultant uncertainty in displacements was presumed to be acceptable for the purposes of this study. When more accuracy was required, the same image set was re-processed later, using DIC settings optimised for accuracy over speed.

Force and pressure data was less voluminous than DIC data. Load acquisition frequency was therefore kept above 25 Hz to ensure a matching force was found for the image at the equivalent DIC time-step. Parameters typical to most evaluations performed in this experimental process are shown in Table 3.3

Table 3.3: *Typical DIC evaluation parameters used*

Evaluation Parameters	
Facet Size (px)	15
Accuracy (px)	0.2
Residuum (Gray values)	30
3D Residuum (px)	0.4
Grid Spacing (px)	10

3.2 Bulge Test Rig

3.2.1 System overview

Figure 3.1 schematically shows the bulge test rig built by Curry [4]. This consisted of a syringe pump and inflation chamber. The rig was operated by two interlinked Arduino Mega boards, one to control the motor and the other to record sensor information from the rotary encoder and pressure transducer.

The syringe was connected to an inflation chamber by means of a rubber hose. The inflation chamber featured a clamping assembly at the top to secure a membrane between a cover and backing plate. Pressure was measured in the inflation chamber by means of a 100 mBar pressure transducer. The transducer output was read by the second Arduino which fed the data to a computer. Displacement of the membrane surface was measured using digital image correlation (DIC) which was run on a separate computer. The DIC images were captured using twin cameras above the bulge surface and illuminated from above using a direct-current LED light source. This arrangement is depicted in Figure 3.1.

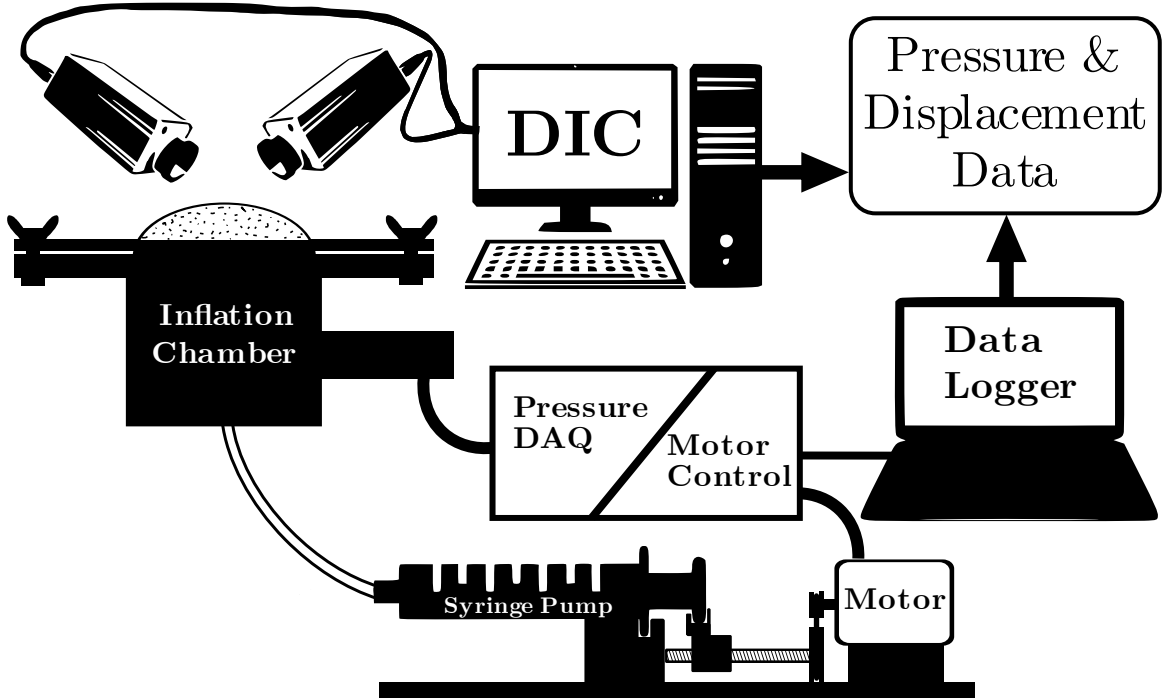


Figure 3.1: *Bulge testing set-up schematic*

3.2.2 Syringe Pump

While most components of the syringe pump were already fit-for-purpose in this project, it was necessary to make some changes to the software controlling the syringe pump.

Curry used silicone (Dragon Skin 10) as an MT surrogate to commission the BTR [4]. He tested silicone thicknesses that could cope with sharp pressure spikes in either polarity while

maintaining an airtight seal. This robustness meant that less control was required to test it. Curry's implementation of the following control system is presented in Figure 3.2(a):

1. Forward, reverse and stop controls.
2. Displacement limits on the syringe to prevent collisions
3. Pressure limit cut-off switch.

The delicate MT used in this project needed more control structures to prevent unintended rupture. These were as follows:

1. A soft limit switch on negative pressures
2. A specified inflation, pause and deflation cycle for a test.
3. Prevention of rapid motion in machine start-up that might burst a mounted specimen.

Figure 3.2(b) shows the inclusion of these pressure controls into Curry's original control system. These changes reduced specimen failures and regulated the pressure-time profiles of the tests. Curry's system would shut down the machine when the test pressure was reached and manual control was then required to deflate.

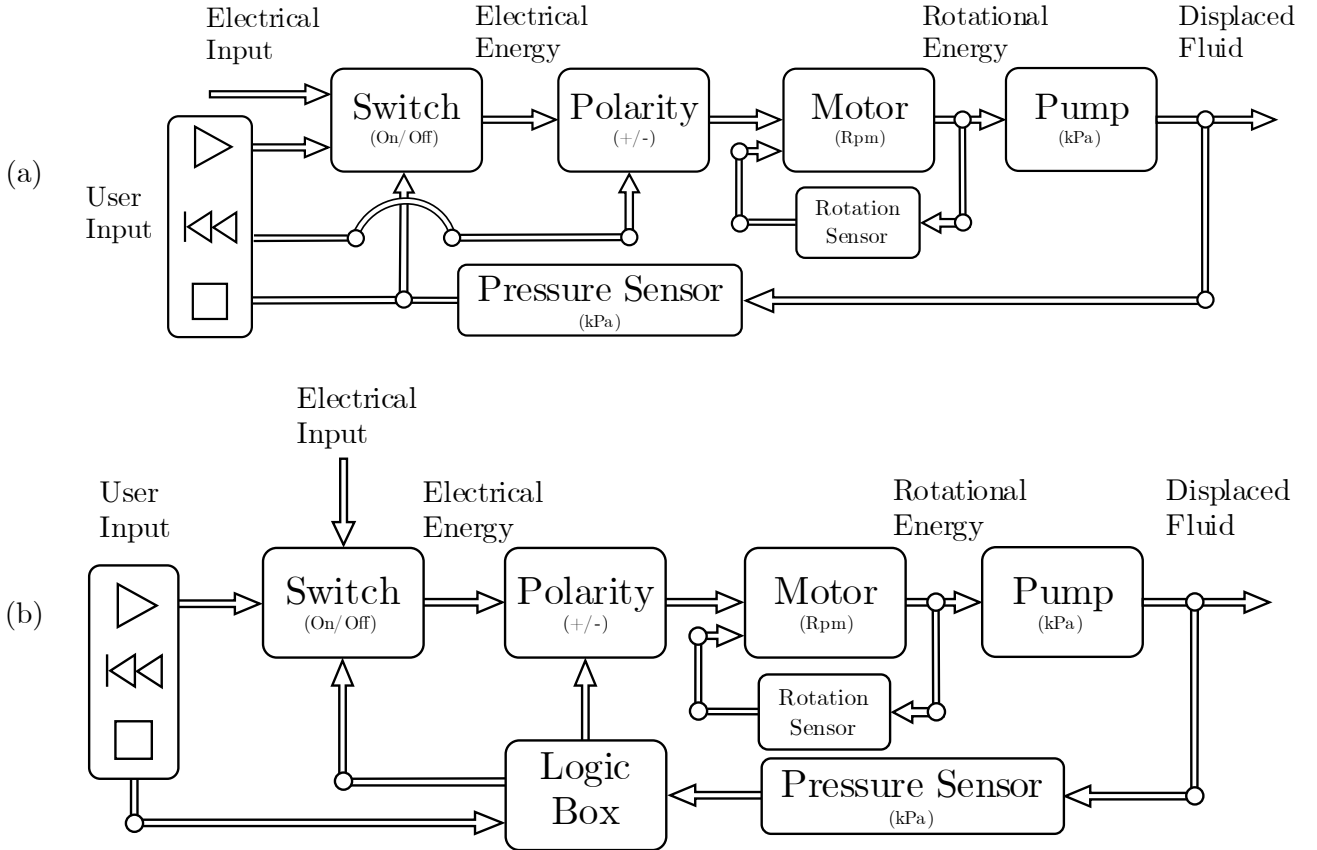


Figure 3.2: *a) Original BTR control system and (b) Updated control system.*

Initially, the BTR electronic systems were still based on prototyping board and jumper cable connections, shown in Figure 3.3(a). These were easily dislodged during operation, leading to errors and unreliable tests. The lab for testing the soft tissue did not afford space for this layout of cabling.

An enclosure was designed and built to contain both Arduinos and to provide pluggable connectors to external hardware such as the motor, PC and pressure transducer.

The enclosed wiring and tight set-up in the lab depicted in Figure 3.3(b) validate the need for the system enclosure. The original set-up would have hampered the testing process and could have led to specimens drying out while debugging was done in the likely event of a fault.

Due to the MT specimens in this project being much more compliant than the silicone rubber specimens used in Curry's MSc, the original 1 Bar pressure transducer was replaced with a 100 mBar pressure transducer to improve resolution and accuracy.

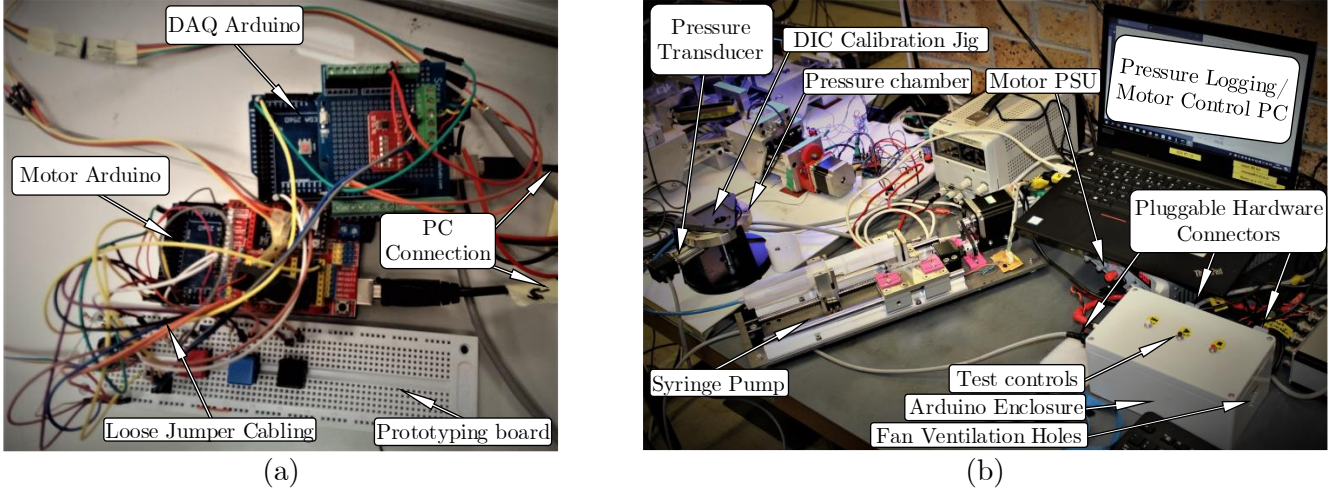


Figure 3.3: (a) Original BTR wiring. (b) Rewired and enclosed Arduinos showing limited lab space.

3.3 Planar Biaxial Tensile Tester

3.3.1 System overview

Figure 3.4 schematically shows the PBT test rig developed by Caine in his MSc dissertation (under examination at the time of writing) [5].

Like the BTR, PBT displacement was captured using 3D DIC on a separate computer with cameras positioned over the specimen. Motor control was achieved via a computer connected to an *Arduino*. This was connected to a GRBL CNC shield to control the motors and limit switches using G-Code.

Hottinger Baldwin Messtechnik (HBM) S2M 50N load cells were connected to HBM ClipX amplifiers/signal conditioner units. These were linked to the same computer as the *Arduino*. The PBT test rig ran one motor for each axis using a leadscrew and carriage arrangement. Each carriage held arms for tissue grip attachment. One arm on each axis was attached to a loadcell. Figure 3.4 below indicates how this arrangement linked together.

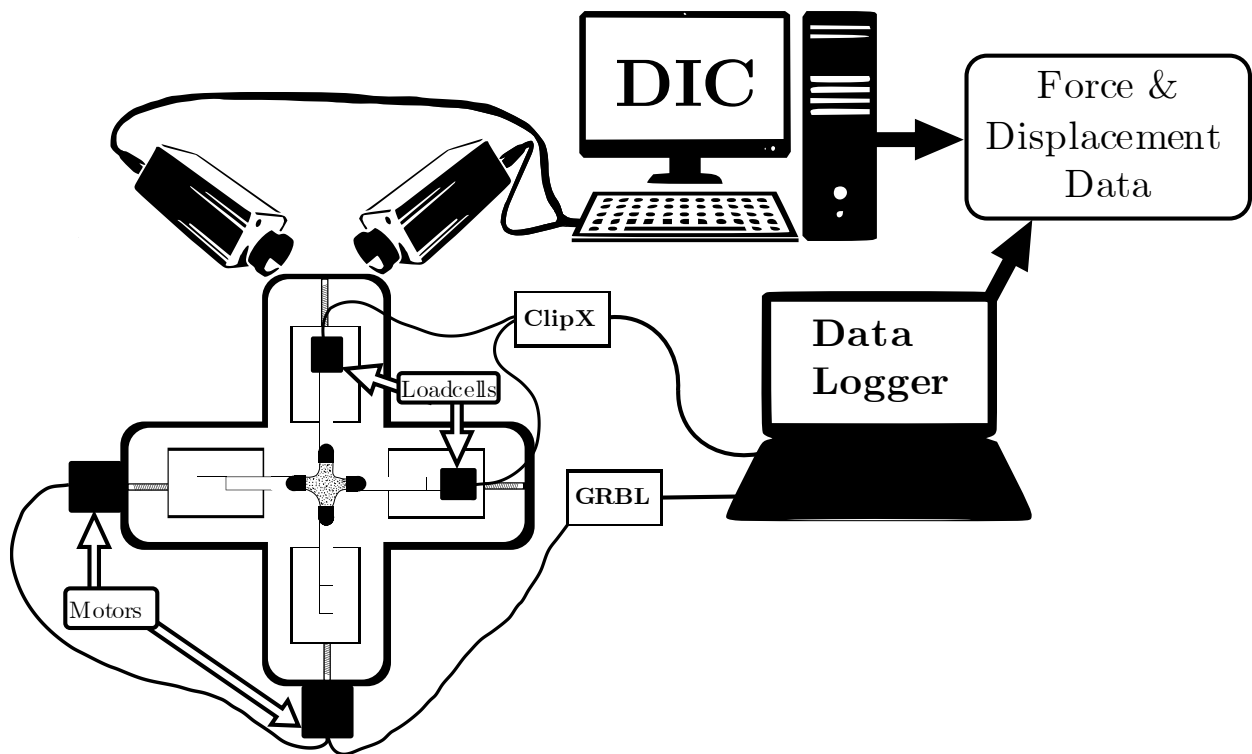


Figure 3.4: *Planar biaxial testing set-up schematic*

Besides modifications to the gripping system and design of a saline bath, no changes to the PBT rig were necessary. New G-Code was written to test the MT, however this was also adapted from Caine's approach [5]. His design is rendered in Figure 3.5 which shows his gripping mechanism and the lack of a saline bath.

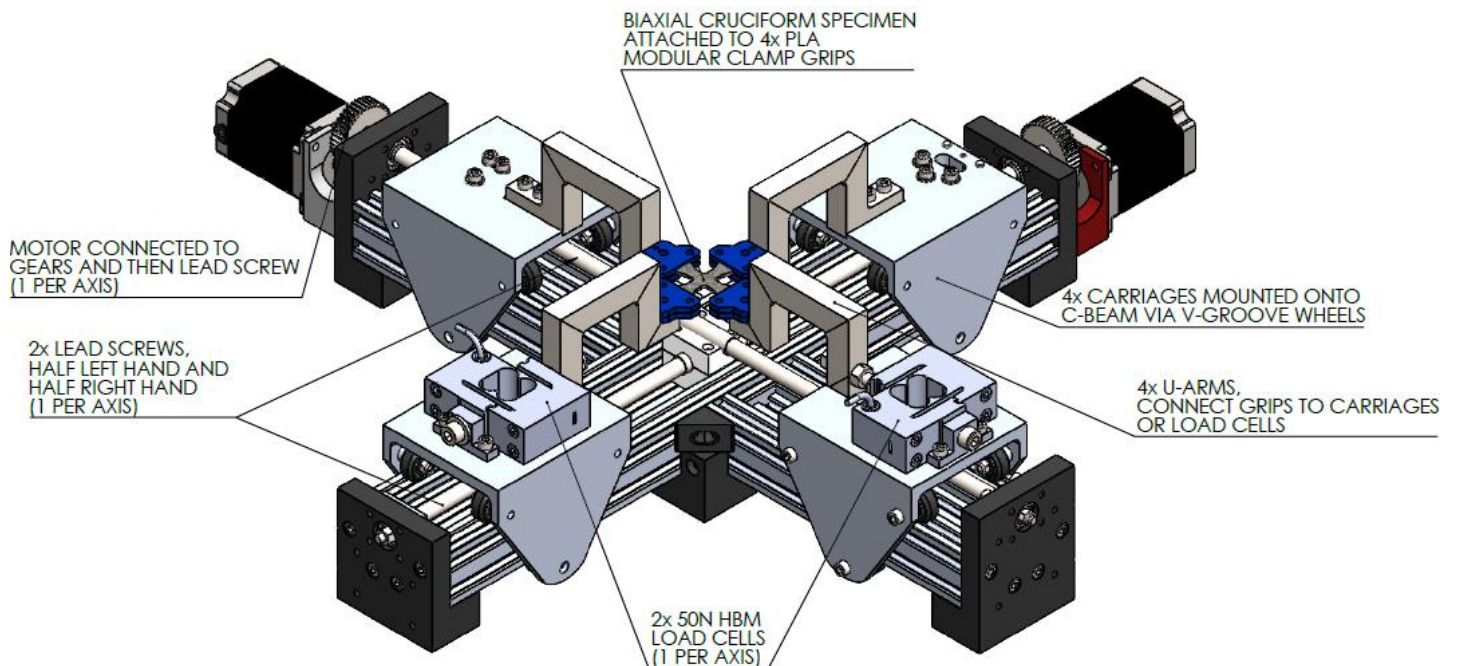


Figure 3.5: *Planar biaxial tensile tester designed by Caine, with permission.[5].*

Chapter 4

Methodology

This chapter contains the methods followed on the machines and tools using in collecting experimental data. Specimens were prepared before bulge testing. Displacement data was captured using 3D Digital Image Correlation (DIC). The mean fibre axis (MFA) was identified using this data, which then informed the orientation of the cruciform specimen excision. This was such that the planar biaxial tensile (PBT) tester always applied extension along MFA and the orthogonal cross fibre axis (CFA).

Force data from these axes was used with the displacement data from PBT tests to show the stress-strain response of the tissue. Stress was calculated using cross-sectional geometry. The tissue thickness was the most difficult dimension to capture for area calculation. Thickness was highly variable and could only be accurately measured using histological methods. Once thickness measurements had been processed from histological slides, the dataset was complete and ready for analysis.

4.1 Requirement Driven Methodology

The objective of this work was to obtain stress and strain data for membranous tissue (MT) with the constraint that specimens should be aligned consistently with respect to the MFA. This objective was broken down into measurable requirements which the methodology aimed to meet.

Table 4.4 shows how this break-down formed a hierarchy of contributing requirements that determined the experimental process required to meet the research objective. Each requirement was assigned a metric which could be measured to evaluate the efficacy of the method in meeting the requirement.

The requirements and metrics form a tree hierarchy with two branches:

1. Load, displacement and geometric data capture for MT samples.
2. PBT specimens consistently aligned to the MT MFA & CFA.

These two requirements were the core of the experiment methodology and all development work was done to ensure that these could be achieved.

Table 4.4: *Methodology Requirements Summary*

	REQUIREMENT	METRIC
1	Complete load, displacement and geometry data capture for multiple MT specimens	Force and displacement data
1.1	Repeatable PBT specimen gripping	Grip failure to success ratio
1.2	Repeatable PBT specimen transfer	Transfer failure to success ratio
1.3	Reliable force measurement at specimen loads	Mean uncertainty to signal ratio
1.4	Reliable displacement measurement	Mean uncertainty to signal ratio
1.5	Cross section dimension measurement	Mean uncertainty to signal ratio
2	Consistent cruciform specimen orientation determined by tissue morphology.	Consistency of MFA to CFA force ratio
2.1	High quality bulge deformation data	Mean uncertainty to signal ratio
2.2	Low bias MFA identification algorithm	Process parameters
2.3	MFA angle preservation from measurement to specimen excision	Uncertainty in excision angle

For the complete data capture of MT tests, there were a few key aspects to control:

- 1.1. *Gripping*: Differences in gripping methods or gripping quality have been shown to induce large variation in MT tensile behaviour [46]. The gripping of the tissue had to be repeatable to at least allow cross-comparison of results within this study.
- 1.2. *Specimen Transfer*: Specimen movement to and from the test rig could lead to issues such as misalignments or tissue damage. This would reduce the quality of test results. Specimens needed to be handled and mounted uniformly such that their results did not vary between specimens due to handling or mounting differences.
- 1.3. *Load Measurement*: High quality loadcells were needed to produce clean signals for the low loads expected for testing such thin materials.
- 1.4. *Displacement Measurement*: tissue deformation from the loading needed to be measured without imposing any load or stiffness change to the MT. Displacement of the MT would be used to calculate the strain in the region of interest.
- 1.5. *Geometric Measurement*: Thickness of the tissue was needed to calculate the stress in the specimen a result of the loads. This paired with the specimen width should be known with minimal uncertainty.

Complete data capture of the MT load response was insufficient to comprehensively characterise the tissue. The repeatable specimen preparation was crucial to generating consistent results. It was shown that MT load response varied depending on the angle between the extension axis and the MFA [26], [55].

Therefore, the following was required to ensure that specimens were excised with one extension aligned to the MFA:

- 2.1. *Bulge deformation Data*: Full field deformation and uncertainty data for MT under a low load test.
- 2.2. *MFA identification*: A consistent method of using BT deformation data to determine MFA orientation. This method should not depend on human skill or require fine-tuned inputs.

2.3. *Angular preservation:* Preservation of tissue rotation from MFA measurement to excision was crucial to ensuring that the specimen be cut correctly. A measure of confidence in this value should be allocated given the overall process.

While this approach prioritised methods that yielded satisfactory metric values, the realities of laboratory access and resource limitations during the COVID pandemic, meant that practicalities of a method could weigh against its potentially superior results.

4.2 Displacement Measurement

Key to both requirement branches, the capture of displacement data in bulge and planar tests proved challenging to do accurately and consistently with MT. The most significant challenge was controlling outside factors that inhibited DIC measurement. Methods for achieving high quality images of tissue under test conditions are explained herein.

4.2.1 Speckling

A “fall-out” speckling method yielded the most suitable speckle patterns. Figure 4.1 below depicts how this method is performed with the surface to be speckled running parallel to the direction of spray such that droplets “fall-out” of the spray profile and onto the specimen.

Larger droplets fell out of the spray profile closer to the nozzle while smaller droplets fell out closer to the waste target. This relationship was represented crudely in Figure 4.1 as linear. This was purely to show how speckle size decreased with increased distance from the nozzle.

Speckle density depended on the number of passes made over the specimen which facilitated fine control of quality. In most cases, fine speckles with a high density were required. This meant that specimens were sprayed with multiple passes at a large distance from the nozzle.

Due to droplet velocity, shadowing was observed when using a mask. This was mitigated by rotating the masked specimen between spray passes.

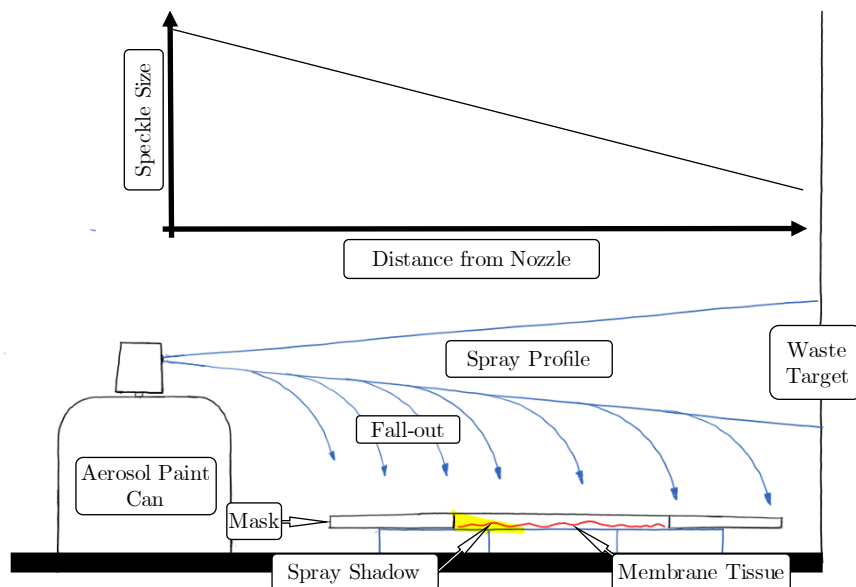


Figure 4.1: A representation of the “fall-out” speckling method.

Speckle pattern efficacy depended largely on whether the DIC software could find enough variation in grey values within an image of the specimen. Speckles that were uniform, dense and had limited speckle coalescence worked well with MT.

The translucent grey-pink SIS could have allowed for black speckles with a white backdrop or white speckles with a black backdrop below the MT. This was convenient as painting solid base coat to the tissue would have influenced tissue load response. Pillay showed how the relatively stiff solid paint layer would also flake or fragment off the more extensible MT [50].

Figure 4.2. shows results for white paint speckles with a matte black backdrop to the tissue. The uneven speckle size and splotching are characteristic of a directly sprayed specimen (ie. The fall-out method was not carried out correctly).

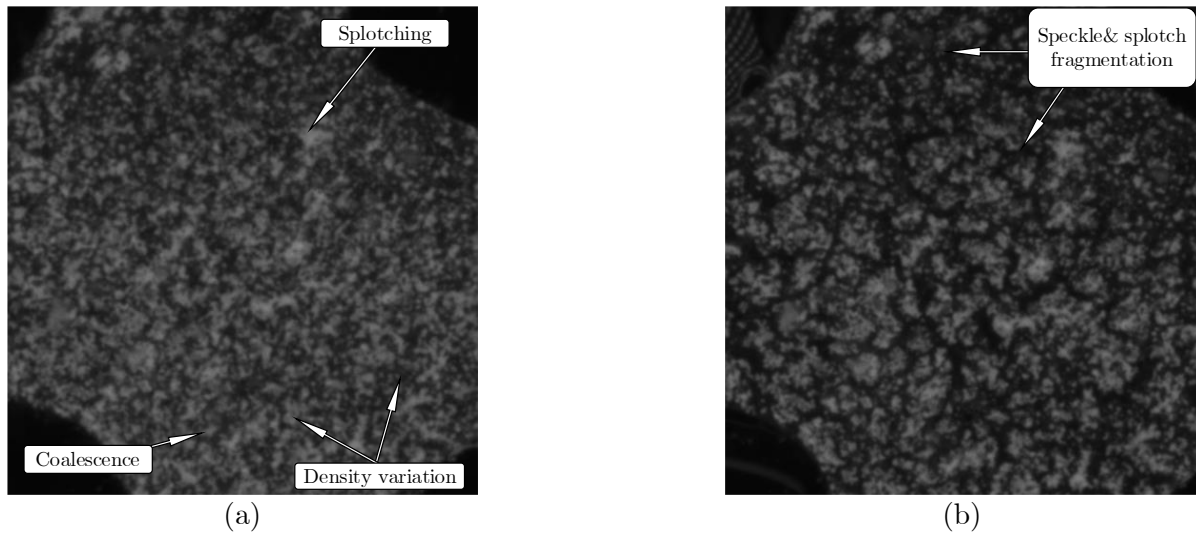


Figure 4.2: Poor speckle pattern performance in (a) reference and (b) deformed configurations

Paint fragmentation occurred when speckle patterns contained splotching and coalescence of the droplets. The paint would harden, and fragmentation of the speckle surface appeared with deformation. This was not observed in Figure 4.3 where the tissue was speckled correctly, as the paint droplets were not large or dense enough to coalesce and stick together in the patches seen in Figure 4.2(b).

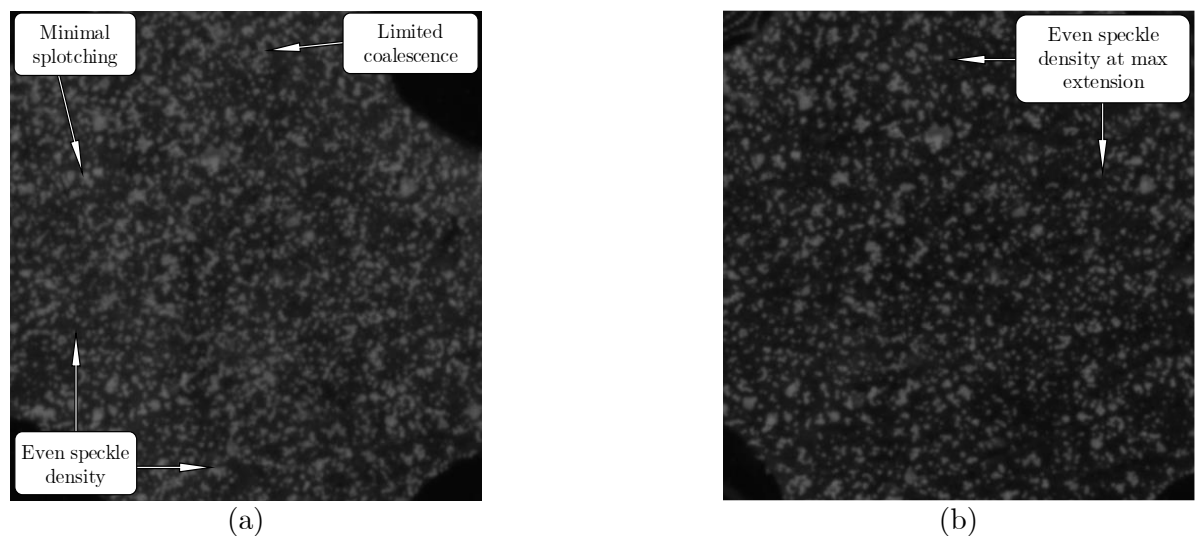


Figure 4.3: Good speckle pattern performance in (a) reference and (b) deformed configurations

4.2.2 Optics and lighting

DIC relied on photographs of the speckled ROI to measure the displacement field. Managing the lighting of the target was key to obtaining quality high-quality displacement data. DIC used the grey values in an image to track displacement, therefore overexposure, underexposure, blurring, temporal artifacts and contrast could each cause issues with correlation of points.

Stereoscopic DIC compounded these issues as it required cross-correlation of the same target features between the images captured simultaneously by each camera. Hence the lens and lighting parameters need to be tightly managed.

Bulge testing held the largest number of challenges with DIC. The wet and shiny ellipsoidal bulge surface reflected sufficient light from some regions to cause overexposure of these pixels. This meant that no displacement data could be captured in that area.

The camera focal length and the depth of field were fixed after calibration. This became an issue with bulge testing as the surface moved closer to the cameras which led focus loss. PBT testing had insignificant out of plane displacement, thus speckles stayed in focus. Both tests required matching brightness levels between left and right images. Repeatable solutions to these issues had to be found to allow the capture of full-field displacement data.

Matching cameras and lenses, with nominally identical aperture settings, were used to ensure similar brightness levels. However, small variations in the aperture mechanisms of the left and right cameras meant it proved difficult to achieve sufficiently similar brightness levels. To account for this slight brightness difference, the shutter speed of one camera was adjusted slightly to match the other.

A jig was mounted on the bulge tester to ensure the DIC calibration target height was set such that the focal point of the cameras lined up with the midpoint of the specimen's maximum displacement. For bulge tests, this allowed the images to remain in sufficient focus for the longest possible duration. Both cameras were set to have the smallest aperture setting possible to maximise the depth of field and mitigate focus loss.

A drawback from using the smallest aperture was that the images were very dark. While this could have been rectified somewhat by adjusting shutter speed, this was limited by the introduction of motion blur.

Increasing the power of the light source was the alternative solution, which exacerbated the surface glare. A dusting of talcum powder after speckling proved to be a reliable method of mitigating surface glare. Polarised light could be considered in the future to reduce specular reflection[56], however, its impact on DIC measurement quality should be measured.

White speckles and a matte black painted backdrop to both bulge and PBT testing provided the best results for reducing glare. To further reduce light hot spots on the membrane surface, a diffused LED light source was used which was directed upward onto a white shroud that covered the whole test rig. This ensured an even light distribution over the membrane surface.

The shroud doubled as a mask to remove any exterior light interference such as AC room lighting flicker or sudden exterior light intensity changes such as switching on/off an exterior

light. A diagram of the optical solutions is provided in Figure 4.4 below. While the diagram shows a bulge test, the set-up was very similar for a PBT test, which exhibited far fewer problems. PBT testing only needed a very small depth of field due to the low vertical displacements, furthermore, light could be directed at the specimen more easily without causing overexposure if the light was angled correctly.

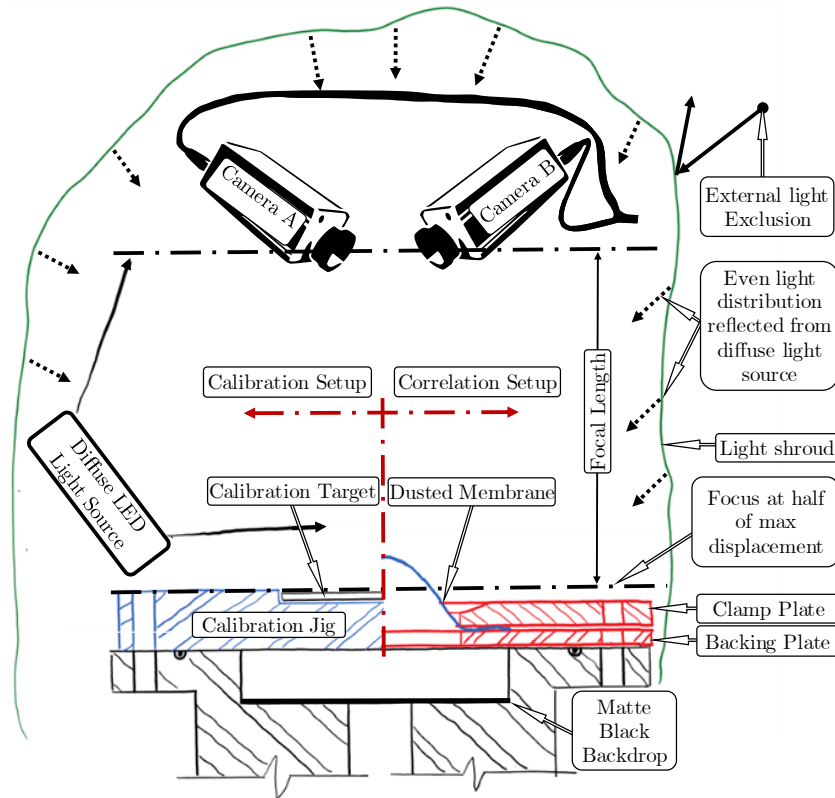


Figure 4.4: *Solutions to optical problems encountered in DIC testing (the same shroud, camera and light setup was used for calibration and correlation)*

Angular preservation from calibration to excision was made possible by the DIC calibration jig which ensured the axes of the DIC coordinate system aligned with a known exterior reference point.

4.3 PBT Specimen Preparation

Unlike other PBT testing protocols, the preparation of specimens here included a low-pressure bulge test of the MT. This was to help determine the MT's axis of least deformation (MFA).

4.3.1 Pre-Bulge Test Preparations

SIS was sourced as sausage casing which came salted and in great lengths (bungs). These were cut down to wieldier 30 *cm* lengths and sealed in bags of five or ten. This was done to prevent the bulk of tissue dehydrating progressively as more and more tissue was removed from a bag.

Tissue was first soaked in water to dissolve the salt crystals on the surface and inside the casing. This was then pulled over a Perspex rod using aqueous lubrication. Figure 4.5(a) below

shows how, once bunched up, the tube of tissue was sliced down its length, forming a long open rectangle. This was cut into $100 - 110\text{ mm}$ lengths, which were used for bulge testing. Note that scissors were used for most cuts as scalpels failed to cut SIS cleanly.

A single length of MT would be placed over the baseplate aperture while avoiding significant pre-tensioning of the tissue. Figure 4.5(b) below shows how an appropriate region of tissue was positioned over the aperture (without holes or defects that might prevent satisfactory air-inflation). The tissue was barely broad enough to cover the aperture completely. Any furling of the edges led to partial coverage and potentially poor sealing. By lifting the leading edge as shown below, furling was prevented.

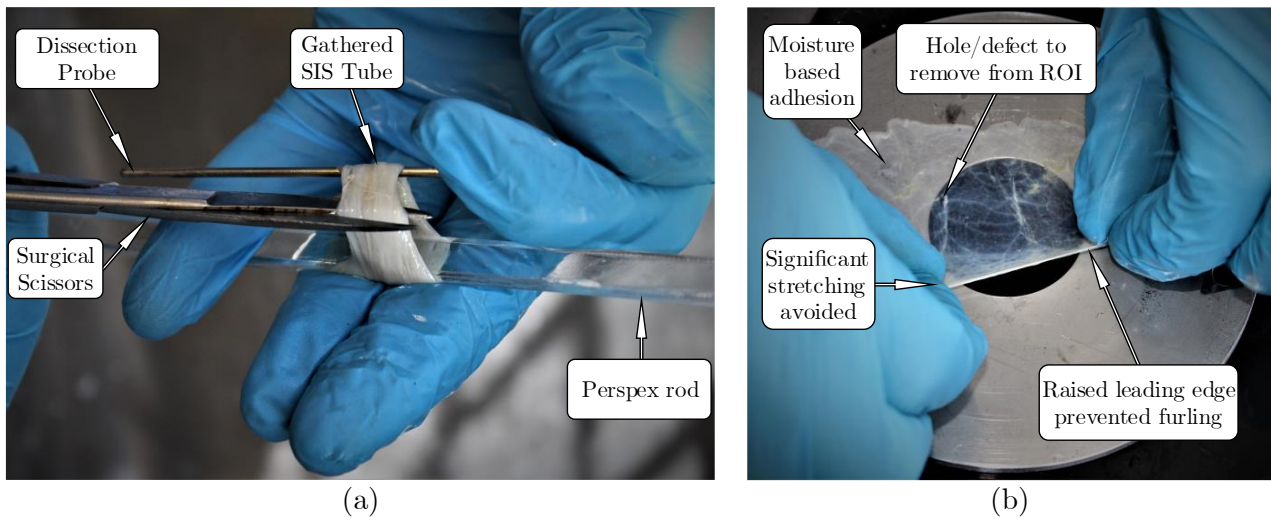


Figure 4.5: (a) Opening tube of tissue into flat rectangular form. (b) Spreading tissue over aperture avoiding defects and edge furling.

Speckling was performed as described previously with special care not to cause smudges. Figure 4.6(a) shows how environmental pressures such as a breeze or trapped air sometimes inflated the membrane enough to smudge on a bounding surface like a hand or a protective cover.

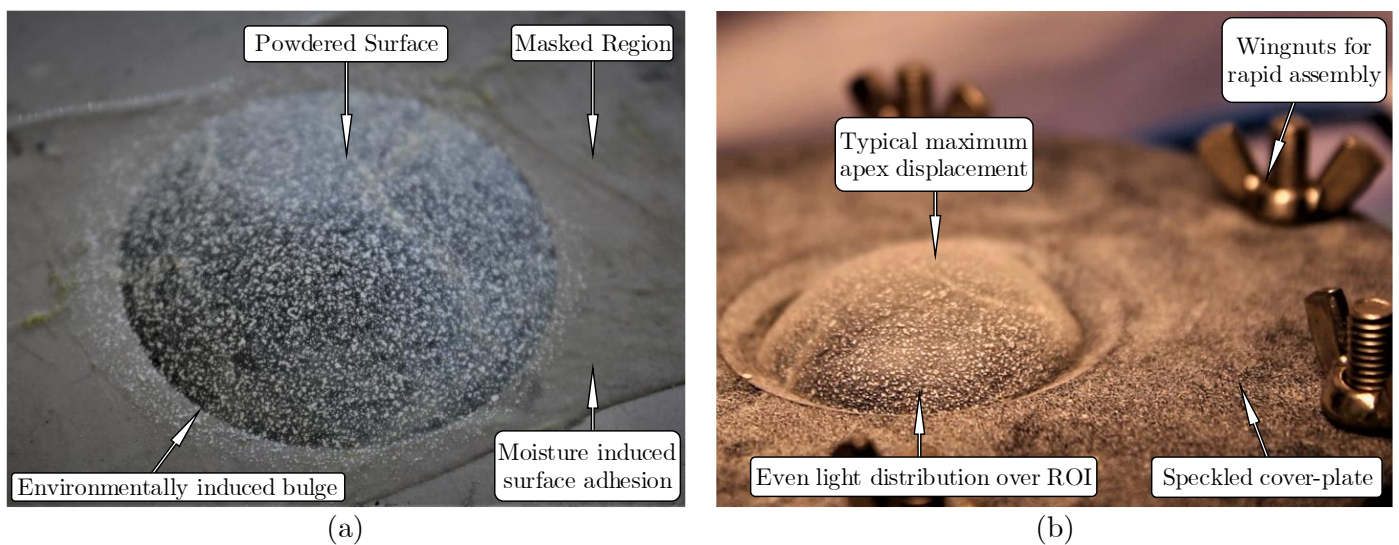


Figure 4.6: (a) Bulged membrane from placing the plate down on a surface trapping some air. (b) Bulge test showing a typical apex displacement at maximum pressure.

4.3.2 Inflation chamber

The inflation chamber was originally designed to be used with (much thicker) silicone cast in a fibreboard frame where the silicone served as its own gasket[4]. This meant that the clamp surfaces were designed without recesses for additional gasketing. Furthermore, the silicone membrane used water as the inflation medium. MT specimens leaked both at the clamp perimeter and across the membrane surface when inflated with water using the original clamp design. This confirmed concerns raised by Pillay [50], whose initial work with MT specimens on the BTR found that water permeated the specimens.

A redesign of the sealing mechanism used in the inflation chamber and consideration of alternative inflation media were actioned. Under pressure, SIS proved to be porous to coconut oil, vegetable oils, hydrogels and water. Before progressing to greases and other more viscous fluids, air was found to work as an inflation medium. While air permeated the SIS and passed through the clamp gaskets in small quantities, it did not form bubbles or puddles that disrupted imaging of the specimen surface. Furthermore, the syringe pump test code was modified to account for air leakage and compressibility. This medium worked best to help satisfy the methodological requirement of high-quality bulge displacement data.

The upper clamping surface was re-designed with a gasket recess and a protruding rounded clamping lip to control the clamping boundary condition on the tissue. Figure 4.7 shows how the gasket rested in the recess and how with the rounded clamping lip, the tissue was pressed tightly down onto the baseplate without allowing the gasket to be squeezed inwards towards the centre. The lip protrusion offered only $100\ \mu\text{m}$ clearance so that the tissue was not pinched by the metal but held firmly by the gasket.

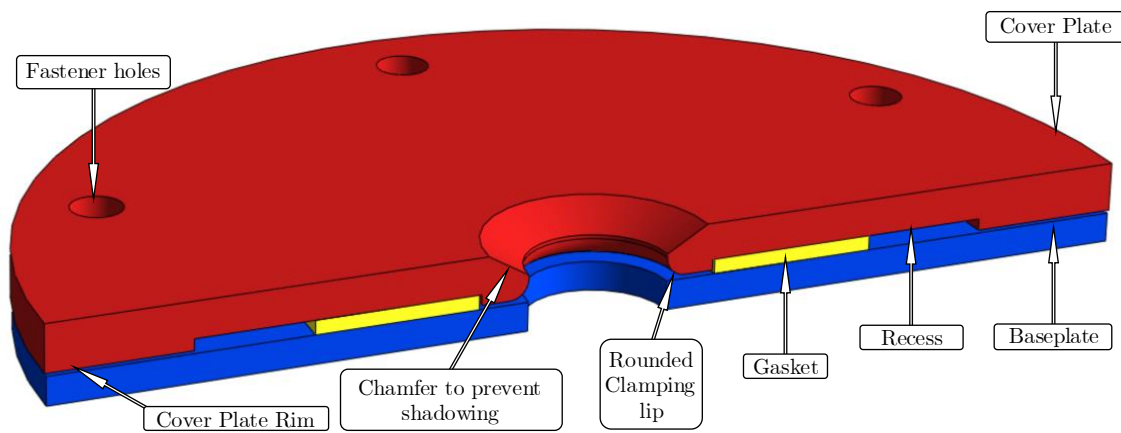


Figure 4.7: *Tissue clamping assembly.*

A gum rubber gasket of $1.2\ \text{mm}$ thickness was soft enough to provide enough clamp force on the tissue without pinching the edges close to the aperture (causing a leak). The cover plate featured a rim that prevented overtightening of the gasket. Thus, the clamping force was controlled by the recess depth and gasket thickness & stiffness. Figure 4.6(b) shows the successful operation of the gasketed cover plate.

4.3.3 Bulge testing

Leakage of air was only considered an issue if the membrane developed a large enough hole to prevent inflation to the test pressure required. The syringe pump proved able to accommodate most minor leakages and still deflect the tissue enough to get the required measurements.

Figure 4.8 below shows how the MT was quasi-statically inflated to pressures between 0.5 – 1 kPa and then held at this pressure for a few seconds before quasi-static deflation. The pressures were purposefully low, as very little pressure was required to bulge the tissue enough to get MFA information. Low pressures were imperative as the bulge test needed to be a non-destructive way of identifying the MFA.

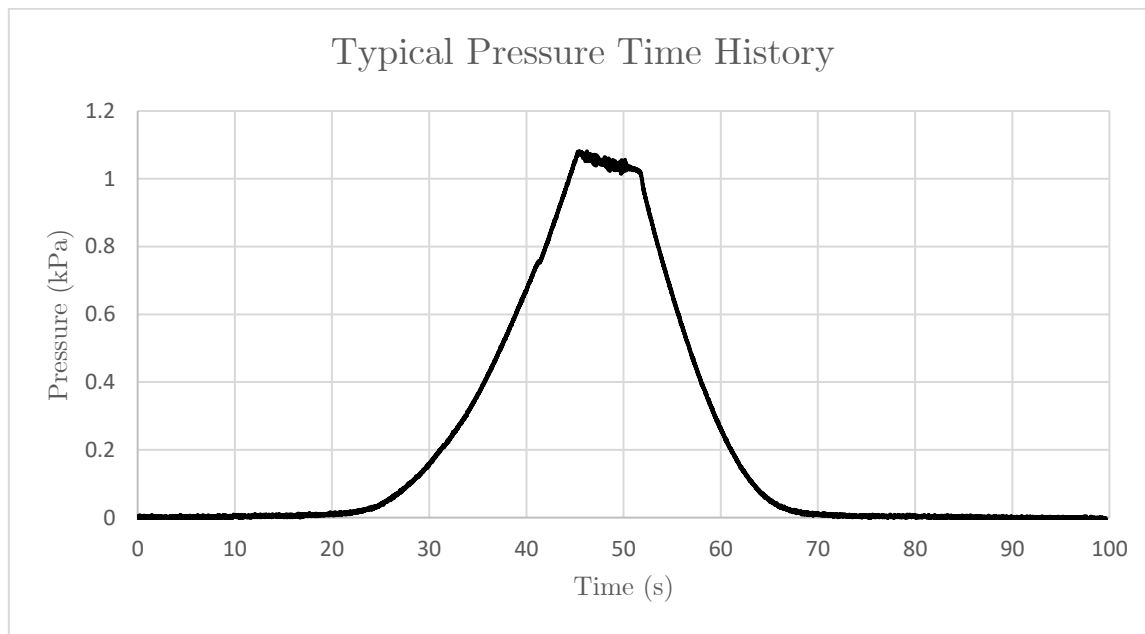


Figure 4.8: A *typical bulge-test pressure profile using the BTR*.

Displacement control of the bulged surface was controlled by setting a maximum pressure for the test, inflation would stop once reached, then the specimen would be returned slowly to zero pressure. As mentioned previously, calculation of stresses for bulge testing was not performed due to the SIS being too variable in thickness. This variation led to flat-spots or pimple-like aberrations on the bulge profile.

Air as an inflation medium could cause rapid dehydration. Changes in hydration levels of the SIS were anecdotally observed to affect mechanical response, which agreed with more rigorous studies on the topic [57].

Steps were taken to mitigate membrane-drying during the bulge tests on both sides of the membrane. Glare reducing talcum powder dried out the tissue to a degree. Further dehydration was observed when the membrane was left exposed to open air. A humidity controlled chamber such as those used in [22], [23] was not available for this study nor was it believed to be necessary. The low-pressure bulge test was not anticipated to be a long process. Thus, the membrane was instead covered when not testing (Figure 4.9(a) shows this). Figure 4.9(b) shows how water was placed in the pressurised system to humidify the air used to inflate the

MT. A saline spritz of the specimen underside also helped keep the tissue hydrated for the test.

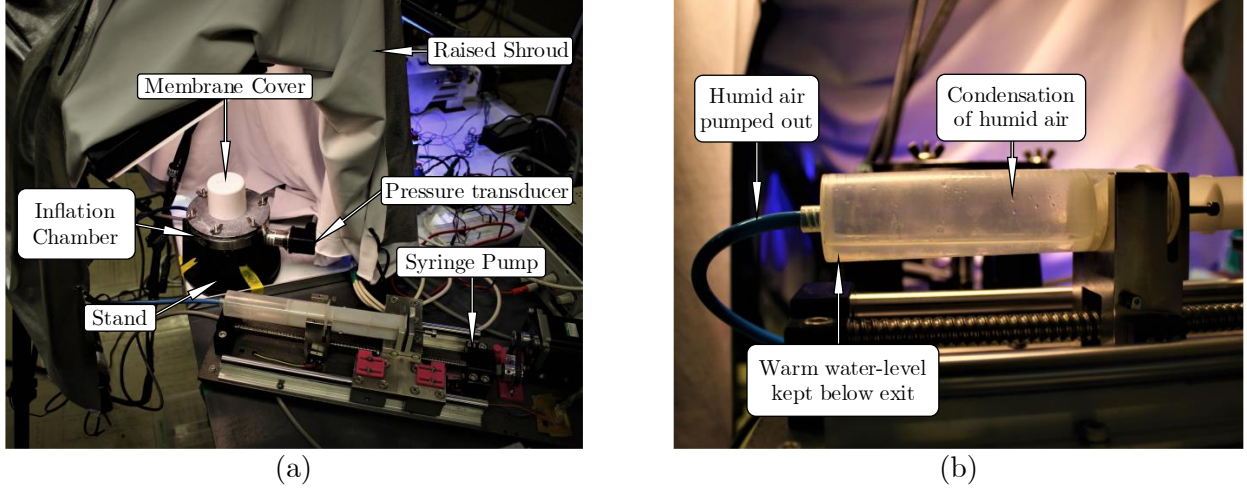


Figure 4.9: (a) *Bulge-testing setup.* (b) *Hot water-filled syringe to maintain MT hydration.*

4.3.4 MFA Identification Algorithm

Algorithmic identification (ID) of the MFA was a key methodological requirement to satisfy. This was to mitigate bias and human error susceptibility.

Anisotropic MT was known to bulge in the shape of an ellipsoid and not as a hemisphere like silicone rubbers. Initially the algorithm used linear regression to fit an ellipsoid to the full-field displacement data. The direction of the axes of this ellipsoid was to inform the directions of the MFA and CFA. The linear regression often struggled to fit an ellipsoid to the data appropriately. In some cases, the three axes of the ellipsoid all pointed out and upward. This made the MFA difficult to identify algorithmically.

Choi and Vito [30] mentioned previously inspired the final method used. For a thin membrane, a bulge test can be shown to be a similar system.

Where Choi and Vito extended the edges of their tissue using weights, a bulge test clamps the edges of the tissue and evenly extends the membrane. Where they marked the tissue at load and relaxed the tissue to form an ellipse, the bulge test method digitally scribed a circle at zero load and tracked the circle temporally transformed into an ellipse during the bulge test. This process of transformation is depicted in Figure 4.10 where the initial circle of points (reference configuration) over time distorted into the elliptical scatter (deformed configuration).

From this we posited that the bulge test was the superior of the two methods. This was because it used the ellipse that was formed under biaxial loading and not multiple discrete uniaxial loads. Further to this, the errors associated with the discrete measurements linked to human error and bias were reduced in the bulge test.

The algorithm would run using the exported DIC data directly after the bulge test completed. The algorithm needed the centre and diameter of a circle of points to pick out from the 3D point cloud to trace through the test timeline.

The centre of this digitally scribed circle was located using the point of maximum displacement of the bulge test. Figure 4.10 shows (in black) the location of the apex relative to the centre of the aperture. The apex did not always lie in the centre of the aperture due to the use of anisotropic & heterogenous specimens. The data was centred wrt. the aperture to help identify the MFA this was justified by the fact that translation of the data would impact MFA-ID.

The operator would give the circle diameter and the tolerance inside which points close to the line of the circle would be included to make a scatter like that of the reference configuration in Figure 4.10. This was necessary because datapoints would rarely lie on the exact path of a chosen circle

The x and y position of these points at maximum displacement was extracted fed into a linear regression to fit an ellipse to the data. The minimum radius of this ellipse was identified as the axis of greatest stiffness. The angle of this axis (the MFA) was swiftly returned to the operator to mitigate tissue dehydration. Figure 4.10 depicts a typical output of the test and shows the datapoints of the reference and the deformed configuration of the ‘scribed’ circle.

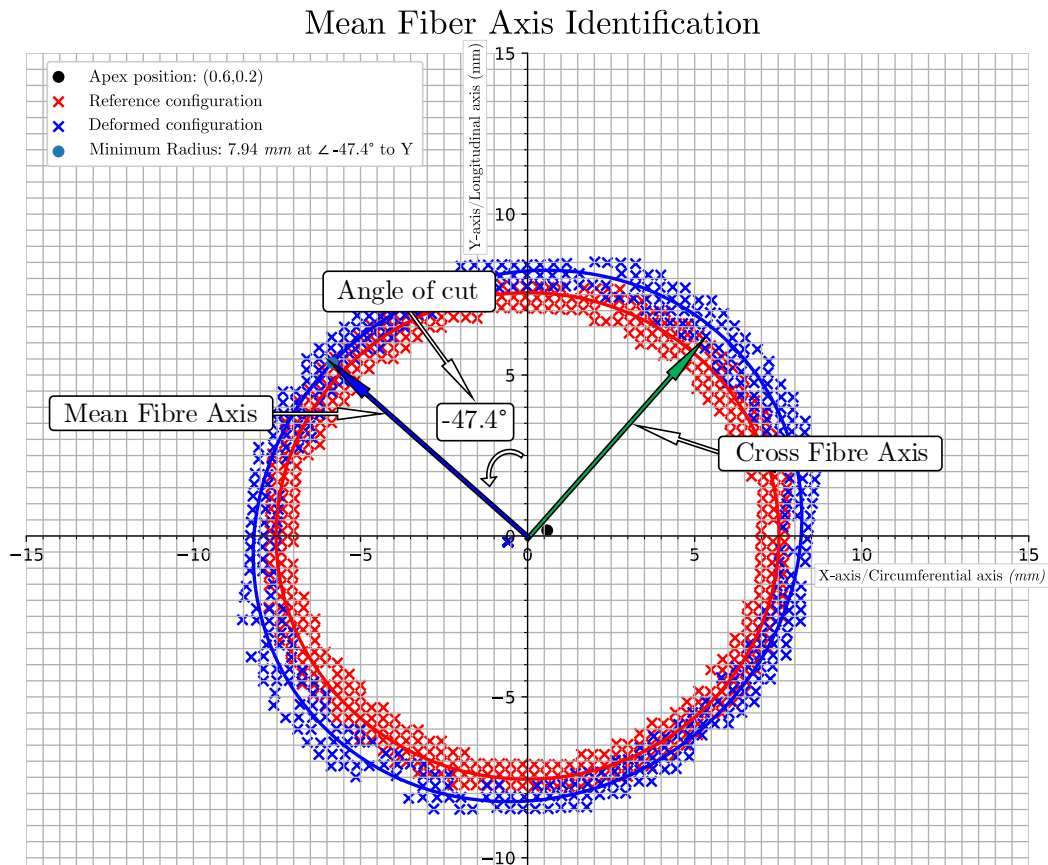


Figure 4.10: *MFA identification algorithm output graph.*

Table 4.5 shows that the algorithm satisfied the methodological requirements by delivering process parameters used for all tests. Small adjustments of the parameters were sometimes necessary to accommodate unusual bulge deformation profiles.

Table 4.5: *Typical MFA identification algorithm parameters used*

Evaluation Parameters	
Point tolerance (mm)	1
Radius (mm)	7.5
$\delta\theta$ ($^\circ$)	1

The point tolerance was the inclusion allowance for points close to the ‘scribed’ circle. Only points (P) in $Radius - \frac{tolerance}{2} < P < Radius + \frac{tolerance}{2}$ were chosen in angular increments of $\delta\theta$. A radius of 7.5 mm was chosen such that the 10 × 10 mm cruciform ROI would fit into this region.

Test specific parameters not shown above were time-steps for:

1. *Reference configuration*: The time when the specimen was flattest.
2. *Deformed configuration*: When the specimen exhibited maximum displacement
3. *Point of interest*: The point in time that could be chosen to assess MFA orientation.

These were the only entry point for user bias in the MFA ID algorithm.

4.3.5 Goniometric Cutter

Consistent specimen excision at a desired orientation required the design of a cutting jig. This needed to overcome the challenges of handling such fragile tissue.

SIS was found to be slice resistant. Shears were the most effective cutting method. Thus, if it was to be cut by pressing a blade onto the tissue, a soft surface had to be beneath the blade to facilitate a shearing effect. Disposable razor blades were chosen due to their fine edge and ability to be bent and form a cruciform cut-out.

Figure 4.11 shows the original cutting block design with guide slots for the razor blades. This was manufactured using fusion deposition modelling (FDM).

The first design iteration did not consider the flex in the assembly of stiffness varying materials. The cutting surface in Figure 4.15 squashed down to be slightly thinner than the baseplate. This resulted in the blades catching the edges of the baseplate and interfering with the cutting process. Furthermore, the unsupported centre of the blades could not apply enough cutting force to achieve complete specimen excision.

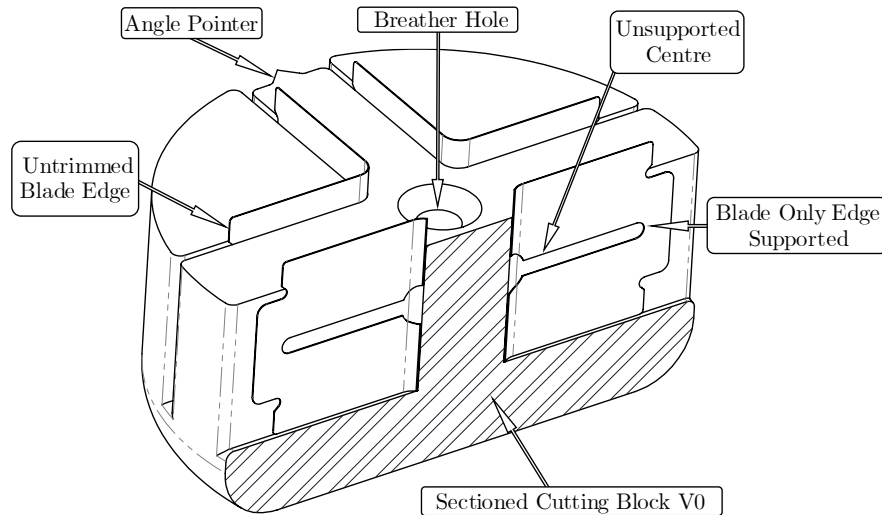


Figure 4.11: *Section-view of the first cutting block with unsupported & untrimmed blades.*

Figure 4.12 shows how the improved design used half as many razor blades and featured even distribution of cutting force to the back of the blade. The trimmed blades did not interfere with the baseplate and remained sharp for longer.

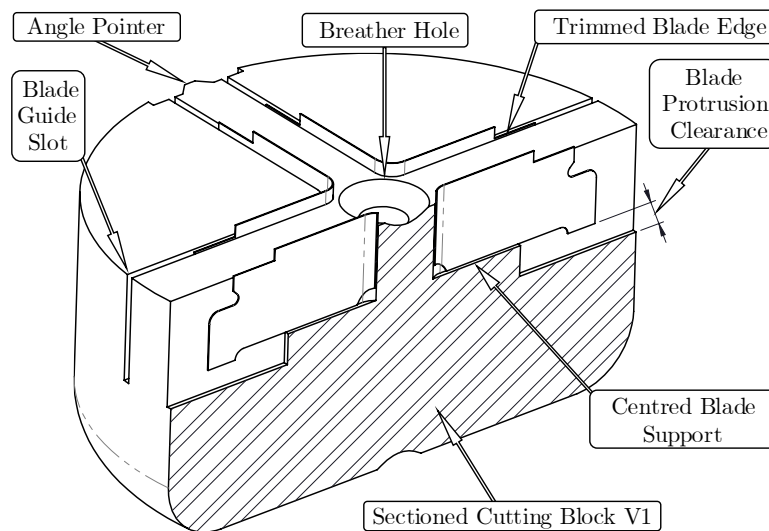


Figure 4.12: *Improved cutting block with the internal blade support & trimming*

Other notable features of the cutting block were the angle pointer and the breather hole. The angle pointer was aligned to one cruciform axis and facilitated angular measurement. The breather hole allowed air to escape if the tissue adhered to the cutting block. This hole would allow a probe to be inserted and the specimen to be gently removed from between the blades. Rounded edges were factored into the tool to facilitate ergonomic use while pressing down hard on the cutting block.

The razor blades would snap if bent 180° , this characteristic was used to halve the blades down the centre as in Figure 4.13 below. The 90° blades were made by bending them over a dissection probe to just beyond 90° , allowing them to spring back to the required angle.

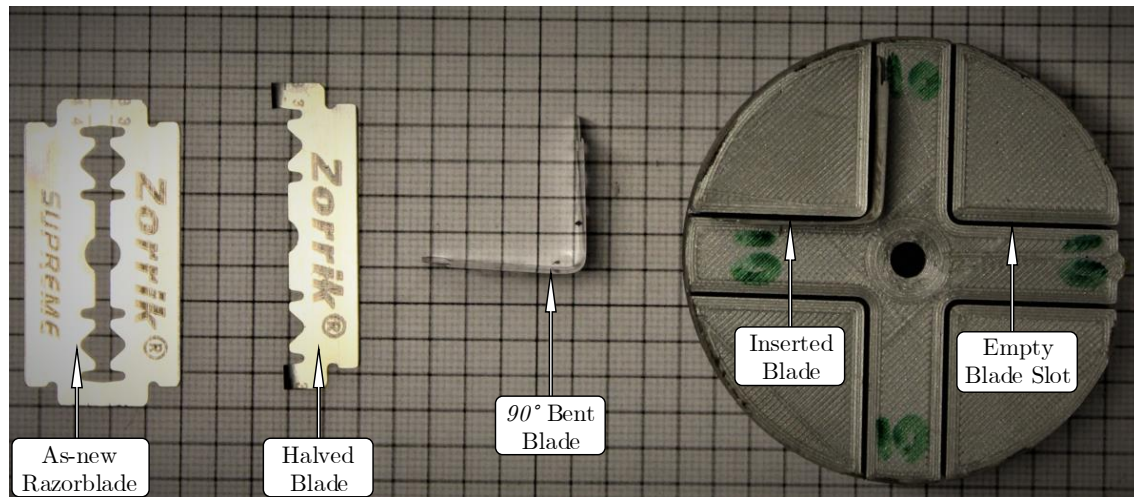
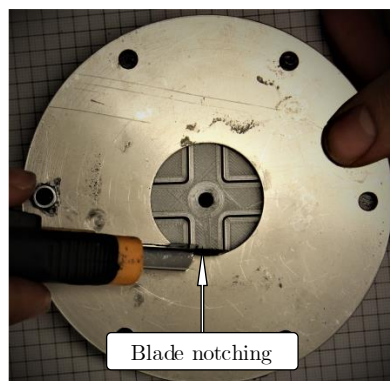


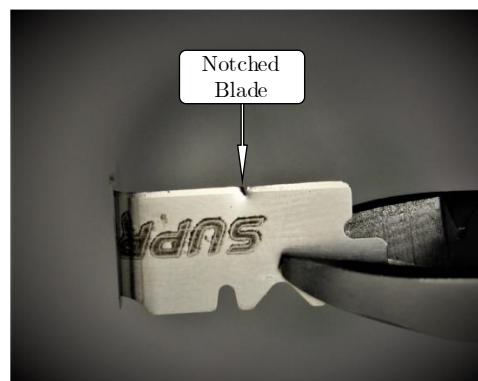
Figure 4.13: *Cutting block blade preparation using disposable razorblades.*

The probe's diameter imposed a bend radius and allowed the razor blade to be gently pushed into the blade's guide slot. A box-cutting blade was used to nick the blades at the edge of the backing plate inner diameter. These nicks were used as tear points for the side cutters to trim away the blades to fit inside the backing plate inner diameter. This process was shown in Figure 4.14.

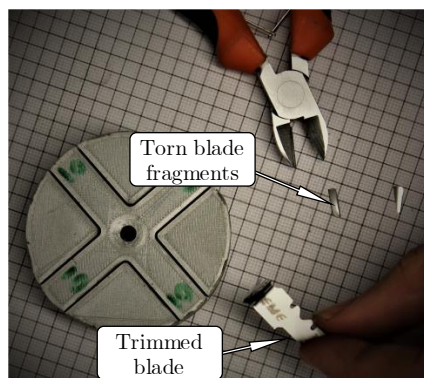
Interference with the backing plate meant that cutting force was not evenly distributed over the tissue. If the blades did not cut evenly, an entire specimen risked wastage as it was difficult to perfectly realign the blades for a second cut. Misalignments created nicks in the cruciform specimen causing stress concentration. This made incomplete excision unacceptable



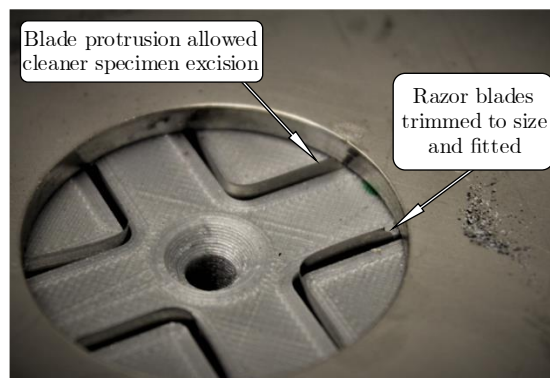
(a)



(b)



(c)



(d)

Figure 4.14: *Razor blade preparation: (a) a box-cutting blade was used to (b) notch razor blades to be (c) shaped to avoid interference with the (d) backing plate when excising a cruciform specimen.*

The cutting block was designed to mate with the goniometric cutting guide, a laser cut MDF board with holes that aligned it to the baseplate by using pins. The alignment of the cutting guide centred the cutting block over the tissue in the aperture. The rotation of the cutting block was measured using the degree markers and the angle pointer. Markers were only placed over 180° due to the symmetry of the cruciform specimens.

Figure 4.15 shows how the soft HDPE cutting surface was inserted into the baseplate aperture to facilitate reliable complete specimen excision.

The selection of a cruciform specimen as opposed to other geometries and setups was a decision that was based on lab availability, time and large delays in the normal manufacture process. Easily accessible materials and methods of manufacture were chosen to ensure progress could be made despite the impedance of the COVID-19 pandemic.

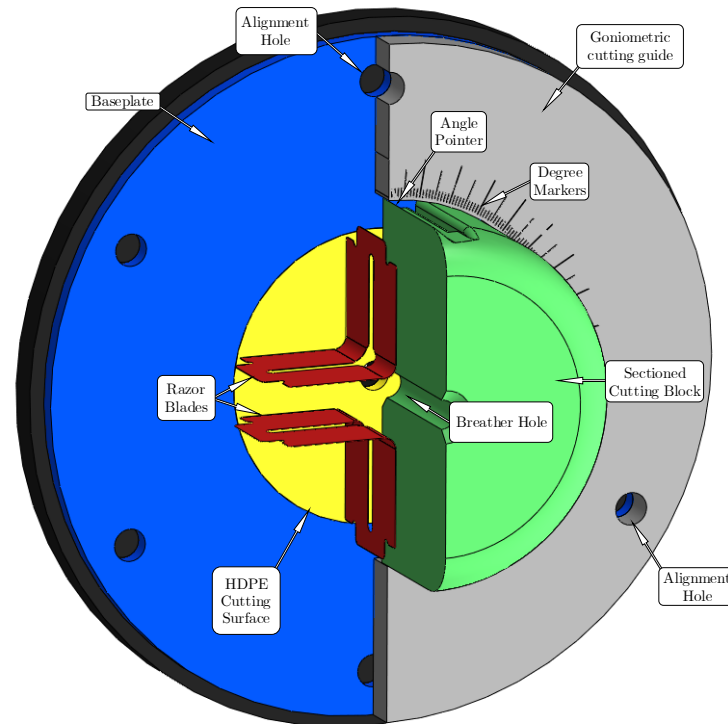


Figure 4.15: *Partially sectioned goniometric cutting jig showing the positioning of the disposable razor blades in the cutting block*

4.3.6 Alignment Preservation and Specimen Excision

The digital identification of the MFA was not useful unless the bulge test data was linked to a physical reference-frame. Specimen excision could then be made at an angle relative to this reference. The same calibration jig used to set the DIC focal length for the bulge test, additionally centralised and aligned the DIC data to what was called the triangle of alignment. Figure 4.16(a) shows how three of the six fastener holes located the apexes of the alignment

triangle. The triangle base was always parallel to the x-axis and the triangle pointed in the y-axis direction. The DIC calibration target set the axes of the reference-frame in this same orientation.

Figure 4.16(b) shows how the triangle of alignment was implemented in the specimen clamping assembly. To standardise the preparations, tissue was always placed with the GIT longitudinal axis parallel to the y-axis and circumferential axis parallel to the x-axis.

Figure 4.16(c) and (d) depict how the goniometric cutting guide and block were placed over the MT. Figure 4.17 shows how the cutting block was designed to excise a cruciform specimen with a $10 \times 10 \text{ mm}$ square in its centre.

The goniometric excision jig and alignment system was an innovation that fulfilled the requirement for MFA angle preservation. This was done from measurement to excision and provided an acceptable excision angle uncertainty owing to minimal play in the system

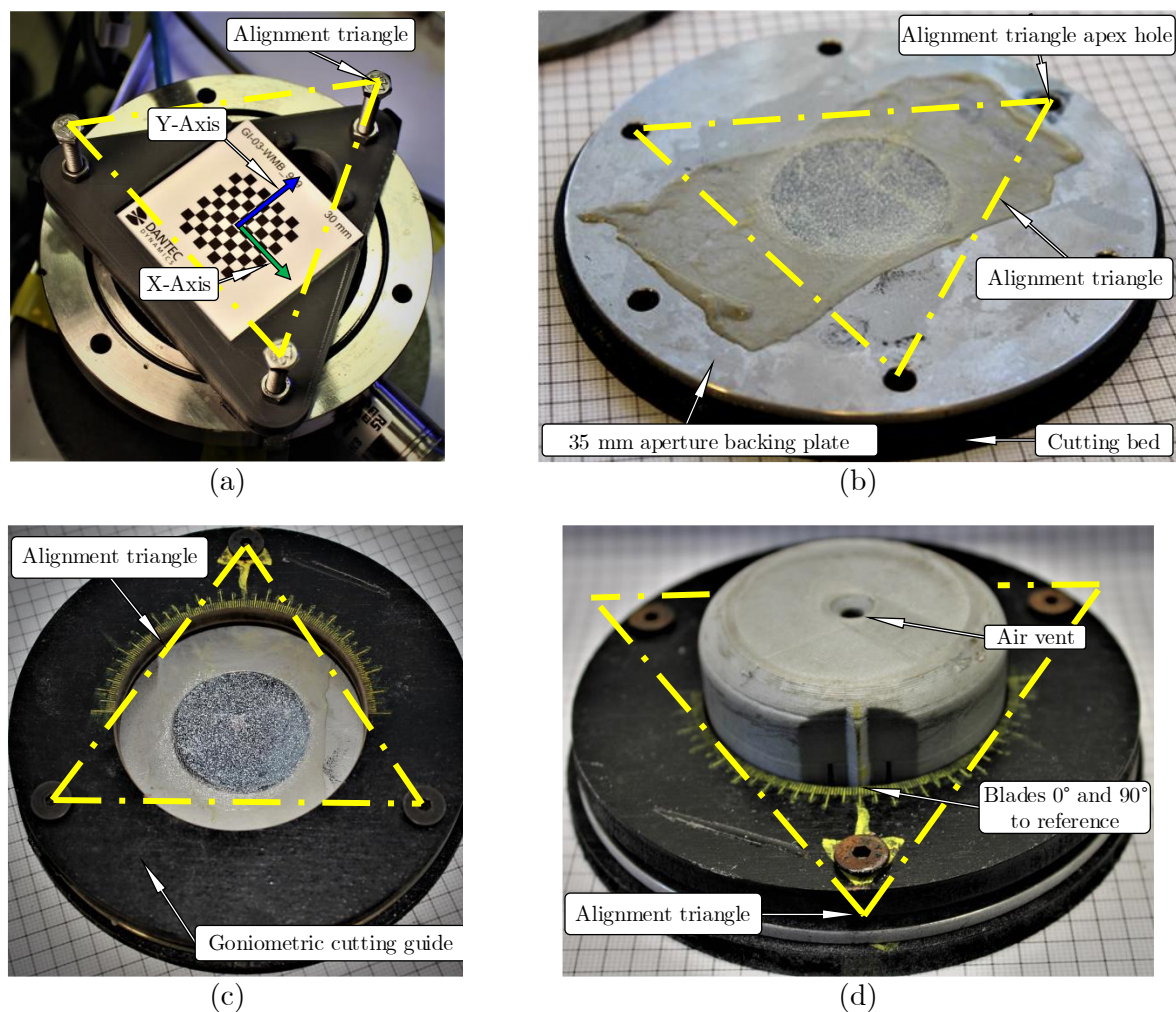


Figure 4.16: (a) Alignment triangle jig ensured a consistent frame of reference for cruciform specimen cutting by locating the DIC calibration target (b) Uncut and speckled tissue on backing plate aligned on cutting bed. (c) goniometric cutter guide placed over backing plate (d) Cruciform cutter aligned at 0° to y-axis.

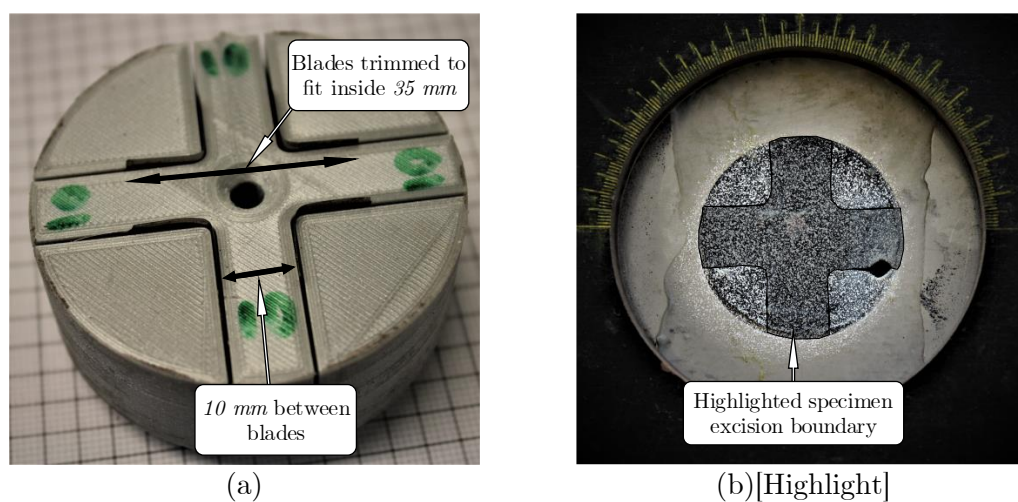


Figure 4.17: (a) 10 mm gauge-width cutter with blades trimmed for a 35 mm aperture plate. (b) Bulge test tissue cut to cruciform shape

4.4 Planar Bi-axial Tensile Testing

Up until this point, the existing PBT systems and methods of testing have been presented. Figure 3.5 depicts the starting point of the setup for PBT testing that was used here. Further discussion here is to highlight noteworthy developments in methodology in this research.

4.4.1 Specimen Transfer and Gripping

Prior testing with silicone PBT specimens did not require design of a specimen transfer system as the silicone was not as delicate as the SIS tissue used in this research.

To reduce opportunities for operator error and misalignment, a specimen transfer card was designed. A relatively rigid 1.2 mm (615 gsm) thick card frame, shown in Figure 4.18, was bonded to the MT specimen using cyano-acrylate adhesive. Bonding was done prior to removing the cut MT specimen from the BTR backing plate assembly.

The card featured a frame that was cut away at the base of each tissue grip. Furthermore, the grips featured alignment edges matching the cruciform specimen arm width of 10 mm . The edges were designed to be aligned on each arm to help the researcher ensure that the specimen was placed centrally in the grips. Figure 4.18 shows a drawing of the card. These were laser-cut to ensure each card was the same.

The fixed distance between the locating pin holes was designed to ensure the PBT tester started from the same location with each test, ensuring alignment of the arms and mitigating uneven pretension.

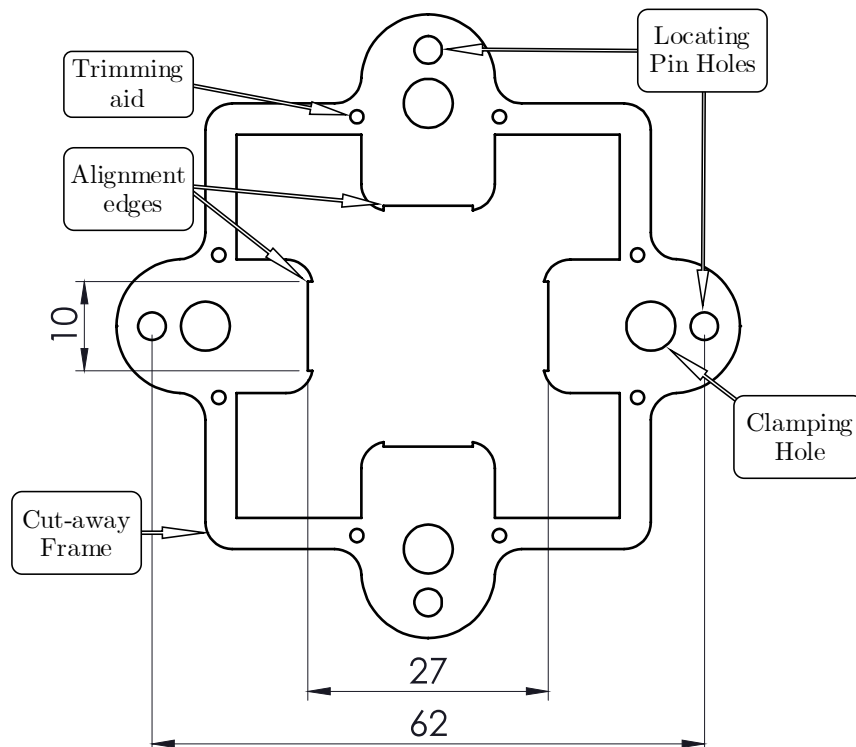


Figure 4.18: *PBT specimen gripping and transfer card*

The card thickness was chosen to keep the specimen rigidly in shape while mounting it to the PBT rig. The card also had a glossy layer on top and bottom which helped it resist waterlogging and breaking apart. The clamping hole in the card was included to allow a bolt to fasten the card to the extension arm when trimming frame from the grips. The trimming aid hole acted as a perforation to reduce time and force required to remove the frame.

Figure 4.19(a) below shows how the DIC was calibrated such that the MFA aligned with the y-axis in the data. This prevented tedious re-alignment of the data axes to the extension axes. Figure 4.19(b) shows how the card was marked with an arrow to align with the MFA. The arrow was used to prevent specimen alignment to the wrong extension axis.

Figure 4.19(c) shows how, once adhered, the card was raised. Excess tissue was then trimmed away. These specimens were tested immediately or placed in saline to prevent dehydration while awaiting testing. Figure 4.19(d) depicts how once placed on the pins; the arms of the card could be trimmed away using a scalpel. A bolt was used to prevent the specimen from rotating once it lost the support of one side of the frame.

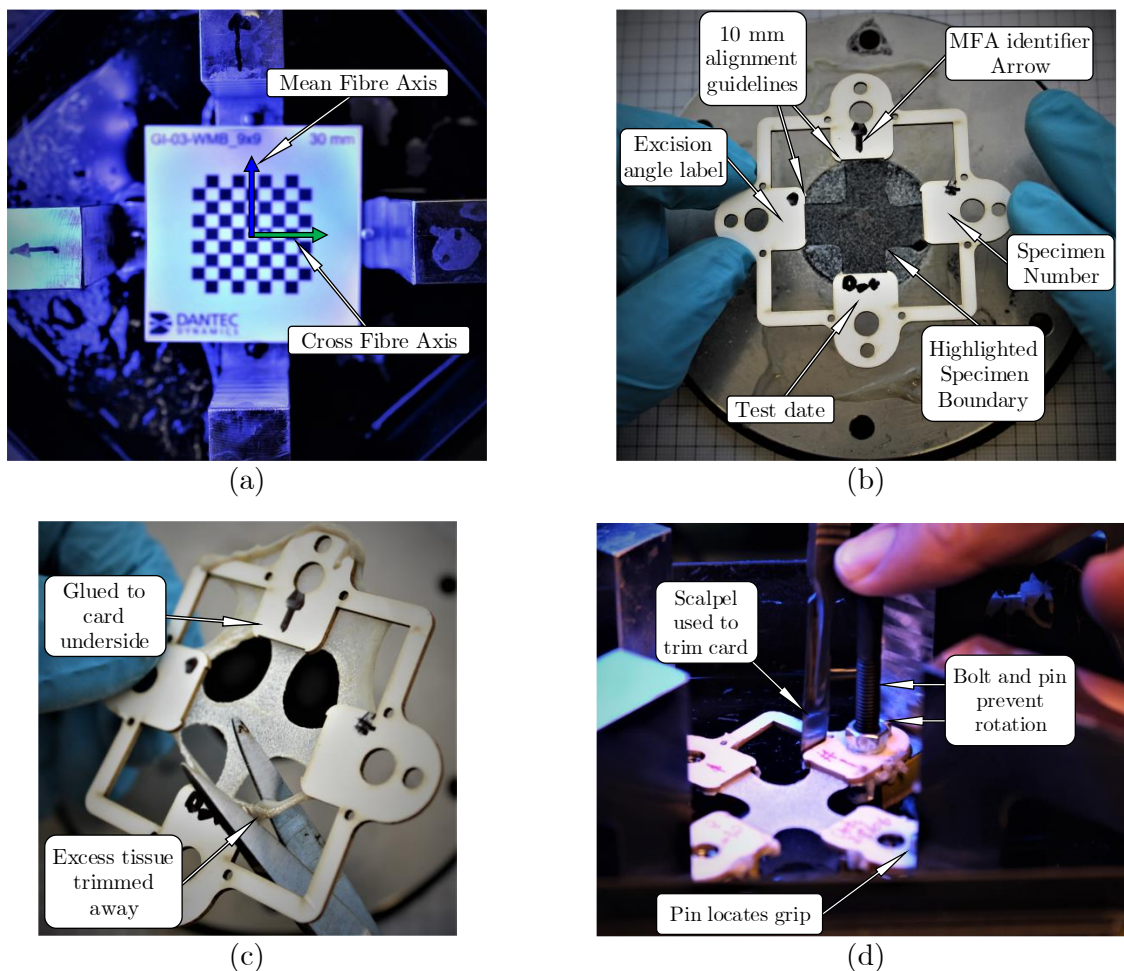


Figure 4.19: (a) PBT tester arms positioned to align DIC axes to the MFA (b) Placement of glued card. (c) Excess tissue trimming. (d) Bolt stabilisation during frame trimming.

Fresh card was used to remove specimens from the test bed by gluing it stacked on the grips. This was useful when formalin fixing, as tissue was to be fixed in its reference configuration.

4.4.2 Moisture control

Specimens awaiting testing floated on a saline solution in a closed petri-dish. Specimens were floated on a saline bath during testing. This was filled to approximately the same level as the grips. This arrangement (as per Figure 4.20) mitigated strain of the tissue under its own weight and kept the tissue adequately moist.

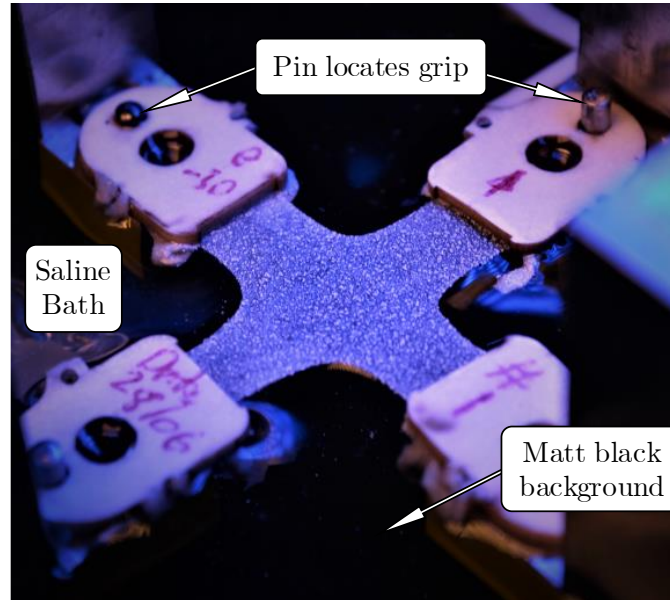


Figure 4.20: *Planar biaxial tensile specimen under load on a saline bath.*

The saline bath container was suspended above the PBT rig but beneath the arms and painted with a matt black paint to reduce glare that might affect the DIC setup.

4.4.3 Extension control and force measurement

Specimen pre-conditioning was equibiaxial and extension was the same as the peak test extension. In agreement with literature, specimens were quasi-statically cycled five times.

Specimens were preconditioned before each test which contained five extension ratios:

- a) 1:1
- b) 1:0.5
- c) 1:0.75
- d) 0.5:1
- e) 75:1.

Each test used these ratios with successively increasing maximum extension. Extension for the tests was determined using some initial test-to-failure data of trial tissue. These trials were not pre-conditioned. In full testing, specimens were taken up to 100% of this pre-determined failure extension level and did not fail. This was likely due to the effect of preconditioning. The three extension levels were: 50%, 75% and 100% of the projected failure extension. These were labelled low, medium and high extension respectively (LE, ME and HE).

Specimens were brought up to the requisite extension level quasi-statically and held for a few moments, then returned to zero displacement at the same rate. They were then rested for a few seconds before the next extension ratio was performed.

Load-control was not possible with the hardware available. Thus, tests were programmed using G-Code to implement extension control. Force was measured on two arms of the PBT test rig, one for each axis.

This was done using an industrial loadcell and DAQ system built by HBM. Two HBM 50N S2M class loadcells were used with two HBM ClipX industrial amplifiers. Together this system was warranted to be accurate to 11.18 mN . Force data acquisition and displacement control was performed on a separate computer to the DIC acquisition.

4.4.4 Post-Testing Procedure

After a specimen had been tested at an extension level, a check was performed to ensure that the DIC data captured was adequate to run an evaluation. Thus, a specimen could be re-tested at an extension level in the case of a DIC acquisition issue. This did not produce substantially different results due to the preconditioning performed.

Sommer *et al.* [29] did work to characterise an orthotropic material and included stress relaxation results to better characterise the material. Stress relaxation was not measured in this project but was observed in bulge and planar test results.

As the objective of this project was not to fully characterise the material, pure shear testing was excluded. Additionally, due to material thickness of SIS, pure shear could only ever be measured in one plane using a rheometer.

Once all data was captured, the specimen was removed from the arms using the card transfer method. Specimens were left in brine until the end of the day when they could be fixed in formalin. All tests were performed with tissue that had been prepared that same day, thus in an eight-hour day, three to four were the most specimens that could be satisfactorily tested.

4.5 Tissue Thickness Measurement

Accurate and repeatable measurement of membrane thickness was necessary to facilitate comparison of stress-strain response between specimens and to inform comparison between separate studies. Methods of tissue thickness measurement were found to differ substantially from study to study [1], [58].

4.5.1 Evaluation of available methods

Prior similar studies reported thickness measurements using the following:

1. Vernier callipers.
2. Micrometres.
3. Optical measurements using microscopes.
4. Mitutoyo non-rotating thickness gauge.

5. A contact force measuring thickness gauge.
6. A commercial hall effect probe.
7. An electrical resistance probe.
8. Fresh-frozen histological sections under polarised light.

Langdon recommended, next to the fresh frozen histology, the relatively inexpensive non-rotating thickness gauge proved to be the easiest and most effective method [24]. Additional methods were not found in the literature. However, one might imagine other methods could include micro-CT scans or similar expensive/specialised methods.

When mechanical probes closed on the soft and thin tissue, there would be almost no increase in torque or force before significant compression. This would be compounded by the mechanical advantage in a micrometre's lead screw.

It was difficult to mechanically measure MT thickness with confidence in absence of significant visual or haptic feedback. Figure 4.21 shows this for a tissue sample. The thicknesses measured were $150\ \mu\text{m}$ and $35\ \mu\text{m}$. The true thickness value sat between the point where the micrometre visually made contact and the point where the torque limit is reached and the first 'click' is heard. The difference of over $110\ \mu\text{m}$ in these thickness values made for noisy stress values.

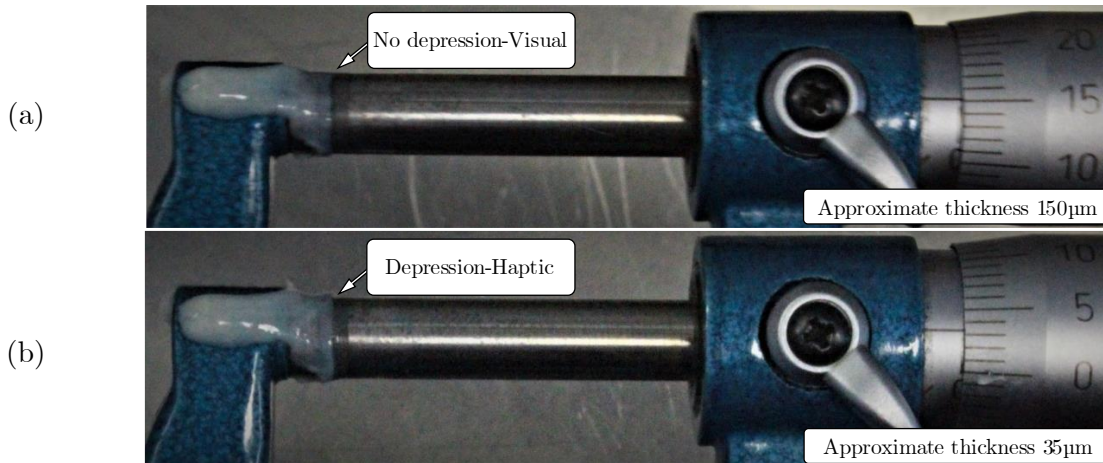


Figure 4.21: (a) Visual tissue thickness measurement. (b) Haptic method where dial was tuned until first 'click'. Note the respective difference in tissue depression.

In this example, the noise to signal ratio (NSR) is very high and can be estimated as below:

$$\frac{u(t)}{t} \cong \frac{150 - 35}{(150 + 35)/2} = \frac{115}{57.5} = 2$$

Where $t \pm u(t)$ mm was defined as tissue thickness and associated uncertainty

It was assumed that the true value was the mean of the upper and lower limit. To accurately do this, repeat measurements should be done using both the visual and haptic measurements to get a standard deviation for both. The calculation above showed that uncertainty was of greater than the "true" value. This was not acceptable.

An optical method was proposed with improved repeatability at the cost of requiring additional equipment. This approach would demand that tissue cross-sections be made after testing and observed under a microscope for measurement of MT thickness.

The additional benefit of this method was thickness data along the sectioned face. The spatial variation in thickness could thus be quantified and used to estimate the uncertainty in a rectangular cross-sectional area assumption.

Bias in measurement of spatial thickness variation would be apparent to the researcher using optical techniques. Spatial thickness variation was very hard to measure using any of the above mechanical methods as the primary measurement step was so fraught with uncertainty.

The first method investigated was to set the specimen in epoxy, cut slowly with a diamond-edged blade and polish the specimen as one might with metal specimens in a metallography microstructure study. This was reconsidered as the heat released from the epoxy exothermic setting process might denature the specimen. Additionally, the blade was not guaranteed to cut cleanly through such a soft material as the SIS. Further investigation led to existing soft-tissue sectioning methods in the field of histology.

4.5.2 Development of histological methods

Histology, the study of tissue microstructure usually involves thinly slicing tissue to view its cross-section. There are three main methods of achieving this: wax, resin fixed tissue histology and cryo-sectioning methods.

Histology labs often provide microscope slides of sectioned specimens and can apply stains to ensure certain tissue morphologies stand out. Without stains, the translucent samples are almost impossible to see in the microscope. The stain of choice for the SIS tissue was a chromotrope aniline blue (CAB) stain which highlighted collagen and some tissue constituents in light blue, and others in blue-black or red (See appendix A.3 for details). This was appropriate given that SIS was rich in collagen and elastin [59].

Due to constraints on time and local expertise and equipment availability, only paraffin wax histology was proposed to obtain a view of the tissue cross-section. An in-house attempt at wax histology were made, however these produced poor results. Figure 4.22(a) showed how the researcher was unable to get clear cross-sectional view using this approach as the tissue was not fixed perpendicular to the view angle and the tissue boundary was unclear due to tissue below the cutting plane. It may have been possible to improve this method, however due to time constraints, professional services were sought.

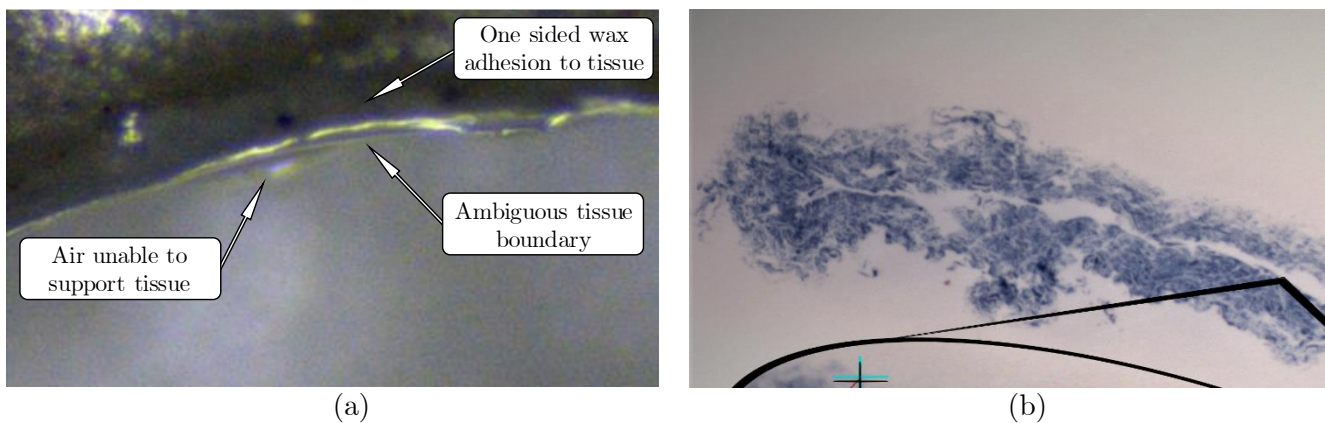


Figure 4.22: (a) Poor quality in-house tissue section. (b) Wax histology thickness measurement.

The UCT Faculty of Health Sciences (FHS) had an existing wax histology service offered to researchers. This laboratory was used to produce and develop micrographs of the membranous tissue. Figure 4.22(b) showed an example of this where some post analysis generated thickness measurements using a calibrated microscope.

It was evident that the tissue cross-section could vary significantly based on the orientation and the relaxation of the tissue. Orientation of the tissue relative to the cutting plane may give skewed impressions of tissue thickness. Figure 4.23 demonstrates this with the angular cross-section of a pipe.

The regions close to the axis of the cutting plane exhibited low distortion of the true thickness value. Regions in-line with the angle of cut exhibited thickness distortion. This was exacerbated when the section is a slice of the pipe and when edges are hard to see.

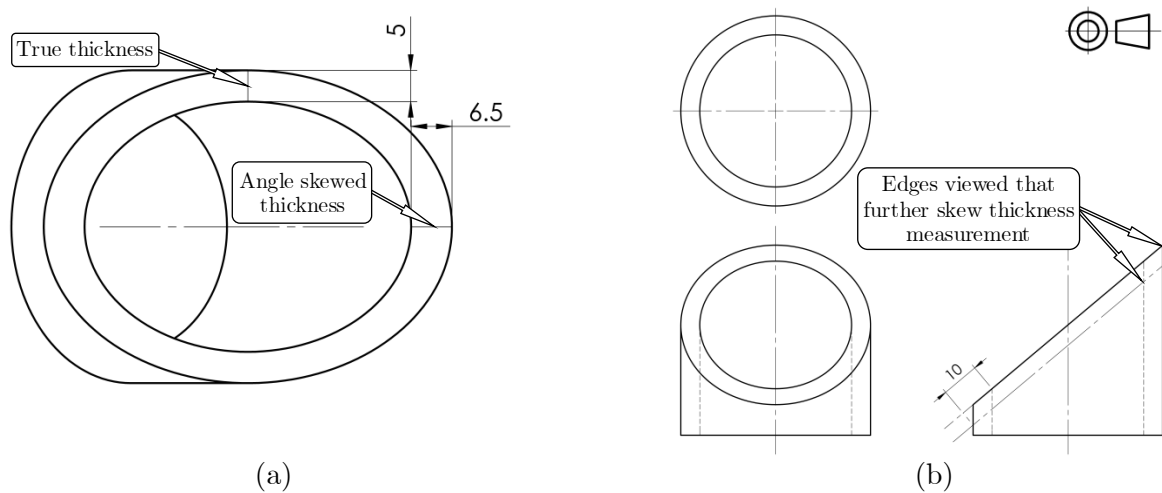


Figure 4.23: (a) View of sectioned pipe normal to cutting plane (b) third angle orthographic projection of Ø50 mm, 5 mm thick pipe sectioned at 40°.

In Figure 4.23(b), the edges seen when viewing the pipe section normal to its surface might give the untrue measurement of thickness as 10 mm. This is double the original 5 mm thickness of the pipe. Distortion like this played a role determining how the tissue was sectioned.

To minimise such distortion, both the section angle and the section thickness should be as small as possible. Section thickness was minimised by setting the microtome cutting depth. Ensuring the true tissue thickness remained parallel to the cutting plane proved more difficult.

An additional issue was illustrated in Figure 4.22(b) where the tissue section was of the unprocessed intestinal tissue. The tissue was contracted and would not give a true indication of initial thickness of a PBT specimen before extension.

A cylindrical wax insert was proposed to keep the tissue from contracting significantly during the histological processing. The diameter of this insert was designed to match the natural operating diameter of the SIS. This was done by measuring the SIS circumference by opening out the cylinder of tissue on a hydrated surface to prevent any stretching during measurement. The results of this are shown in Figure 4.24 below.

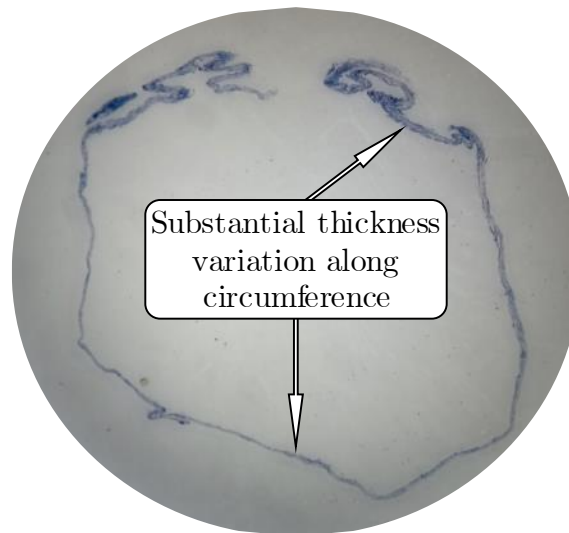


Figure 4.24: *Circular cross-section of the SIS using a cylindrical wax insert.*

What was found in initial histology illustrated in Figure 4.22(b) was reinforced by examination of the circular micrographs illustrated in Figure 4.24. There was substantial tissue thickness variation across a single section and between samples. Thickness measurements ranged between $40 - 140 \mu\text{m}$.

Due to this large variation, the tissue thickness at the edges/arms of the cruciform specimen would be measured instead of using an average thickness for all specimens. This would allow the calculation of stressed area per specimen. This mitigated the skewing effect of thin spots on stress calculation and facilitated better load response comparison between specimens.

4.5.3 Final method

Specimens were fixed in 10% buffered formalin after testing. After two weeks of formalin fixing in their test reference configuration, they were cut from their frames and the MFA was stained with gentian violet. Rectangular wax prisms were cast, from which $10 \times 10 \times 5 \text{ mm}$ blocks were cut. Figure 4.25(a) shows how specimens were wrapped up on these blocks and (b) showed the resulting shells after pre-processing. These were then mounted for tissue sectioning.

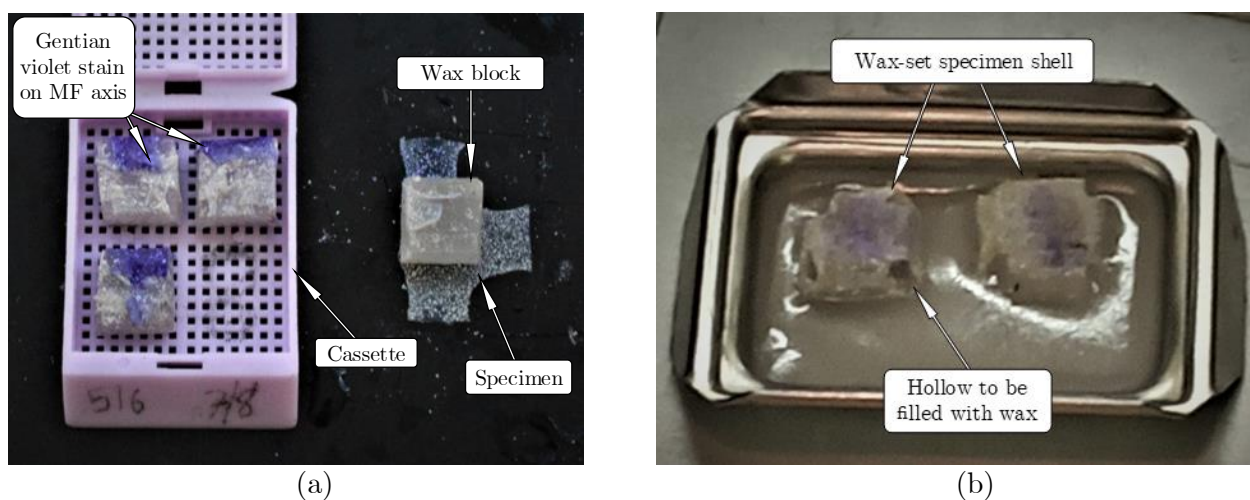


Figure 4.25: (a) *Specimen preparation process* (b) *Results after twelve-hour processing before wax mounting, showing maintained shell structure and MFA stain.*

A $7\mu\text{m}$ cut depth mitigated the angular section errors discussed previously. These sections were CAB stained and examined under a microscope. Images of each arm were taken. Fiji ImageJ with an adapted version of the ThicknessTool macro [60] was used to get an unbiased indication of membrane thickness on each arm of the specimen. Some sections showed delamination of the arm fibres. Such regions were ignored and other slides/regions used to take measurements. In cases where the tissue separated cleanly into two parts, the sum of both means would be used. Figure 4.26(a) below shows a cruciform arm cross-section. The y-axis indicates the MFA and the x-axis indicates the CFA. Figure 4.26(b) shows how the ThicknessTool macro was applied to a processed image of the tissue cross-section.

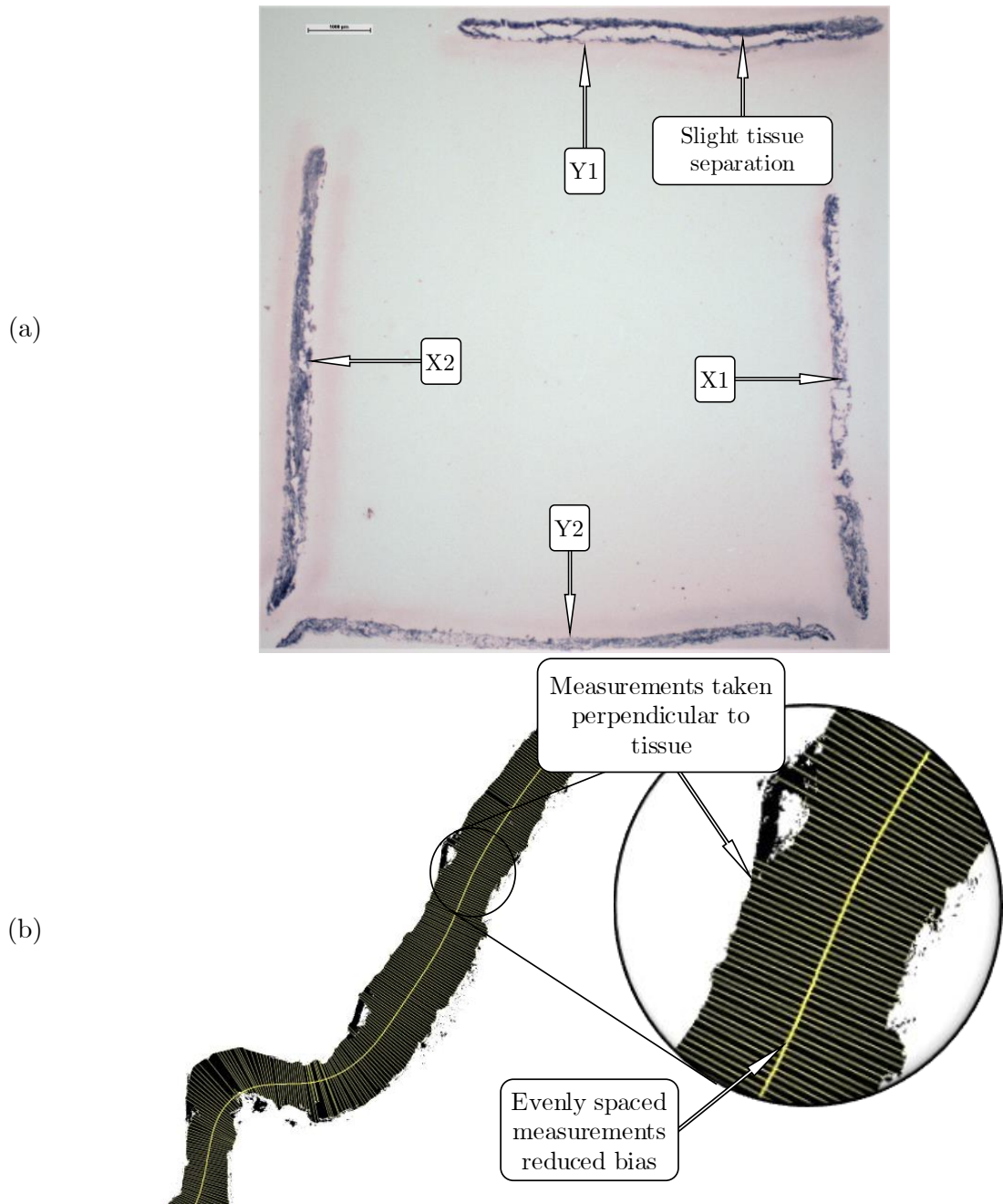


Figure 4.26: (a) Micrograph showing each arm used for thickness measurement with minor tissue separation in one arm. (b) Post-processed micrograph using the adapted ThicknessTool macro.

4.6 Data Processing & Calculations

This section contains the method of converting PBT load data into stresses and basic curve fitting principles applied for evaluation of the MFA ID method.

4.6.1 Engineering Stress Calculation

For a cruciform specimen, conversion from applied load and initial cross-sectional area to a normal stress was not a simple procedure. This was due to geometry and boundary conditions. Stresses at the centre of any PBT specimen are not analytically determinate.

Square specimens made for simple cross-sectional area calculation but discontinuous loading or edge effects of gripping led made for difficult stress approximation. Cruciform specimens exhibited well distributed loads. However, the calculation of the appropriate cross-sectional area remained a challenge with anisotropic specimens.

There were two methods to estimate stresses in the centre of a PBT specimen [47]:

1. Stress correction factors based on data from other tests using the same specimen shape and mounting methods usually found in a testing standard.
2. Computational approaches such as finite element analysis (FEA).

The difficulty of applying either method came with the anisotropic behaviour or asymmetrical mechanical coupling. With SIS, these approaches had limited effectiveness[7].

An inverse FEA or iterative approach may be applied to address this problem [47]. The reason for this being that the modulus of the material is an unknown and thus the loads had to be used with a material model whose parameters had yet to be determined. This was done by comparing the difference between the simulated and experimental displacements until this difference had been minimised[61].

As computational simulations were excluded from the scope of this specific project, any stress calculation was highly simplified.

Methods of experimental stress calculation in the literature were mostly very similar and typically used Cauchy stresses in the plane of testing (σ_{ii}) with the axes of deformation being the reference frame. Vertical stresses were of course zero. Cauchy stresses were derived by means of an incompressibility assumption and the first Piola-Kirchoff stresses [1], [26], [29], [46].

Bellini *et al.* provided a continuum mechanics approach to determine the stresses on their SIS specimen for further material modelling [1]. A summarised version of this with adaptations specific to this project has been given in appendix A.7.

Given the following:

1. Limitations of the PBT specimen shape
2. Shortcomings in the evaluation of BTR results
3. Time limitations

Detailed specimen specific material modelling was deemed unnecessary. The mechanical behaviour measured in this project could only be meaningfully characterised with an inverse FEA approach. This was left for future study.

The simplest measure of stress for the MFA and CFA was determined to be engineering stress. In this case the load was the measured load from the load cells on each axis and the initial area was calculated using the initial thickness of the specimen and the width of the arms.

This simplistic stress calculation was combined with mean engineering strain for both MFA and CFA in the region of interest (ROI).

4.6.2 Curve Fitting

The non-linear curve fitting function (*curve_fit*) of the well-known python library SciPy was used to fit exponential functions of the form of equation 4.4. to the 1:1 extension ratio stress-strain data to allow curvature/stiffness comparison of the MFA and CFA curves.

$$\sigma(\epsilon) = a \cdot e^{b(\epsilon-c)} + d \quad 4.4$$

σ & ϵ represent engineering stress and strain. This was used to estimate and compare the slope parameters of the MFA and CFA. Translational parameters c & d were found to be small and were not considered for slope comparison for simplicity. Equation 4.5 below shows how parameters a & b were used to quantify the slope relationship between MFA and CFA.

$$(\alpha \quad \beta) = \left(\frac{a_{MFA}}{a_{CFA}} \quad \frac{b_{MFA}}{b_{CFA}} \right) \quad 4.5$$

MFA & *CFA* subscripts denote the parameters from their respective exponential curve fit. These were used to build an indicator of dominant fibre direction in 4.6.

$$\nu(\alpha, \beta) = \frac{\alpha + \beta}{2} \text{ where } \begin{cases} 0 < \nu < 1 & \text{CFA dominant} \\ \nu = 1 & \text{Isotropic} \\ 1 < \nu < 2 & \text{MFA dominant} \end{cases} \quad 4.6$$

This dominance value was not intuitive enough and was therefore converted to an isotropy indicator with the help of a sign function shown in equation 4.7.

$$\psi(\nu) = \frac{\nu - 1}{|\nu - 1|} \text{ where } \begin{cases} \psi < 0 & \text{CFA dominant} \\ \psi > 0 & \text{MFA dominant} \end{cases} \quad 4.7$$

This sign function isolated the MFA-CFA dominance from the level of isotropy. Equation 4.8 was used to quantify isotropy as a percentage with the sign function included to give the isotropy index ξ .

$$\xi(\psi, \nu) = \psi(1 - |\nu - 1|) \text{ where } \begin{cases} \xi = 100\% & \text{isotropic} \\ \xi = 0\% & \text{anisotropic} \end{cases} \quad 4.8$$

This function only worked if ν behaved within the ranges of values specified in equation 4.6, which meant that it would not work for compressive testing or extremely anisotropic materials.

Chapter 5

Results and Discussion

The performance of the methodology and the developed components is herein presented and evaluated. This chapter contains interdisciplinary content, design evaluation, algorithmic evaluation and stress-strain analysis. Therefore, the inclusion of the discussion along with the results was determined to be fit as a means of best preserving clarity.

The performance of the mechanical components was adequate yet left room for improvement. The mean fibre axis (MFA) angle identification (ID) algorithm performance hinged upon high quality digital image correlation (DIC) displacement data.

While the algorithm found direction of greatest stiffness, rather than fibre angle specifically, it did so reliably. Where the algorithm indicated low confidence in the angle of greatest stiffness, planar biaxial tensile tests showed these specimens to relatively close to isotropy.

5.1 Design and Process Performance

5.1.1 Tissue Clamping System

The adapted cover plate and gasket improved the sealing capacity of the original mechanism and prevented leakage from the sides of the aperture. Leakage was not eliminated as the membrane was shown in development to be porous to air and leaked rapidly at elevated pressures. Due to the membrane porosity, the improved performance of the modified clamping system is described qualitatively rather than quantitatively.

Figure 5.1(a) shows leakage in the original clamp system (as designed by Curry[1]). Figure 5.1(b) shows the improved clamp system response. The two images are of slightly different test conditions where the pooling liquid seen in (a) was coconut oil and in (b) was water. Note that seepage performance did not vary significantly under matching test conditions with differing inflation media.

The bubbling visible in Figure 5.1(a) shows that air and liquid were forced past the weaker steel-on-steel clamped tissue seal and is largely absent in (b). The minor edge leakage seen in Figure 5.1(b) was not a continuous flow. This was found to be moisture from the tissue that was forced out of the gasket recess, that evaporated over time.

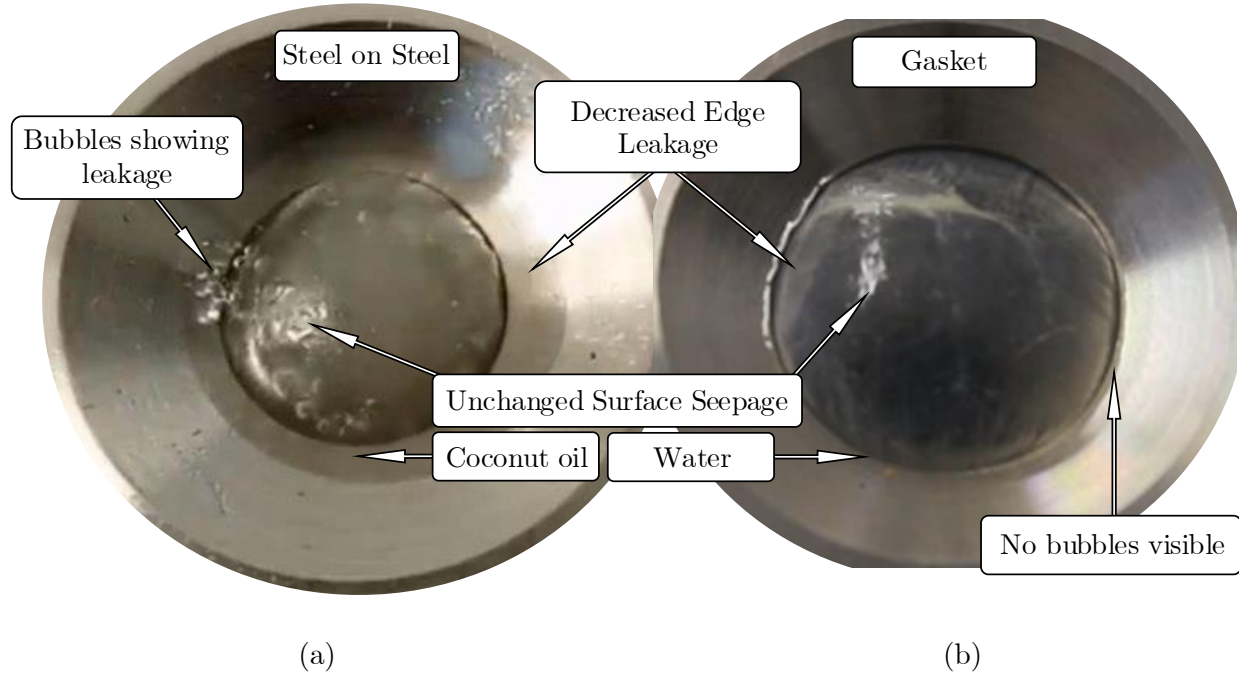


Figure 5.1: (a) Coconut oil inflation of a rudimentary steel on steel clamping system with leakage of inflation media (b) Air inflation of an adapted system with a gasket showing no visible signs escaped inflation media.

The revised tissue and gasket recesses ensured that the clamping plates were always tightened flush, without over-compressing or distorting the tissue. The recesses cut for the gasket also served as a reservoir for the excess fluids between the plates and prevented this fluid from reaching the specimen as it did in Figure 5.1(a). The gasket also gripped the tissue better, this prevented uneven ballooning of the specimen that would occur when the membrane slipped out between the clamp plates under pressure.

Due to the successful seal and tight clamping forces of the new system, the tissue would often adhere to the gasket as shown in Figure 5.2. This led to some issues:

1. Peeling off the gasket risked shifting the original tissue position, misaligning its excision.
2. Mishandling during peeling could lead to the smudging of speckles or the damage of a specimen.
3. As the specimen needed to be handled away from its saline bath to remove it from the clamp, time delays here caused the following:
 - a. Dehydration caused the specimen to shrink and tighten like a drum-skin over the aperture.
 - b. This caused pre-tensioning of the specimen before excision.
 - c. Tensions released when the tissue was rehydrated on the saline bath.
 - d. Resulting specimen slackness led to null force results given the fixed displacement mode of testing.

Unfortunately, the application of lubricant to prevent adhesion proved to reduce the gripping capacity of the gasket. This led to ballooning of the membrane under pressure which resulted in an uneven membrane tension and sag when excising the cruciform specimens.

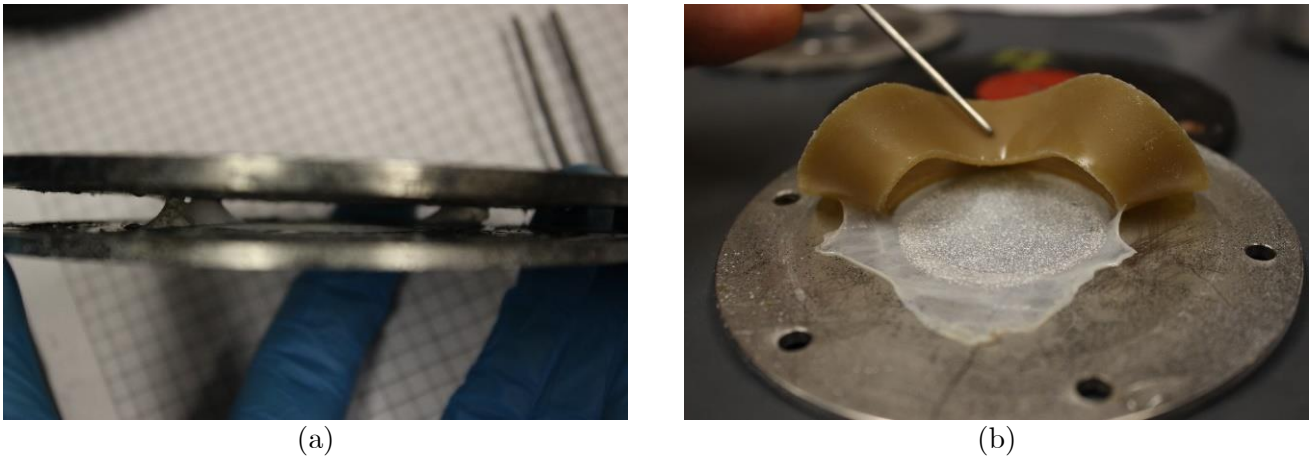


Figure 5.2: *The difficult release of tissue from the clamping mechanism where (a) tissue stuck to gasket and cover plate and (b) tissue stuck to gasket.*

Moisture also caused notable adhesion between the smoothly machined flat steel surfaces. Once adhered, the plates could not be separated by hand, but a blade or pin was needed to introduce a sufficient airgap to break the suction between the plates.

A suggested improvement to remedy this would be three evenly spaced threaded holes on the top plate with matching grub screws to introduce a controlled separation of the plates. Manual insertion risked damage to the specimen, in the event of a slip and violent separation.

Figure 5.3 shows a bolt and wingnut clamp fastening (an improvement to the original system). Unfortunately, tightening the clamp still took too long and was awkward to do while maintaining alignment of the pressure chamber after calibration. A wing-bolt or bolt & electric driver should be used with threaded holes in the pressure chamber body. This would also mitigate risk of dropping nuts onto the membrane surface.

An aperture plug clipped into the cover-plate could protect the membrane from objects, smudging and dehydration. A simplified prototype was made that proved this concept but was not adapted to fit the new cover plates. Figure 5.3 shows a spray-can lid that performed adequately in lieu of this device.

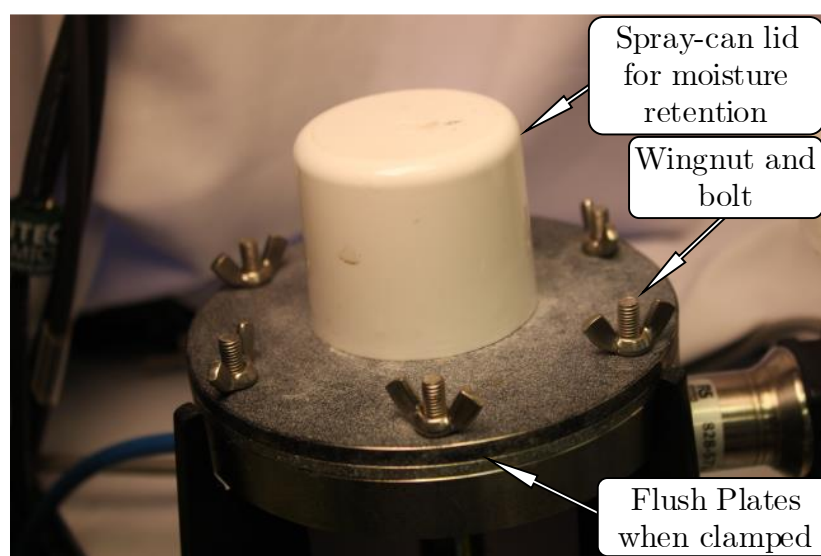


Figure 5.3: *Design issues found with the clamp assembly.*

5.1.2 Chain of alignment preservation

The system designed to retain alignment between the calibration of the DIC for bulge testing and PBT specimen excision worked well. Some future revisions would simplify the system operation and reduce opportunities for error to creep in.

5.1.2.1 Fixation of the BTR

One of the shortfalls of the alignment preservation system was the lack of appropriate locating features for the pressure chamber and stand assemblies.

Firstly, the pressure chamber stand did not have any convenient points with which to clamp it firmly to a tabletop. Instead of this, as seen in Figure 5.4 it was taped down into a corner of the testing tray. Fortunately, this tray was weighed down by the entirety of the PBT tester which made for semi-rigid location of the stand. The use of a clamp for the stand would have helped avoid having to recalibrate the DIC axes to the system axes when the stand was bumped.

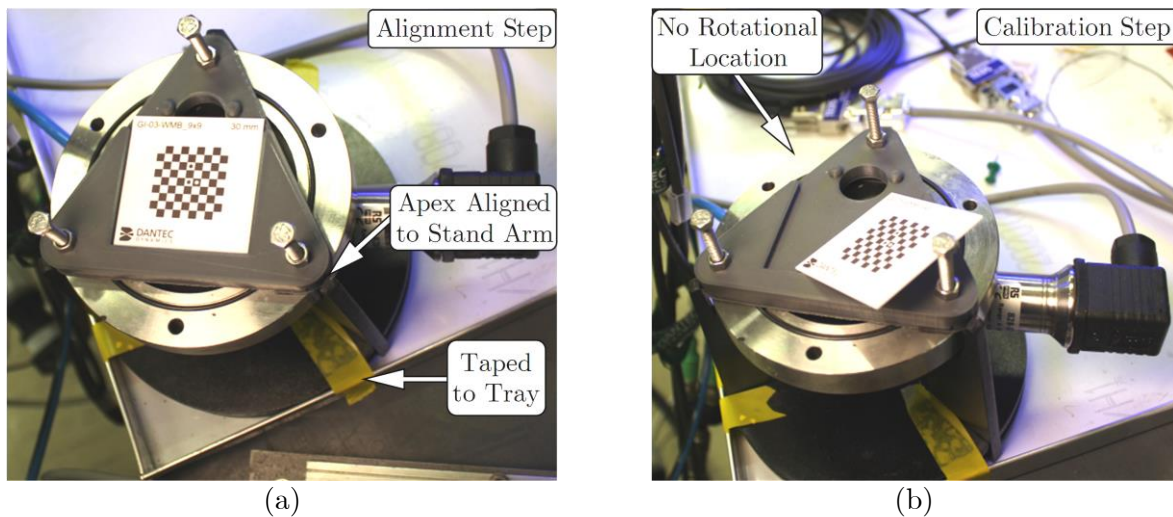


Figure 5.4: *BTR DIC (a)alignment and (b)calibration steps.*

With the stand mostly fixed in place, the pressure chamber was translationally located by it. Lifting motion was unconstrained to allow for rapid setup of specimens. Rotation about the vertical axis was unconstrained which significantly slowed down the testing process.

As angles wrt. to the calibrated position were key to determining excision angle, any accidental rotation had to be corrected immediately. With no points of location for rotational-alignment, this was done by eye/feel such that the triangle of alignment bolts aligned with the stand arms. Disturbing the pressure chamber after calibration was impractical to avoid as specimen setup was more effective with the chamber off the stand. Furthermore, torque from fastening the bolts would inevitably have disturbed the alignment anyway.

This design shortcoming (an artifact of scope change) could be mitigated by a pressure chamber modification. Notches on the circular chamber interfacing with each stand arm would constrain relative rotation. The pressure chamber could then be removed easily for setup and be slotted back into its calibrated position. Due to limited workshop functionality at the time and project time constraints, this modification was not possible.

5.1.2.2 DIC Calibration

The jig used in Figure 5.4 was very effective at ensuring repeatability in the calibration of the DIC equipment. The height at which the jig placed the calibration target made for easier displacement measurement of bulge testing with minimal depth of field issues arising.

The difference in height between the bulge tester and PBT specimens meant it was necessary to re-focus the cameras and sometimes to re angle them when moving to the other test rig. This made it more efficient to batch test on the BTR before moving to the PBT tester. This specimen downtime was a dehydration risk.

Simply raising or lowering cameras did not resolve this issue effectively. The stereoscopic setup made it difficult to compose both views correctly while doing this. Furthermore, refocussing would be needed to retain high quality DIC measurement.

This could be resolved by raising or lowering the rigs to ensure the specimens were on the same focal plane. The whole camera rig could be moved quickly without camera adjustment. The expensive alternative would be to have two camera rigs to switch between on the DIC software.

5.1.3 Goniometric Cruciform Specimen Cutter

The mechanism for excising specimens at a specific angle, developed by several design iterations entirely within this project, proved to be highly effective.

5.1.3.1 Cut quality

Figure 5.5 shows several specimens cut with the final iteration of the cruciform specimen cutter. The cutting block design improvements worked well to ensure a consistent cut at the arm apices. Less force was required to get a clean cut and reduced the damage to the soft cutting surface below the MT. Figure 5.5(S11) shows how the cutting block left specimen 11 once removed. S13 and S6 show progressive retraction of tissue, leaving clean cruciform specimens.

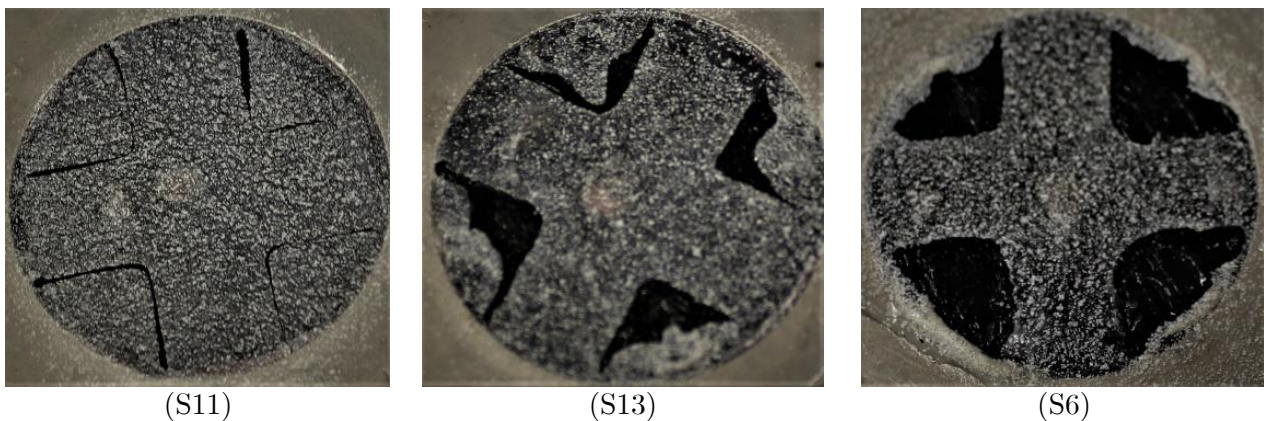


Figure 5.5: *Progression of specimen excision quality assessment.*

5.1.3.2 Process issues

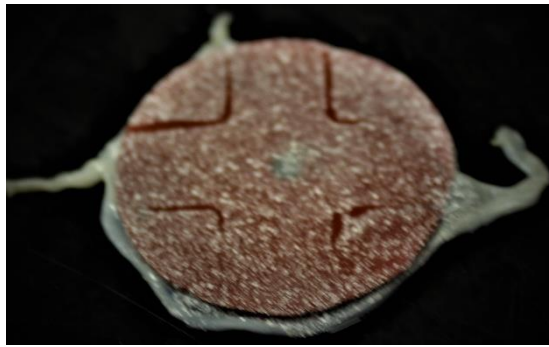
The specimen cutter occasionally suffered from adhesion of the cutting surface to the blades when the cutter was removed (taking specimen and cutting surface with it). Figure 5.6(a)

shows how the excess MT used for mounting the grips got wrapped around the cutting surface. This would happen if the blade was forced through the soft cutting surface into the rubber cushion below it. Using fresh cutting surfaces for each specimen would mitigate this.

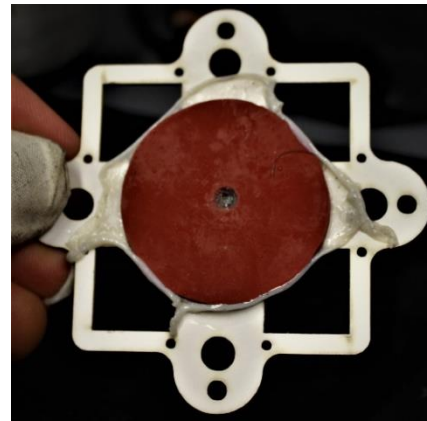
Figure 5.6(b) shows how the cutting surface remained adhered after raising transfer card. This pre-test loading held potential to skew results. Were the cutting surface vertically located using a flush central screw, the issue would be resolved.

The MT-Gasket adhesion issue mentioned in 5.1.1 could be mitigated if the blade protruded above the gasket and not otherwise as shown in Figure 5.6(c). This would have allowed specimen excision before gasket removal and lowered the risk of specimen misalignment.

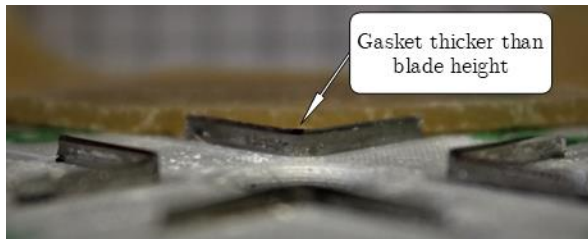
Figure 5.6(d) shows how cruciform cutter and guide tolerancing did not ensure coaxiality between the components. A doubled layer of the cutting guide board would have mitigated coaxial deviation for the same tolerancing.



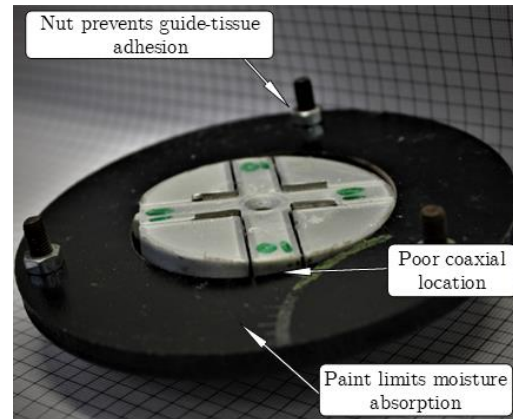
(a)



(b)



(c)



(d)

Figure 5.6: (a) MT & cutting surface adhesion, (b) cutting surface not fully located, (c) blade height insufficient to clear gasket (d) and imperfect cutter-guide coaxial location.

Nuts added to the alignment bolts prevented the guide from resting on MT and adhering to it. Contact between MDF board and MT caused instant adhesion as the moisture was sucked out from the tissue via capillary action. Multiple layers of paint resolved this.

5.1.4 Moisture preservation measures

Due to the absence of keratinised layers, SIS lost moisture very rapidly when exposed to atmosphere. Speed was used as much as possible to get the specimens prepared and through the MFA identification process to sit on a saline bath to be PBT tested. This process could be slowed by many possible issues with speckling, the BTR, or DIC to name only a few. Any delay left the specimen exposed to atmosphere, drying it out and consequently change in shape and material properties. Raw tissue was kept in saline until speckling. From bulge speckling until cut and afloat in the PBT tester bath, specimens had large areas exposed to atmosphere. Thus, additional measures were taken.

Gentle spraying of the specimen underside with saline solution worked well to keep the specimen moist on the inside of the chamber. This was later accompanied by humidifying the pressure chamber which further prevented dehydration. Atmospheric humidity was not controlled in the same way. Figure 5.3 shows a plastic cap over the bulge aperture which was occasionally spritzed with saline in efforts to humidify the air contained within.

This process could have been improved by bulge testing inside a humidified chamber, but this posed concerns for fogging the DIC camera lenses and corrosion of camera electronics, that need to be investigated.

Figure 5.7 shows the saline bath mounted on the PBT tester which worked remarkably well at maintaining specimen moisture levels for a first iteration design. The bath mounting method hampered PBT tester troubleshooting more than once. The bath had to be removed to allow realignment of the specimen grips which was an awkward process. Special care had to be taken not to bump the PBT arms while working it under the arms during re-installation.

The existing bath mounts used a cylinder of hot glue to locate the bolt without rotational constraint. This did not require holes in the bath (mitigating leakage) but meant that bolts were tightened awkwardly from the side using pliers to get a good purchase. This also made it tricky to get the t-nuts to engage in the aluminium channel.

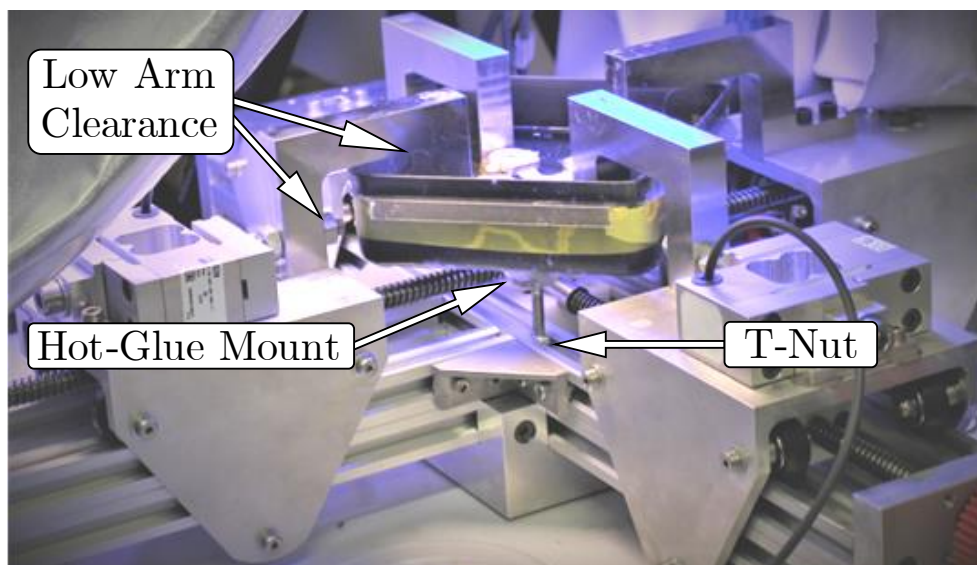


Figure 5.7: *Saline bath used to maintain specimen hydration during PBT tests.*

A second iteration saline bath should be performed for future research with careful attention to the following:

1. Ease of installation: bolts to be tightened from above with an Allen-key tool.
2. Allowance for arm re-alignment without bath removal.
3. Ease of draining saline.
4. Integration with an arm-assembly re-design to allow ease of use.

5.1.5 Planar-biaxial MT Grips

The tissue grips performed well given they were a first iteration design which saw little change from conception to implementation beyond some minor adjustments, namely the rounding of the back edge and the addition of a bolt-hole.

The rounded back edge of each grip allowed free planar rotation during testing and mitigated shear stress in the specimen. The process of arm trimming risked disturbing or damaging the specimen. As shown in Figure 4.19(d), the bolt helped prevent rotation during arm trimming.

The grips proved to be highly versatile and able to withstand significant abuse despite being made of cardboard. In the case of Specimen 6, the glue held for a full program of testing the following day despite prolonged soaking and freezing the night before.

In cases like this and where arm alignment issues were picked up after the specimen had been mounted, the card's stacking ability (seen in Figure 5.8) proved very useful in facilitating specimen removal.

Figure 5.8(b) shows how a specimen was removed by gluing a fresh card (arms intact) on top of the old card which linked the grips and mitigated any loads that might void the specimen. When re-installing the specimen, the process was procedurally the same as the first installation. Specimens 10 and 6 below showed how specimens could be installed and removed multiple times using this approach.

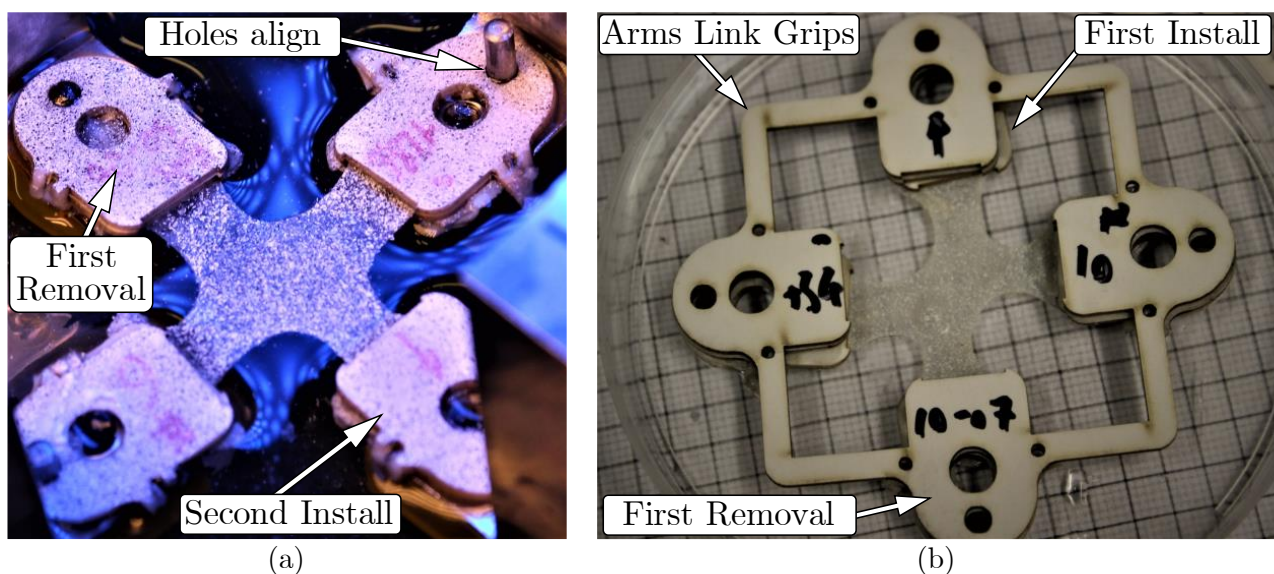


Figure 5.8: *Grip performance with two specimen installations and (a) one/(b) two removals.*

Sixteen specimens were tested close to failure using the same gripping method. Their grips experienced a wide variation in soak time before being tested. This was the main weakening factor for the grips, however, not one grip failure was observed.

The grips performed well, rotating on the pins when necessary and were able to withstand the flexure and loads in cutting away the arms. The trimming process seen in Figure 4.19(d) could have been improved by using slightly thinner card, as the thick card made for a very square cross-section along the arms which could not be cut with scissors easily. Scissors were preferred over scalpel blades as the shearing process of cutting with scissors did not lead to a resultant force that would risk overloading the loadcell. Scalpel sawing motions risked breaking the water surface tension around the specimen and causing it to sink.

5.1.6 Uncertainty and Error Propagation

As this project focussed predominantly on methodological evaluation, quantification of uncertainty in measurement was a key metric in determining improvements to the method. Error was calculated and propagated through all calculations under the guidance of *ISO budgets* publications on the topic [2]. For the sake of brevity, the resulting error was not always shown but formed a major part of the analysis of the method. Appendix B.7 contains more detailed explanations of the error propagation and uncertainty budget.

5.2 DIC Data Quality Evaluation

The DIC speckling strategy employed to enable full-field displacement measurement was adequate. Due to the skills required achieve consistency, the quality of speckling improved with time and was reflected in the DIC data quality. DIC evaluation was initially performed with parameters that reduced experiment time at the expense of data quality. The extent of this expense was investigated here.

5.2.1 Mechanical Effects of Speckling

The mechanical effects of speckling with spray paint were quantified on a 15 mm bulge specimen. Figure 5.9 compares this specimen's pressure histories before and after speckling.

The pressure responses were very similar. Factors such as dehydration between tests and the small difference in test speed (98 rpm vs 97 rpm) are just as likely contributors to the minor differences observed as the effect of speckling. Additionally, the histories were indistinguishable at lower pressures. This meant that, for the purposes of this project, the mechanical characteristics of SIS were not influenced by speckling.

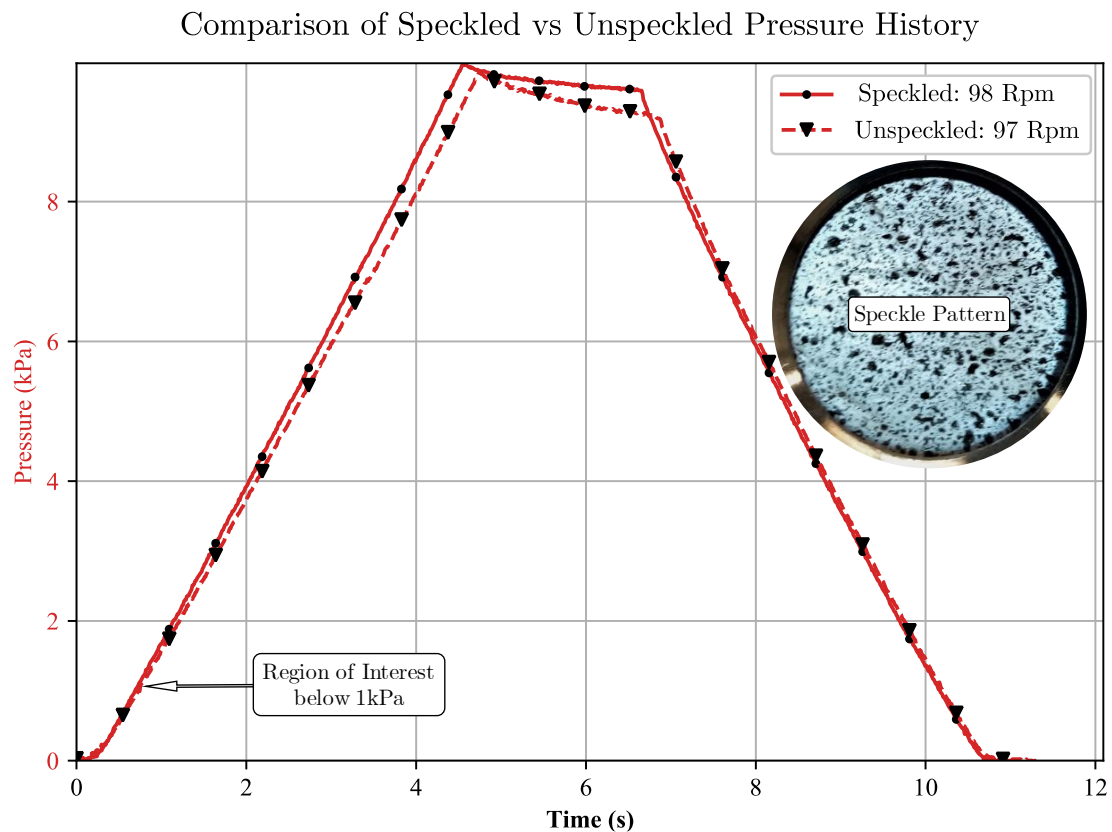


Figure 5.9: *Spray paint speckling shown to little influence specimen pressure history.*

5.2.2 Evaluation Parameters

Speckling strategy effectiveness was difficult to isolate from the impact of data evaluation quality. Strong correlation was observed between speckle pattern quality and displacement error. Figure 5.10(a) shows how the peak noise to signal ratio (NSR) varied with each specimen while using the initial DIC evaluation parameters in Table 3.3

Specimens 1,8,9 and 11 exhibited the lowest NSR under these parameters. Specimens 3 and 6 had the highest NSR, the reasons for this are discussed in the next section. The progressive NSR mitigation in Figure 5.10(b) & (c) show the effect of post-processing DIC data with an increased facet size.

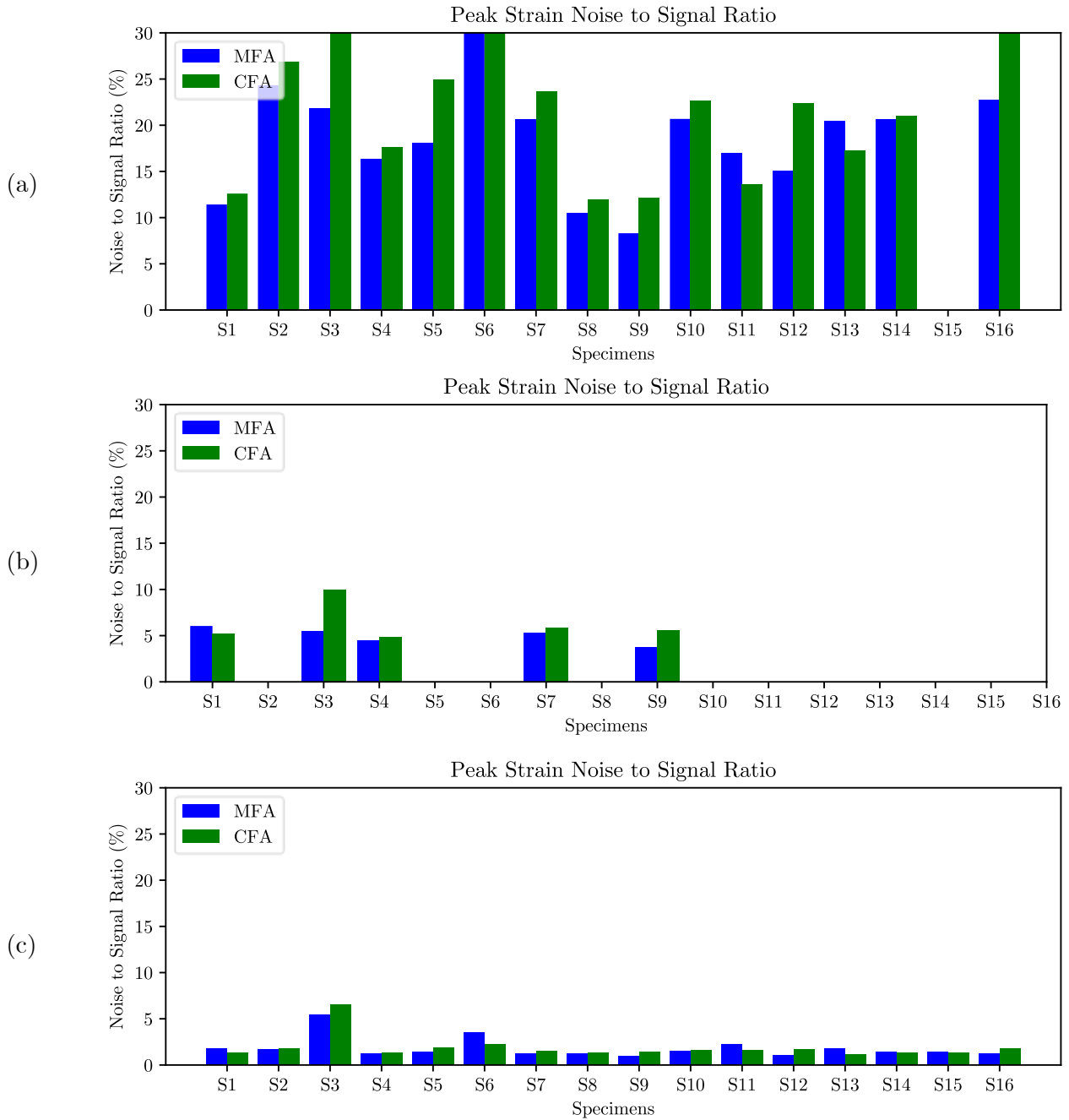


Figure 5.10: *HE specimen peak strain NSR evaluated at (a)15 px,(b)29 px and (c)59 px facet sizes*

While the increased computational expense of larger facets added significant time to the DIC evaluation, the gains in data quality made this a highly worthwhile process improvement. Increasing the facet size to 59 pixels, without any other changes to evaluation parameters, yielded a further improvement in NSR, shown in Figure 5.10(c).

In the absence of live data quality assessment, faster evaluations were useful in confirming if data was suitable for more accurate evaluation later. Due to tissue degradation and dehydration associated with long evaluations the only other alternative was to skip preliminary evaluations all together. This would have risked losing complete datasets that only required a re-test at little detriment to the specimen to produce usable data.

If time was no longer a major constraint due to adequate planning and specimen moisture control, the slower yet more accurate evaluation parameters could be used for each specimen.

5.2.3 Impact of Speckling on DIC Noise

Given the above impact of evaluation parameters on NSR, an attempt was made to isolate the effect of speckle quality on NSR. ImageJ was used to assess speckle pattern statistics. Table 5.6 shows these statistics for six specimens and correlates speckle quality metrics to the specimen NSR values of Figure 5.10. The speckle quality metrics used were:

- Speckle area density (ρ_{spec}) measured in $\frac{\text{Speckles}}{\text{mm}^2}$
- Mean speckle diameter (ϕ_{spec}) measured in μm
- Standard deviation (σ_ϕ) of the speckle diameter in μm .

Table 5.6: *Summary of the impact of speckle statistics on NSR.*

	LOW NSR			HIGH NSR		
Specimen	1	8	9	11	3	6
ρ_{spec} (Speckles/mm ²)	6	5	4	3	2	2
ϕ_{spec} (μm)	49	55	76	105	114	128
σ_ϕ (μm)	89	138	209	318	1077	824

High NSR specimens correlated with low ρ_{spec} , ϕ_{spec} and high σ_ϕ . Specimens with a large variation in speckle size (σ_ϕ) made it difficult for the DIC to evaluate thus increasing NSR. The ρ_{spec} and ϕ_{spec} for low NSR specimens aligned with the theory of ideal DIC speckling. An even distribution of small specimens usually correlated with a good speckle pattern. This was seen in the specimens presented.

Specimen 3 and 9 grey-value histograms in Figure 5.11 may point to an additional quality metric. Detailed analysis of the histogram shape in a quantitative sense was beyond the scope of this project. The qualitative analysis, however, is not. It was observed that the best performing speckle patterns all had a shark-tooth shape. Figure 5.11 shows this for specimen 9 where it had a sharply defined maxima and a concave curve on either side.

Low quality specimens such as specimen 3 formed much blunter shapes with more pixels distributed towards higher and lower grey values. This observation was understood in the

following way: low NSR speckle patterns featured distinction between speckle and background (sharper peaked histogram) without too high a contrast (fewer pixels towards the max and min grey values).

None of these speckle quality metrics can stand alone as an indicator. They all worked together to indicate speckle quality, the details of which could be the subject of further study in its application to DIC with MT. For further reference, [3] offers more depth to DIC speckle quality assessment.

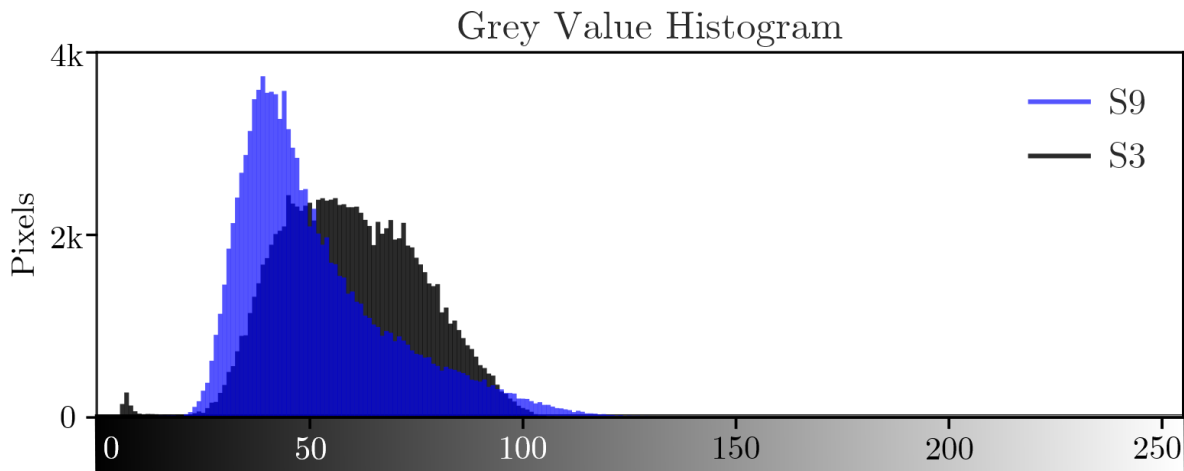


Figure 5.11: *ImageJ speckle pattern histogram analysis comparison.*

5.3 MFA Identification

The process of theoretically identifying a MFA using a bulge test and a full-field displacement analysis algorithm was evaluated and found to be reliable given proper use. The scope of this appraisal covered how specimens were bulge-tested, DIC parameters that led to the best performance wrt. accuracy & time and finally the sensitivity of the algorithm to user-inputs.

5.3.1 Test pressure cycle

Little pressure was required to significantly deform the membrane to an ellipsoidal shape. Pressure increases to achieve further displacement yielded diminishing returns. A test pressure of $0.5 - 1 \text{ kPa}$ on a 35 mm aperture achieved sufficient displacement for elliptical deformation contours to be identified by the algorithm.

Specimens lost pressure over time during the pause period of the pressure profile. As the syringe pump was operated primarily in displacement control mode, the addition of a closed loop pressure control subroutine to the system would be necessary to limit pressure reduction in this step.

The specified pressure profile proved useful in data post-processing as there were more time-steps at peak displacement which increased the likelihood finding a noise-free apex step. There were also double the reference and point of interest steps to choose from. This helped where the specimen was not very flat to start but reached a flatter reference state at the end of the test cycle.

5.3.2 DIC Facet Size Optimisation

The initial choice of DIC parameters favoured processing speed over positional accuracy, in the interests of reducing testing time and the effects of dehydration. After testing was completed and the processed DIC data was examined, it was found that the error that the DIC software calculated for the initial evaluation parameters was much higher than anticipated and warranted further investigation of the DIC evaluation parameters and processing time.

Figure 5.12 illustrates how angular error was calculated using the positional error $(\delta x, \delta y)$ at a point (x, y) with $(0,0)$ being the centre about which the angle was calculated. The angular position β was calculated using the original coordinates, however the angular error $\delta\beta$ was calculated using the combination of $(\delta x, \delta y)$ that led to the largest angular error. In the example, Figure 5.12, this maximum combination was $(x - \delta x, y + \delta y)$ and $(x + \delta x, y - \delta y)$.

This method of calculating the angular error was applied to each point along the elliptical contour to calculate the average $\delta\beta$ for the fit. This was carried out for each of the facet sizes chosen to investigate its effect on MFA angle and associated error.

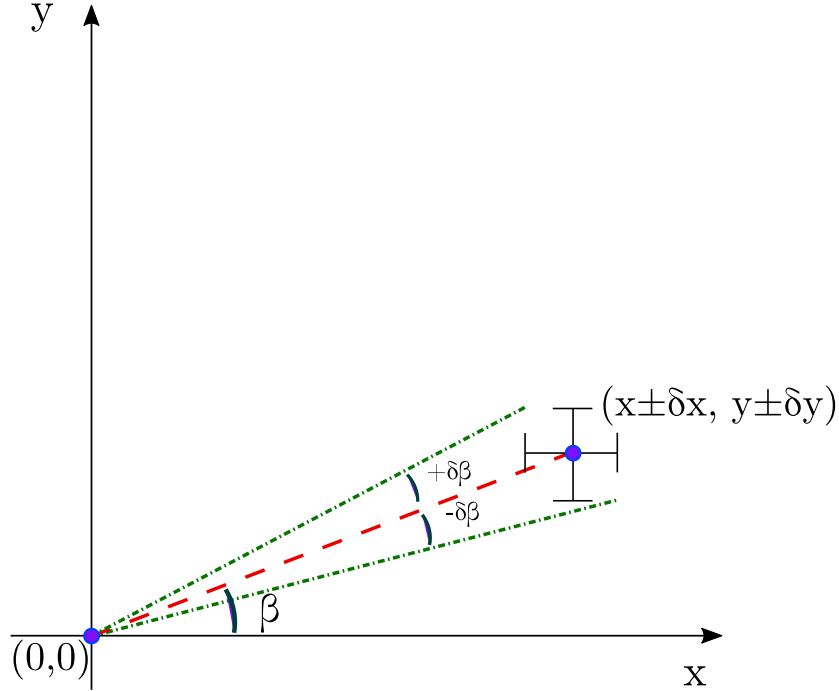


Figure 5.12: Angular error calculation for a single datapoint.

A similar approach was taken for the measure of isotropy determined for bulge testing. The isotropy index (ξ_{bulge}) is defined in equation 5.9:

$$\xi_{bulge} = \frac{r_{min} - r_{roi}}{r_{max} - r_{roi}} \quad 5.9$$

Where r_{roi} is the reference circle radius, r_{min} is the ellipse minor radius which corresponds to the least stretch and hence the MFA. r_{max} is the major radii, corresponding to the largest stretch and hence the CFA.

It can be seen from these calculations that the angular error would be drastically larger for the same positional error at a position closer to the centre (0,0). This meant that the quality of MFA angle calculation would improve with increased ROI size with respect to positional error.

The angle, angular error and isotropy indices for the different specimens at the various facet sizes were compiled to form Figure 5.13. The angular error of individual specimens decreased substantially with increased facet size. The MFA angle did not change substantially beyond a **49 px** facet size.

Similarly, the isotropy of each specimen didn't change substantially after the first increment in facet size. For most cases (besides specimen 10), the difference between ξ_{bulge} at **119 px** and **89 px** was less than that of **119 px** and **15 px**. This, together with the impact on MFA angular error, makes a strong argument for the use of large facet sizes.

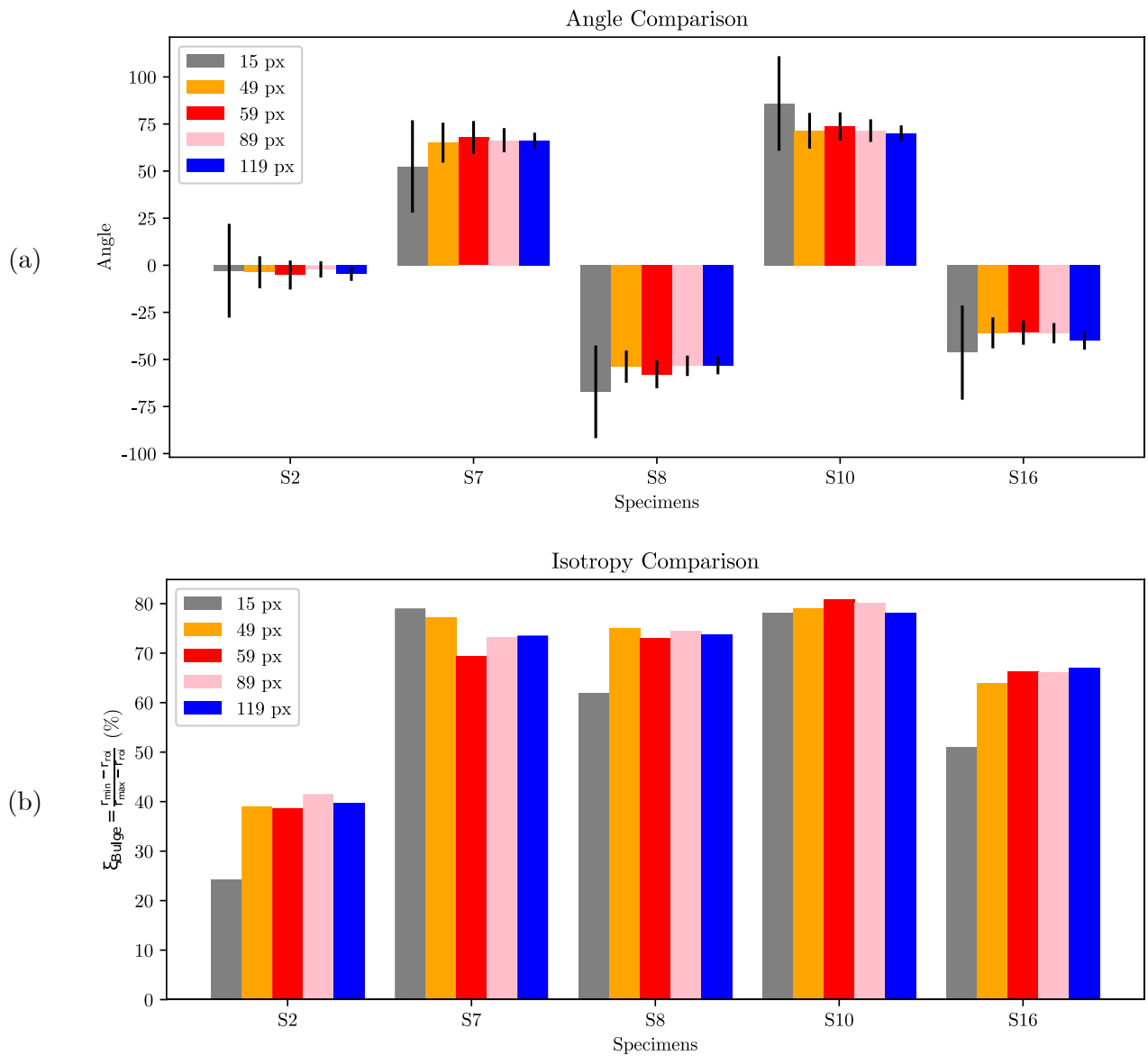


Figure 5.13: *DIC facet size optimisation findings show that (a) error reduced with increased facet size while angle identification and (b) isotropy, did not vary substantially above 15 px.*

The 15, 59 and 119 *px* facet sizes ran for approximately 5, 15 and 45 *min* respectively. Balancing the competing needs of lower NSR and quick processing to reduce dehydration, a facet size of 59 *px* was chosen for all further DIC evaluations.

Note that specimens were excised at the mean angle determined from the 15 *px* facet DIC evaluations and the investigation of larger facets was performed after all experiments were completed. As this angle lay within or close to the confidence limits of the larger facet evaluations, this was deemed sufficient for further evaluation of the methodology.

5.3.3 Parameter Selection Dependence

The MFA identification (ID) algorithm was dependent on some initial parameters, however, those that varied from specimen to specimen were the time-steps of the reference, apex and point of interest (POI). Figure 5.14 shows the shape of the specimen surface with a vertical displacement colour map superimposed onto its surface. The reference step (a) corresponds to the flattest bulge specimen surface, while the apex step (b) corresponds to the largest displacement, which sometimes lost facet data around the perimeter of the ROI. The POI step (c) was chosen to be the largest deflection with an acceptable loss of facet data around the ROI perimeter. The POI was when the bulge specimen had both the largest deflection and the least noise along the circumference of the elliptical contour.

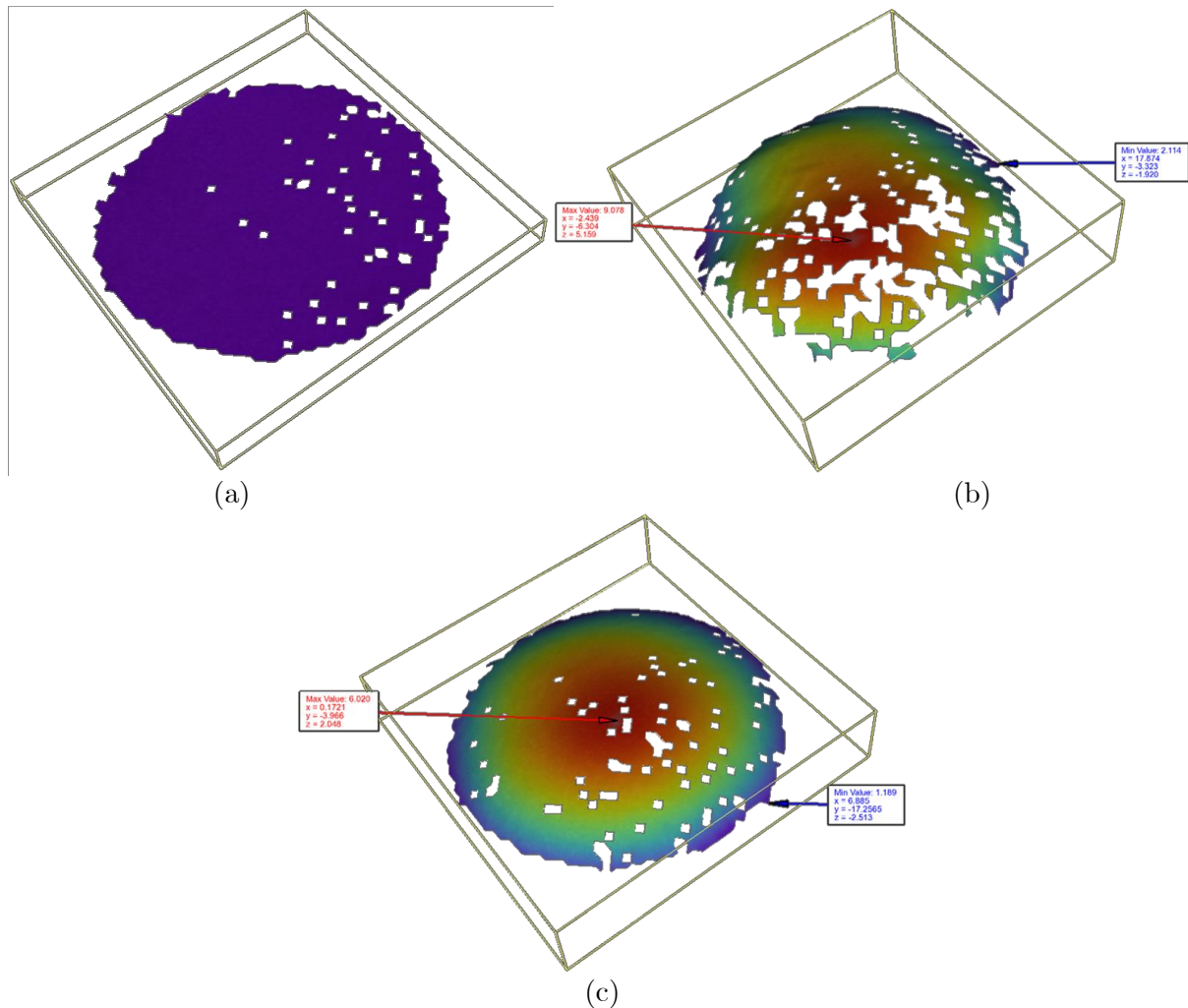


Figure 5.14: Examples of (a) reference, (b) apex and (c) POI time-steps of the bulge test.

Selection of these time-steps was entirely manual and thus there was introduction of human error/bias to the calculation process. Therefore, the sensitivity of this algorithm to user input-parameter perturbations was investigated

Given lists of possible time-steps for reference, apex and POI positions of lengths n_{ref} , n_{apex} and n_{poi} respectively, the number of different permutations in test parameters can be represented by equation 5.10.

$$P = n_{ref} \times n_{apex} \times n_{poi} \quad 5.10$$

From this we can see that P increases drastically with the size of each list. Were these problems to be solved in series, the run-time was estimated to take well over one hundred days per specimen.

This called for a multiprocessing approach, performed in *python* using standard libraries, that brought run time down to about four hours on average. Owing to the time expense, this analysis was performed for a few specimens at the upper and lower facet sizes of Figure 5.13.

Figure 5.15 and Figure 5.16 feature selected algorithm test outputs. The box and whisker plots represent variation of the metrics wrt. input parameters. Parameter lists were conservative estimates of the worst-case range of values. Skilled users would have chosen parameters like those for Figure 5.13.

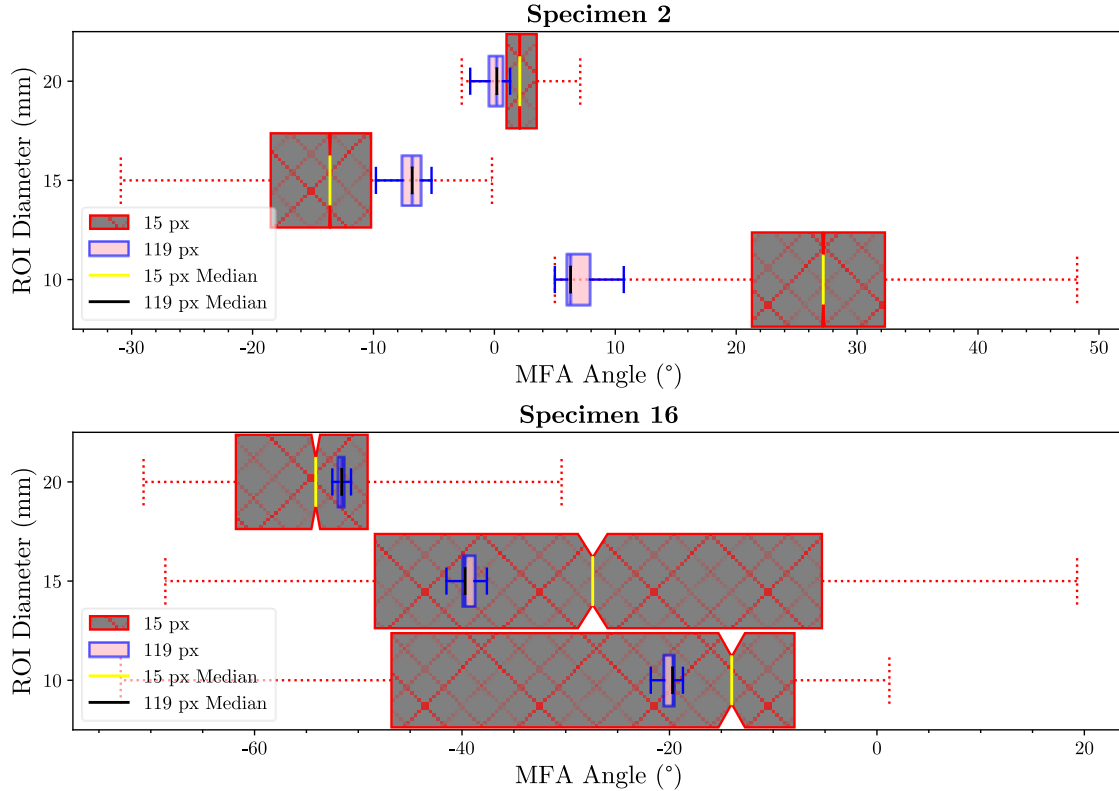


Figure 5.15: *MFA angle statistics using a range of MFA ID algorithm inputs.*

It is clear from the data range reduction and increased sharpness of the median notch that performance dependence on user input decreased with larger facet size. This made sense as larger facet size led to fewer gaps in the data and lower positional error which reduced error in the MFA ID algorithm.

The increased data range with smaller ROI validated the analytical prediction posed in 5.3.2. Thus, if given a larger ROI, the algorithm was less sensitive to user perturbations.

Figure 5.16 shows that the isotropy also varied with the ROI diameter. A larger ROI may have passed through vascularised regions of tissue depending on how the specimen was cut from the SIS tract. In summary, an increased facet size reduced user input dependency.

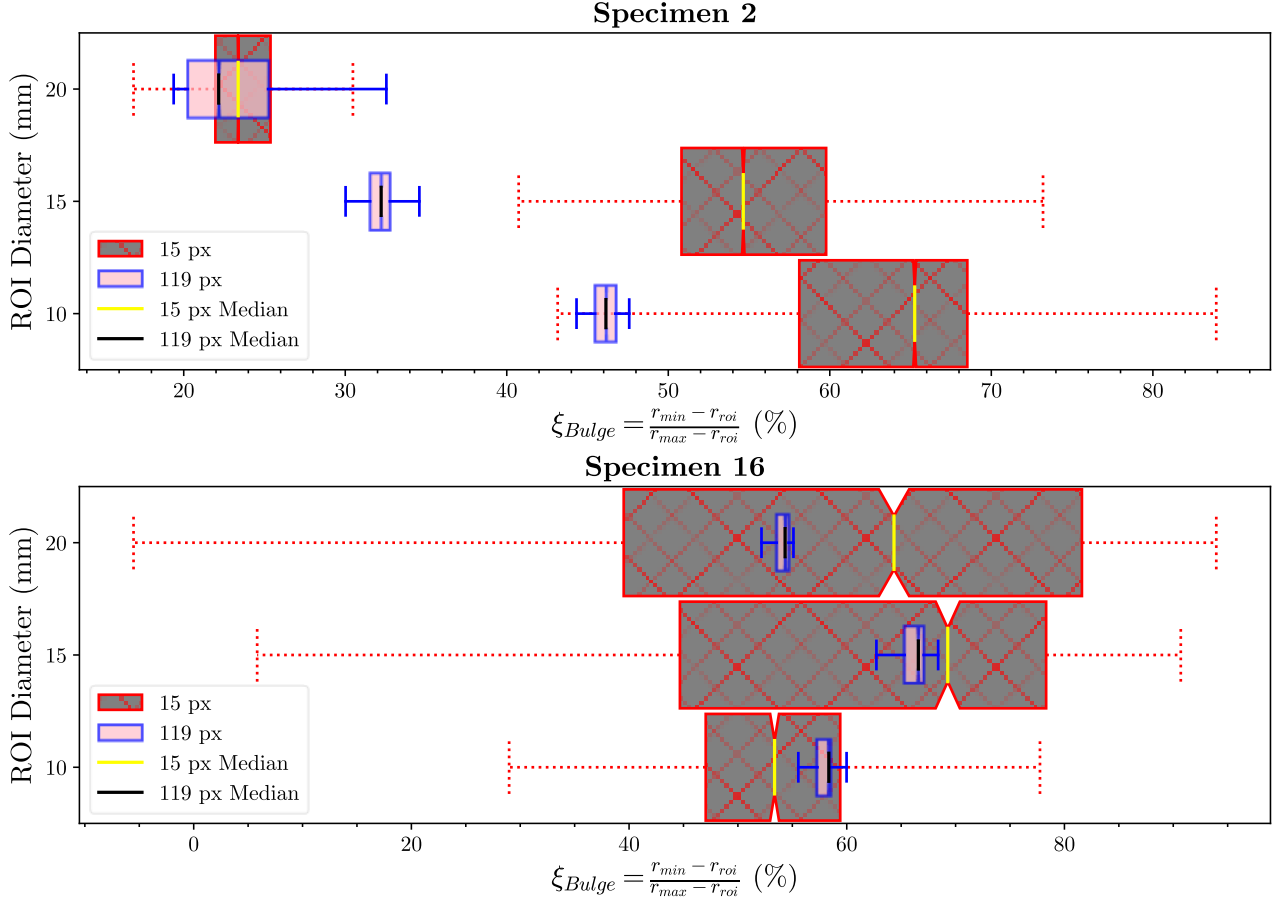


Figure 5.16: *Isotropy statistics using a range of MFA ID algorithm inputs.*

From comparison of the median isotropies, it was apparent that improved data quality shows the isotropy to be significantly lower than that of the smaller facet size. This was likely to do with the elliptical contour curve fitting process. With more noise in the data, it is possible that there is a bias towards a higher calculated ξ_{bulge} value.

The change in median isotropy and MFA angle agrees with Sacks' findings of often highly localised fibre alignment for SIS [4].

Less parameter dependent estimations of the isotropy index and MFA angle were thus achievable with larger DIC facet sizes chosen for evaluation. Although facet size increased the DIC evaluation time, risking dehydration, the benefit of a more trustworthy algorithm output made it worthwhile.

5.3.4 Process Performance

The MFA identification algorithm was under continual development during its use and did not offer all the same features from the start. The current checks & balances, angular error and isotropy index measures would initially have been very helpful.

When these features were not present, the algorithm still performed well and in most cases the angle that was calculated was the angle that was cut. In the case of specimen one, the radii of the MFA and CFA were very close to equal (which would have given a high isotropy index). Here the researcher deliberately chose the typical MFA angle of 30° that was given in the literature to test the theoretical angle against a measured angular indeterminacy (a high ξ_{bulge} value).

A summary of the angles cut vs. those calculated is given in Figure 5.17(a) which gives the angle calculated by that version of the algorithm. With the updated parameters of the newer revisions (such as the ROI size, angle tolerance and radius tolerance) and improved facet size in post processing of the data, these values would change slightly. Increased facet size would have led to the reduction in error associated with the calculated angle seen in Figure 5.17(a).

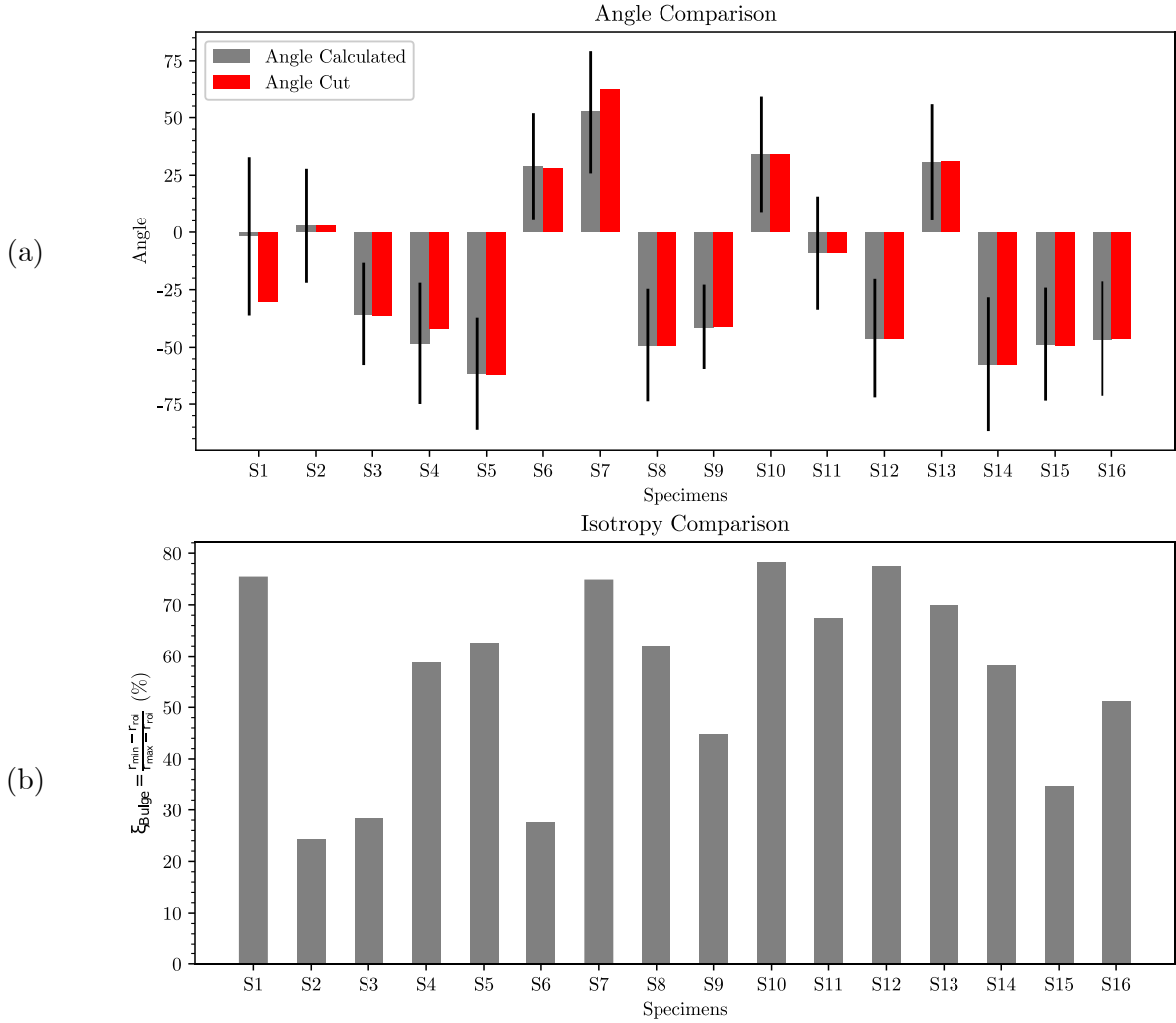


Figure 5.17: Comparison of (a) angles calculated vs angles cut across all specimens and (b) the bulge test isotropy index for each specimen.

It would not be meaningful to compare these ideal cut angles with the PBT results as they would not reflect the true excision angle. This would have also required re-evaluation of all bulge tests with little potential for new understanding, as it would be difficult to quantify the impact of an erroneous angular excision on the PBT results.

As seen in Figure 5.13(a), the calculated MFA angle value changed very slightly with improved data quality. Therefore, these angles were adequate for evaluating this methodology.

The MFA angles were sometimes close to the findings of other methods which determined the MFA of Ovine SIS to be generally at either $+30^\circ$ *or* -30° at lower strains and up to $+50^\circ$ *or* -50° for higher strains using advanced microscopy techniques [4], [5]. The findings presented in Figure 5.17(a) agreed with Sacks in that fibre distributions were inconsistent in SIS [4].

The literature offered little qualification of what “high” and “low” strain were. In this project, bulge specimens had, for the most part, a peak engineering strain of 12%, which happened to be the same value used by Sacks *et al.* [4] for porcine SIS. In most cases, the PBT tests were strained up to a value ranging between (15 – 25)%. Given the nonlinearity of strain in PBT, this peak strain was difficult to standardise for all specimens. This may have been achievable with extension control if the initial configuration had been based on a specific pretension as with other studies.

SALS techniques used by Sacks *et al.* [6] and Giorgio *et al.* [5] could not measure MFA angle mid-test [7]. This was due to the extensive chemical clearing and formalin fixing of the specimens for optical analysis.

Choi and Vito also only measured MFA angle for one load-scenario [8]. They claimed an accuracy of 7.5° with their method. This level of accuracy was not surpassed by the MFA-ID algorithm until less noisy data was used. Given high quality speckle images and enough time to run a large facet size DIC evaluation, the MFA-ID algorithm could achieve accuracies of close to 3° (given specimen dehydration mitigation) for multiple levels of strain throughout a test. Furthermore, it was able to quantify the ellipticity of the deformation contour which indicated the specimen isotropy level.

While not done in this study, the strain dependency of MFA could have been investigated using the angle identification algorithm. This study used peak deformation values but could have also chosen to always measure MFA at a particular level of strain and perhaps should be the subject of future study.

Improved DIC evaluation before specimen excision paired with the implemented algorithm improvements should be used in future tests to give the best results.

Figure 5.17(b) shows how the isotropy index (calculated after the completion of testing) changed from specimen to specimen. Given 5.3.3, this would have been a facet size dependent finding. These values, like the MFA angle were assumed sufficiently accurate for methodology appraisal.

Variation in bulge isotropy index per specimen will be compared with the PBT behaviour of each specimen in the sections to follow.

5.4 Specimen Geometric Measurement

5.4.1 Through Section Thickness Variation

Thickness measurement via image measurements efficiently quantified the variation in thickness along the MFA and CFA, which is presented in Figure 5.18. It was interesting to note that the MFA thickness was seldom exceeded by the CFA thickness.

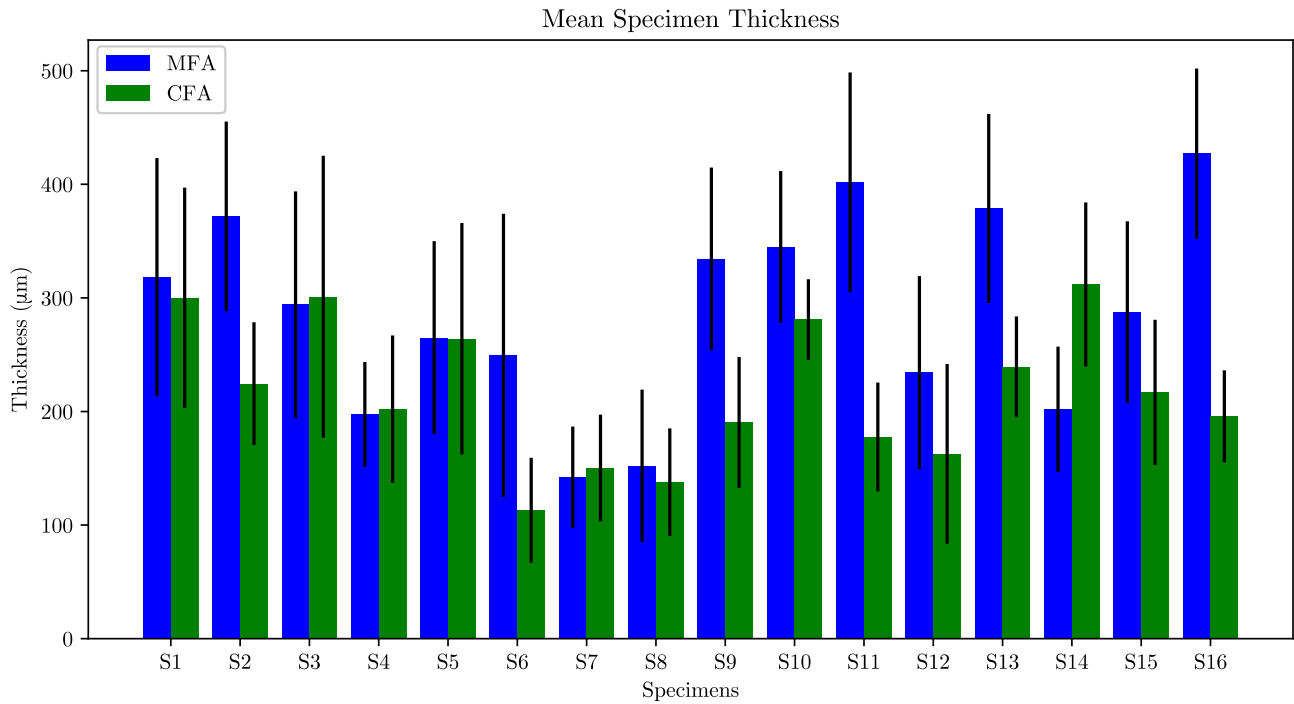


Figure 5.18: *Mean cruciform specimen thickness along the edges of the ROI.*

The error bars in Figure 5.18 show the standard uncertainty (one standard deviation) of the thickness data. Though some error bars allow thicknesses in the different axes to be viewed as equal, specimens 2, 9, 11, 13 and 16 show that in many cases the MFA was substantially thicker than the CFA. The CFA narrowly exceeded MFA thickness in specimens 3, 4 and 7 with the only exception being specimen 14.

Prior studies did not record directional thickness which may have produced misleading results. In the case of this set of specimens, 11/16 (69%) exhibited axis independent thickness given the full accommodation of uncertainty. Only 6 specimens (38%) exhibited axis independent thickness without much dependence on uncertainty. This was an important confounding factor to rule out when performing analysis of PBT data to validate fibre direction observations.

This analysis has proved that there was substantial specimen to specimen thickness variation and that a blanket MT thickness value would skew stress calculations substantially.

It is to be further noted that the method of thickness measurement in this project was not the ideal method. Paraffin wax shrinkage in histology was known to change dimensions of the tissue. Figure 5.19 shows how wax histology could lead to fragmentation of tissue structure and make thickness measurement highly uncertain and sometimes impossible.

Cryo-section histology would mitigate shrinkage while preserving of tissue structure. Future projects in this area, which would likely focus more on characterisation of a specific tissue rather than developing methodology, should plan for cryogenic histology and include input from the histology technicians. Alternatively, if a laser thickness measurement device like that developed by Cavinato *et al* [9] were available to future researchers, this should be used as the rapid process could be done even before the MFA-ID step of this process. The two dimensional map of thickness could additionally be overlayed on the MFA-ID graph to help separate fibre and thickness related stiffness behaviour.

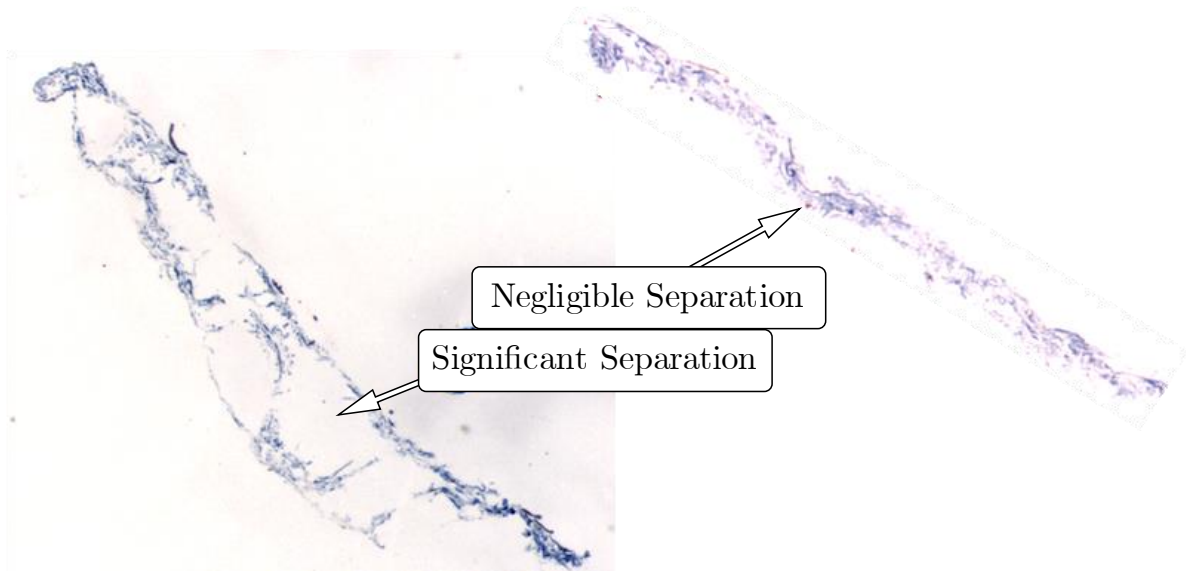


Figure 5.19: *Varied separation between specimens due to wax histological method.*

5.4.2 Width measurement

All PBT specimens were cut with the same tool and were mounted consistently using the same method. However, mounting the MT on the bulge test clamp involved spreading over the large aperture, which lead to variations in the pre-tension prior to the bulge test that were not possible to measure. Figure 5.20 shows the specimen floating on saline, freed of any pretension, and clearly distorted somewhat from the cut cruciform shape. This geometry change between excision and the start of testing required new measurement of width to better estimate the cross-sectional area under load.

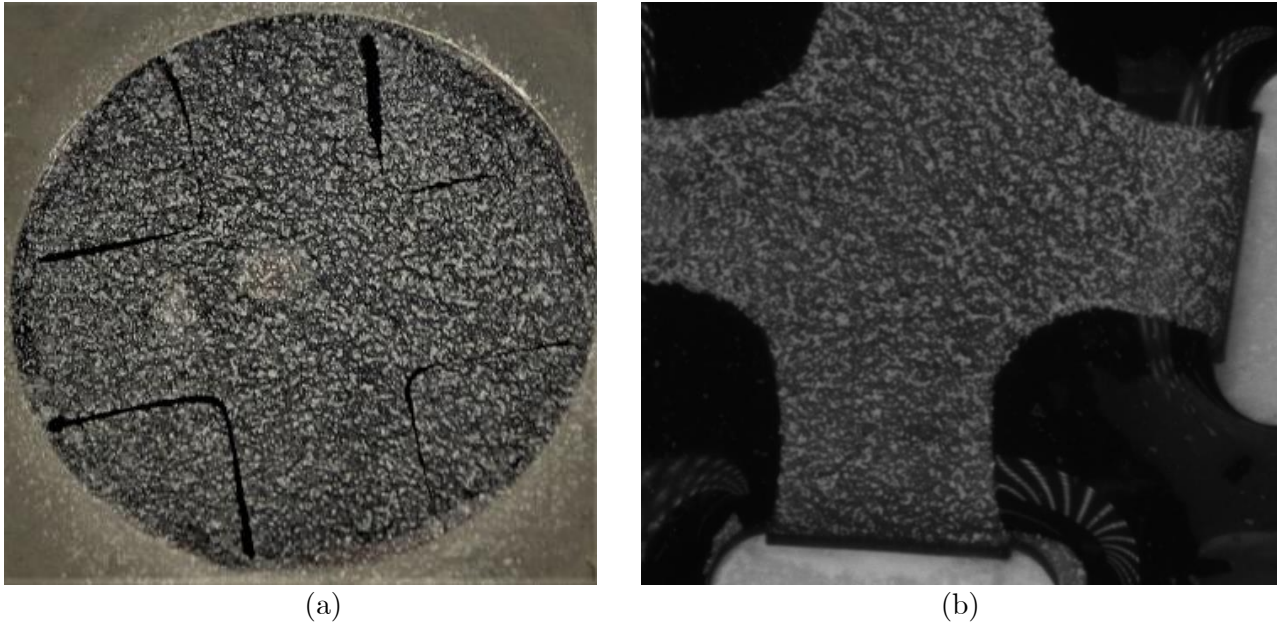


Figure 5.20: *Specimen 11 shape change between (a) excision and (b) after preconditioning*
Unfortunately, the width of the evaluated data in DIC did not represent the true width of the specimen due to the impact of facet size in the algorithm.

Image analysis was performed to measure width using DIC images of the specimens before testing began. These images had been calibrated using the DIC target and thus could accommodate for slight parallax errors. To mitigate this, however, the most square and perpendicular images were chosen in any case.

Width measurements were taken perpendicularly across the narrowest portion of the arms on all four arms. This meant that an average width could be calculated for the MFA and CFA. Figure 5.21 shows the results of this analysis with a minimal uncertainty linked to the ability to define the edge of the membrane using pixel brightness.

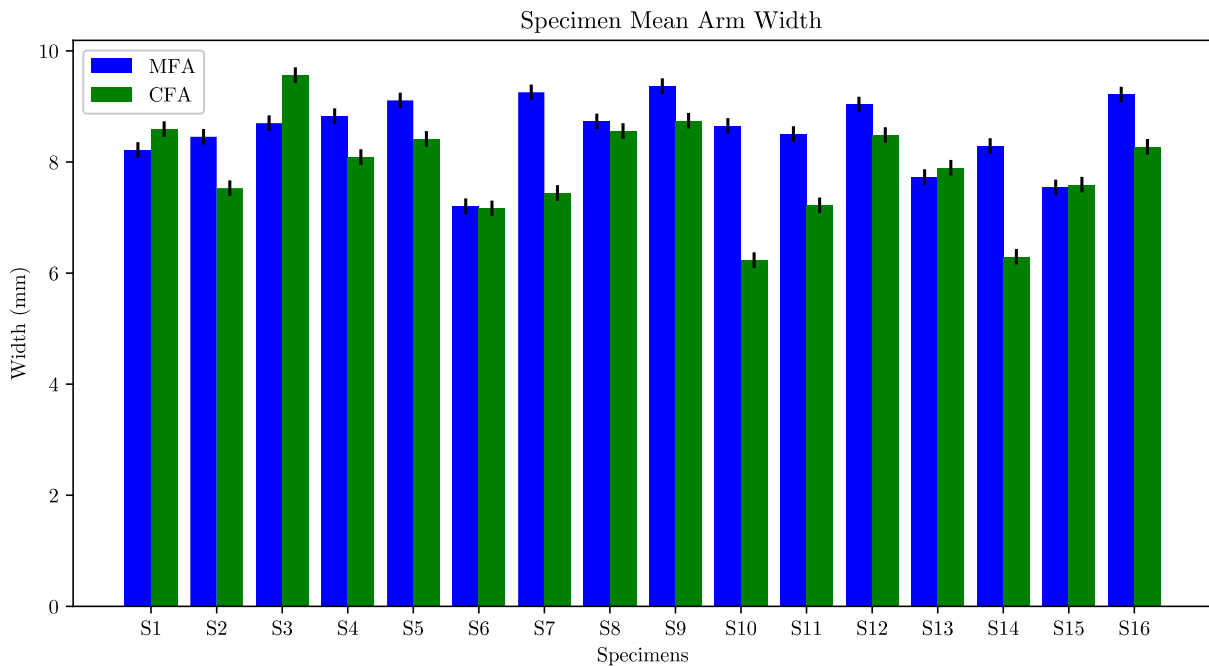


Figure 5.21: *Mean arm width along each axis for all specimens.*

5.5 MFA Verification Through PBT Testing

The purpose of testing the specimens first on the BTR was to help prepare specimens with axes aligned to the axes of material symmetry, (MFA and CFA). This was verified by assessing the PBT test data for consistent stiffer stress-strain response in the MFA direction.

5.5.1 Extent Dataset Selection

PBT testing was performed with displacement control. To avoid testing to failure, specimens were tested at equally spaced increasing extension levels, these were low, medium and high extension (LE, ME and HE). There was need to assess whether the LE, ME datasets were unique or if the HE dataset contained them already in efforts to simplify analysis.

Peak load increases in Figure 5.22 show the incremental testing to reach HE tests. It was clear from specimen eight's MFA engineering stress-strain curves that curvature was consistent despite an equal offset along the strain axis between curves. To validate this suspicion, Figure 5.23 was made to show this by shifting the curves to account for an even spacing.

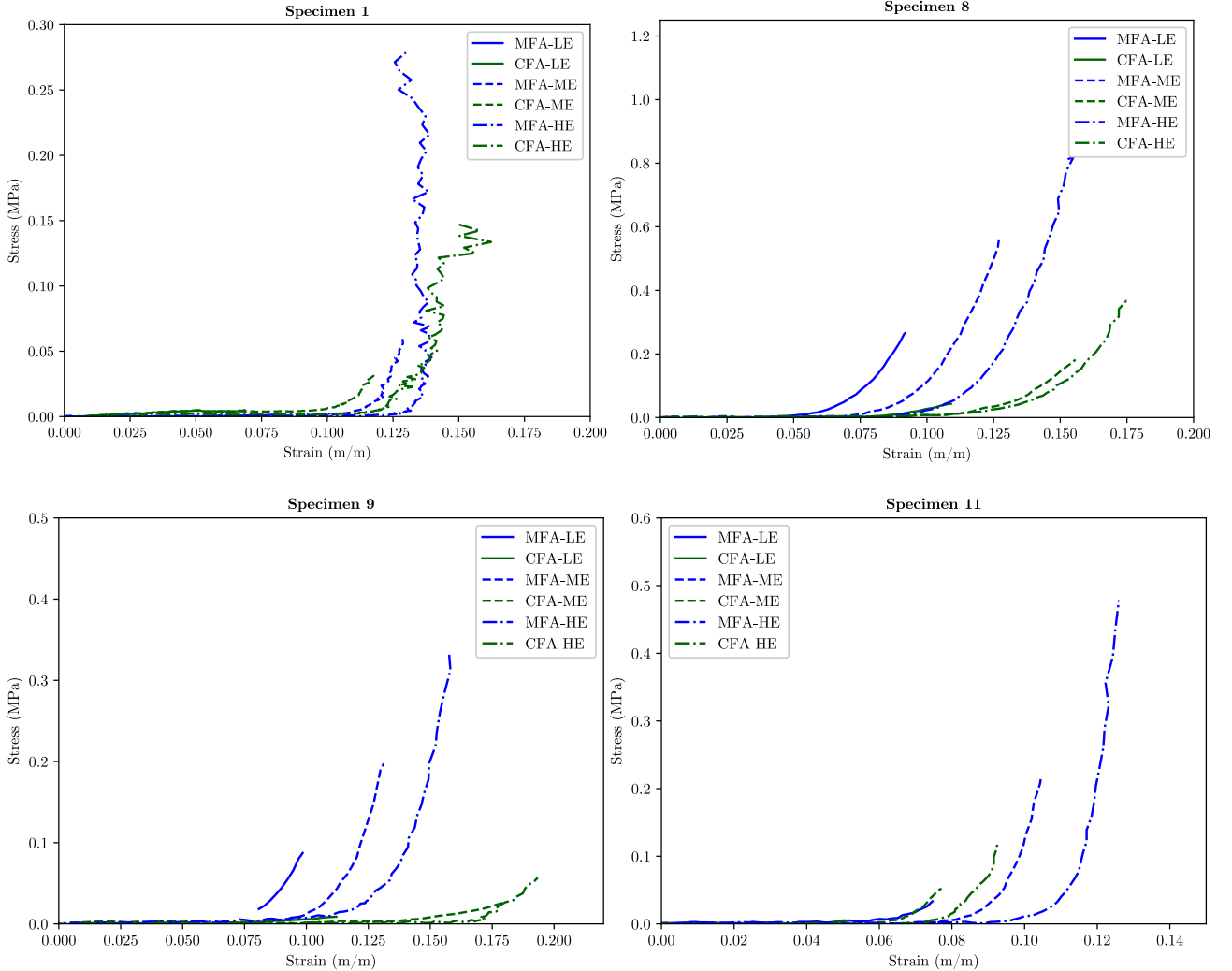


Figure 5.22: *Equibiaxial engineering stress-strain curves for low NSR specimens at LE, ME, & HE.*

The shifted strain values were calculated based on specimen eight using the method below:

$$\epsilon'_{HE} = \epsilon_{HE}$$

$$\epsilon'_{ME} = \epsilon_{ME} + f$$

$$\epsilon'_{LE} = \epsilon_{LE} + 2f$$

Where ϵ indicates (engineering) strain, ϵ' indicated the shifted strain and $f = 1.88\% \frac{m}{m}$. In other words, high extension tests remained the same and low extension strain was shifted up twice as much as the medium extension strain data.

The shift constant f was optimised manually based on specimen eight, f worked well for the other specimens shown here. Computational optimisation of f was not done as the scaling between the magnitudes of equal incremental shift in strain and peak grip displacement is not important. This could of course be done in the future, but it would depend largely on specimen shape and the material characteristics of the specimen. It was sufficient to show that there is an equal shift in strain that relates to the equal increase in grip displacement between tests.

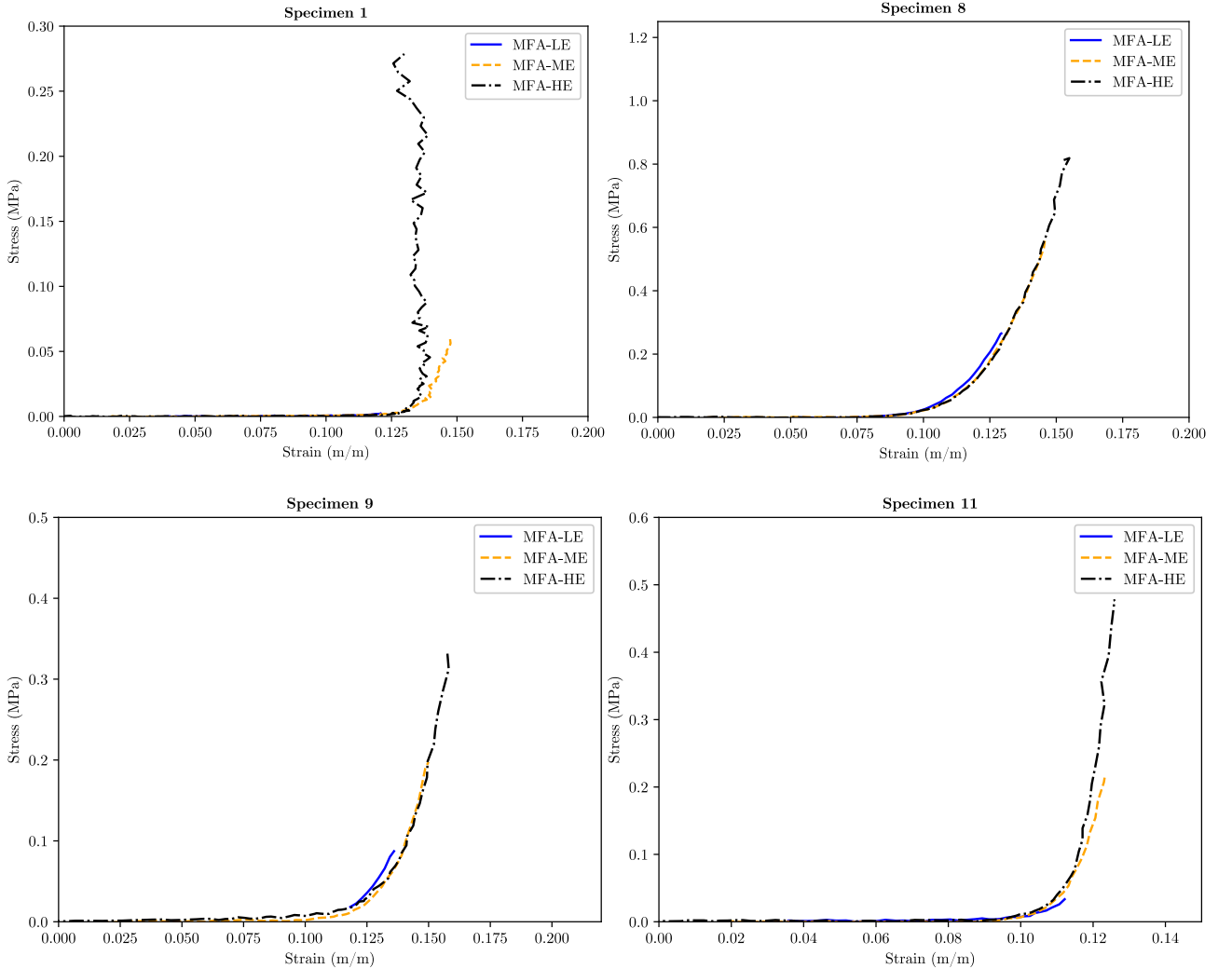


Figure 5.23: *Shifted MFA equibiaxial engineering stress-strain curves.*

Pre-stretching of the tissue in the preconditioning phase of testing was the likely cause for the “slack” that was mitigated by specimen strain-shifting. Like the stretching of a heap of tangled strings, once stretching of the strings has gone past a previous peak extension, there will be a

new maximum extension before strings begin to disentangle further. This analogy is used in polymer science to explain visco-elastic and visco-plastic behaviour of polymers. MT also typically displays this kind of behaviour, due to the analogous uncrimping and fibre rearrangement.

Once this was accounted for LE, ME and HE all followed the same stress strain curve (give or take some uncertainty). This meant that for a preconditioned specimen, choice of an extension level only affected the peak load and not its load response. This method also worked well for most CFA load response curves.

The LE and HE tests exhibited the largest load NSR. Thus, it was decided that HE tests would be used for analysis which may prove to be more useful in any case, because these tests terminated closest to the UTS of the tissue.

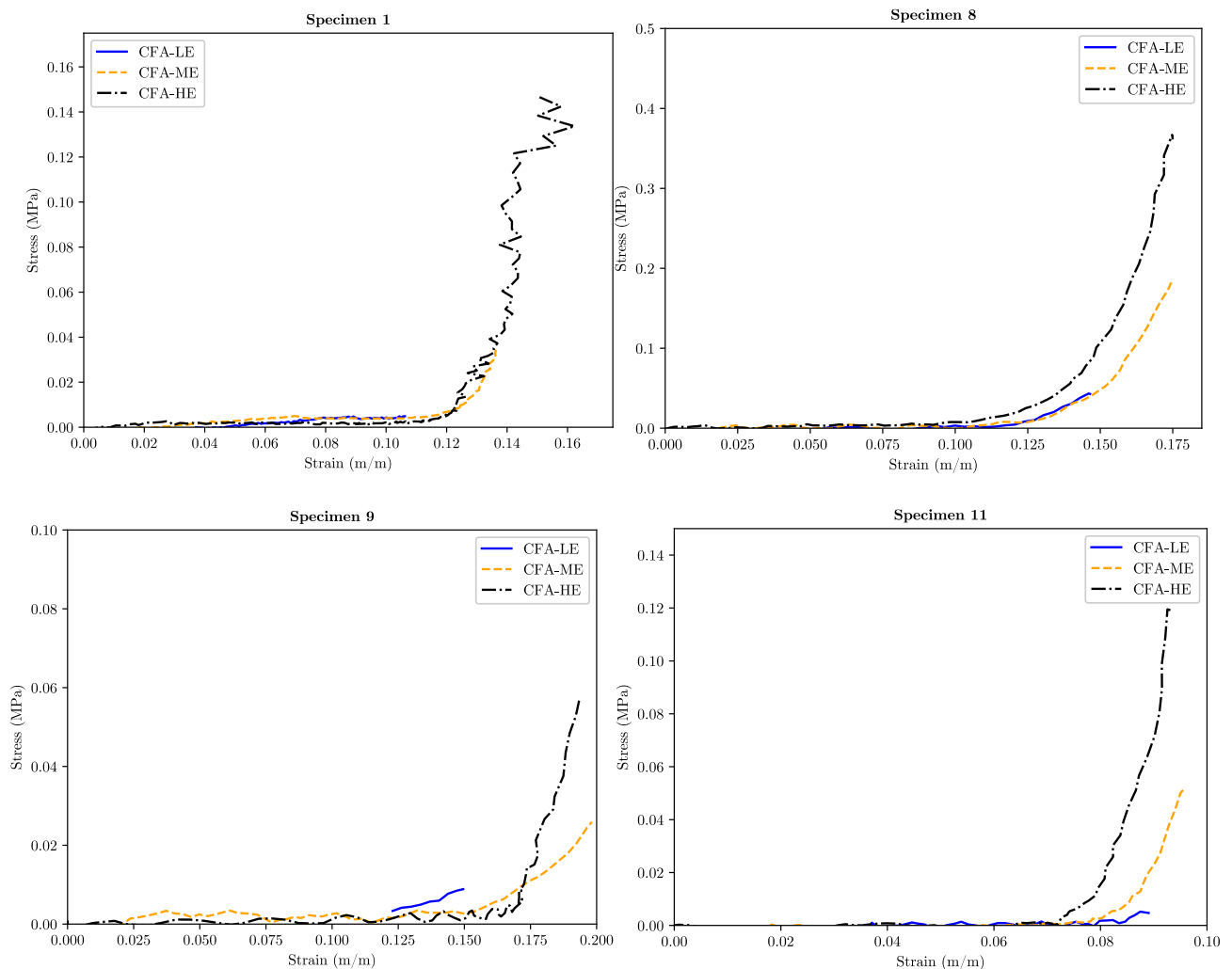


Figure 5.24: *Shifted CFA equibiaxial engineering stress-strain curves*

5.5.2 PBT Stress-Strain Overview

Strain was calculated as a mean engineering strain over the PBT region of interest (ROI). Engineering stress was determined using a cross-sectional area calculated from optical geometric measurements of the width and thickness of the specimen arms. These measures of

stress and strain were quantified in MFA and CFA directions to gain understanding of specimen isotropy.

The 1:1 extension ratio test data for specimens 1, 2 & 8 in Figure 5.25 offer the reader insight into the stress-strain response of the specimens. Exponential curves were fitted to this data as a means of quantifying the difference in response of the tissue. The method of this curve fitting is explained in the next section.

These curve shapes should be noted by the reader with reference to Figure 5.17(b). Here specimen one exhibited highly isotropic behaviour and this is reflected in the similarity of the MFA and CFA curve shapes below. Specimen two featured comparatively much lower levels of isotropy in the bulge test, which was reflected in the PBT response below. Lastly, specimen eight also had a similar isotropy level in the bulge and PBT tests even though the level of isotropy was between that of specimens 1 & 2.

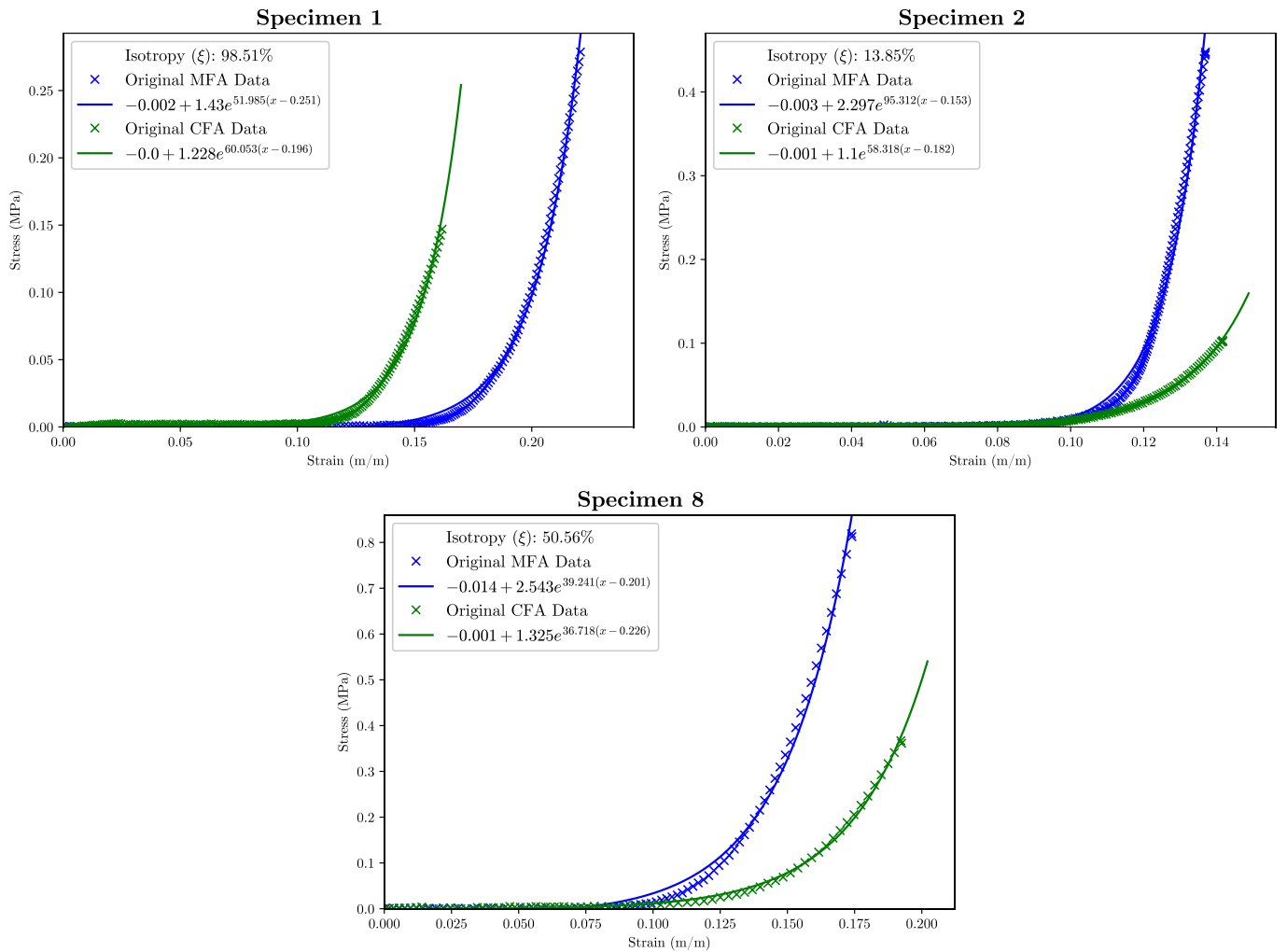


Figure 5.25: *MFA and CFA stress-strain curve-fits featuring a range of isotropy values.*

5.5.3 Curve Fitting

The PBT curve fitting method from 4.6.2 was successfully applied to the engineering stress-strain data. Furthermore, the measure of isotropy determination for the PBT curves did not

break-down for any of the tests performed and therefore it was quoted on each of the curve fitting plots below.

Specimens 12, 13 and 14 exhibited excessive load signal aberrations from poor alignment of PBT arms. Specimen 3 exhibited DIC correlation failure and specimen 15 failed prematurely in HE. These specimens were excluded however, their stress-strain curves can be found in appendix B.6

Specimens 1, 2 and 8 were shown earlier in Figure 5.25, specimens 4 & 5 are shown in Figure 5.26. These curves show that the quality of curve fitting with a simple exponential function worked for most datasets. Some curves did not capture the behaviour perfectly as is shown in Figure 5.26.

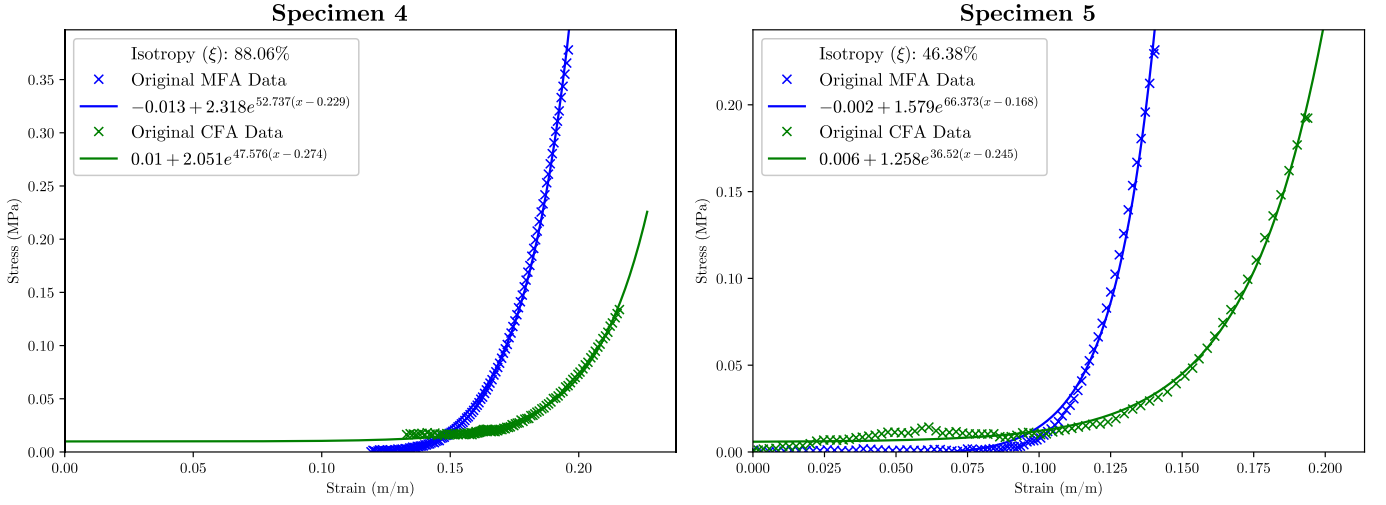


Figure 5.26: *Imperfect curve fitting to stress-strain datasets with exponential functions.*

Specimen 4 exhibited a data-discontinuity while specimen 5 was a complete dataset. In both cases the vertical shift of the exponential function led to a nonsensical stress value for zero strain.

Secondly the MFA fitting in specimen five failed to capture the behaviour of the knee-point of the j-shaped curve. In Figure 5.27, we see this same corner-cutting behaviour of the exponential function for the specimen six MFA, which led to an under-estimation of the PBT isotropy index in comparison to its BTR counterpart.

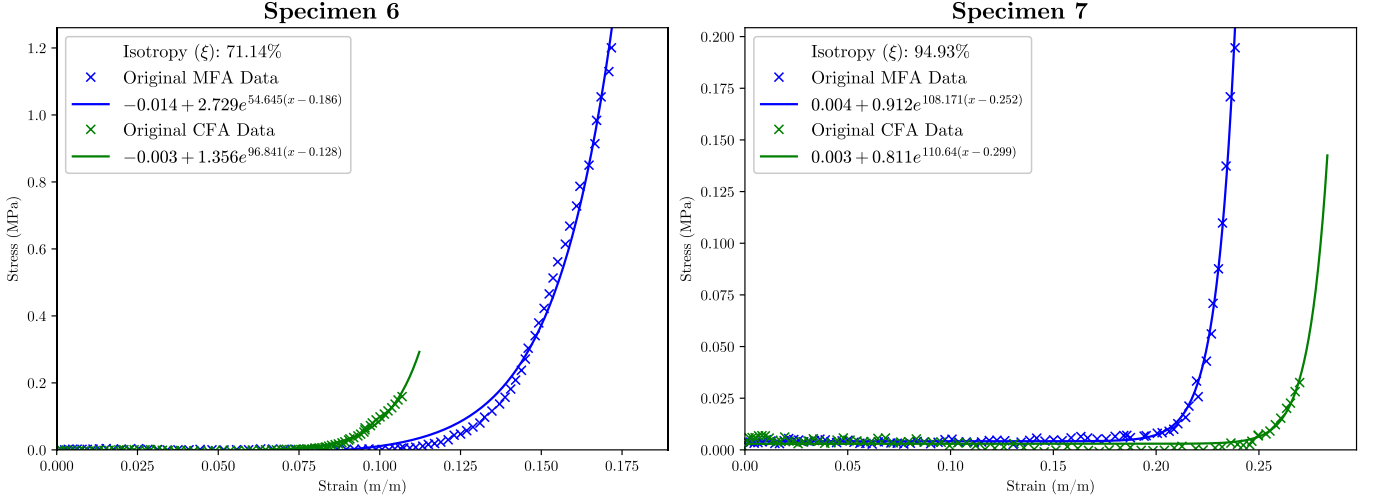


Figure 5.27: *Exponential curves fitted to equibiaxial extension data.*

In other cases, such as in specimen 7 in Figure 5.27 and both specimens in Figure 5.28, the curve path fitted the data very well and led to a much reduced disparity between the PBT and BTR isotropy indices compared to specimen 6.

While there were differences in isotropy between specimens and thus differently shaped curves, only specimen 10 incorrectly identified the MFA. Figure 5.28 shows how specimen 10 gave a negative isotropy, which indicated that the CFA was dominant in this specimen based on the curve fitting. As the curves happen to fit the data quite well in this case, the accuracy of MFA identification must be reduced for isotropic specimens.

This was expected and had a little impact on the overall performance of the MFA ID algorithm. This was because highly isotropic specimens would produce PBT data with very similar MFA/CFA curvatures in any case.

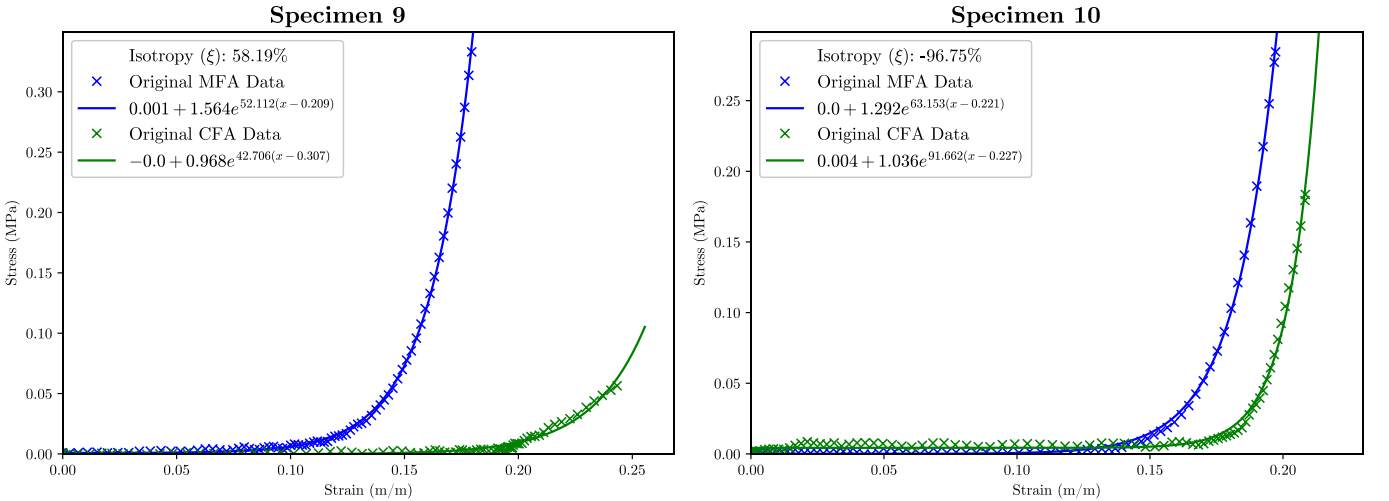


Figure 5.28: *(S9) A highly anisotropic specimen and (S10) a mis-identified MFA on a highly isotropic specimen*

Further investigation of the behaviour of specimen 10 at other extension ratios showed that this apparent misidentification may have been due to some noise in the 1:1 extension data.

Figure 5.29 offers comparison of the CFA and MFA curvatures at swapped extension ratios (1:0.5 and 0.5:1) where the MFA exhibited greater curvature than the CFA.

In the 1:0.5 curve, the CFA reversed in strain direction with elevated MFA strain, this showed that the CFA behaviour was highly dependent on the MFA behaviour. When the ratios were reversed, the MFA did not behave in the same way which indicated that the MFA did not depend as much on the CFA. More detail is shown in appendix B.5.

From these observations, it appeared that the equibiaxial data (1:1 extension ratios) might be sufficient for an initial approximation of the material model fit. Understanding the response and characterising it would require data at different extension ratios due to asymmetrical fibre distribution.

Additional extension ratios were not presented here for brevity's sake, but the full stress-strain curves for all specimens are presented in appendix B.5.

A shortfall evident in the MFA identification process was that the algorithm could only measure differences in the stiffness of a membrane along orthogonal axes. Given the highly variant thickness measurements of SIS, it became difficult to distinguish thickness related stiffness from underlying fibre behaviour. By comparing results from Figure 5.17 and Figure 5.30 we see that a stiffer directionality was identified in specimen 16. During the bulge test, it was impossible to determine if the behaviour was thickness or fibre related.

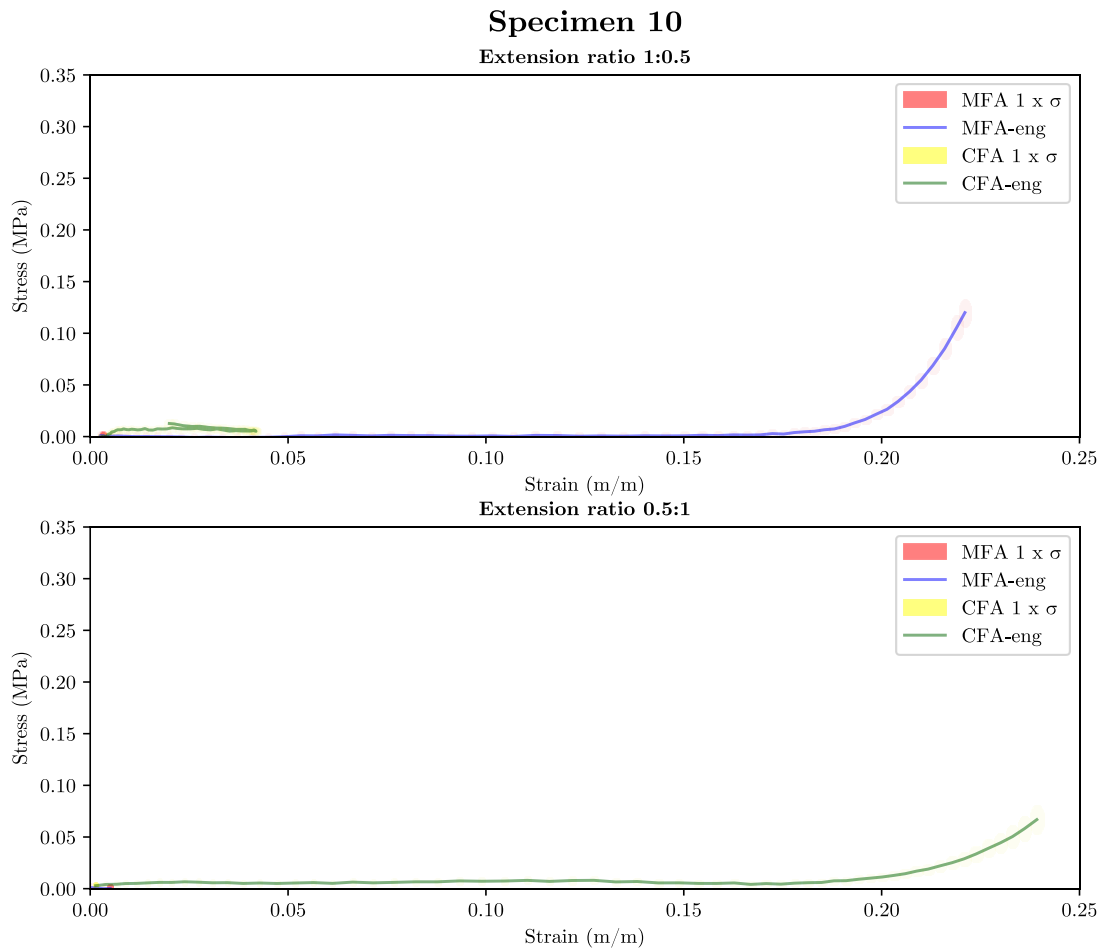


Figure 5.29: *Swapped extension ratios showed MFA & CFA curvature differences.*

This was due to the shortcomings of readily available thickness measurement tools when measuring highly flexible materials. Short of using equipment such as a micro-CT scan to generate a thickness map and SALS microscopy [6] to identify the angle of the fibres, it would be impossible to separate fibre from thickness contributions to stiffness in an axis.

What was clear from the success in MFA identification was that concerted effort to measure individual specimen thickness(es) could help isolate the fibre related stiffness in the PBT test. If the MFA direction calculation was skewed by significant thickness differences, they would be measured after PBT testing, allowing for correction of the PBT stress data.

Therefore, accurate thickness measurement has been shown to be a crucial component to this methodology. It was critical to know the thickness of each axis accurately to identify if certain BTR tests yielded incorrect MFA results due to thickness irregularities. Thus, improvement in specimen thickness measurement should be prioritised for improvement in follow up studies.

Figure 5.31 offers a comparison of the performance of the bulge test measure of isotropy to that of the PBT. Assuming that the bulge test was the least accurate measure of true isotropy owing to the unavoidable influence of thickness in the stiffness along the major and minor axes of the elliptical bulge contour. The BTR tests were consistently within about 25% of the PBT calculated isotropy. Unfortunately, the specimen shape may have confounded aspects of this quantification. The long specimen arms would have affected load transfer to the ROI and the approximated cross-sectional area of the ROI for engineering stress analysis was highly idealised.

None of the papers found in the literature surrounding MT testing seemed to discuss or quantify the levels of isotropy in the way that has been done in this study. Many left this value to be quantified using inverse FEA model fitting with PBT specimens that had been cut without MFA alignment.

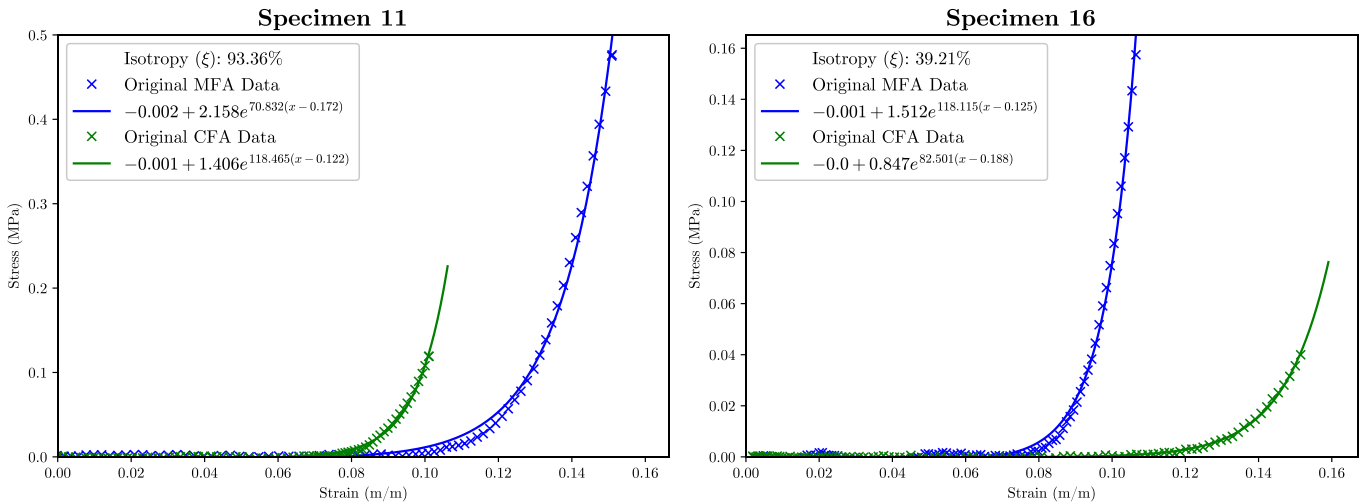


Figure 5.30: *Exponential curves fitted to equibiaxial extension data.*

Shortcomings observed in the specimen preparation were made apparent by isotropy variation from specimen to specimen. Sacks explained in his study of porcine SIS [4] that they cut the SIS down the mesenteric artery such that the minimally vascularised region formed the centre of the ROI during testing.

As the position along the GIT and the longitudinal cut position relative to the mesenteric artery was respectively not known and not measured or noted, this was posed as a possible reason for such significant variation in isotropy.

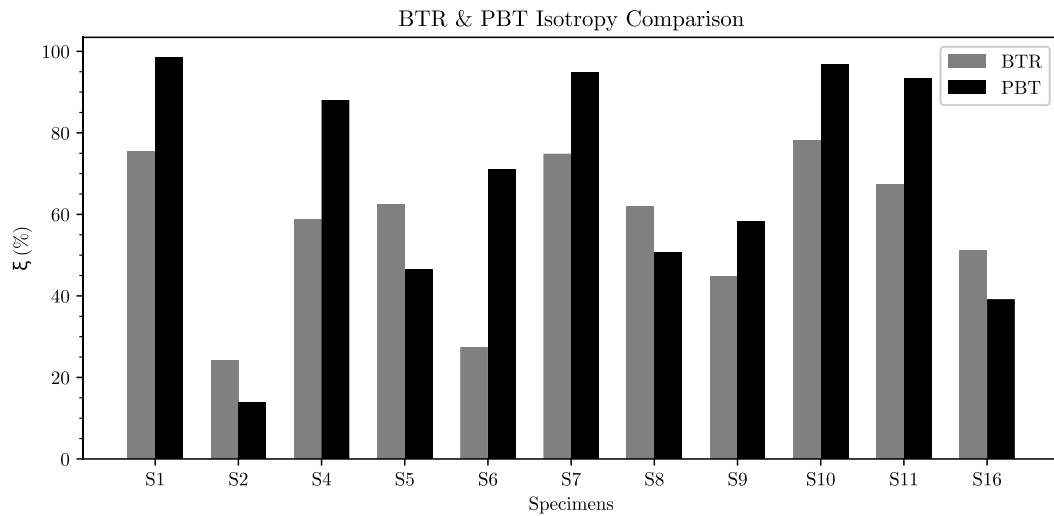


Figure 5.31: A comparison of the two isotropy measures for the curve-fitted specimens.

5.6 Requirement Metric Performance

As discussed from the beginning, the performance of the methodology developed in this project was measured against requirements according to metrics determined in chapter 4. Table 5.7 repeats these with the addition of the status of each requirement.

Table 5.7: Requirement achievement analysis.

	REQUIREMENT	METRIC	STATUS
1	Complete load, displacement and geometry data capture for multiple MT specimens	Force and displacement data	ACHIEVED
1.1	Repeatable PBT specimen gripping	Grip failure to success ratio	No Failures
1.2	Repeatable PBT specimen transfer	Transfer failure to success ratio	No Failures
1.3	Reliable force measurement at specimen loads	Mean uncertainty to signal ratio	NSR<6%
1.4	Reliable displacement measurement	Mean uncertainty to signal ratio	NSR<2%
1.5	Cross section dimension measurement	Mean uncertainty to signal ratio	NSR<25%
2	Consistent cruciform specimen orientation determined by tissue morphology.	Consistency of MFA to CFA force ratio	91% Success Rate
2.1	High quality bulge deformation data	Mean uncertainty to signal ratio	NSR<15%
2.2	Low bias MFA identification algorithm	Process parameters	ACHIEVED
2.3	MFA angle preservation from measurement to specimen excision	Uncertainty in excision angle	$\pm 20^\circ$

The performance of the methodology against the requirement metrics was good, passing all requirements except for 1.5, 2.1 and 2.3

As discussed in section 5.4, the material thickness variation could not be avoided but was at least quantified in this research. The method of thickness measurement could be improved in future work by using cryo-histological techniques to give the true, wet thickness of the tissue.

Requirements 2.1 and 2.3 were interlinked and have already been addressed with facet size improvements suggested and performed in section 5.3.2. Should these recommendations be followed in future testing, these noise/error values would decrease substantially. The NSR of 2.1 would easily drop to around 2% with a 59 px facet size during DIC Evaluation. The angular uncertainty would drop to close to $\pm 2^\circ$ depending on the ROI diameter chosen.

By and large, all other aspects of Table 5.7 exceeded expectations of a first iteration methodology.

Chapter 6

Conclusions & Recommendations

As the focus of this project was methodological development, the conclusions focussed on this. The methodology was presented initially with a general list of requirements which were given finality in the pages to follow.

6.1 A Promising Methodology

The method of using a bulge test rig (BTR) to non-destructively identify the mean fibre axis (MFA) was largely successful given the constraints of the specimen material and limitations of the instruments available. This method consistently identified the MFA for specimens with significant anisotropy, allowing the excision of PBT specimen at the required angle within acceptable certainty.

6.1.1 An Alternative Use for a BTR

This project opened new pathways to integrate the use of a quasi-static BTR with PBT testing in a highly symbiotic way. The simplicity of the BTR's operation paired with the rigor and adjustability of the PBT in testing specific extension ratios achieved high levels of specimen control.

Thus, elliptical deformation contours of bulged anisotropic tissue could be induced with circular clamps to determine MFA. Other means of identifying the MFA (light scattering, histology) required tissue treatments guaranteed to permanently alter mechanical response, while low pressure inflation with appropriate hydration management was less likely to alter the tissue stiffness.

6.1.2 A Robust Algorithm was Developed

The algorithm achieved its purpose of quickly ($t < 30 \text{ sec}$) identifying the directions of the major and minor axes of an elliptical deformation contour given a suitable DIC dataset. It achieved repeatable MFA identification in a non-contact and non-destructive manner. The uncertainty of the MFA identified by the algorithm was sensitive to the quality of the DIC data. However, the MFA did not vary substantially once reasonable DIC data was evaluated.

The algorithm currently presents the user with feedback on dataset quality and features an option to help optimise input parameters all in a fraction (10%-20%) of the DIC evaluation time. A user would also be able to investigate the MFA angle history or strain dependency from a test using multiprocessing versions of the algorithm already in use.

The success of this process meant that the MFA of a tissue sample can be determined without a surgeon needing to excise the tissue and maintain its orientation with great precision.

6.1.3 Effective Specimen Transfer

The use of the specimen transfer card proved useful to mitigate tissue damage or over-extension during the installation and removal. This approach can and should be adapted for future work with MT as it was highly effective and helped lower the researcher dexterity requirements for specimen installation and removal.

6.1.4 A Stress Confounding Specimen Design

Specimen material inconsistencies at the preparation stage limited potential conclusions regarding isotropy variation between specimens. Mitigation of vascularised tissue in the ROI by means of location-controlled MT excision from the gastro-intestinal tract (GIT) would have resolved this.

Specimen shape selection and arm design was not ideal. This was driven by project data collection time constraints. While the design allowed for rapid completion of the testing owing to its simplicity, it would have required extensive FEA to accurately calculate true stresses in the ROI. As detailed FEA was beyond the scope of this MSc, the simplified approach of reporting engineering stresses was adopted. This meant fitting advanced constitutive models to the data was of limited use and not pursued further.

6.1.5 A Requirement Satisfying Method

Not all requirements were achieved in this iteration of testing, but analysis certainly marked out the path to achieving these requirements consistently in the future. Users of this methodology should now have a good understanding of the uncertainties associated with all the measurements in the process and means of quantifying these uncertainties as well as to reduce their impact on the final data quality.

6.2 Recommendations

6.2.1 Load Control for the Planar Biaxial Tester

As the PBT could only run in extension control, and the tissue had significant initial take up, maintaining consistency was challenging. Specimens with unexpected initial slackness could easily result in low measured forces. Further development of the PBT control system to enable load control would simplify this, allow easier comparison with data in the literature and limit the number of null-force datasets. This would allow for ease of comparison with literature methodologies and limit the number of null-load datasets that were commonplace with extension control.

6.2.2 Cryogenic or Laser Thickness Analysis

As a first step to improve the quality of thickness, cryogenic histological methods would eliminate shrinkage and separation concerns. Ideally, a following researcher would verify the work of Cavinato *et al* by replicating their non-contact laser thickness measurement device [1]. This rapid process would precede MFA-ID allowing the generation of a two dimensional map of thickness. This could additionally be overlayed on the MFA-ID graph to help separate fibre and thickness related stiffness behaviour.

6.2.3 BTR Specimen Humidification

Developing a humidity-controlled chamber for the BTR would limit dehydration of the MT specimens. This reduces the time constraint on the DIC evaluations, improving the quality of the 3D deformation data and allowing for MFA identification with better certainty.

6.2.4 MFA ID Parameter Optimisation

It is recommended that the MFA ID multiprocessing algorithm approach be taken on every specimen before PBT specimen excision. This should be done with very limited parameter selection on a high-performance CPU to get the best indication of the true MFA angle and ξ_{bulge} for a specimen. Furthermore it would mitigate user error in the MFA ID process.

6.2.5 Computational Investigation

With improved specimen design and better data quality at the MFA-ID stage, an implicit FEA model to analyse the PBT results using a square specimen would be of significant benefit to the validation of the results of this study and would offer a more complete understanding of the tissue behaviour and would open opportunities for in-depth analysis of the impact of incorrect MFA-ID.

References

- [1] C. Bellini, P. Glass, M. Sitti, and E. S. Di Martino, “Biaxial mechanical modeling of the small intestine,” *J. Mech. Behav. Biomed. Mater.*, vol. 4, no. 8, pp. 1727–1740, 2011, doi: 10.1016/j.jmbbm.2011.05.030.
- [2] A. Kalra and A. Lowe, “Mechanical Behaviour of Skin: A Review,” *J. Mater. Sci. Eng.*, vol. 5, no. 4, 2016, doi: 10.4172/2169-0022.1000254.
- [3] M. Abbasi, M. S. Barakat, K. Vahidkhah, and A. N. Azadani, “Characterization of three-dimensional anisotropic heart valve tissue mechanical properties using inverse finite element analysis,” *J. Mech. Behav. Biomed. Mater.*, vol. 62, 2016, doi: 10.1016/j.jmbbm.2016.04.031.
- [4] A. M. Curry, “Design build and test of a low strain rate bulge tester for skin and membrane tissue,” *UCT MSc Eng Diss.*, 2019, doi: <http://hdl.handle.net/11427/32220>.
- [5] J. Caine, “Design, build and test of a planar biaxial tensile testing machine for skin and other collagenous soft tissues,” *UCT MSc Eng Diss.*, 2022.
- [6] H. Fehervary, J. Vastmans, J. Vander Sloten, and N. Famaey, “How important is sample alignment in planar biaxial testing of anisotropic soft biological tissues? A finite element study,” *J. Mech. Behav. Biomed. Mater.*, vol. 88, no. May, pp. 201–216, 2018, doi: 10.1016/j.jmbbm.2018.06.024.
- [7] M. S. Sacks and D. C. Gloeckner, “Quantification of the fiber architecture and biaxial mechanical behavior of porcine intestinal submucosa,” *J. Biomed. Mater. Res.*, vol. 46, no. 1, pp. 1–10, 1999, doi: 10.1002/(SICI)1097-4636(199907)46:1<1::AID-JBM1>3.0.CO;2-7.
- [8] G. Machado, D. Favier, and G. Chagnon, “Membrane Curvatures and Stress-strain Full Fields of Axisymmetric Bulge Tests from 3D-DIC Measurements. Theory and Validation on Virtual and Experimental results,” *Exp. Mech.*, vol. 52, no. 7, pp. 865–880, 2012, doi: 10.1007/s11340-011-9571-3.
- [9] A. Graham, “Design and implementation of a high strain rate biaxial tension test for elastomeric materials and biological soft tissue,” *UCT MSc Eng Diss.*, 2019, doi: <http://hdl.handle.net/11427/32689>.
- [10] A. N. Annaidh *et al.*, “Automated estimation of collagen fibre dispersion in the dermis and its contribution to the anisotropic behaviour of skin,” *Ann. Biomed. Eng.*, vol. 40, no. 8, pp. 1666–1678, 2012, doi: 10.1007/s10439-012-0542-3.
- [11] G. Giorgio, “The cross-ply arrangement of collagen fibres in the submucosa of the mammalian small intestine,” *Cell Tissue Res.*, no. 248, pp. 491–497, 1987, doi: <https://doi.org/10.1007/BF00216474>.
- [12] C. C. Roth, B. P. Kropp, and E. Y. Cheng, “Natural biomaterials for urological tissue engineering,” *Biomater. Tissue Eng. Urol.*, pp. 255–280, Jan. 2009, doi: 10.1533/9781845696375.3.255.
- [13] G. D. Webster and N. D. Sherman, “Cystocele Repair Using Biologic Material,” *Female Urol.*, pp. 655–661, Jan. 2008, doi: 10.1016/B978-1-4160-2339-5.50114-2.

References

- [14] T. Aboushwareb, A. Atala, and A. Elkassaby, “Regenerative medicine for the urethra,” *Biomater. Tissue Eng. Urol.*, pp. 454–469, Jan. 2009, doi: 10.1533/9781845696375.3.454.
- [15] A. Pissarenko *et al.*, “Tensile behavior and structural characterization of pig dermis,” *Acta Biomater.*, vol. 86, pp. 77–95, 2019, doi: 10.1016/j.actbio.2019.01.023.
- [16] M. S. Sacks, D. B. Smith, and E. D. Hiester, “A small angle light scattering device for planar connective tissue microstructural analysis,” *Ann. Biomed. Eng.*, vol. 25, no. 4, pp. 678–689, 1997, doi: 10.1007/BF02684845.
- [17] H. Swatland, “STRUCTURE OF FARM ANIMALS,” 2006. https://animalbiosciences.uoguelph.ca/~swatland/ch1_1_5.htm.
- [18] “Catgut | cord | Britannica.” <https://www.britannica.com/technology/catgut> (accessed Jun. 06, 2021).
- [19] Y. Lanir and Y. C. Fung, “Two-dimensional mechanical properties of rabbit skin—I. Experimental system,” *J. Biomech.*, vol. 7, no. 1, pp. 29–34, Jan. 1974, doi: 10.1016/0021-9290(74)90067-0.
- [20] S. Bose, S. Li, E. Mele, and V. V. Silberschmidt, “Dry vs. wet: Properties and performance of collagen films. Part I. Mechanical behaviour and strain-rate effect,” *J. Mech. Behav. Biomed. Mater.*, vol. 111, no. May, p. 103983, 2020, doi: 10.1016/j.jmbbm.2020.103983.
- [21] J. D. Humphrey, D. L. Vawter, and R. P. Vito, “Quantification of strains in biaxially tested soft tissues,” *J. Biomech.*, vol. 20, no. 1, pp. 59–65, 1987, doi: [https://doi.org/10.1016/0021-9290\(87\)90267-3](https://doi.org/10.1016/0021-9290(87)90267-3).
- [22] T. K. Tonge, L. S. Atlán, L. M. Voo, and T. D. Nguyen, “Full-field bulge test for planar anisotropic tissues: Part I-Experimental methods applied to human skin tissue,” *Acta Biomater.*, vol. 9, no. 4, pp. 5913–5925, 2013, doi: 10.1016/j.actbio.2012.11.035.
- [23] P. Lakhani, K. K. Dwivedi, and N. Kumar, “Directional dependent variation in mechanical properties of planar anisotropic porcine skin tissue,” *J. Mech. Behav. Biomed. Mater.*, vol. 104, no. February, p. 103693, 2020, doi: 10.1016/j.jmbbm.2020.103693.
- [24] J. M. Lee and S. E. Langdon, “Thickness measurement of soft tissue biomaterials: A comparison of five methods,” *J. Biomech.*, vol. 29, no. 6, pp. 829–832, 1996, doi: 10.1016/0021-9290(95)00121-2.
- [25] M. Palanca, G. Tozzi, and L. Cristofolini, “The use of digital image correlation in the biomechanical area: A review,” *International Biomechanics*, vol. 3, no. 1. 2016, doi: 10.1080/23335432.2015.1117395.
- [26] W. D. Meador *et al.*, “The regional-dependent biaxial behavior of young and aged mouse skin: A detailed histomechanical characterization, residual strain analysis, and constitutive model,” *Acta Biomater.*, vol. 101, pp. 403–413, 2020, doi: 10.1016/j.actbio.2019.10.020.
- [27] L. Yu, R. Tao, and G. Lubineau, “Accurate 3D shape, displacement and deformation measurement using a Smartphone,” *Sensors (Switzerland)*, vol. 19, no. 3, 2019, doi: 10.3390/s19030719.
- [28] P. J. Rae, H. T. Goldrein, N. K. Bourne, W. G. Proud, L. C. Forde, and M. Liljekvist, “Measurement of dynamic large-strain deformation maps using an automated fine grid technique,” *Opt. Lasers Eng.*, vol. 31, no. 2, pp. 113–122, Feb. 1999, doi: 10.1016/S0143-8166(99)00003-2.
- [29] G. Sommer *et al.*, “Biomechanical properties and microstructure of human ventricular myocardium,” *Acta Biomater.*, vol. 24, pp. 172–192, 2015, doi: 10.1016/j.actbio.2015.06.031.

- [30] H. S. Choi and R. P. Vito, "Two-dimensional stress-strain relationship for canine pericardium," *J. Biomech. Eng.*, vol. 112, no. 2, pp. 153–159, 1990, doi: 10.1115/1.2891166.
- [31] K. L. Campbell and C. A. Lichtensteiger, "STRUCTURE AND FUNCTION OF THE SKIN," *Small Anim. Dermatology Secrets*, pp. 1–9, Jan. 2004, doi: 10.1016/B978-1-56053-626-0.50005-7.
- [32] M. Diab *et al.*, "Characterization of human female breast and abdominal skin elasticity using a bulge test.," *J. Mech. Behav. Biomed. Mater.*, vol. 103, no. November 2019, p. 103604, 2020, doi: 10.1016/j.jmbbm.2019.103604.
- [33] N. Kumaraswamy, H. Khatam, G. P. Reece, M. C. Fingeret, M. K. Markey, and K. Ravi-Chandar, "Mechanical response of human female breast skin under uniaxial stretching," *J. Mech. Behav. Biomed. Mater.*, vol. 74, 2017, doi: 10.1016/j.jmbbm.2017.05.027.
- [34] Y. Fung, *Biomechanics: mechanical properties of living tissues*, 2nd ed. New York: Springer Science & Business Media, 2013.
- [35] J. Vastmans *et al.*, "Biomechanical evaluation of a personalized external aortic root support applied in the Ross procedure," *J. Mech. Behav. Biomed. Mater.*, vol. 78, no. May 2017, pp. 164–174, 2018, doi: 10.1016/j.jmbbm.2017.11.018.
- [36] M. S. Sacks, "Biaxial mechanical evaluation of planar biological materials," *J. Elast.*, vol. 61, no. 1–3, pp. 199–246, 2000, doi: 10.1023/A:1010917028671.
- [37] W. L. E. Wong, T. J. Joyce, and K. L. Goh, "Resolving the viscoelasticity and anisotropy dependence of the mechanical properties of skin from a porcine model," *Biomech. Model. Mechanobiol.*, vol. 15, no. 2, 2016, doi: 10.1007/s10237-015-0700-2.
- [38] D. W. . Hukins, *Biomechanical properties of collagen*. Edinburgh and New York: Churchill Livingstone, 1982.
- [39] Y. C. Fung, "Elasticity of soft tissues in simple elongation," *Am. Physiol. Soc.*, vol. 213, no. 6, pp. 1532–1544, 1967, doi: 10.1152/AJPLEGACY.1967.213.6.1532.
- [40] T. K. Tonge, L. M. Voo, and T. D. Nguyen, "Full-field bulge test for planar anisotropic tissues: Part II-A thin shell method for determining material parameters and comparison of two distributed fiber modeling approaches," *Acta Biomater.*, vol. 9, no. 4, pp. 5926–5942, 2013, doi: 10.1016/j.actbio.2012.11.034.
- [41] H. Seibert, T. Scheffer, and S. Diebels, "Biaxial testing of elastomers - Experimental setup, measurement and experimental optimisation of specimen's shape," *Tech. Mech.*, vol. 34, no. 2, pp. 72–89, 2014, doi: <https://doi.org/10.24352/UB.OVGU-2017-054>.
- [42] T. T. Tower, M. R. Neidert, and R. T. Tranquillo, "Fiber alignment imaging during mechanical testing of soft tissues," *Ann. Biomed. Eng.*, vol. 30, no. 10, pp. 1221–1233, 2002, doi: 10.1114/1.1527047.
- [43] K. Langer, "On The Anatomy And Physiology Of The Skin I. The cleavability of the cutis," *Br. J. Plast. Surg.*, pp. 3–8, 1978, doi: 10.1016/0007-1226(78)90003-6.
- [44] F. Sulejmani *et al.*, "Biomechanical properties of the thoracic aorta in Marfan patients," *Ann. Cardiothorac. Surg.*, vol. 6, no. 6, 2017, doi: 10.21037/acs.2017.09.12.
- [45] M. Slazansky, S. Polzer, V. Man, and J. Bursa, "Analysis of Accuracy of Biaxial Tests Based on their Computational Simulations," *Strain*, vol. 52, no. 5, pp. 424–435, 2016, doi: 10.1111/str.12205.
- [46] H. Fehervary, M. Smoljkić, J. Vander Sloten, and N. Famaey, "Planar biaxial testing of soft

References

- biological tissue using rakes: A critical analysis of protocol and fitting process,” *J. Mech. Behav. Biomed. Mater.*, vol. 61, pp. 135–151, 2016, doi: 10.1016/j.jmbbm.2016.01.011.
- [47] A. Avanzini and D. Battini, “Integrated experimental and numerical comparison of different approaches for planar biaxial testing of a hyperelastic material,” *Adv. Mater. Sci. Eng.*, vol. 2016, 2016, doi: 10.1155/2016/6014129.
- [48] M. Sasso, G. Chiappini, M. Rossi, L. Cortese, and E. Mancini, “Visco-Hyper-Pseudo-Elastic Characterization of a Fluoro-Silicone Rubber,” pp. 315–328, 2014, doi: 10.1007/s11340-013-9807-5.
- [49] D. Fischer, “The Design and Construction of a Bulge Testing Device Platform for Human Skin Tissue Applications,” *UCT MSc Eng Diss.*, 2020, doi: <http://hdl.handle.net/11427/32670>.
- [50] D. Pillay, “Marking strategies for optical tracking of skin and biological membrane deformation,” *UCT BSc Eng Res. Rep.*, 2019.
- [51] M. F. Graham *et al.*, “Collagen content and types in the intestinal strictures of Crohn’s disease,” *Gastroenterology*, vol. 94, no. 2, pp. 257–265, 1988, doi: 10.1016/0016-5085(88)90411-8.
- [52] B. Manjunatha, A. Agrawal, and V. Shah, “Histopathological evaluation of collagen fibers using picrosirius red stain and polarizing microscopy in oral squamous cell carcinoma,” *J. Cancer Res. Ther.*, vol. 11, no. 2, pp. 272–276, 2015, doi: 10.4103/0973-1482.154061.
- [53] Y. Zeng *et al.*, “Collagen fiber angle in the submucosa of small intestine and its application in gastroenterology,” vol. 9, no. 4, pp. 804–807, 2003, doi: 10.3748/wjg.v9.i4.804.
- [54] Dantec Dynamics, *Istra 4d Software Manual Q-4xx System*, 2.84., vol. 2.8.4. Nova Instruments, 2016.
- [55] G. Sommer *et al.*, “Quantification of Shear Deformations and Corresponding Stresses in the Biaxially Tested Human Myocardium,” *Ann. Biomed. Eng.*, vol. 43, no. 10, pp. 2334–2348, Oct. 2015, doi: 10.1007/s10439-015-1281-z.
- [56] V. Müller, “Elimination of specular surface-reflectance using polarized and unpolarized light,” *Lect. Notes Comput. Sci. (including Subser. Lect. Notes Artif. Intell. Lect. Notes Bioinformatics)*, vol. 1065, pp. 626–635, 1996, doi: 10.1007/3-540-61123-1_176.
- [57] P. F. Lozano *et al.*, “Water-content related alterations in macro and micro scale tendon biomechanics,” *Sci. Rep.*, vol. 9, no. 1, pp. 1–12, 2019, doi: 10.1038/s41598-019-44306-z.
- [58] R. A. Macrae, K. Miller, and B. J. Doyle, “Methods in Mechanical Testing of Arterial Tissue: A Review,” *Strain*, vol. 52, no. 5, pp. 380–399, 2016, doi: 10.1111/str.12183.
- [59] A. M. Turner, R. Subramaniam, D. F. M. Thomas, and J. Southgate, “Bladder tissue engineering,” *Tissue Eng. Using Ceram. Polym.*, pp. 445–465, Jan. 2007, doi: 10.1533/9781845693817.2.445.
- [60] D. E. Maidana *et al.*, “ThicknessTool: automated ImageJ retinal layer thickness and profile in digital images,” *Sci. Rep.*, vol. 10, no. 1, pp. 1–11, 2020, doi: 10.1038/s41598-020-75501-y.
- [61] W. L. E. Wong *et al.*, “On the correct interpretation of measured force and calculation of material stress in biaxial tests,” *J. Mech. Behav. Biomed. Mater.*, vol. 47, no. 3, pp. 2043–2054, Oct. 2016, doi: 10.1016/j.jmbbm.2015.08.019.
- [62] R. Hogan, “7 Steps To Calculate Measurement Uncertainty,” ISOBudgets LLC, Virginia Beach, 2020. [Online]. Available: <https://www.isobudgets.com/measurement-uncertainty-guide-download/>.

- [63] G. Crammond, S. W. Boyd, and J. M. Dulieu-Barton, "Speckle pattern quality assessment for digital image correlation," *Opt. Lasers Eng.*, vol. 51, no. 12, pp. 1368–1378, 2013, doi: 10.1016/j.optlaseng.2013.03.014.
- [64] C. F. A. CULLING, "Chapter 8 - Preparation of Stains," in *Handbook of Histopathological and Histochemical Techniques (Third Edition)*, Third Edition., C. F. A. CULLING, Ed. Butterworth-Heinemann, 1974, pp. 165–177.
- [65] T. C. Gasser, R. W. Ogden, and G. A. Holzapfel, "Hyperelastic modelling of arterial layers with distributed collagen fibre orientations," no. July 2005, pp. 15–35, 2006, doi: 10.1098/rsif.2005.0073.
- [66] A. Çağlar, Y. Bor, O. Tomar, M. Beykaya, and V. Gök, "Mechanical and microbiological properties of natural casings using in meat products," *Kafkas Univ. Vet. Fak. Derg.*, vol. 24, no. 3, pp. 327–334, 2018, doi: 10.9775/kvfd.2017.18885.
- [67] K. Amini Khoiy, S. Abdulhai, I. C. Glenn, T. A. Ponsky, and R. Amini, "Anisotropic and nonlinear biaxial mechanical response of porcine small bowel mesentery," *J. Mech. Behav. Biomed. Mater.*, vol. 78, no. August 2017, pp. 154–163, 2018, doi: 10.1016/j.jmbbm.2017.11.017.

Appendices

Appendix A:

Detailed Experimental Methods

A.1 Specimen Preparation

The specimen preparation process is summarised visually in Figure A.1.1.

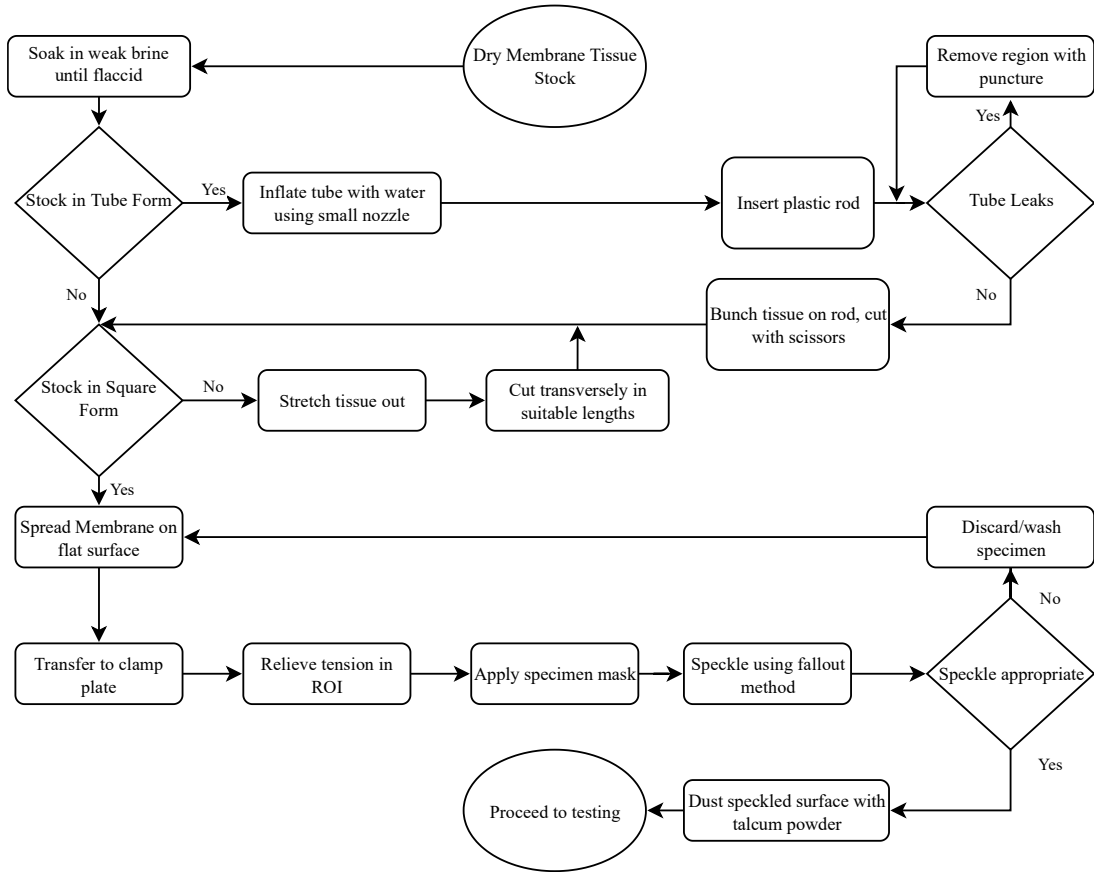


Figure A.1.1: *Process flow diagram describing the specimen preparation procedure.*

The process of preparing specimens began with the dry lamb intestinal tissue which was hydrated and prepared from its tubular form into flat squares for bulge or planar testing.

The squares were placed on a clamp surface and speckled. These specimens were then ready for bulge testing. After bulge testing these same specimens were cut into a cruciform shape for planar biaxial tensile (PBT) testing. Specimen disposal simply followed normal food waste hygiene practice.

A.2 Digital Image Correlation

A.2.1 Setup and Calibration

The DIC procedure followed for setup and calibration has been summarised in Figure A.2.2.

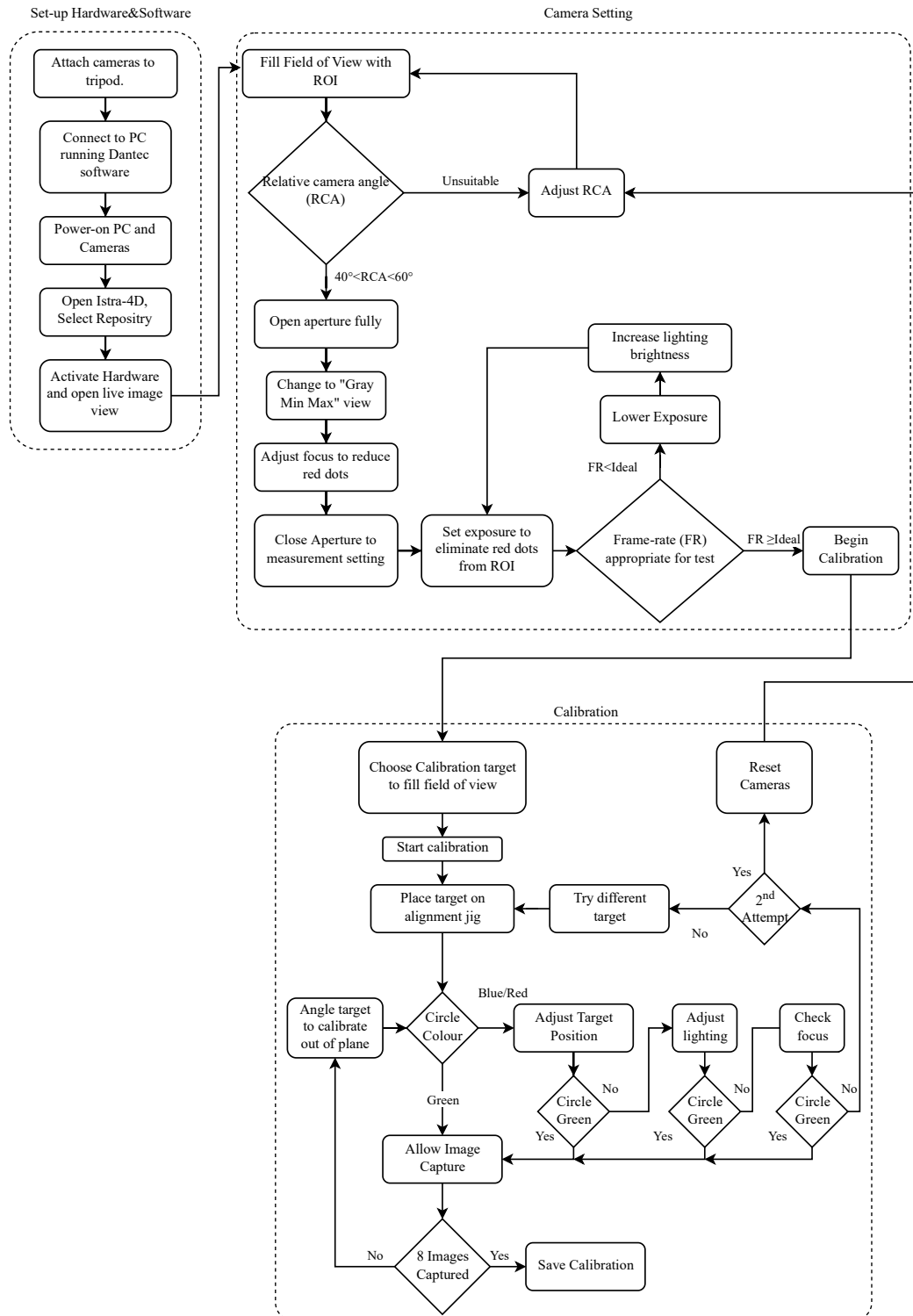


Figure A.2.2: DIC setup and calibration procedure

A.2.2 Correlation

The correlation process involved the live image capture of the specimen during the test. The steps followed are numbered below:

1. Start New Correlation setup.
2. Ensure ROI size is set on both cameras to be as tightly bounding the specimen as possible.
3. Set appropriate acquisition frequency (for BTR tests, too high for too long a test results in too many steps to evaluate efficiently, aim for about 300 time-steps)
4. Check all analogue signal cables are working (ensure both PBT and BTR are setup initially to standardise the dataframe width during export)
5. Simultaneously start the test and start recording DIC (Or set up triggering).

A.2.3 Evaluation and Data Export

The process of running an evaluation is summarised in the following step:

1. Start new evaluation
2. Define mask in ROI
3. Select a start point, choose a point with some motion and place marker on the grey area between white and black on a speckle with a “V” shaped corner.
4. Run start-point finder
5. Check for loss of correlation errors, adjust point if need be
6. Run evaluation.
7. Export data as ascii text file

The logic of the above steps can be best understood by examining Figure A.2.3.

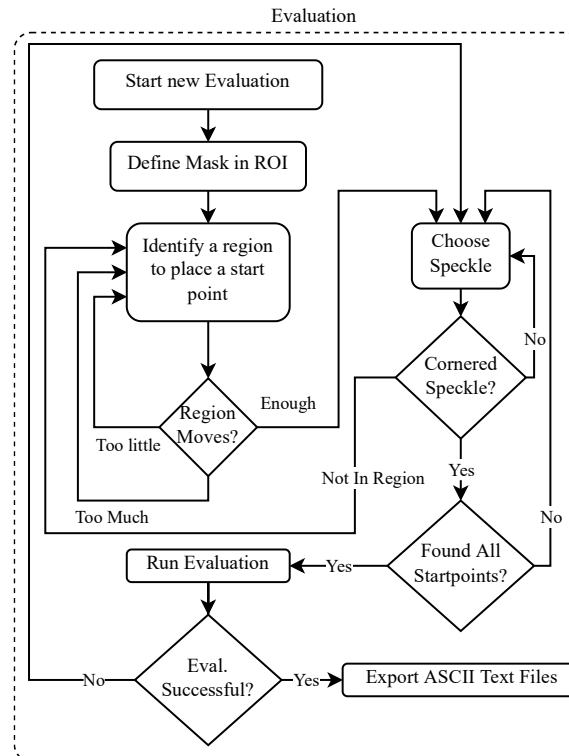


Figure A.2.3: DIC evaluation and data export protocol.

The location of a start-point on a particular speckle was found to impact the effectiveness at finding all the start-points. The process of selecting a start-point has been given in Figure A.2.4 below.

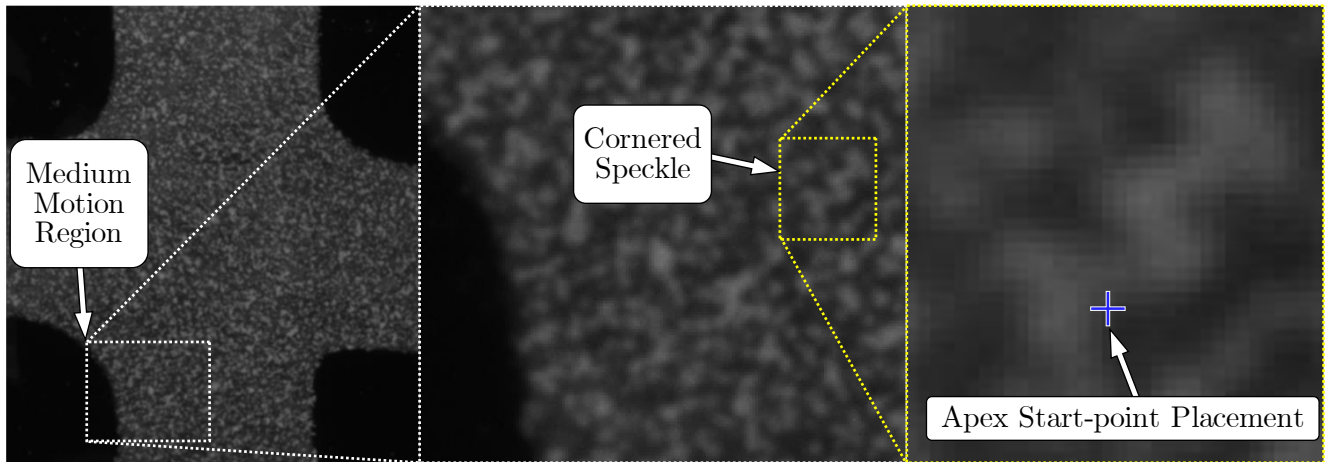


Figure A.2.4: *DIC evaluation start-point selection.*

A.3 Chromotrope Aniline Blue Stain

Chromotrope aniline blue (CAB) stain methodology supplied by Lizette Fick, UCT Surgical Studies Histology [64] for collagen staining.

A.3.1 *Method:*

Modification of Masson's and Mallory page 415 of [64].

- | | |
|---------------------------------------|------------|
| 1. Dewax in xylol | 10 min × 2 |
| 2. Rehydrate through alcohol to water | 2 min each |
| 3. Weigert's Iron Haematoxylin | 10 min |
| 4. Rinse in distilled H_2O | |
| 5. 1% Phosphomolybdic Acid | 3 min |
| 6. Rinse well in distilled H_2O | |
| 7. Stain with CAB | 8 min |
| 8. Rinse in distilled H_2O | |
| 9. Blot Dry | |
| 10. Dehydrate quickly | |

A.3.2 *Reagents*

Weigert's Iron Haematoxylin

- | | | |
|----------------------|--|--------|
| • Solution A: | Haematoxylin | 1 g |
| • Absolute Alcohol: | | 100 ml |
| • Solution B: | 30% Aqueous Ferric Chloride (anhydrate). | 4 ml |
| • Concentrated HCl | | 1 ml |
| • Distilled H_2O | | 95 ml |

Mix equal volumes of Solution A and Solution B before use (good for a few hours)

Colour of mixture: deep purple (If muddy brown, discard)

CAB Solution

- 1.5 g Aniline Blue in 2.5 ml concentrated HCl
- 200 ml Distilled H_2O
- Dissolve with gentle heat
- 6 g Chromotrope 2 R

A.3.3 *Results*

Nuclei	blue-black
Cytoplasm, muscle acidophil granules	red
Collagen, cartilage, mucin and basophil granules	light blue

A.4 Safety Datasheets

1. [Formalin](#)
2. [Saline](#)
3. [Spray Paint](#)
4. [Talcum Powder](#)

A.5 Micrograph Calibration

Specimen thickness micrographs were measured on a Nikon Digital Microscope. This was calibrated using the graticule pictured in Figure A.5.5 and was a feature of the Nikon software that came with the microscope.

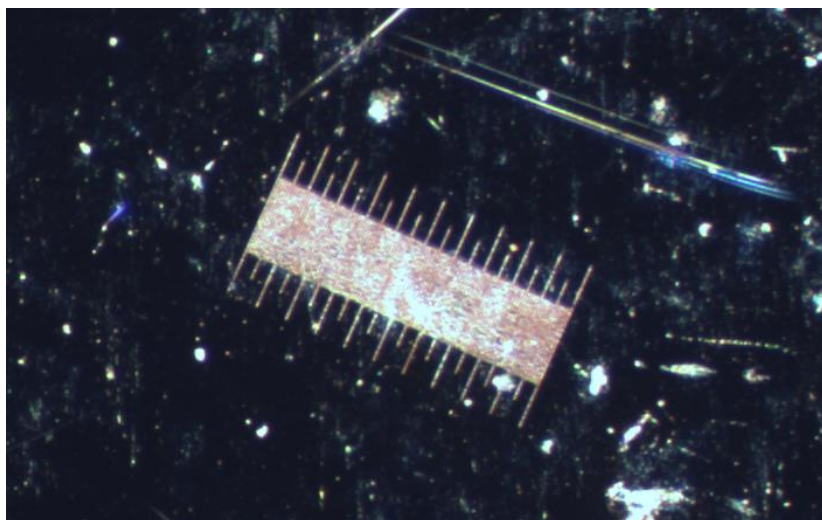


Figure A.5.5: 1 mm optical calibration graticule

A.6 Testing Procedure Overview

The process of identifying an MFA using a bulge test and then excising a cruciform specimen and then testing it in PBT is given in the list below. Details not given here can be found in the sections covered already.

1. Prepare a bulge specimen according to Appendix A.1
2. Place DIC calibration jig on the BTR pressure chamber ensuring orientation aligns with the triangle of alignment.
3. Perform DIC Setup and calibration on the BTR according to Appendix A.2.1
4. Ensure specimen is moist and pressure chamber has recently been flushed with some hot water.
5. Fill syringe partially with hot water.
6. Replace calibration jig with the specimen clamped between the bulge aperture plates.
7. Ensure pressure chamber bleed valve is closed for testing
8. Ensure alignment of the specimen with triangle of alignment.
9. Run a bulge test while simultaneously running a DIC correlation according to appendix A.2.2

10. Evaluate this correlation with an appropriate facet size (59 *px* is recommended given the results of this study) and export the data according to Appendix A.2.3.
11. Cover the specimen to prevent dehydration.
12. Run the MFA-ID Python script.
13. Ensure values are sensical based on the plotted graph.
14. Remove the clamp assembly and lift off the cover plate and gasket carefully.
15. Place the specimen & backing plate on the goniometric cutter bed.
16. Align cutter block with the angle output of the MFA-ID Algorithm
17. Mark the MFA on the specimen transfer card and label the angle cut and specimen number
18. Apply cyanoacrylate to the card grips and place it on the excised specimen.
19. Gently trim away excess tissue.
20. Place specimen in a petri dish with some saline to keep it moist from underneath.
21. Set up DIC cameras (re-calibrate if necessary) as before but for the PBT Tester.
22. Ensure Saline bath level is correct
23. Transfer Specimen to PBT arms.
24. Check loadcell cables for friction points that could perturb load signal.
25. Run preconditioning test Gcode (Record data if necessary to ensure correct set-up)
26. Start correlation according to appendix A.2.2 and run the test Gcode simultaneously.
27. Run evaluation of data as before and export for a quick check of test quality using analysis codes.
28. Re-run test if any data capture issues arose.
29. Remove specimen using a new specimen transfer card glued to the first (ensure labelling is preserved on the new card)
30. Place specimen in a petri-dish filled with formalin enough to cover the specimen.
31. Seal up petri dishes in a Ziplock bag and place in a fume hood.
32. Leave specimens for one week to formalin fix.
33. Cut small wax block
34. Remove specimen from formalin (Ensure fume hood is on)
35. Stain the arm of the specimen with gentian violet at the MFA axis.
36. Trim off arms from specimen card.
37. Place wax block in centre of specimen and wrap the arms over the wax block.
38. Place block in a histology cassette.
39. Send for histology.
40. Get slides and capture scaled images of the arm cross-sections
41. Pre-process images and run the Image J ThicknessTool protocol to get specimen thickness for each axis.
42. Measure specimen width using ImageJ and DIC calibrated *.hdf image files.
43. Compile all captured data for analysis.

A.7 Continuum Material Modelling Method

Due to the cruciform specimen geometry, stress calculations had to be simplified greatly. For a square specimen, the following approach could be applied and was included for completeness.

A.7.1 Stress Calculations

The approach that follows largely mirrors their method which was deemed to be most prudent owing to highly similar specimen material.

Before PBT testing, the unloaded and stress-free reference configuration (a continuum body) was given by $\mathbf{\Omega}_0 \subseteq \mathbb{R}^3$. Here, each material point in the continuum was given by the three coordinates of:

$$X_I \text{ and } I = 1,2,3 \quad \text{A.7.11}$$

The deformed configuration under PBT loading was described by the continuum $\mathbf{\Omega}_t \subseteq \mathbb{R}^3$ where each material point was given by the coordinates \mathbf{x}_i where $i = 1,2,3$ are such that:

$$\mathbf{x} = \mathbf{x}(\mathbf{X}) \quad \text{A.7.12}$$

Assuming a homogeneous region of interest has been done in the past for feature tracking ODM methods in PBT stress calculations [36]. This was explained to be reasonable given suitable distance from discontinuous loading [36]. Though this assumption was found to be false in some cases (Using 3D DIC), alternative approaches (Such as FEA) were not feasible to consider in this project due to time constraints. Thus, an assumption of homogeneity was made in the ROI.

This allows one to map the PBT deformation between the reference and current configuration using:

$$\mathbf{x}(\mathbf{X}) = \begin{pmatrix} \lambda_{11}X_1 + \kappa_{11}X_2 \\ \lambda_{22}X_2 + \kappa_{22}X_1 \\ \lambda_{33}X_3 \end{pmatrix} \quad \text{A.7.13}$$

Where λ_{ii} and κ_{ii} are the axial stretch and in-plane shear ratios respectively. The deformation gradient tensor of such motion (\mathbf{F}) was calculated as follows:

$$\mathbf{F} = \frac{\partial \mathbf{x}(\mathbf{X})}{\partial \mathbf{X}} = \begin{bmatrix} \frac{\partial x_1}{\partial X_1} & \frac{\partial x_1}{\partial X_2} & \frac{\partial x_1}{\partial X_3} \\ \frac{\partial x_2}{\partial X_1} & \frac{\partial x_2}{\partial X_2} & \frac{\partial x_2}{\partial X_3} \\ \frac{\partial x_3}{\partial X_1} & \frac{\partial x_3}{\partial X_2} & \frac{\partial x_3}{\partial X_3} \end{bmatrix} = \begin{bmatrix} \lambda_{11} & \kappa_{11} & 0 \\ \kappa_{22} & \lambda_{22} & 0 \\ 0 & 0 & \lambda_{33} \end{bmatrix} \quad \text{A.7.14}$$

The out of plane component λ_{33} can be calculated by using the incompressibility constraint:

$$J = \det \mathbf{F} = 1 \quad \text{A.7.15}$$

Equation A.7.15 appeared across the literature and for materials like MT with very high water content, this assumption of incompressibility is rational [29].

Using this deformation gradient, we can define the left Cauchy-Green deformation tensor (\mathbf{b}), the right Cauchy-Green deformation tensor (\mathbf{C}) and the Green-Lagrange strain tensor (\mathbf{E}) respectively:

$$\begin{aligned}
\mathbf{b} &= \mathbf{F}\mathbf{F}^T \\
\mathbf{C} &= \mathbf{F}^T\mathbf{F} \\
\mathbf{E} &= \frac{1}{2}(\mathbf{C} - \mathbf{I})
\end{aligned}
\tag{A.7.16}$$

Under the assumption of homogeneity, the field of stresses in a PBT specimen under load can be estimated from the measured loads during experiments[1]. This was done in terms of the first Piola-Kirchoff stress tensor (\mathbf{P}). These are typically known as normal stresses calculated from applied load divided by the cross-sectional area ($\sigma = \frac{L}{A}$). Here, some stress correction factors might have been applied as Avanzini *et al.* suggested [47]. This was not possible given that no standardised specimen shapes were used and deformations of the MT would have limited the application of such correction factors to hyperelastic materials.

In a PBT test, the upper and lower surfaces are unconstrained and unloaded, thus the planar stresses are given by:

$$P_{ii} = \frac{T_{ii}L_{jj}}{L_{jj}h} \text{ where } i, j = 1, 2 ; 2, 1 \tag{A.7.17}$$

Tractions T_{ii} were the measured load per unit width of a specimen. L_{jj} were the in-plane undeformed tissue widths, ie. the widths of the PBT specimen square or the cruciform arms and h is the specimen thickness.

Using \mathbf{P} , the second Piola-Kirchoff stress tensor (\mathbf{S}) and the Cauchy stress tensor (\mathbf{t}) was calculated as follows:

$$\mathbf{S} = \frac{1}{J}\mathbf{P}\mathbf{F}^{-T} = \frac{1}{J} \begin{bmatrix} P_{11}\lambda_{22}\lambda_{33} & -P_{11}\kappa_{22}\lambda_{33} & 0 \\ -P_{22}\kappa_{11}\lambda_{33} & P_{22}\lambda_{11}\lambda_{33} & 0 \\ 0 & 0 & 0 \end{bmatrix} \tag{A.7.18}$$

$$\mathbf{t} = \frac{1}{J}\mathbf{P}\mathbf{F} = \frac{1}{J} \begin{bmatrix} P_{11}\lambda_{11} & P_{22}\kappa_{11} & 0 \\ P_{11}\kappa_{22} & P_{22}\lambda_{22} & 0 \\ 0 & 0 & 0 \end{bmatrix} \tag{A.7.19}$$

Given a hyperelastic material under negligible shear ($\kappa_{ii} = 0 \ i = 1, 2$) the strain energy function used to describe its mechanical behaviour becomes constrained in form [1]. Further assumptions of $S_{I3} = t_{i3} = 0$ for $I = i = 1, 2, 3$ result in all off-diagonal entries of \mathbf{S} and \mathbf{t} becoming zero and thus the material is under plane stress.

Like Bellini *et al.* the SIS was modelled as a hyperelastic, homogenous and incompressible material undergoing finite quasi-static isothermal deformation [1]. This legitimised a strain energy function W that defined the purely elastic response of the material. The specific forms of the strain energy function were chosen in section A.7.2. W was given in terms of \mathbf{C} , \mathbf{E} , their invariants or other material specific factors. Given a hypothetical W , the second Piola-Kirchoff stress tensor can be written as:

$$\mathbf{S} = p\mathbf{C}^{-1} + \frac{\partial W(\mathbf{E})}{\partial \mathbf{E}} = \mathbf{C}^{-1} + 2 \frac{\partial W(\mathbf{C})}{\partial \mathbf{C}} \tag{A.7.20}$$

The Lagrange multiplier p was introduced to enforce incompressibility and the known equivalence of $\frac{\partial W(\mathbf{E})}{\partial \mathbf{E}} = 2 \frac{\partial W(\mathbf{C})}{\partial \mathbf{C}}$ was applied. With $J = 1$, the Cauchy Stress tensor can be expressed as:

$$\mathbf{t} = p\mathbf{I} + \mathbf{F} \frac{\partial W(\mathbf{E})}{\partial \mathbf{E}} \mathbf{F}^T = p\mathbf{I} + 2\mathbf{F} \frac{\partial W(\mathbf{C})}{\partial \mathbf{C}} \mathbf{F}^T \quad \text{A.7.21}$$

Experimental stresses (calculated using equation A.7.19) could thus be used to determine the parameters of W once chosen using a non-linear regression algorithm.

A.7.2 Material Modelling

Constitutive parameters may be found for a particular specimen, however these parameters may not be able describe the general load response of the MT rendering them less useful for implementation in simulations where the loading is not always known [1]. In linear elastic tensile testing, one would simply take the mean or median modulus of the specimens tested. Due to the nonlinear material behaviour of MT, averaging of the specimen-specific parameters will not describe the behaviour of the tissue in general [1].

An alternative to this suggested by Bellini *et al.* was to rather parameterise an average model by rather creating an average stress-strain curve [1]. Thus, Fehervary *et al.*'s testing specific PBT tension ratios matching the loading on the MT *in vivo* became clearer[46]. For better estimation of material behaviour in a model, it becomes important to understand the mechanics of the loading.

As no particular load case was planned for this study, an average model from the range of tension ratios tested was planned based on the approach of Bellini *et al.* [1].

For each datapoint of every test under all tension ratios, the traction T_{ii} was related to deformation E_{ii} by the exponential function in equation A.7.22 below which approximated the J-shaped curves common to MT.

$$T_{ii} = C_1 e^{C_2 E_{ii}} \quad \text{A.7.22}$$

Given constants C_1 and C_2 , this was linearised by taking the natural logarithm on both sides:

$$\ln(T_{ii}) = \ln(C_1) + C_2 E_{ii} \quad 0.23$$

This was used to perform a linear fit of $\ln(T_{ii})$ to E_{ii} using a Python polyfit function which gave the constants C_1 and C_2 . Therefore, the average first Piola-Kirchoff stresses were calculated by converting T_{ii} as follows:

$$\bar{P}_{ii} = \frac{\bar{T}_{ii}}{n} \sum_{i=1}^n \frac{1}{h_i} \quad \text{A.7.24}$$

Where overbar notations on \bar{T}_{ii} and \bar{P}_{ii} indicate the average values, n was the number of specimens and h_i was the specimen-specific thickness.

After this, the average deformation gradient tensor $\bar{\mathbf{F}}$ was calculated using:

$$\bar{\mathbf{E}} = \frac{1}{2} (\bar{\mathbf{F}}^T \bar{\mathbf{F}} - \mathbf{I}) \quad \text{A.7.25}$$

Continuing the negligible shear assumption, the diagonal components of $\bar{\mathbf{F}}$ could be approximated by:

$$\bar{F}_{ii} \approx \sqrt{2\bar{E}_{ii} + 1} \quad \text{A.7.26}$$

Using equations A.7.24 and A.7.26 the average second Piola-Kirchoff stress was given by:

$$\bar{\mathbf{S}} = \bar{\mathbf{P}} \cdot \bar{\mathbf{F}}^{-T} \quad \text{A.7.27}$$

This was used with equation A.7.20 to attempt to find the average constitutive model parameters from the strain energy functions used by [1]. These were a Neo-Hookean form:

$$W(I_1) = c_1(I_1 - 3) \quad \text{A.7.28}$$

And a Mooney-Rivlin form:

$$W(I_1, I_2) = d_1(I_1 - 3) + d_2(I_2 - 3) \quad \text{A.7.29}$$

Where I_1 and I_2 are the invariants of the right Cauchy-Green deformation tensor \mathbf{C} and c_1, d_1, d_2 are material parameters.

There exist more detailed strain energy functions that can capture anisotropic behaviour linked to fibre distributions [26], [65]. An example of which is used by Meador *et al.* has been given below:

$$[26], [65] \quad W(I_1, I_4) = \frac{\mu}{2}(I_1 - 3) + \frac{k_1}{4k_2} [e^{k_2(\kappa I_1 + (1-3\kappa)I_4 - 1)} - 1] \quad \text{A.7.30}$$

The shear modulus μ determine the isotropic material response while k_1 and k_2 determine the anisotropic material response. The fibre dispersion parameter κ with $\kappa \in [0, \frac{1}{3}]$ was such that $\kappa = 0$ enforced a pure anisotropic response in the exponential term of equation A.7.30 and $\kappa = \frac{1}{3}$ would enforce pure isotropy. Here, I_4 is the fourth invariant of \mathbf{C} , where $I_4 = \mathbf{C} : \mathbf{M}$ and \mathbf{M} is a structural tensor which was computed from:

$$\mathbf{M} = \mathbf{M}_0 \otimes \mathbf{M}_0$$

Where \mathbf{M}_0 is the vector constructed using the MFA orientation vector α as follows:

$$\mathbf{M}_0 = \begin{pmatrix} \cos(\alpha) \\ \sin(\alpha) \\ 0 \end{pmatrix}$$

A strain energy function of this order would require a non-linear least squares fit between the experimentally determined stress-strain data and the data derived from equation A.7.30 [26], [65]. Bellini *et al.* found that equations A.7.28 and A.7.29 did not fit the data very well but preferred a Fung model.

The above serve to inform the reader of different approaches that can be taken to model an MT specimen's material response. These would typically be validated by applying the material model to a FEA model to predict a known material response [1]. As FEA was excluded from the objectives of this study, no further presentation of such methods has been offered.

Appendix B:

Detailed Experimental Results

B.1 Sealing

The comparison of inflation profiles is shown in Figure 5.1 where the slopes of the inflation profiles did not differ significantly between sealing methods. It was not possible to test the different sealing methods with the same specimen as the improved sealing method involved modifying the old cover plate. The slight slope increase was not deemed significant as a repeat test of Figure 5.1(a) yielded a slope exceeding that of Figure 5.1(b)

Based on the evident decreased

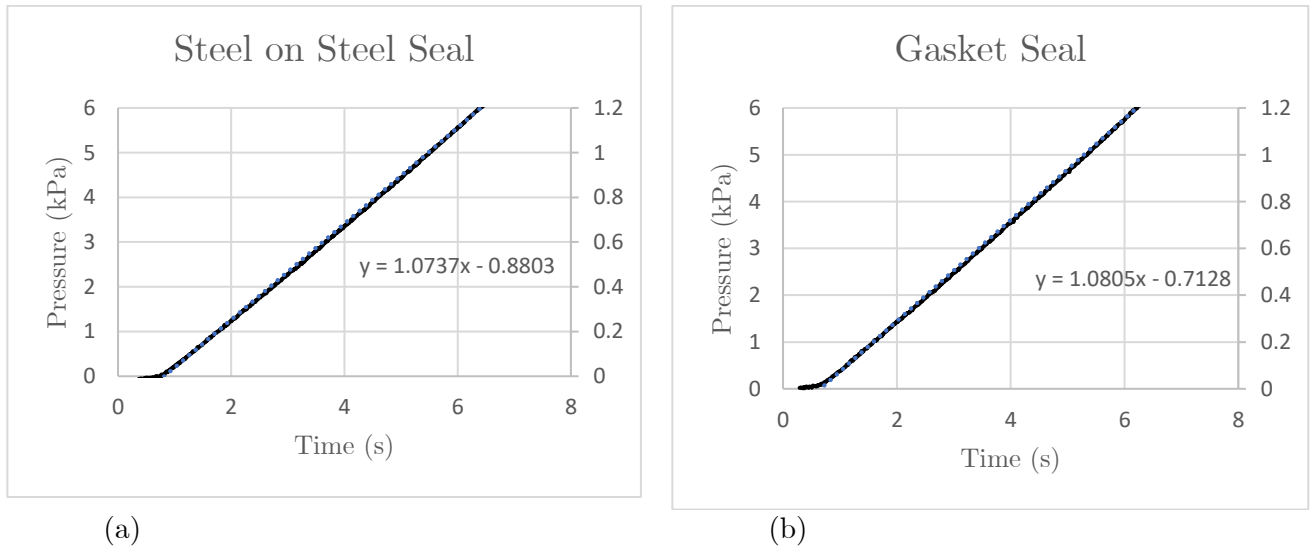
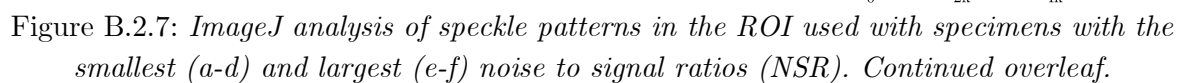


Figure B.1.6: (a) *Rudimentary simple steel on steel clamping system with rupture* (b) *Adapted system with gasket*

B.2 Displacement Data Quality

B.2.1 DIC Speckle Quality

Speckle quality was assessed statistically in the following figures.



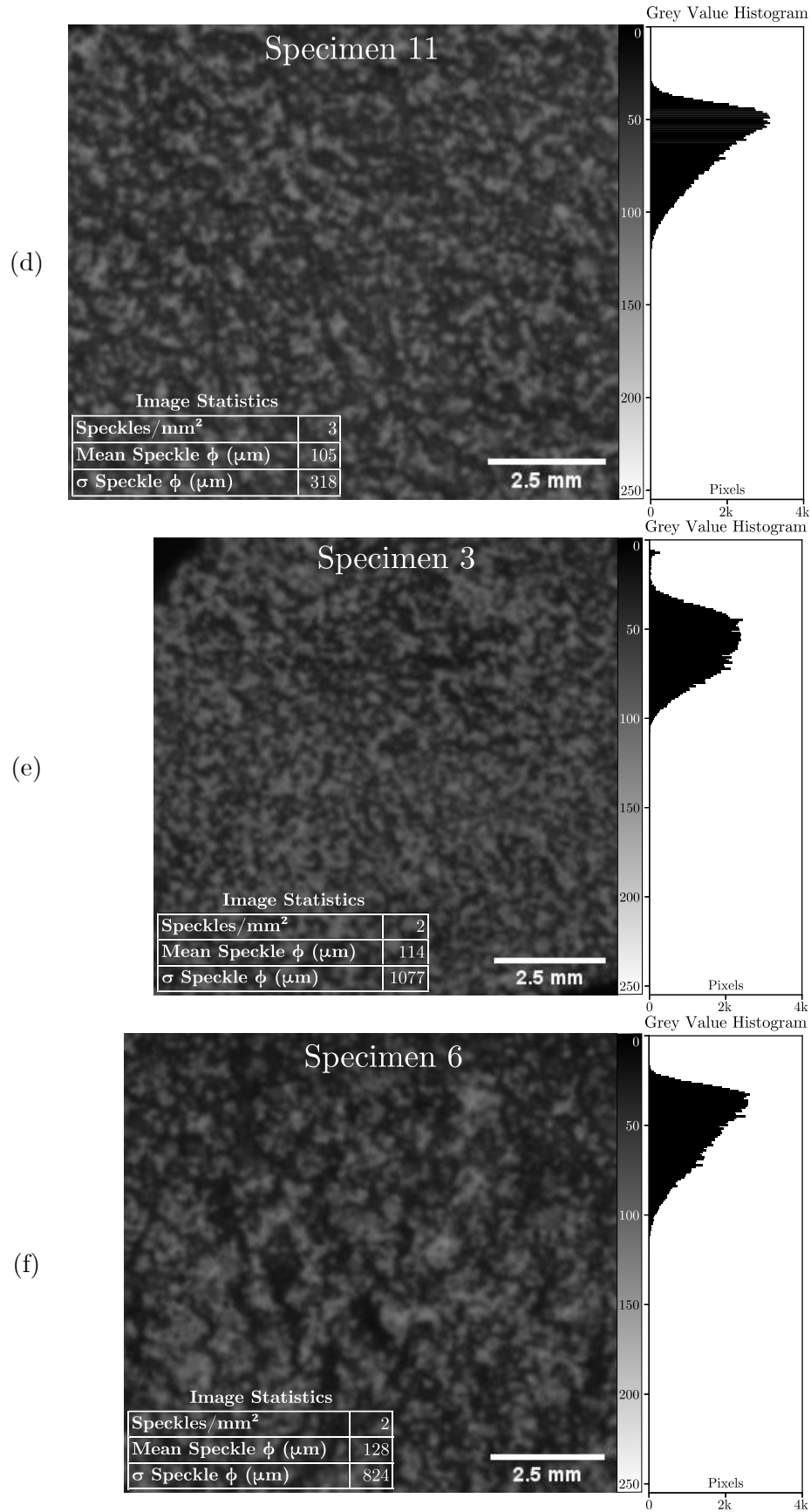


Figure B.2.8: *ImageJ* analysis of speckle patterns in the ROI used with specimens with the smallest (a-d) and largest (e-f) noise to signal ratios (NSR).

B.3 Bulge Summary

A summary of bulge test parameters and results has been given in the Table B.3.8 below.

Table B.3.8: A summary of all the bulge testing MFA-ID parameters and results

Spec.	Facet Size (<i>px</i>)	POI Step	Apex Step	Ref. Step	Tol. (mm)	<i>r</i> (mm)	$\delta\theta$ (°)	$\theta_{suggested}$ (°)	θ_{cut} (°)	<i>r</i> _{minor} (mm)	<i>r</i> _{major} (mm)	θ_{err} (°)	ξ_{BTR}
1	15	168	154	14	1	6	2	-1.7	-30	6.4	6.53	34.50	0.75
2	15	138	62	11	1	7.5	2	2.9	3	7.64	8.06	24.90	0.24
3	15	129	103	18	1	7.5	1	-35.7	-36	7.8	8.58	22.40	0.28
4	15	108	79	15	1	7.5	1	-48.46	-42	8.2	8.69	26.50	0.59
5	15	162	162	15	1	7.5	1	-61.64	-62	8.24	8.69	24.50	0.63
6	15	150	138	11	1	7.5	1	28.6	28	7.81	8.62	23.30	0.27
7	15	106	97	192	1	7.5	1	52.5	62	8.65	8.96	26.70	0.75
8	15	95	110	14	1	7.5	1	-49.2	-49	7.98	8.11	24.60	0.62
9	15	50	52	75	0.5	7.5	1	-41.3	-41	7.55	7.85	18.50	0.45
10	15	78	86	133	1	7.5	1	34	34	8.16	8.32	25.10	0.78
11	15	54	56	5	0.5	7.5	1	-9	-9	7.84	8	24.70	0.67
12	15	104	104	160	0.5	7.5	1	-46.2	-46.2	7.97	8.21	25.90	0.77
13	15	140	156	239	0.5	7.5	1	30.5	31	8.4	8.78	25.30	0.70
14	15	126	126	212	0.5	7.5	1	-57.5	-58	8.32	8.91	29.20	0.58
15	15	98	98	159	0.5	7.5	1	-48.8	-49	7.83	8.44	24.70	0.35
16	15	100	100	165	0.5	7.5	1	-46.4	-46	7.88	8.24	25.00	0.51

B.4 Additional Algorithm Check Specimens

Two additional specimens were run through the multiprocessing algorithm check process to inform the statements made about the algorithm performance. The results for MFA-ID and isotropy have been given below in Figure B.4.9 and Figure B.4.10.

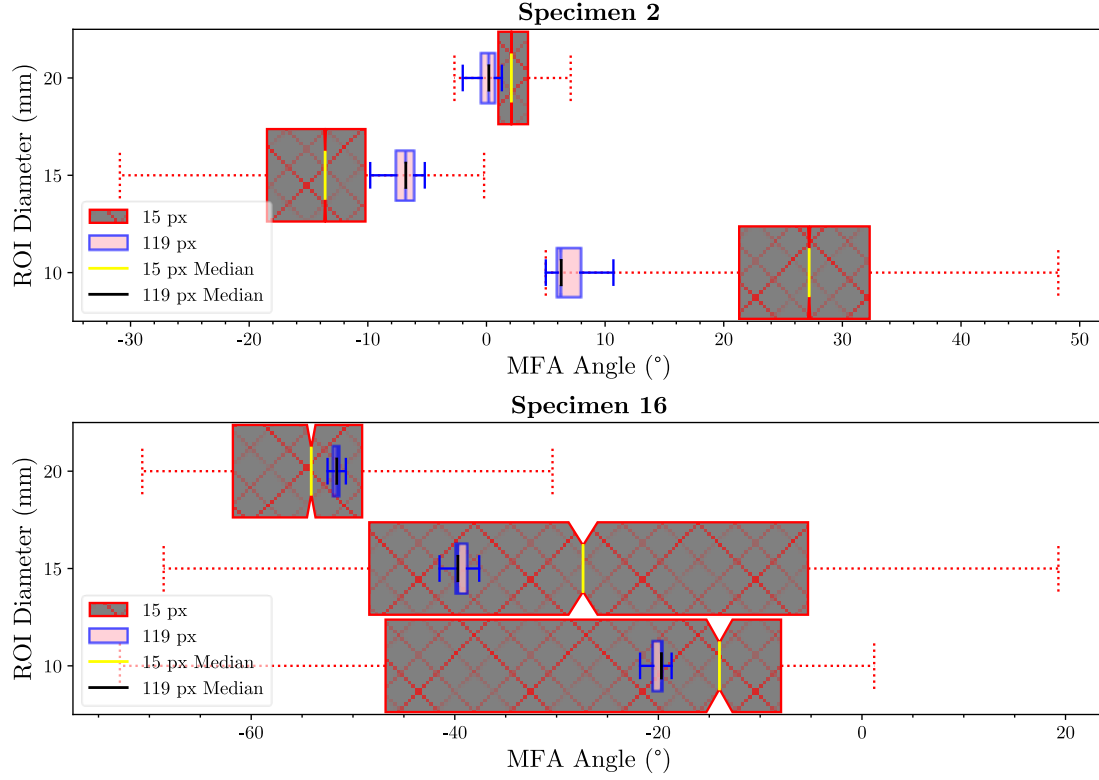


Figure B.4.9: *MFA angle statistics for specimens 2 and 16 using a range of MFA ID algorithm inputs.*

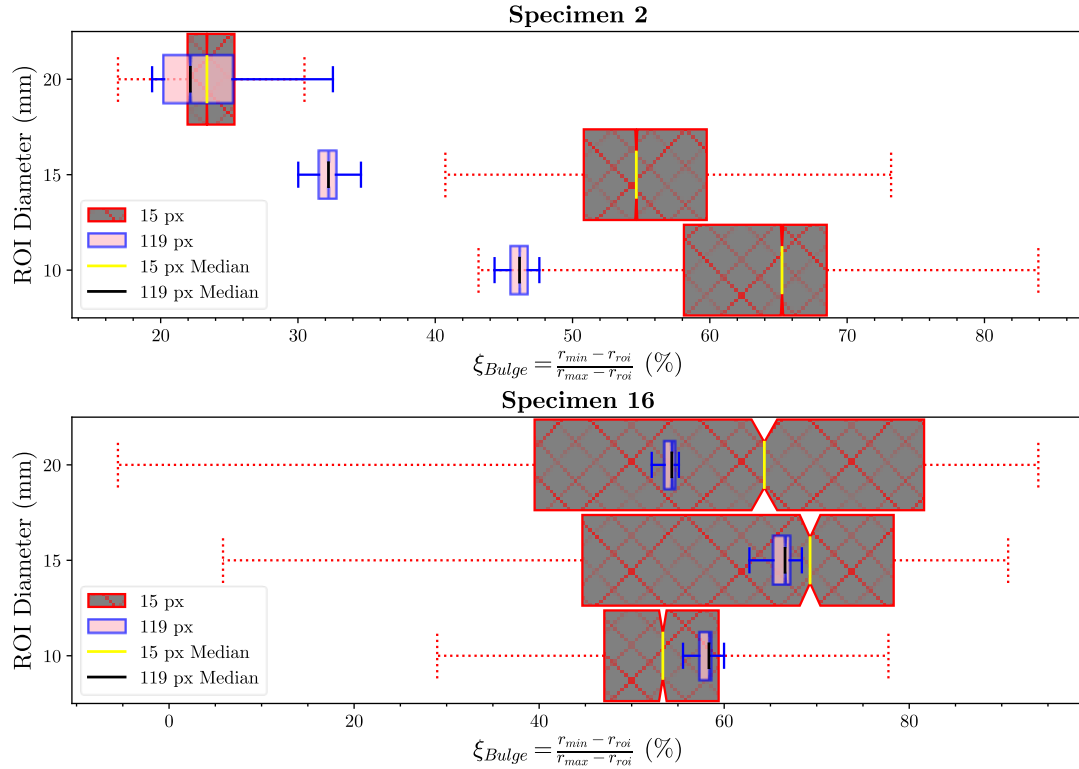
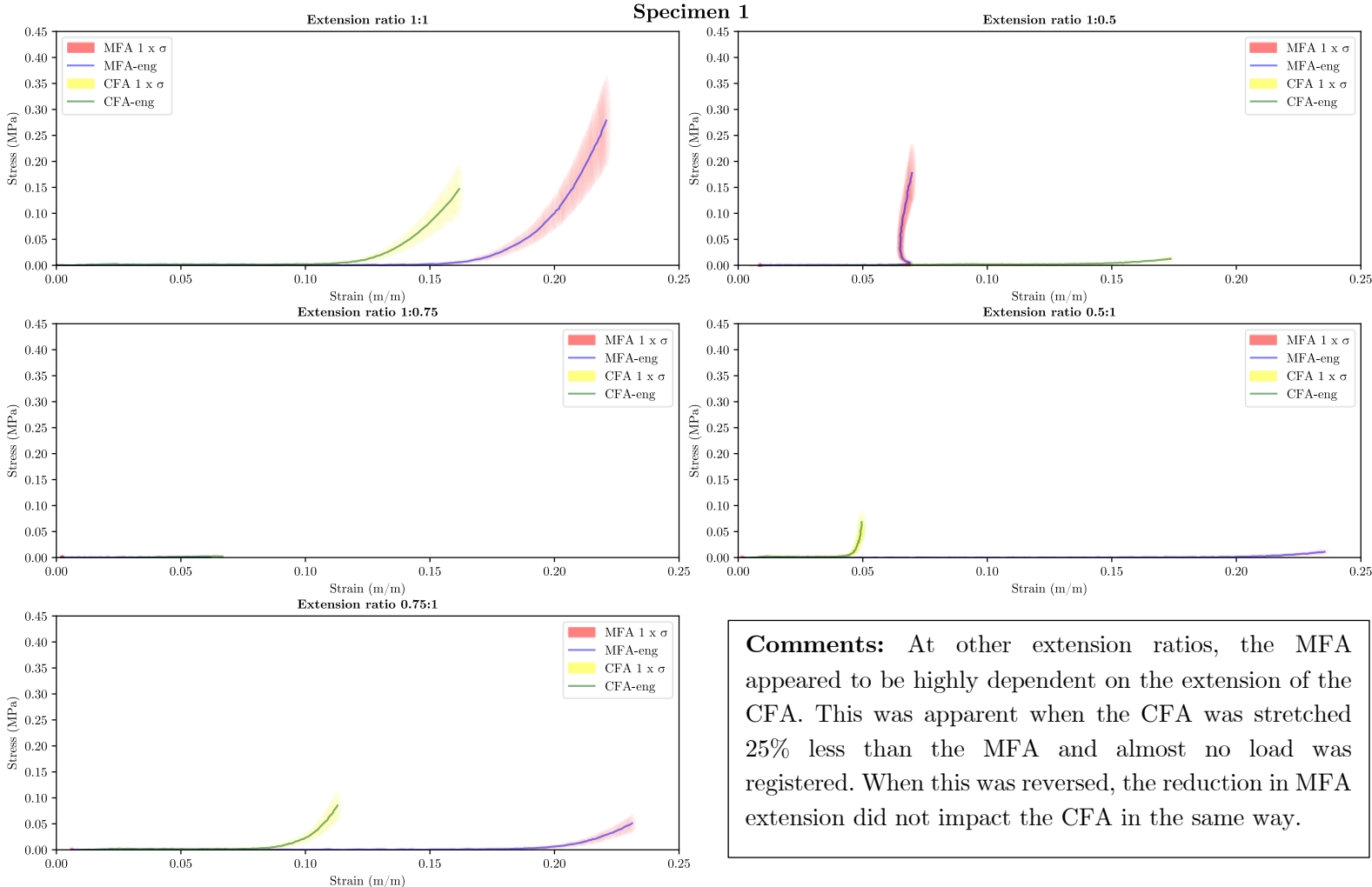


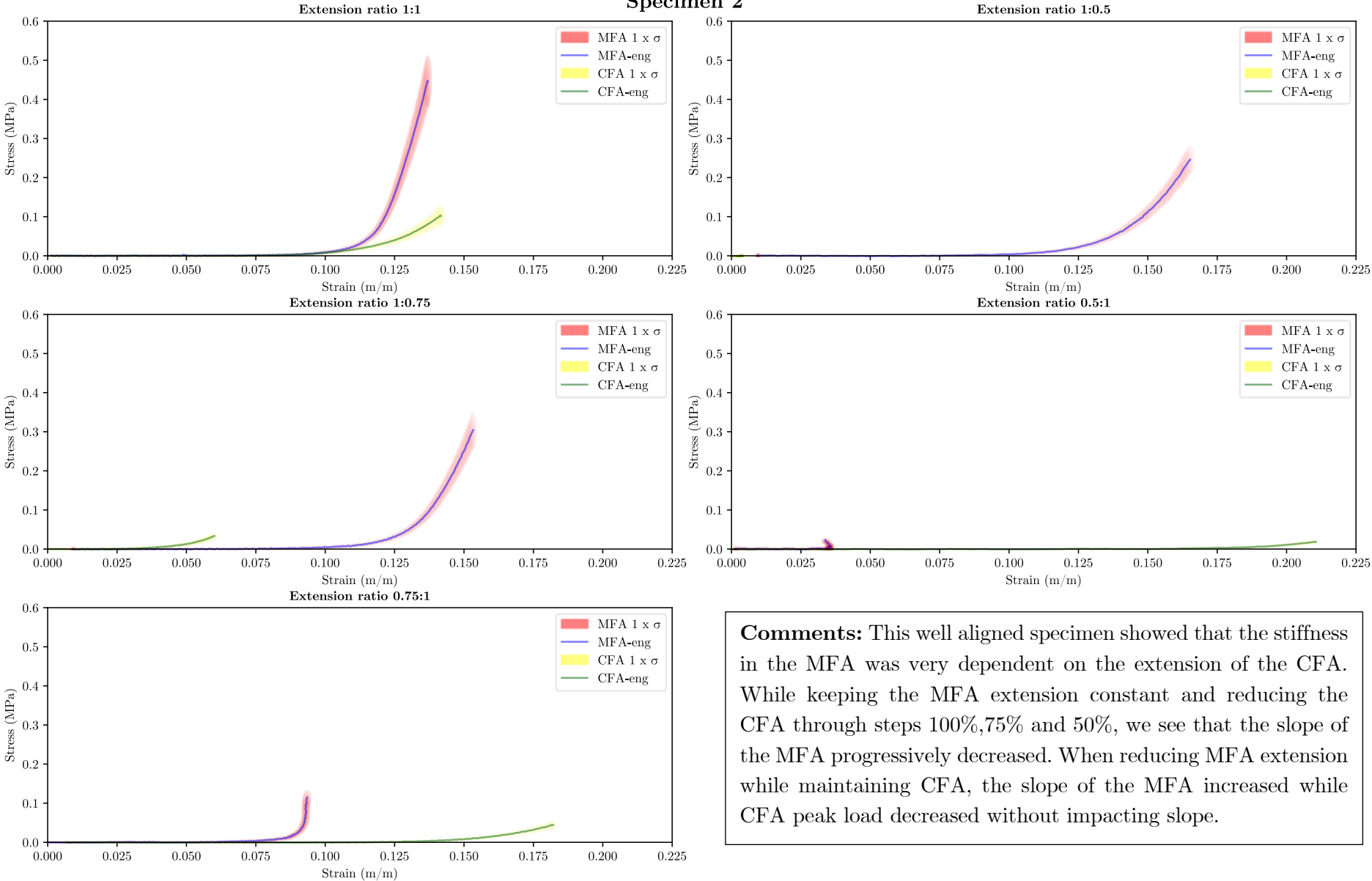
Figure B.4.10: *Specimen 2 and 16 isotropy statistics given a range of MFA-ID inputs*

B.5 Full Stress-Strain Data

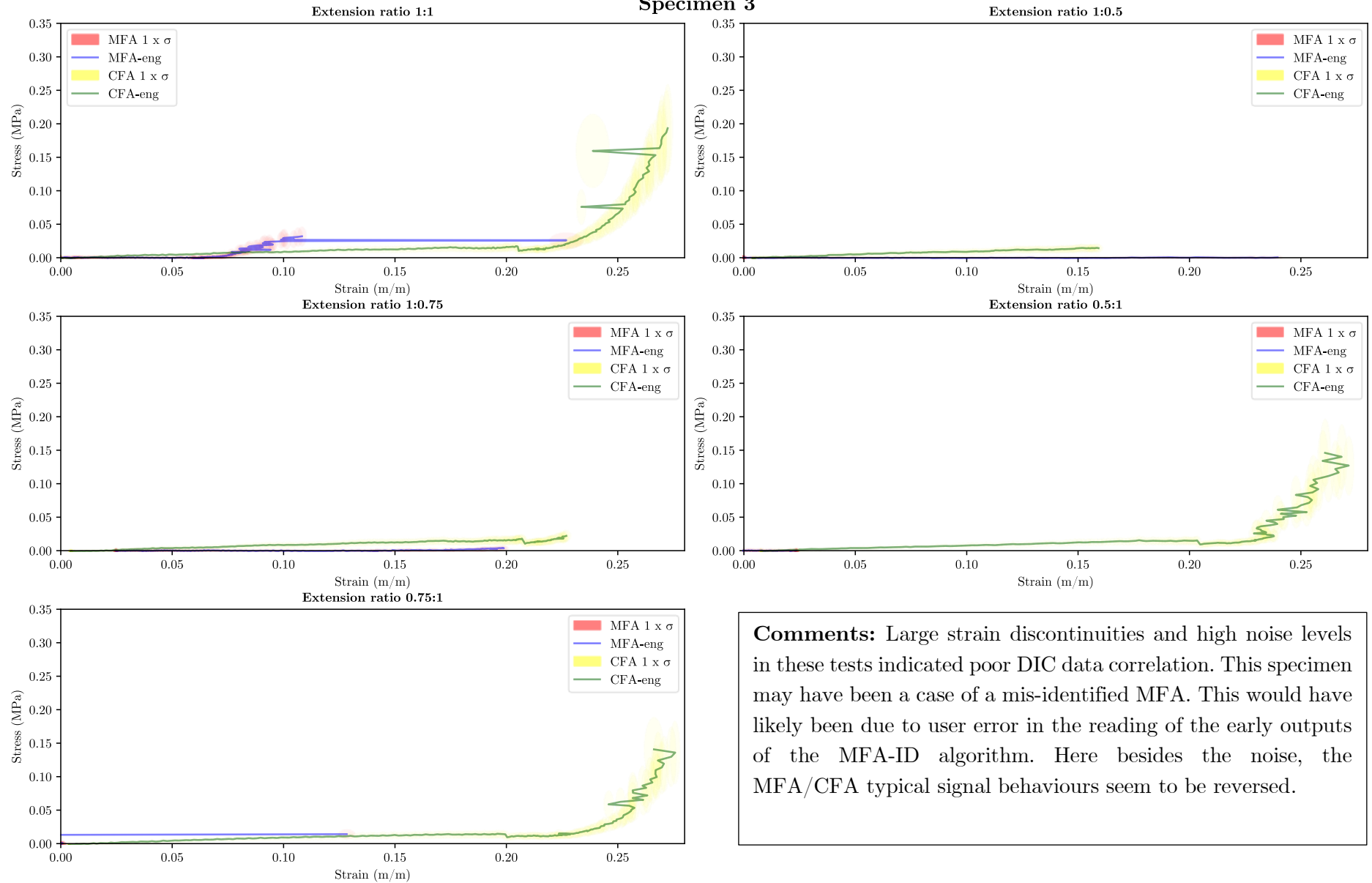
The following pages show the full stress-strain data for each specimen and at each extension ratio at the high extension level (except for specimen 15 which has been given at medium extension). The calculated uncertainties in stress and strain have been represented by shaded ellipses around each datapoint.



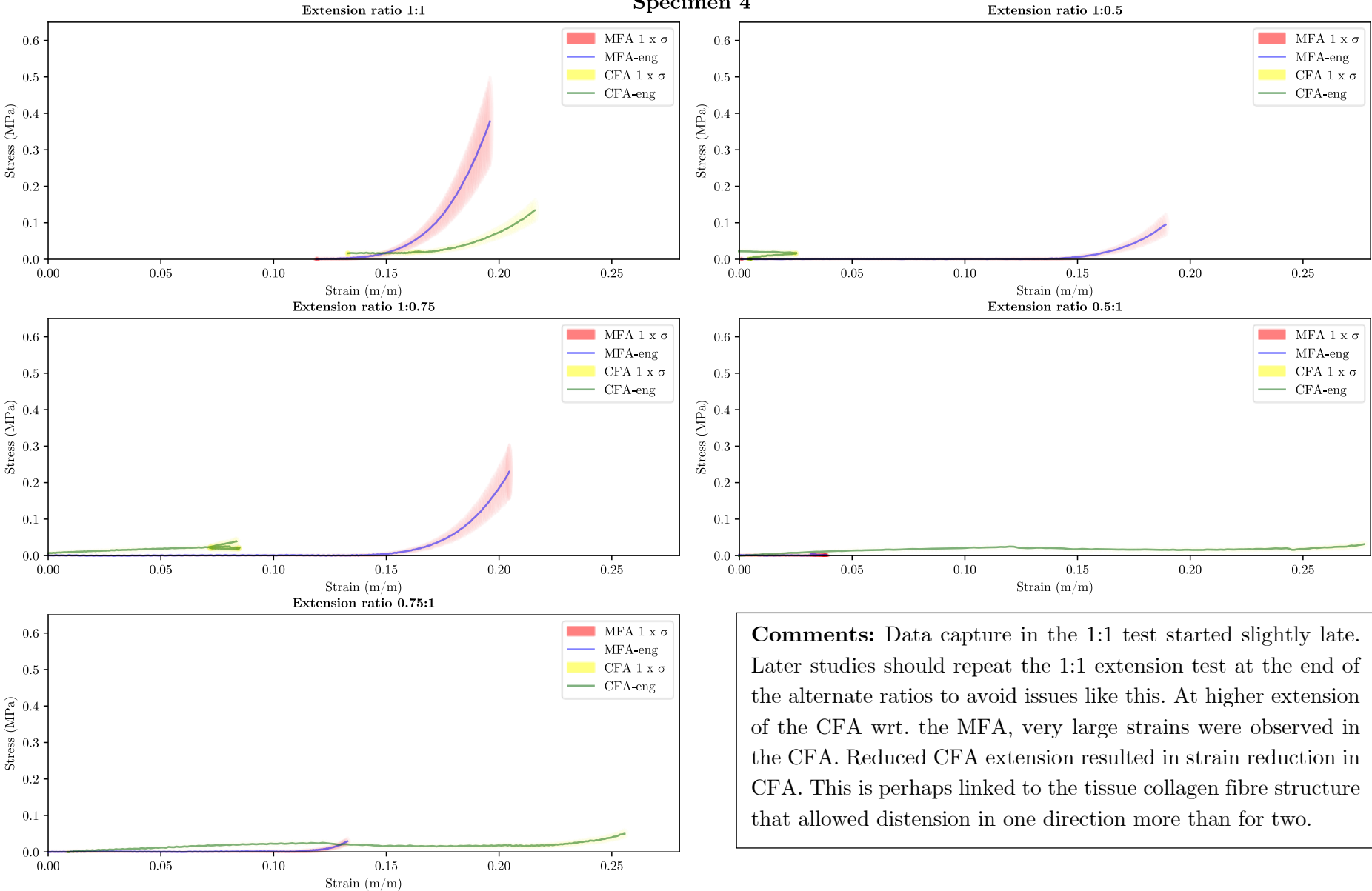
Specimen 2



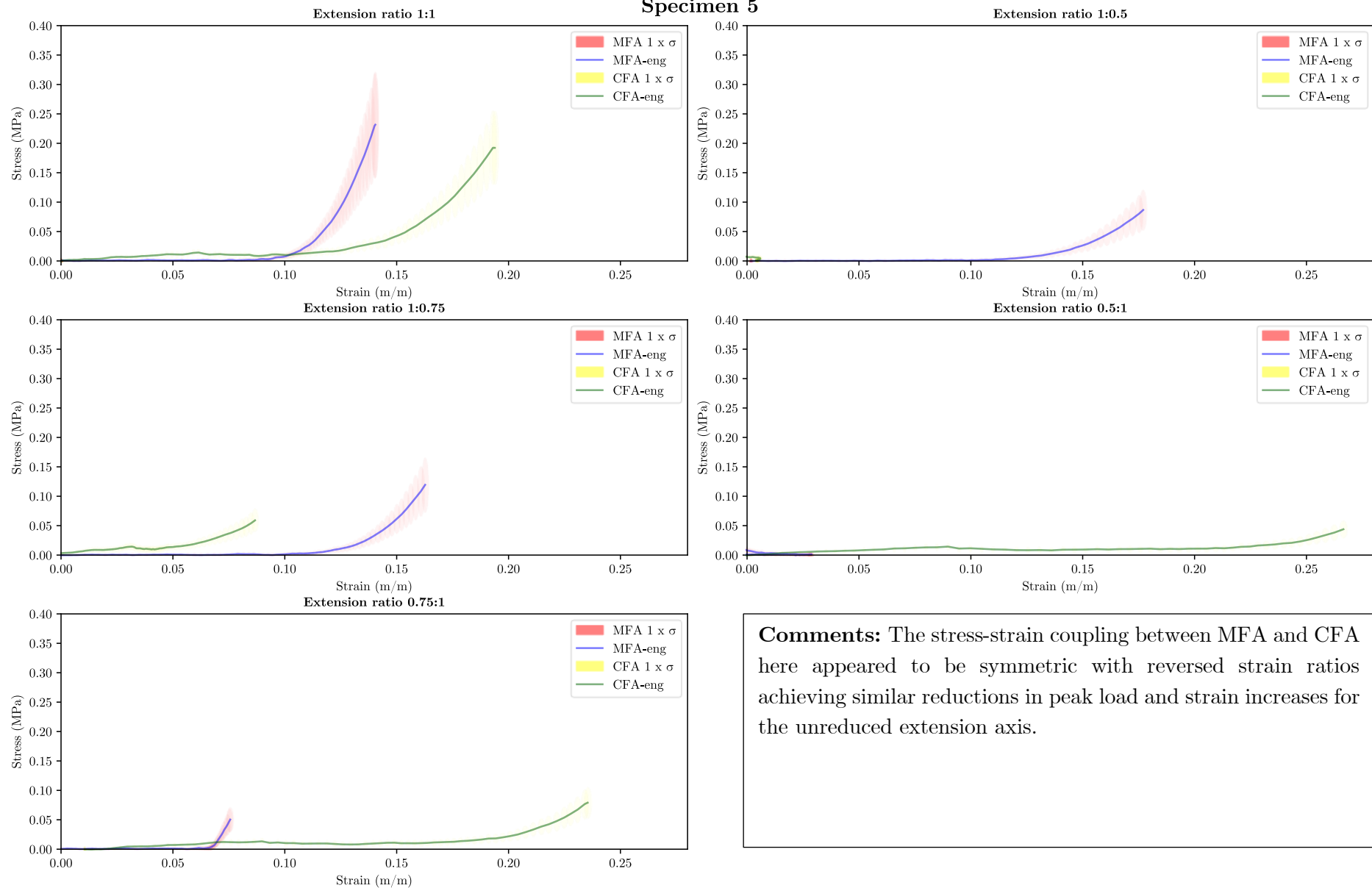
Specimen 3



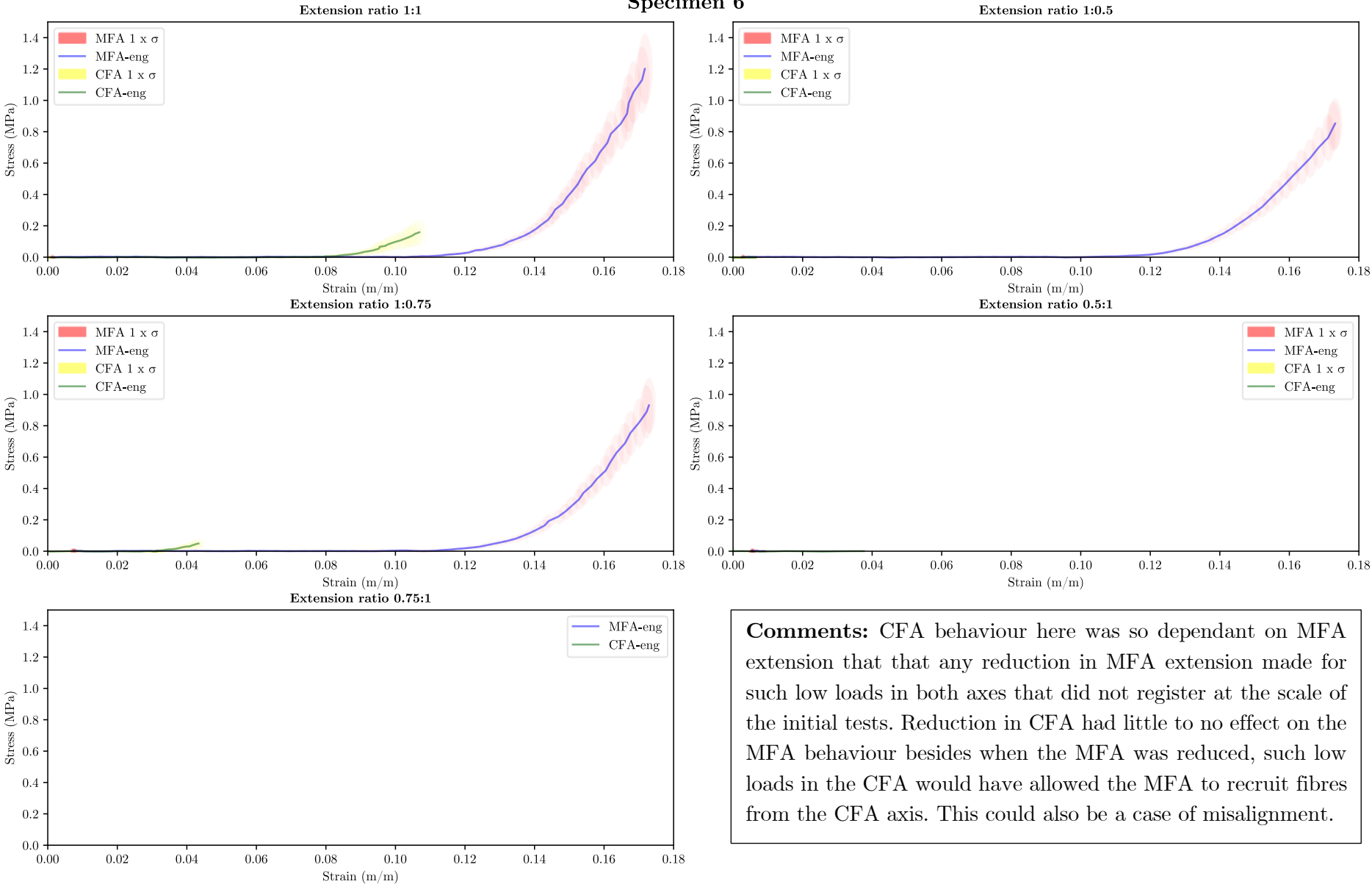
Specimen 4



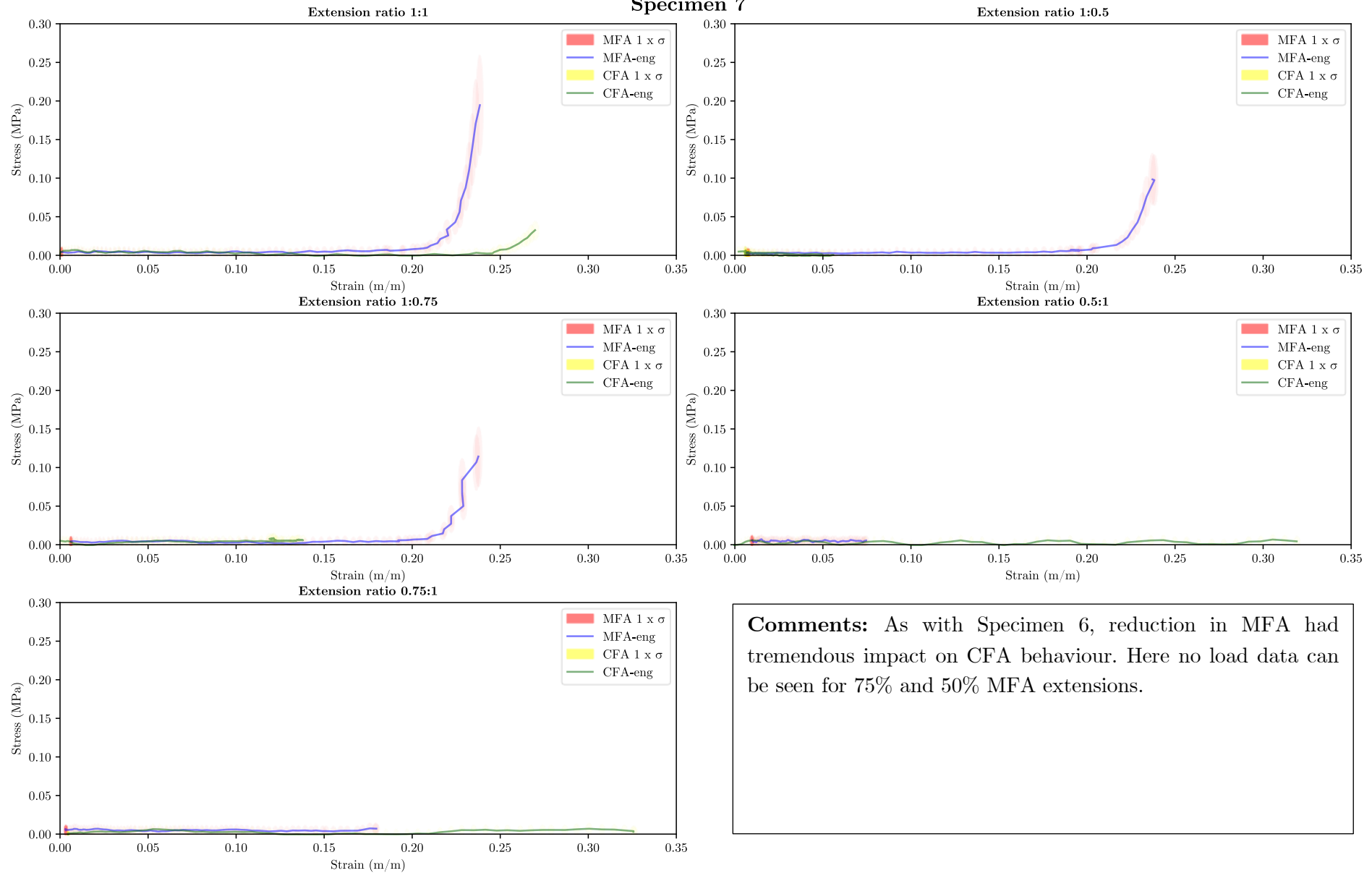
Specimen 5



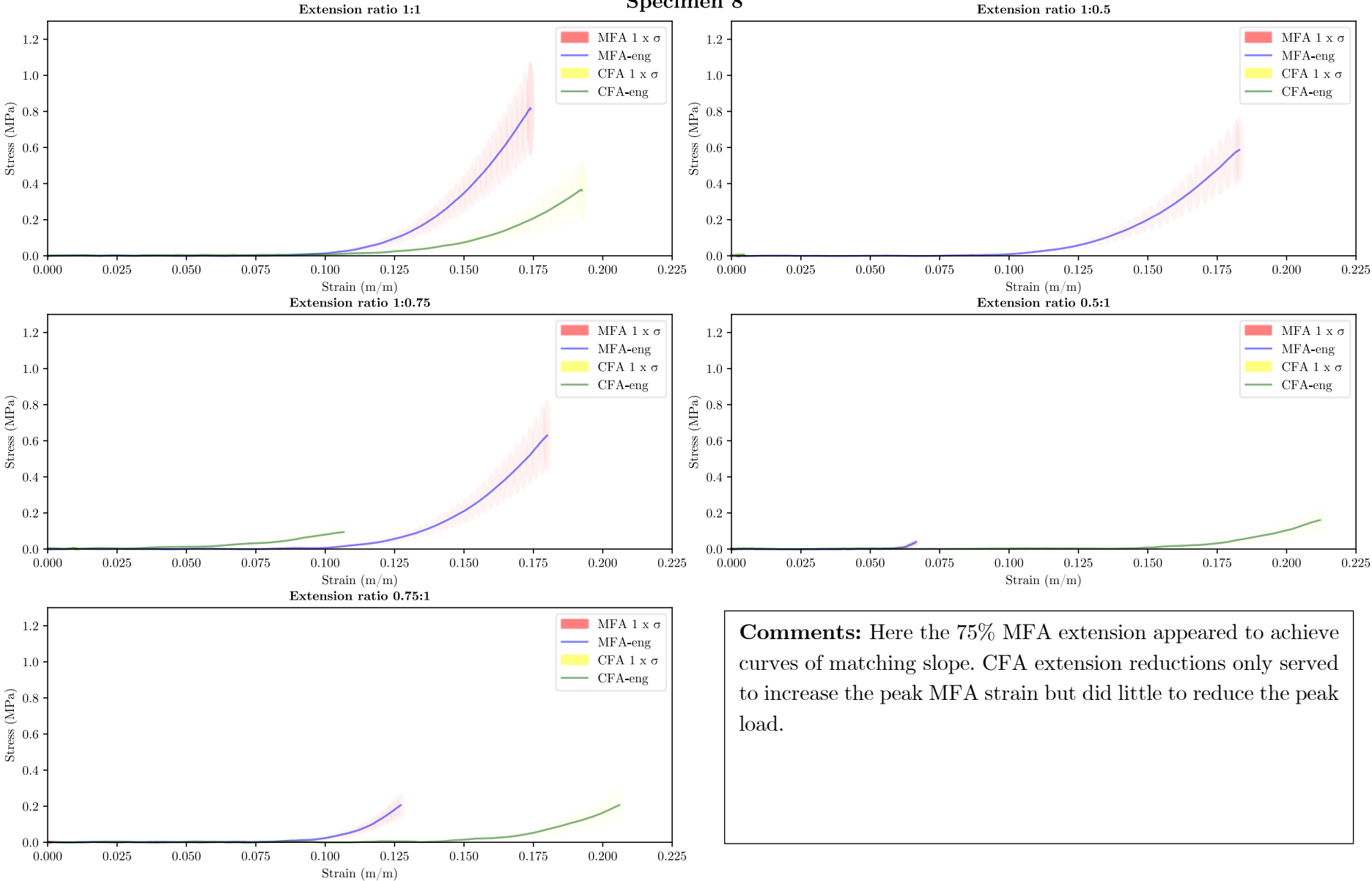
Specimen 6



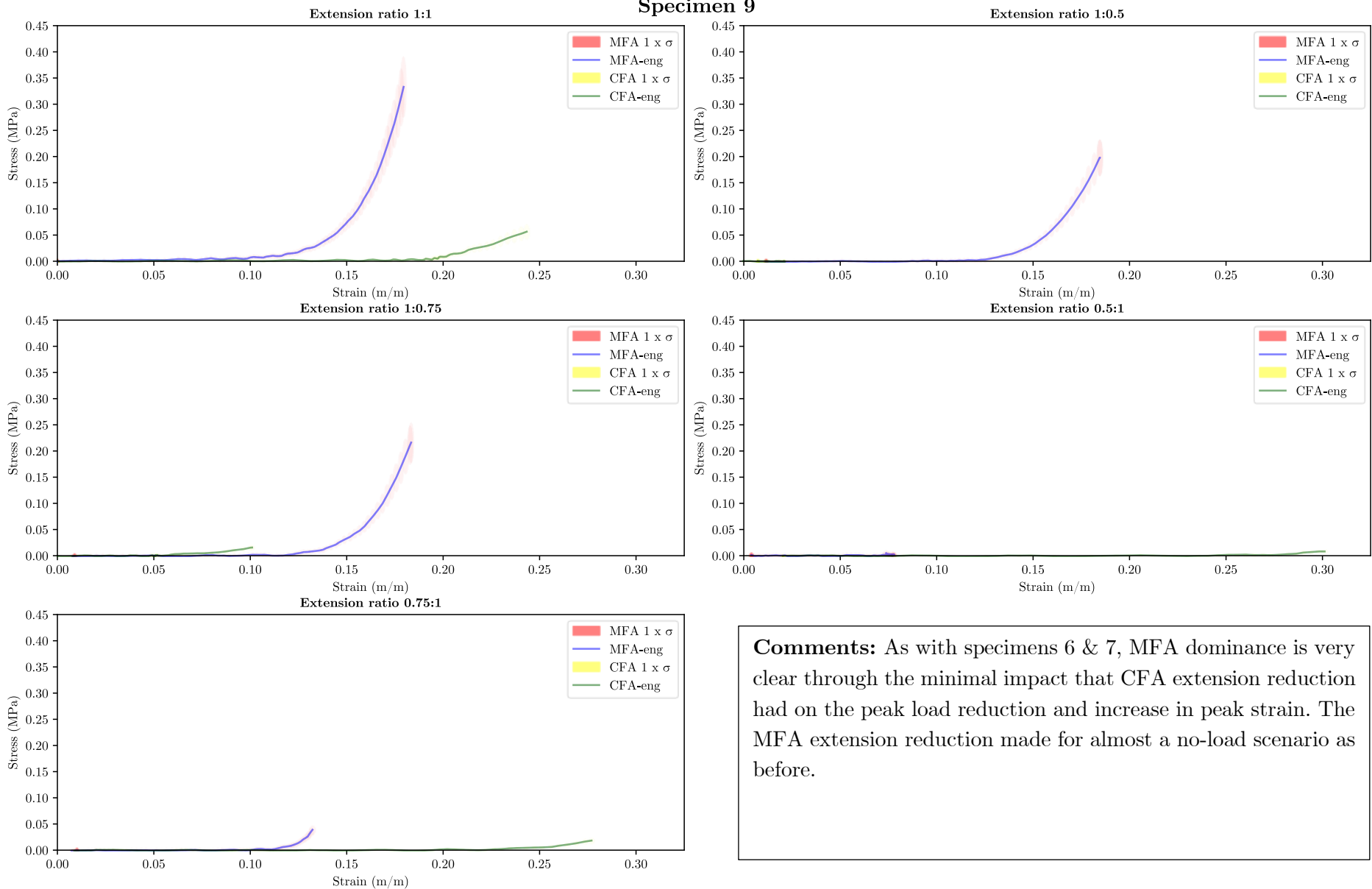
Specimen 7



Specimen 8

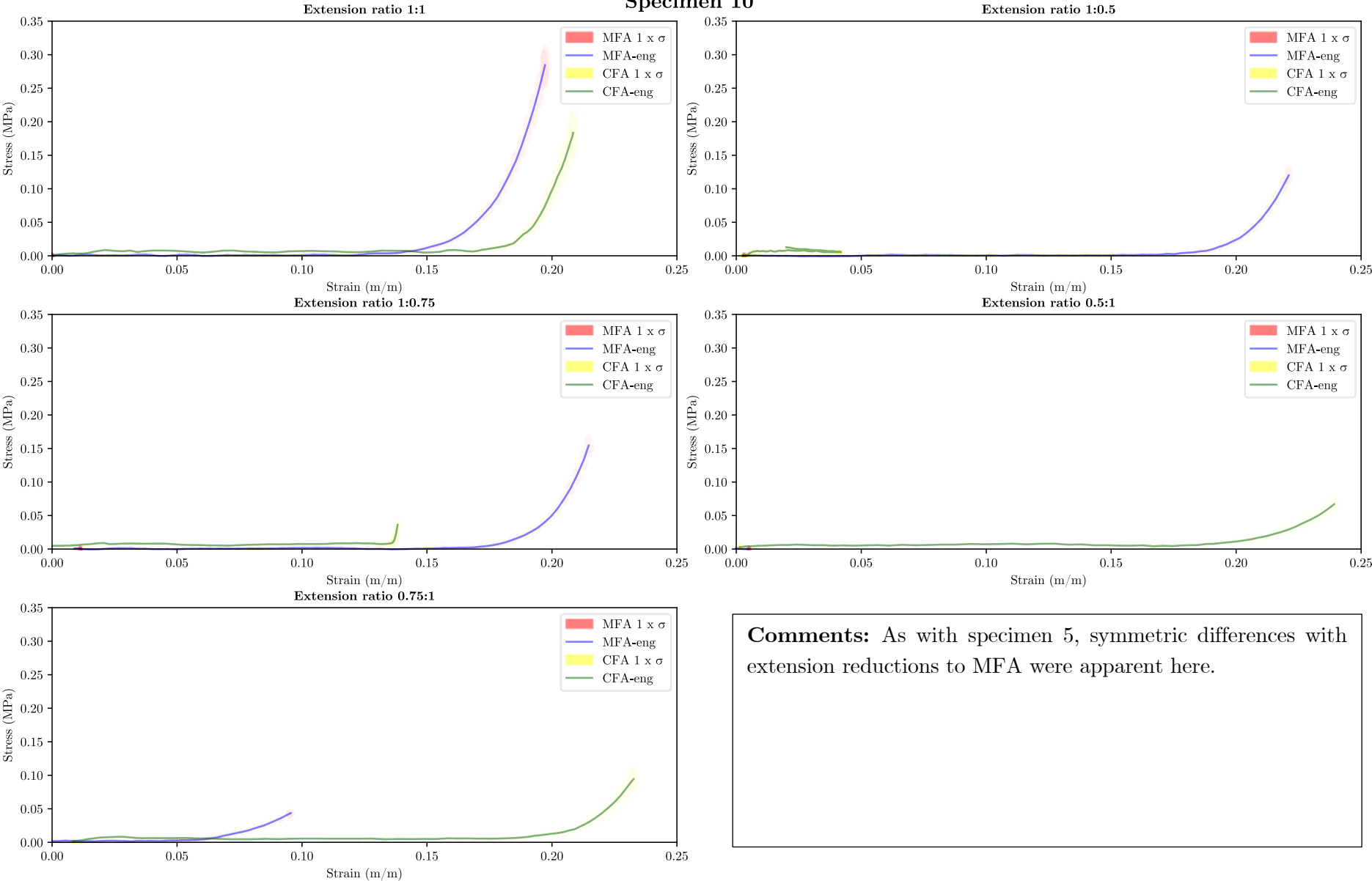


Specimen 9

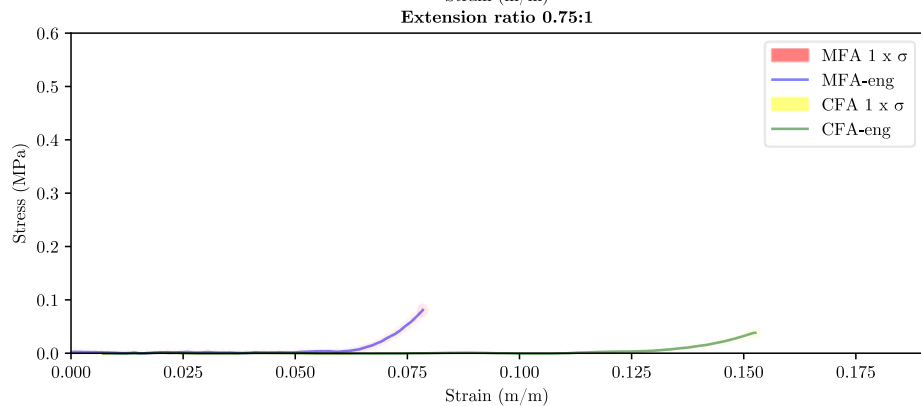
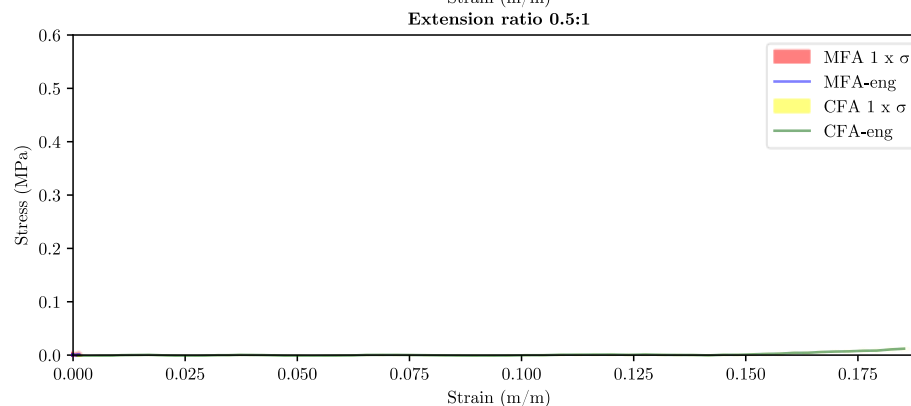
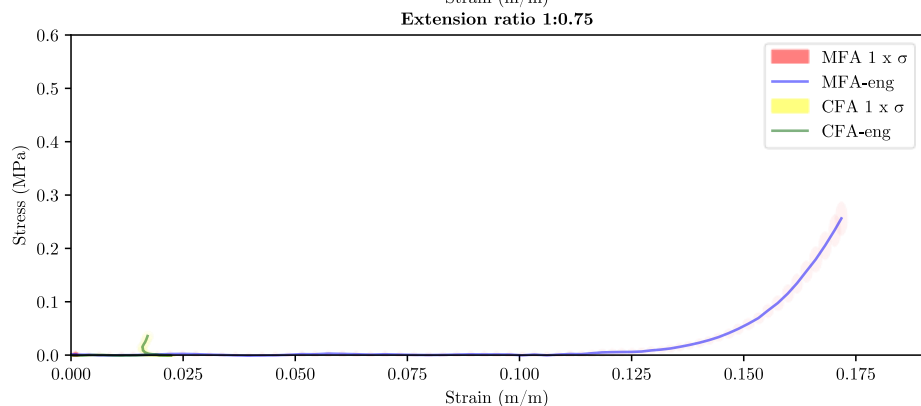
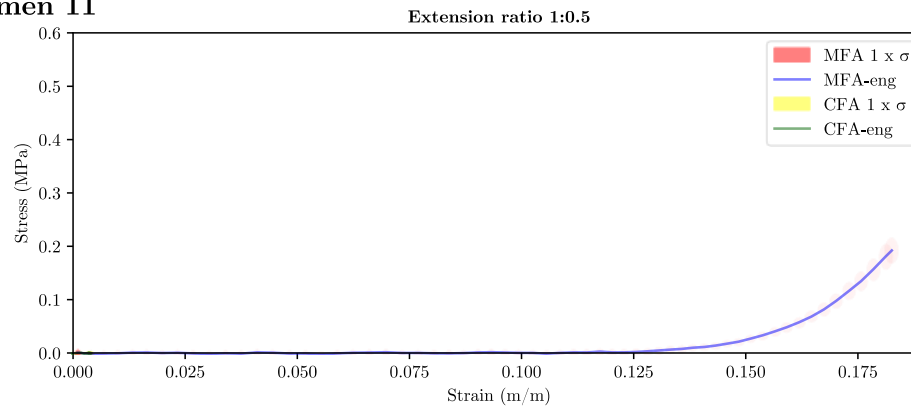
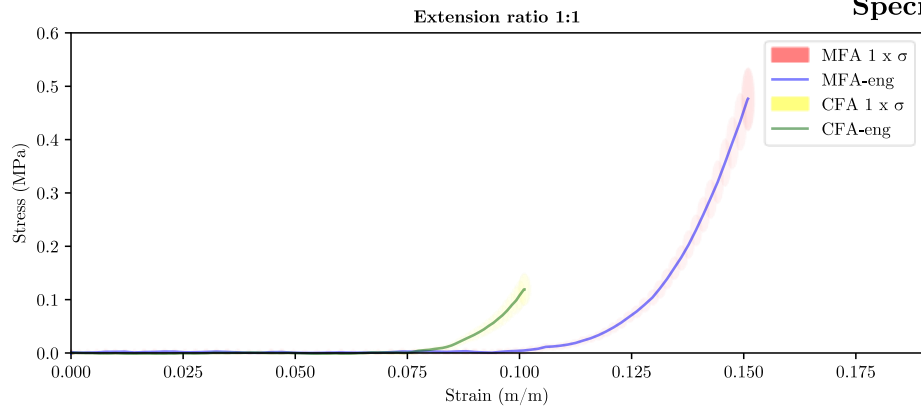


Comments: As with specimens 6 & 7, MFA dominance is very clear through the minimal impact that CFA extension reduction had on the peak load reduction and increase in peak strain. The MFA extension reduction made for almost a no-load scenario as before.

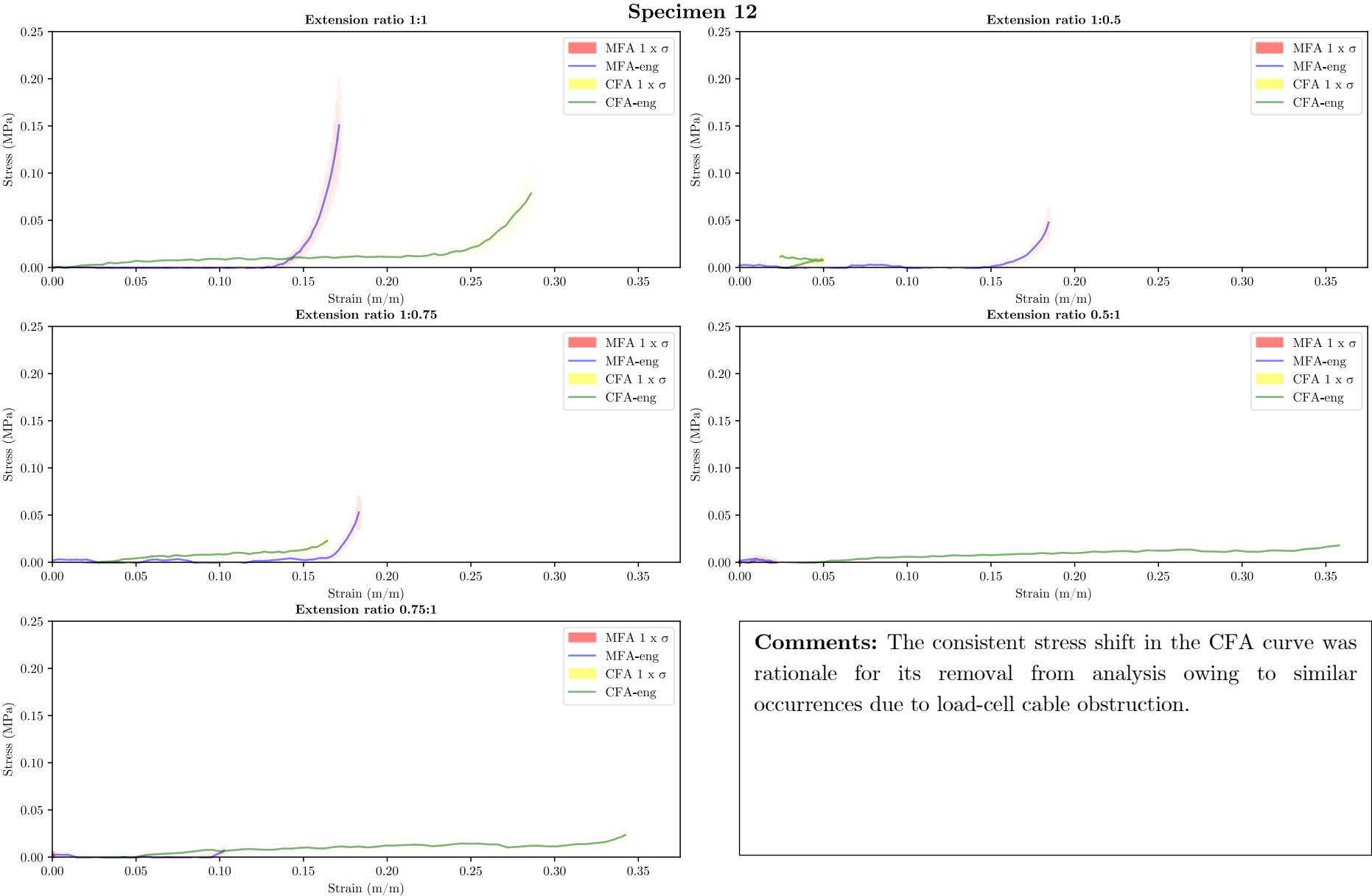
Specimen 10



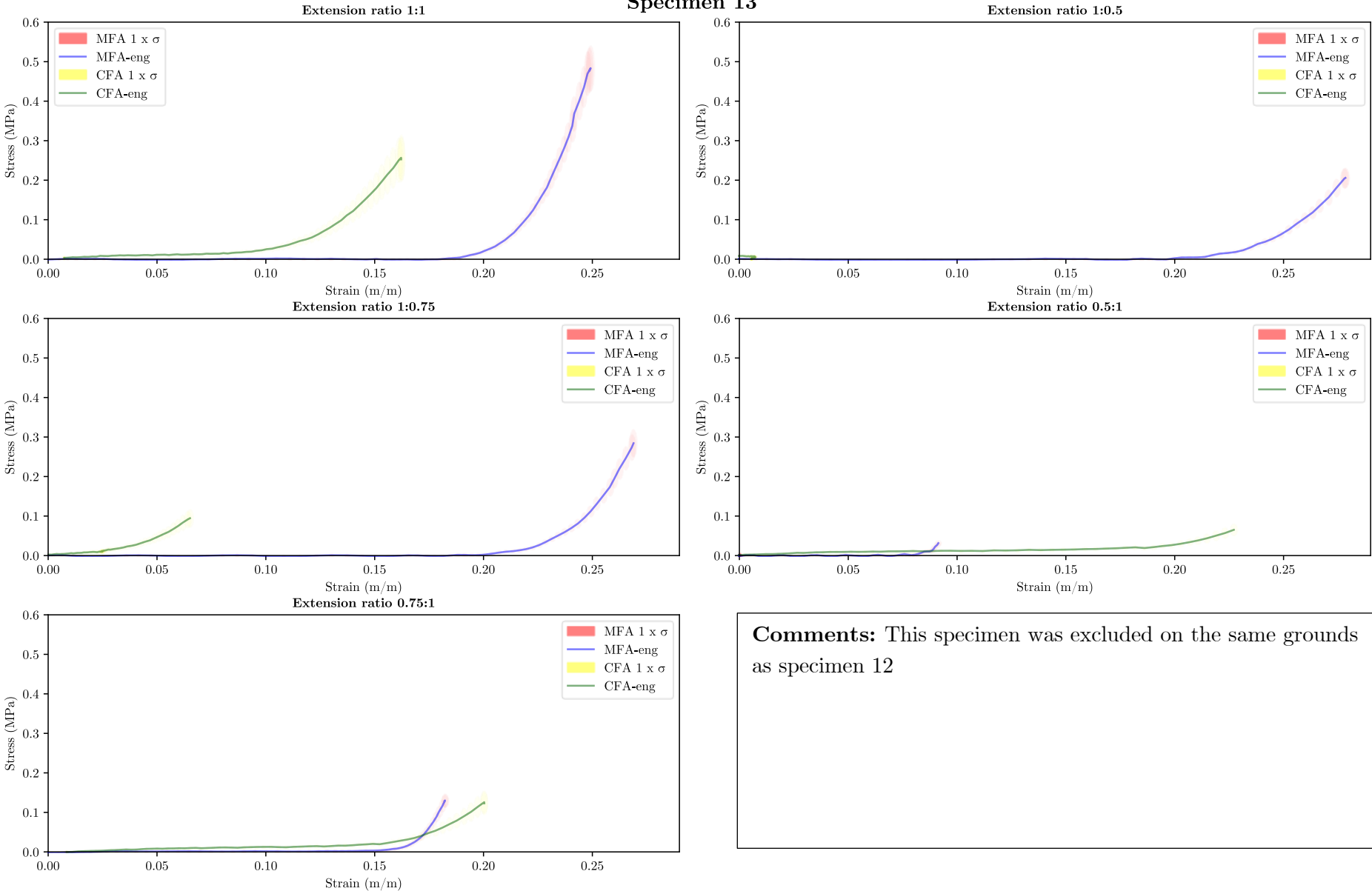
Specimen 11



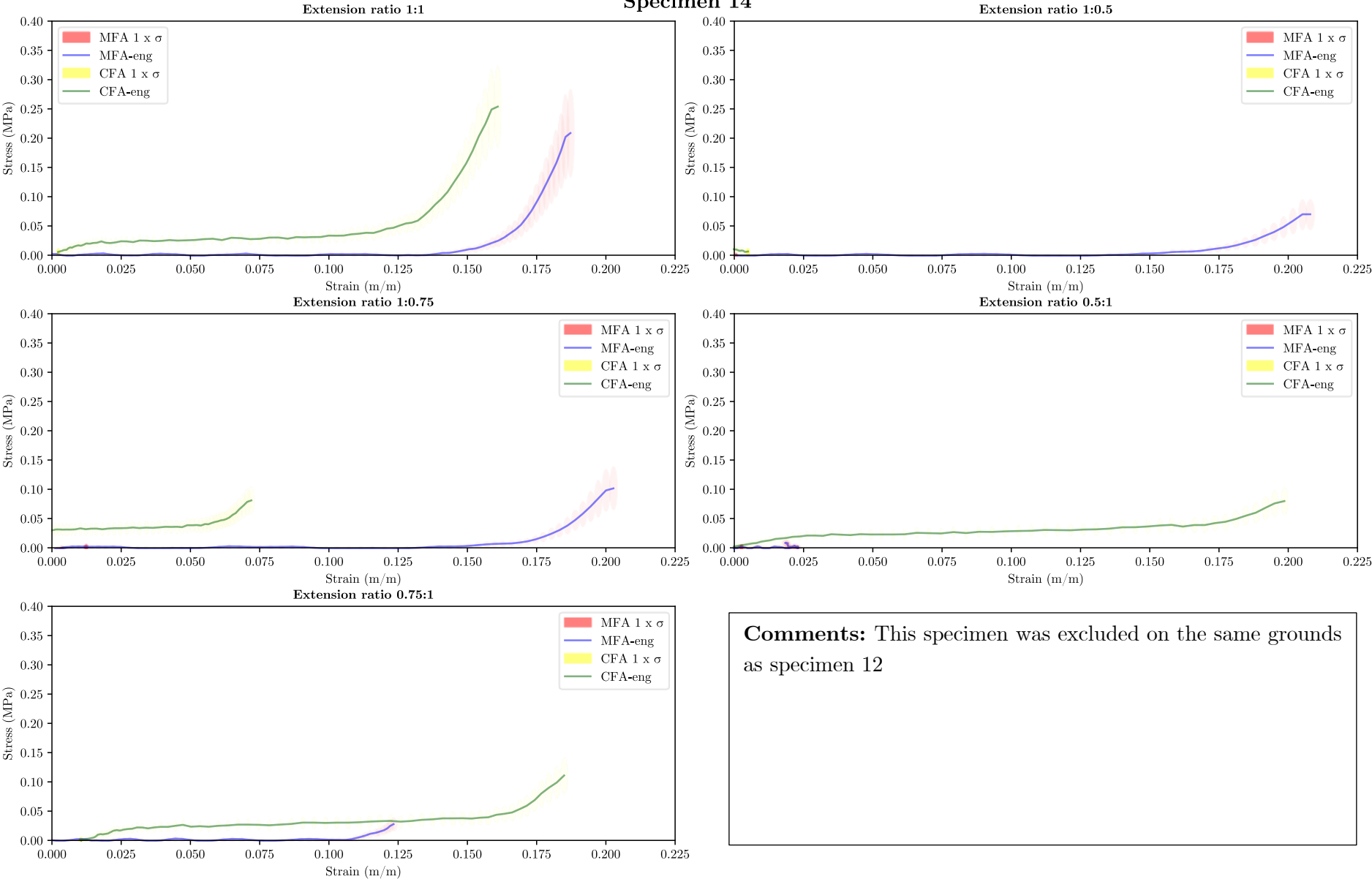
Comments: Asymmetric coupling evident through the near no load in the reduced MFA extension tests.



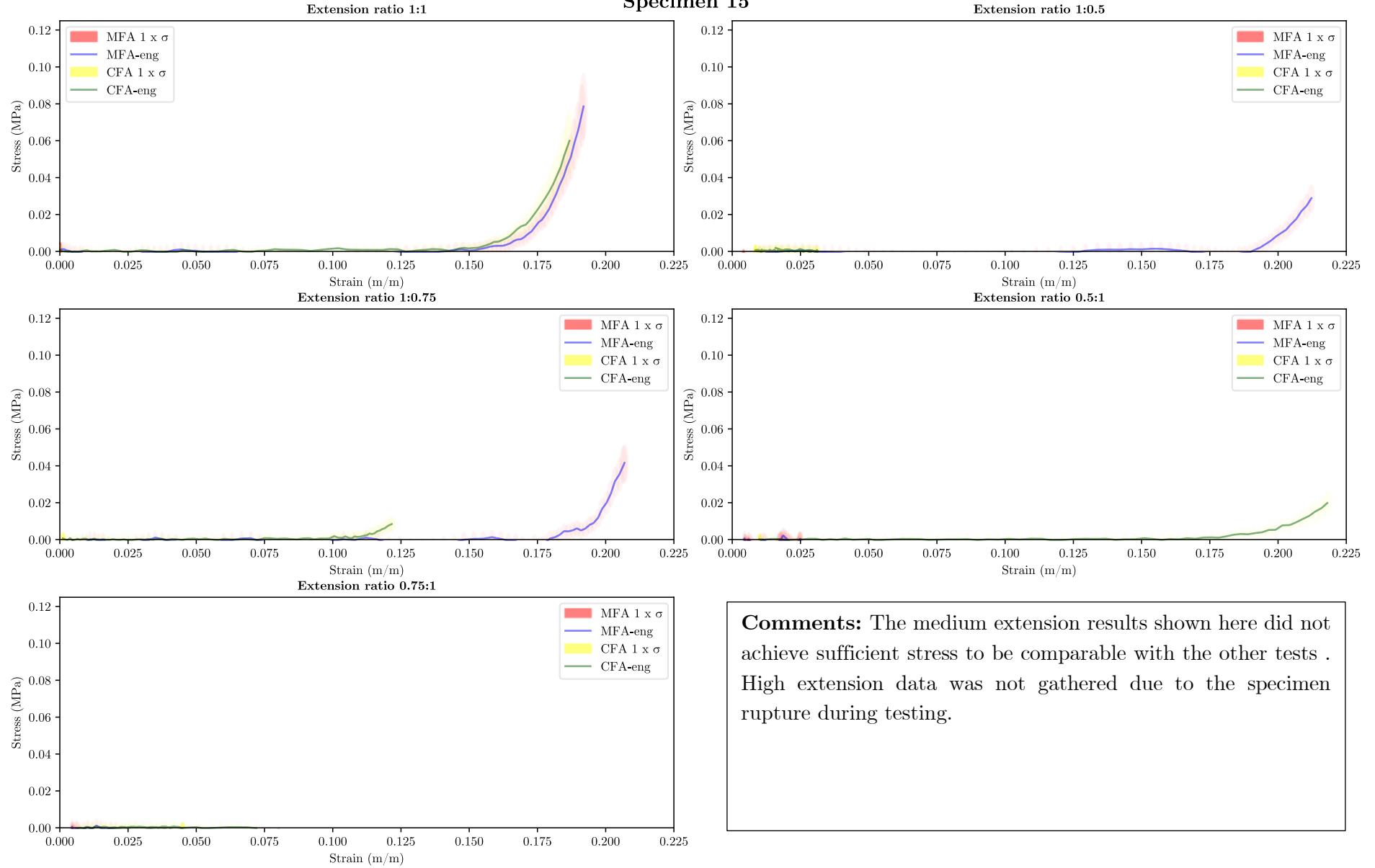
Specimen 13



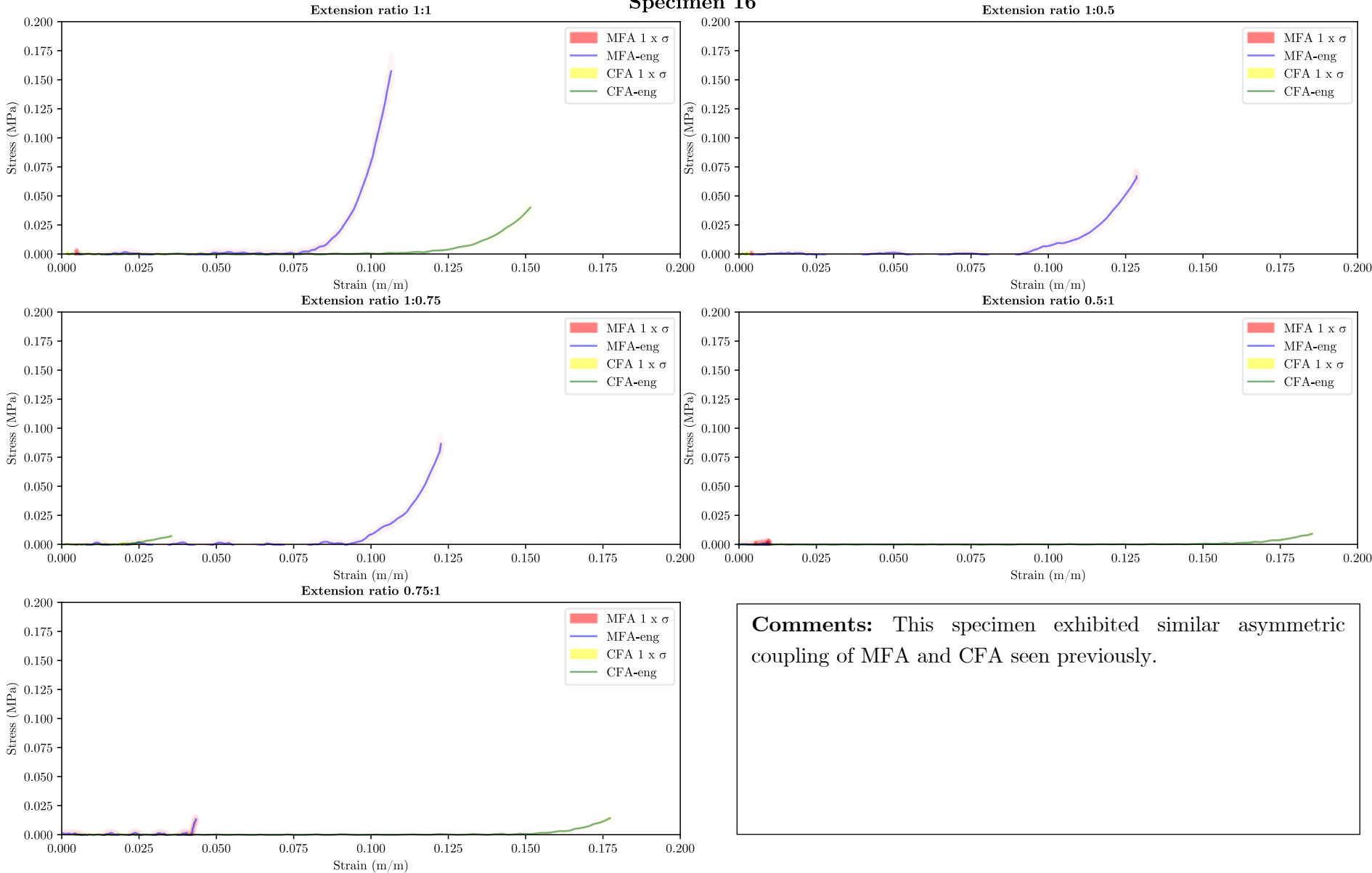
Specimen 14



Specimen 15



Specimen 16



B.6 Excluded Curve Fits

Specimens 3,12,13,14 *and* 15 that were excluded from the study due to various load measurement aberrations or displacement discontinuities are shown below.

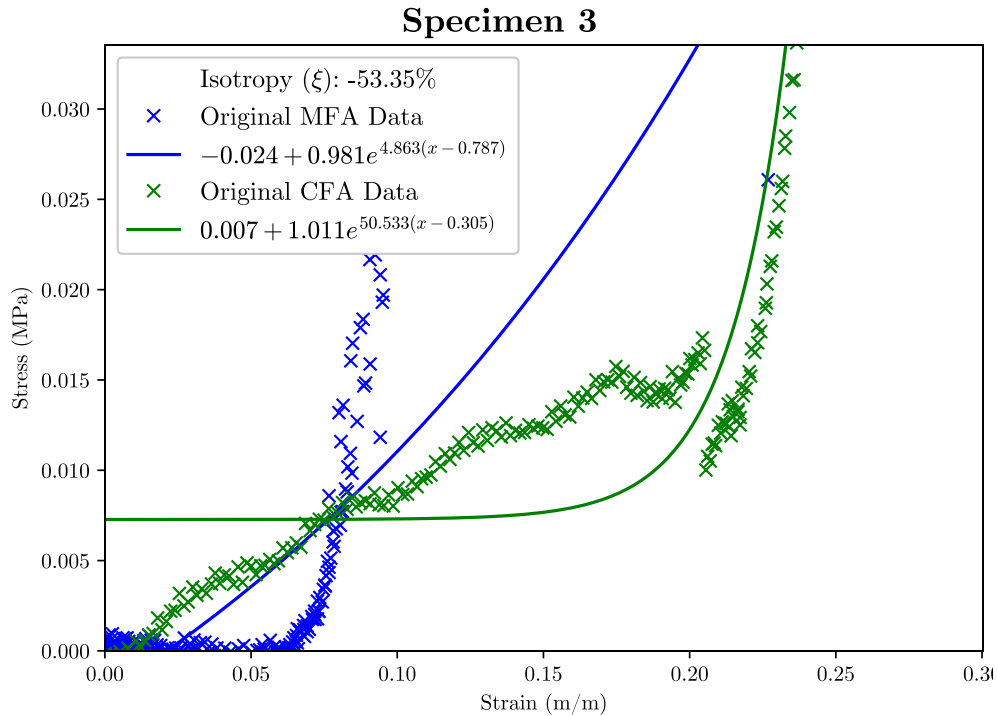


Figure B.6.11: *Specimen 3 excluded on the grounds of load discontinuity.*

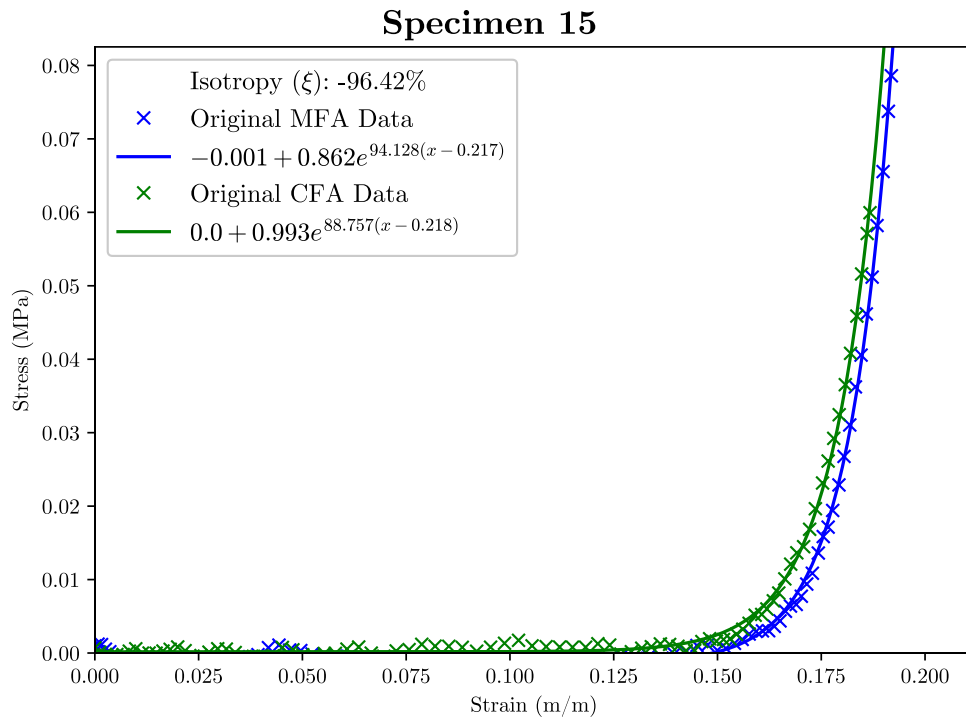


Figure B.6.12: *Specimen 15 excluded on the grounds of low load as the specimen ruptured at high extension.*

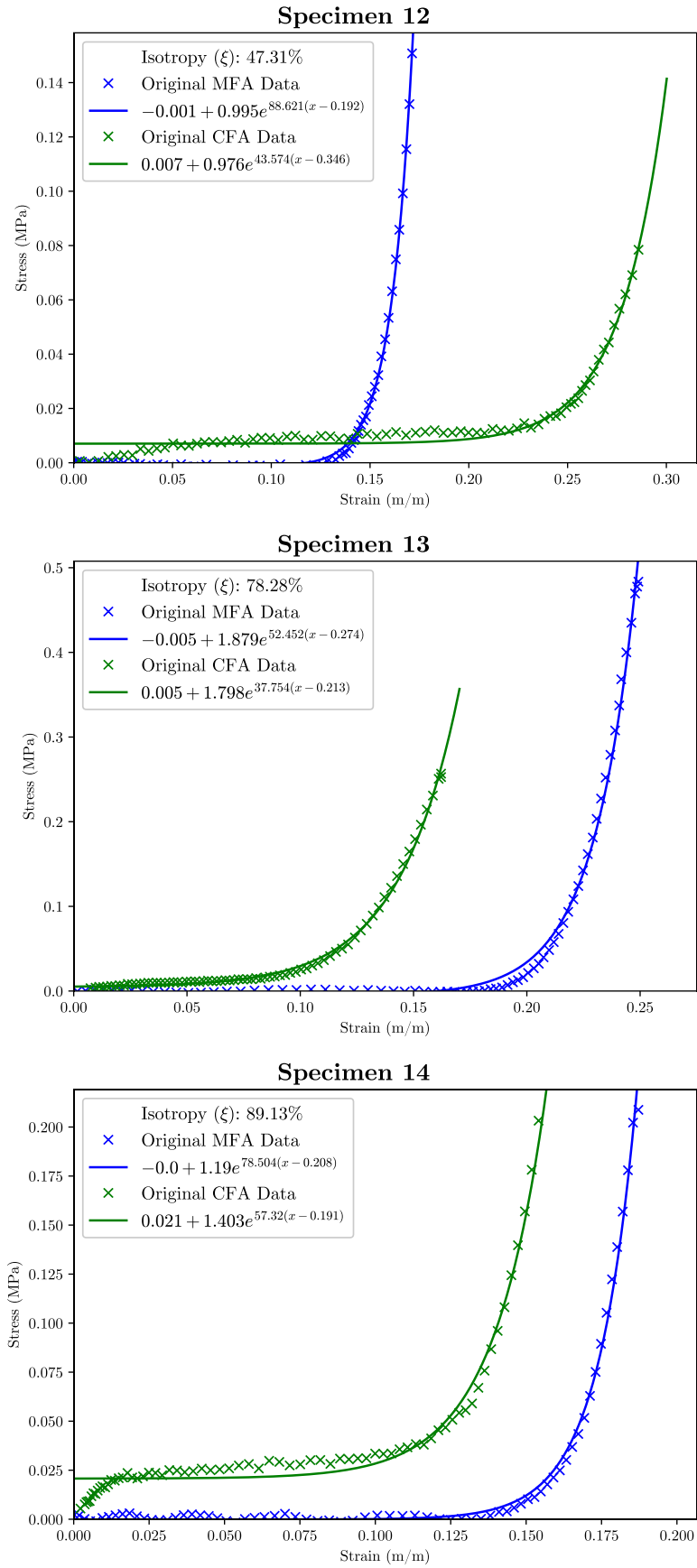


Figure B.6.13: *Specimen 12,13,14 excluded on the grounds of load noise from a snagged load-cell cable.*

B.7 Uncertainty Budgeting

The uncertainty of most measured values and their impacts on calculated values has been summarised in the following tables. This shows the sources of error and items of the methodology to target for improvement should a higher data quality be required.

Table B.7.9: *Uncertainty budget with typical BTR DIC values for different facet sizes*

UNCERTAINTY COMPONENTS	VALUE	UNIT
15 px Positional Error	2.2	mm

Table B.7.10: *Uncertainty budget with typical PBT DIC values for different facet sizes*

UNCERTAINTY COMPONENTS	VALUE	UNIT
15 px Positional Error	3.863	μm
15 px Strain Error	0.018	m/m
59 px Positional Error	1.078	μm
59 px Strain Error	0.003	m/m

Table B.7.11: *Uncertainty budget for a typical PBT specimen width measurement*

UNCERTAINTY COMPONENTS	VALUE	UNIT
Calibration Repeatability	40	μm
Vernier Calliper Resolution	20	μm
ImageJ Resolution	100	μm

Table B.7.12: *Specimen eight uncertainty budget for PBT specimen thickness*

UNCERTAINTY COMPONENTS	MFA VALUE	CFA VALUE	UNIT
ThicknessTool Repeatability	66.5	46.7	μm
ImageJ Resolution	14.9	14.9	μm

Table B.7.13: *Uncertainty budget for PBT load measurement*

UNCERTAINTY COMPONENTS	VALUE	UNIT
Loadcell Repeatability	0.01	N
ClipX Accuracy	0.005	N

Appendix C:

Drawings and Design

C.1 Clamping Assembly

C.1.1 *Gasket*

The gasket served to seal the MT between the cover plate and the backing plate as well as to grip the specimen and prevent slippage. Appropriate gasket thickness and recess design was key to achieving this without causing damage to the specimen. Assembly was as per Figure C.1.14.

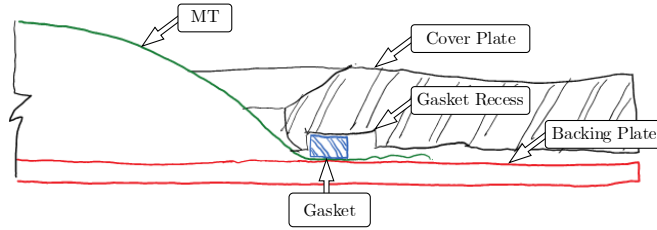


Figure C.1.14: *Gasket assembly*

The gasket deformation was simplified to the model in Figure C.1.15.

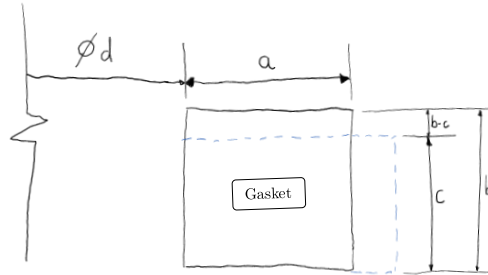


Figure C.1.15: *Simplified gasket deformation*

Once clamped, the clamp force would deform the gasket as per:

$$\delta = b - c$$

This was converted to a strain using:

$$\epsilon = \frac{b - c}{b}$$

Resulting stress was calculated using $\sigma = E\epsilon$ where stiffness was calculated using Shore hardness A f as follows:

$$E = e^{0.0235(f+50)-0.6403}$$

Given a shore A hardness of $f = 60$, we can compute $E = 2.159 \text{ MPa}$.

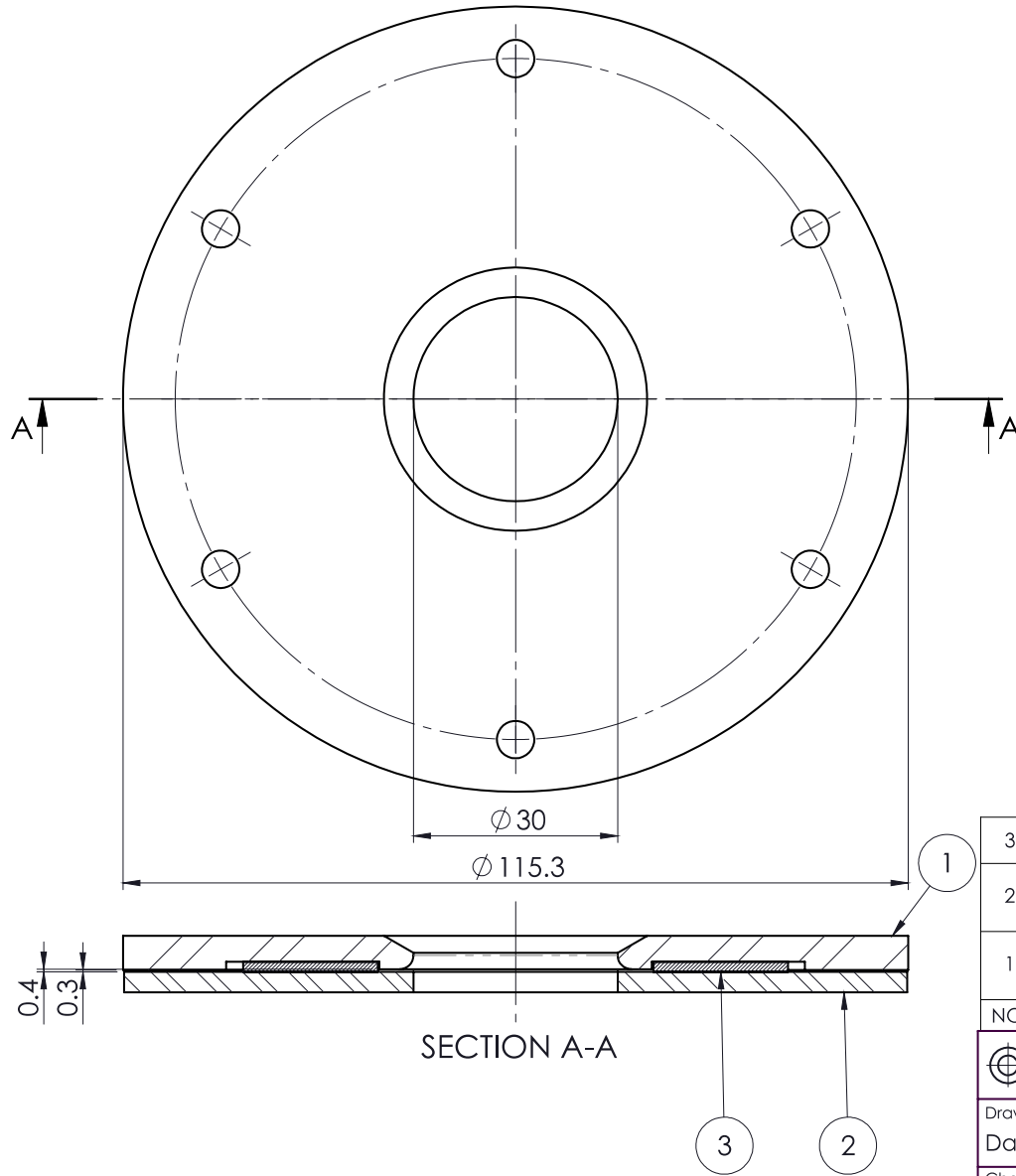
The total area of the gasket compressing the MT was given by:


$$Area = \frac{\pi}{4} ((d + a)^2 - d^2)$$

We will assume values of a and d based on the upper clamping plate limitations for the aperture used in the study. The width of the gasket was kept above 15 mm to improve sealing characteristics. Calculations were similar for other apertures. Thus, area was calculated to be $Area = 1563 \text{ mm}^2$ Given a typical failure stress of $UTS = 15 \text{ MPa}$ for natural sausage casing [66], it was ensured that clamp stresses would never get close to this value.

Available gasket material was in 1.5 mm thickness, this led to the selection of a $\delta = 0.3 \text{ mm}$ clearance/clamping displacement that resulted in a clamp stress of $\sigma_{clamp} = 0.43 \text{ MPa}$ and a distributed bolt force of 675 N . These were deemed to be safe values that would not damage the tissue. The gasket recess was also sized using a clearance on the compressed geometry determined by the Poisson's ratio of the gasket material.

Note that the above procedure was followed for all gasket sizes shown in the drawing overleaf, each was made to match the recess on a specific cover plate.



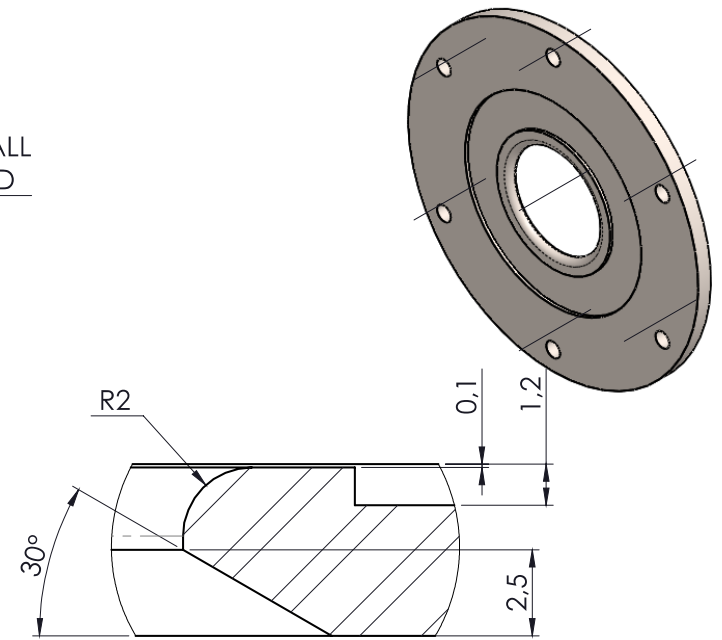
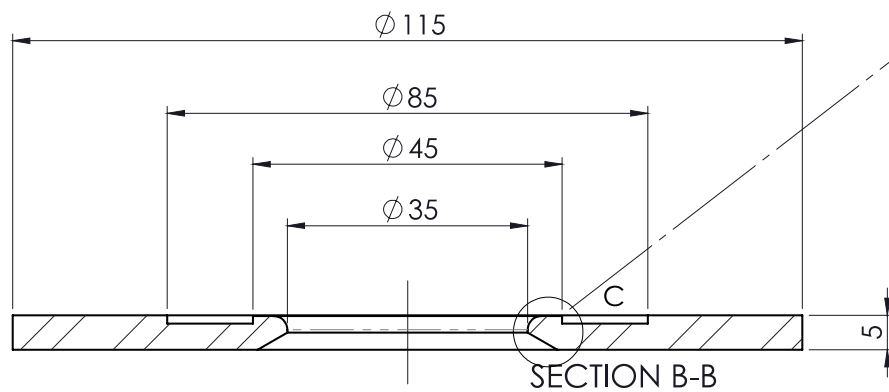
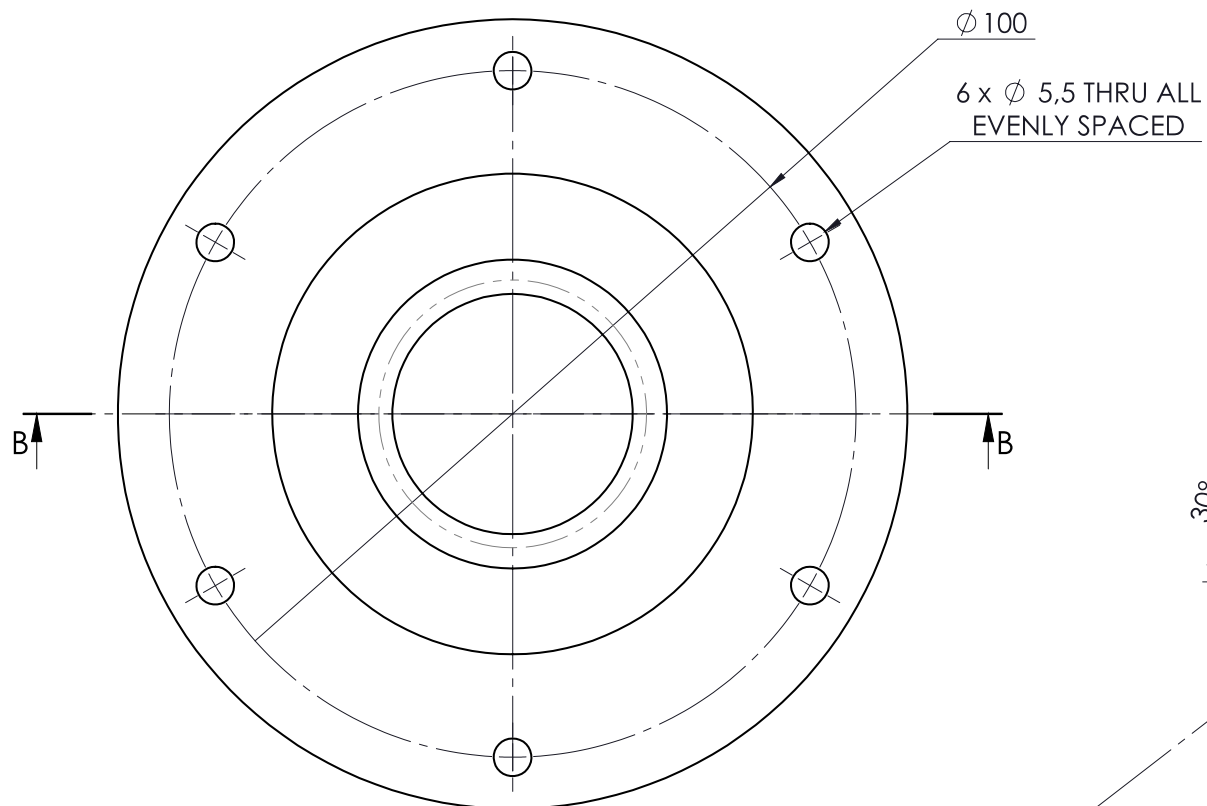
3	008SP_0303_20_PNSDAN002	35 mm Aperture Gasket	See DWG for details, Nat. Rubber	1
2	049SP_0225_21_PNSDAN002	35 mm Base Plate	See DWG for details, SS	1
1	010SP_0305_19_PNSDAN002	35 mm aperture top cover	See DWG for details, SS	1
NO.	PART NUMBER	DESCRIPTION	SPECIFICATION	QTY
 Scale: 1:1 on A4		University of Cape Town Department of Mechanical Engineering		
Drawn By: Daniel Pons		All un-toleranced dimensions to adhere to ISO 2768-m	Title: Gasket Clamp Assembly	
Checked :		Assembly Drawing	Drawing Number :	Rev. : A
				Sheet : 1 of 1

C.1.2 Cover Plate and Base Plate

The cover plate was made with a recess that could accommodate the gasket when deformed and it was sized to allow the gasket material to deform. The sides of the gasket ensured a flat surface to limit the clamp force applied to the MT. The lip of the clamp had a **100 μm** clearance to allow for material thickness. Lastly the edges of the clamp lip were radiused to reduce stress concentrations. The cover plate was based on a design by Curry, however the **35 mm** plate and other sizes tried were not made by him [4].

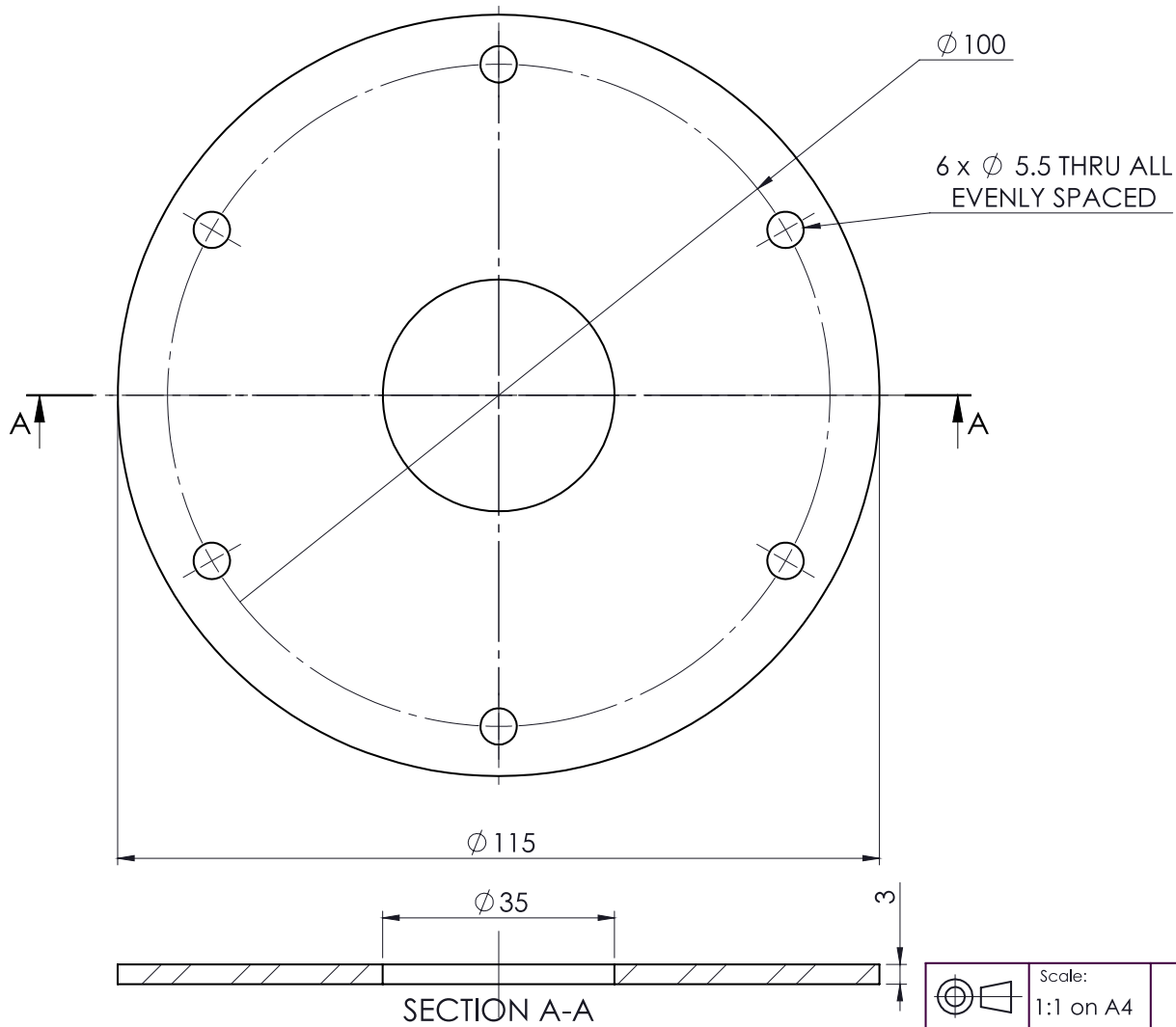
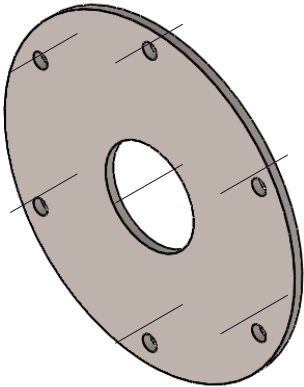
The drawing to follow was for the cover plate was used in testing, others were made, however the **35 mm** proved to be best for the size of SIS we had available. Please refer to C.1.1 for perspective on its assembly relative to the gasket and base plate.

The Base Plate is shown here as well, it was made to match the cover plate.



DETAIL C
SCALE 5 : 1

	Scale: 1:1 on A4	University of Cape Town Department of Mechanical Engineering			
Drawn By: Daniel Pons	All un-toleranced dimensions to adhere to ISO 2768-m	Title: COVER PLATE			
Checked :	Material : AISI 316 Stainless Steel Sheet (SS)	Drawing Number : 050SP_0225_21_PNS DAN002	Rev. : A	Sheet : 1 of 1	



QTY: 1
BREAK ALL SHARP EDGES

	Scale: 1:1 on A4	University of Cape Town Department of Mechanical Engineering		
	Drawn By: Daniel Pons	All un-toleranced dimensions to adhere to ISO 2768-m	Title: Base plate	
Checked :	Material : AISI 316 Stainless Steel Sheet (SS)	Drawing Number : 049SP_0225_21_PNSD AN002	Rev. : A	Sheet : 1 of 1

C.2 Pressure Chamber Stand

The pressure chamber stand was an adaptation of the stand built by Curry [4]. Curry's FDM approach was not suitable for the bending stresses imposed at the base of the arms when tightening the clamping assembly. This resulted in its failure during operation. A new stand was built that could withstand the loads.

Super wood was chosen due to its favourable material properties and ease of local laser cutting. The assembly was painted with multiple layers of paint to prevent moisture ingress.

Due to tolerancing issues, one of the arms was weakened by a failure of the protruding tongue insert (pictured in Figure C.2.16). This did not result in catastrophic failure due to redundancy incorporated in the design of the interlocking rings.

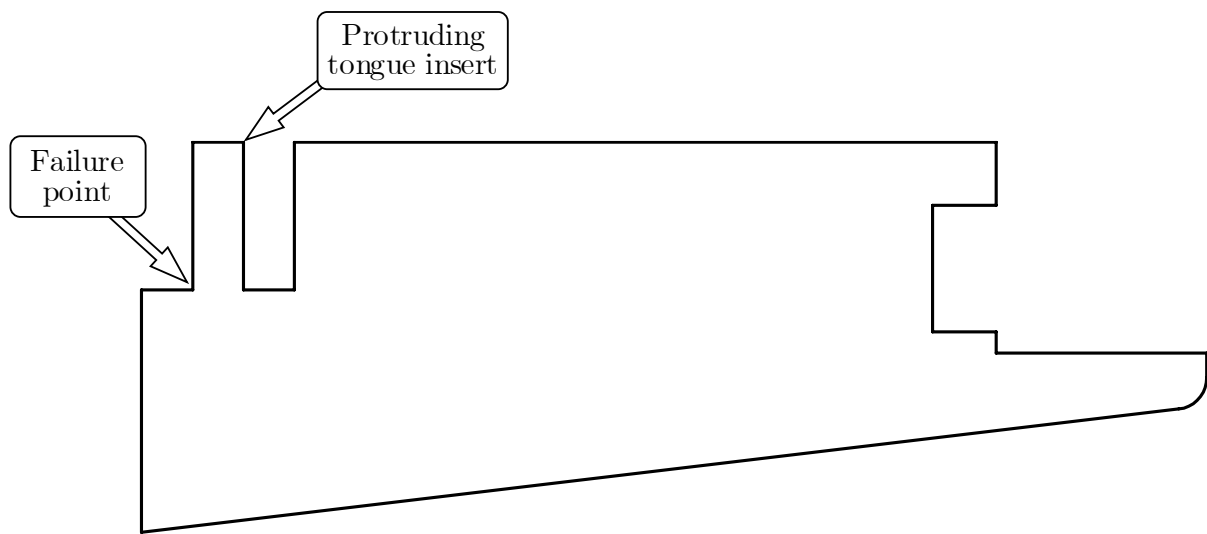
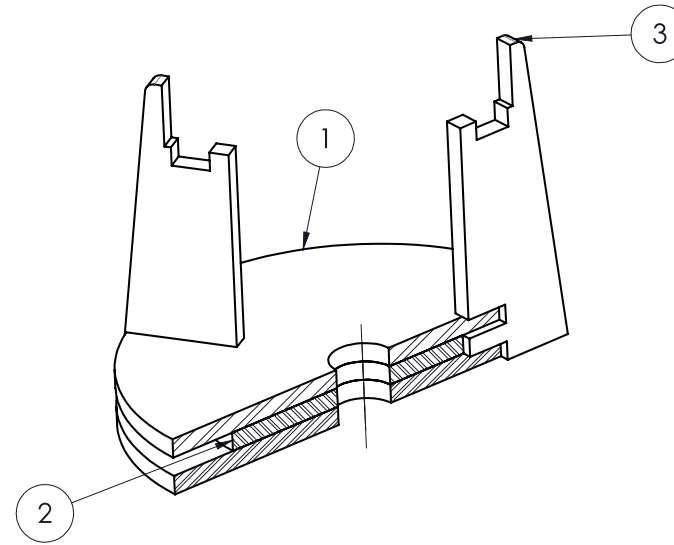
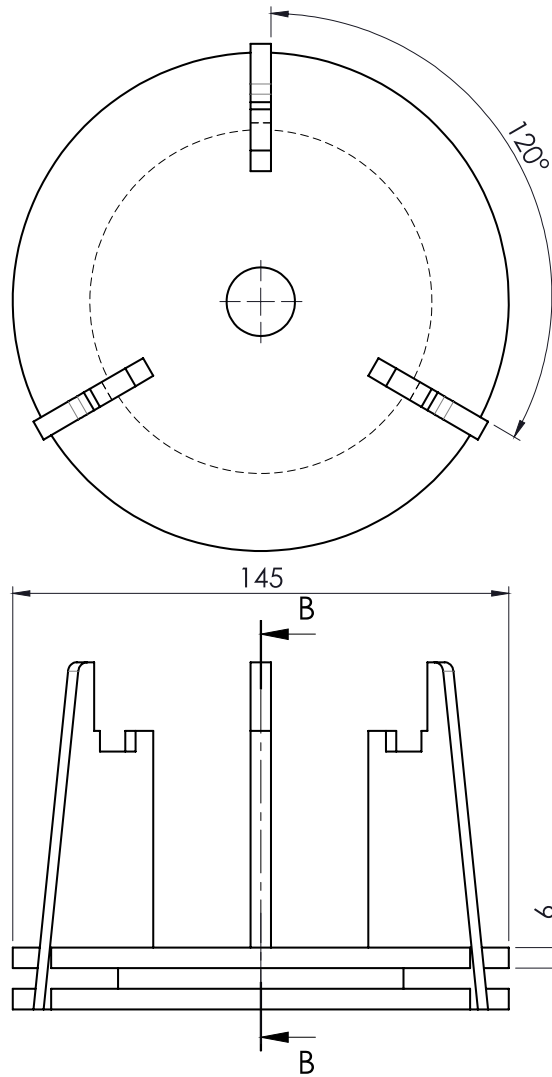



Figure C.2.16: *Failed point of pressure chamber stand arm*

Drawings of the complete assembly and cut drawings are shown overleaf.



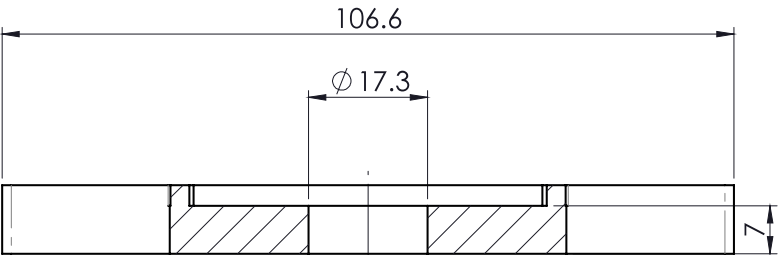
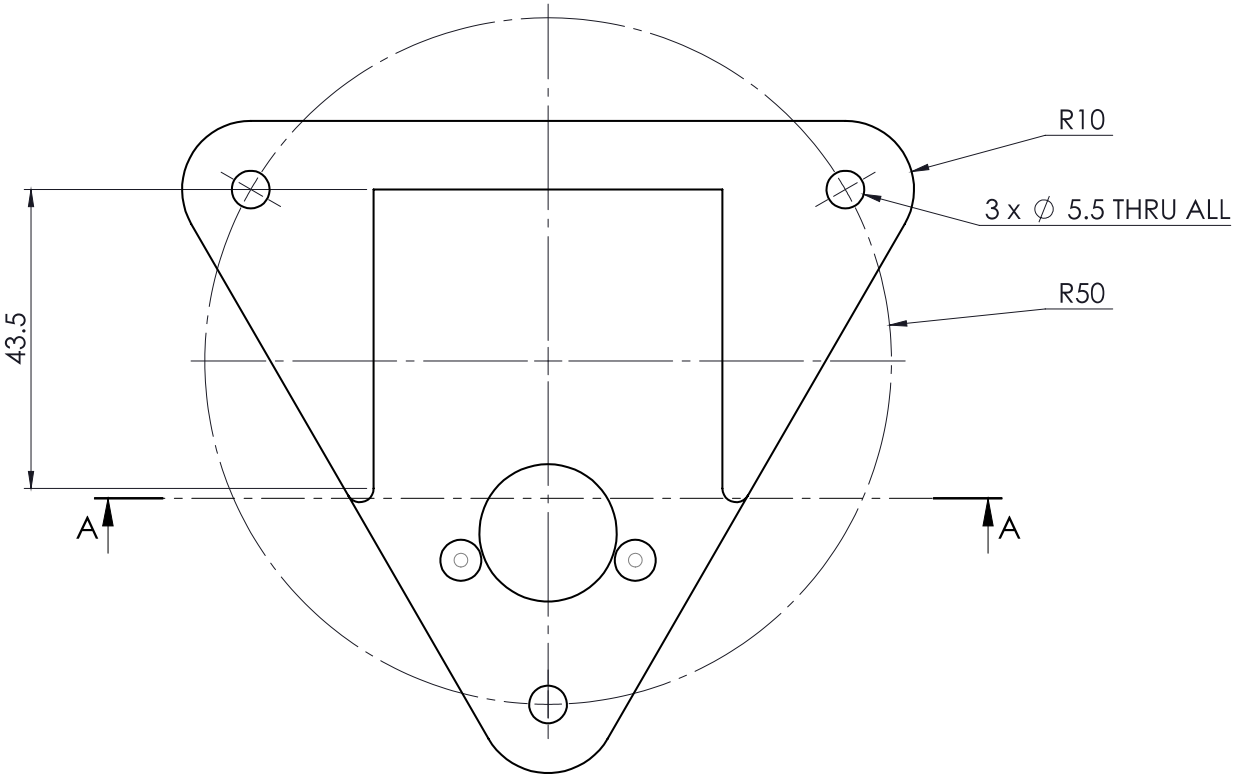
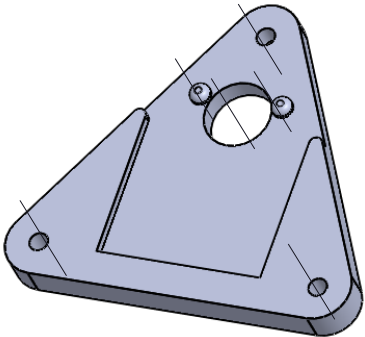
SECTION B-B

3	023SP_0915_20_PNSDAN002	Side Support	Super Wood	3
2	021SP_0915_20_PNSDAN002	Stand Spacer	Super Wood	1
1	022SP_0915_20_PNSDAN002	Stand Base	Super Wood	2
NO.	PART NUMBER	DESCRIPTION	SPECIFICATION	QTY
		Scale: 1:2 on A4	University of Cape Town Department of Mechanical Engineering	
Drawn By: Daniel Pons		All un-toleranced dimensions to adhere to ISO 2768-m	Title: Pressure Chamber Stand	
Checked :		Assembly Drawing	Drawing Number : 024SP_0915_20_PNSDAN002	Rev. : B
			Sheet : 1 of 1	


C.3 Calibration Target Guide

The tool used to align the DIC coordinate axes was designed to fit the DIC calibration target supplied by DANTEC Dynamics. This tool was FDM manufactured in polylactic acid (PLA).

The drawing is shown overleaf.



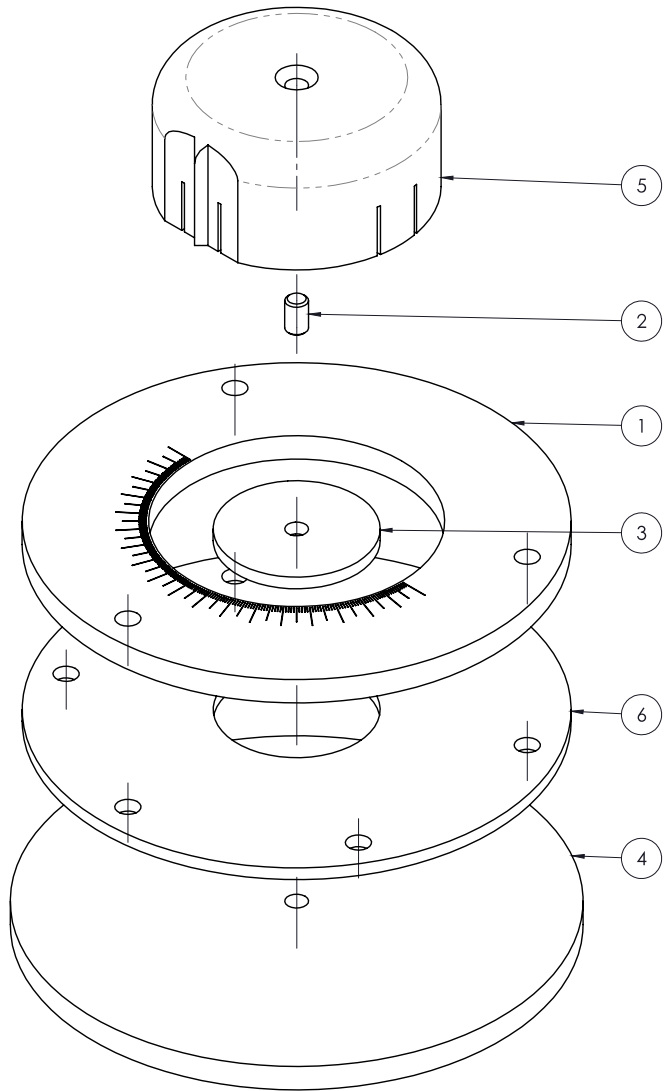
SECTION A-A


	Scale: 1:1 on A4	University of Cape Town Department of Mechanical Engineering			
	Drawn By: Daniel Pons	All un-toleranced dimensions to adhere to ISO 2768-m	Title: CALIBRATION TARGET GUIDE		
Checked :	Material : PLA	Drawing Number : 032SP_1116_20_PNSDAN002	Rev. : A	Sheet : 1 of 1	

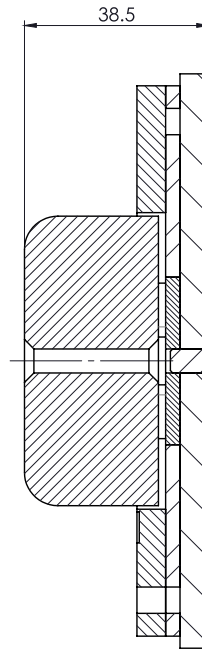
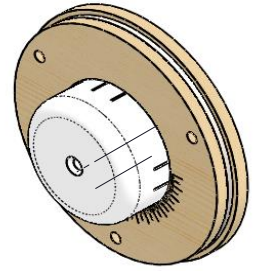
C.4 Goniometric Cutting Jig

C.4.1 Full Cutting Jig Assembly

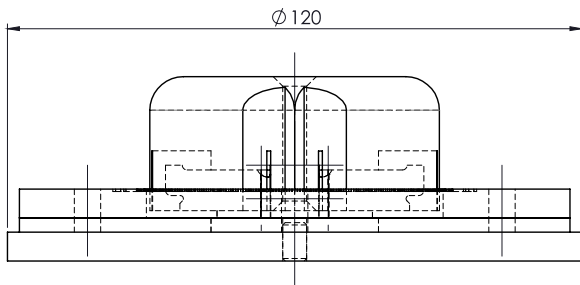
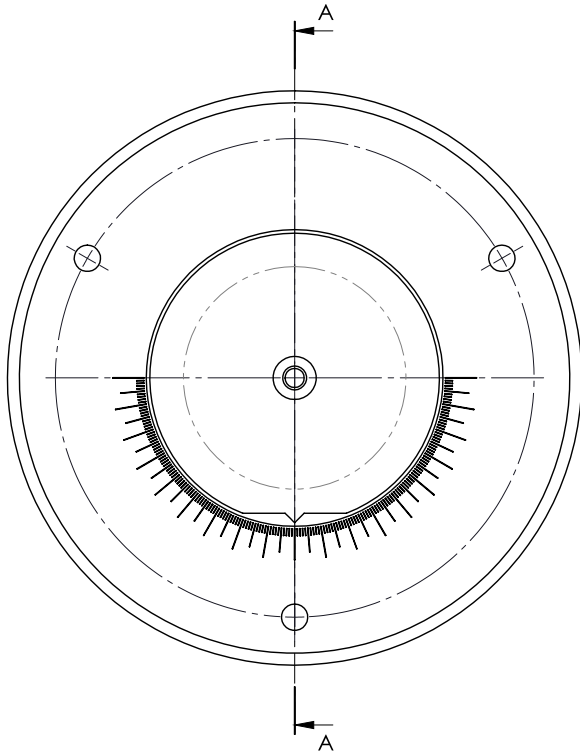
The following drawing shows the assembly of the cutting jig used to excise a cruciform specimen at the MFA angle. The guiding components were all made using laser cutting methods.



6	049SP_0225_21_PNSDAN002	35 mm Base Plate	See DWG for details, SS	1
5	058PB_0219_22_PNSDAN002	Cruciform Cutter Assembly	See DWG for details	1
4	035PB_1116_20_PNSDAN002	Cutting Base	See DWG for details, MDF	1
3	034PB_1116_20_PNSDAN002	Disposable Cutting Surface	See DWG for details, HDPE	1
2	037PB_1116_20_PNSDAN002	Dowel	See DWG for details, Pine	1
1	033PB_1116_20_PNSDAN002	Cutting Guide	See DWG for details, MDF	1
NO.	PART NUMBER	DESCRIPTION	SPECIFICATION	QTY.
<div><div><div>Scale: 1:1 on A3</div></div><div><div>University of Cape Town Department of Mechanical Engineering</div><div>Drawn By: Daniel Pons</div><div>Checked :</div></div><div><div>All un-toleranced dimensions to adhere to ISO 2768-m</div><div>Drawing Number : 036PB_1116_20_PNSDAN002</div><div>Rev. : A</div></div><div><div>Title: Goniometric Cutting Jig Exploded View</div><div>Rev. : A</div><div>Sheet : 1 of 1</div></div></div>				



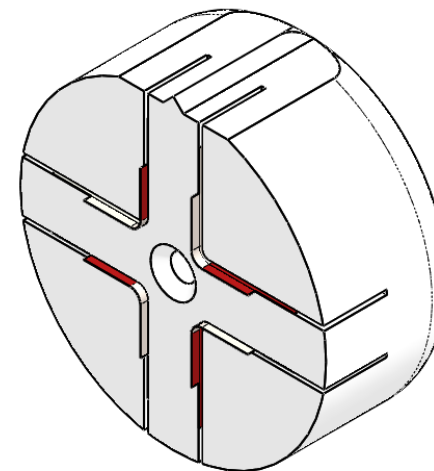
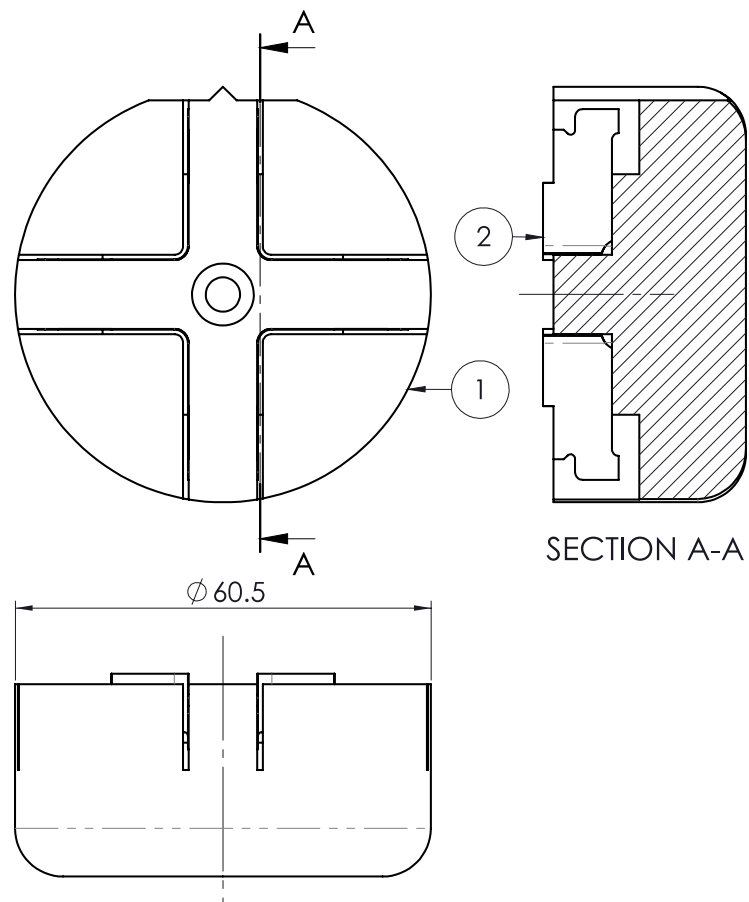
SECTION A-A




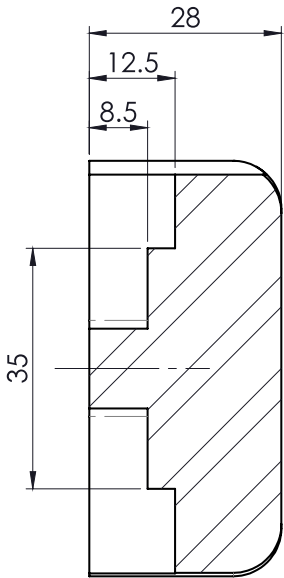
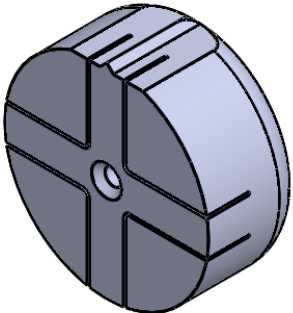
	Scale: 1:1 on A3	University of Cape Town Department of Mechanical Engineering			
Drawn By: Daniel Pons	All un-toleranced dimensions to adhere to ISO 2768-m		Title: Goniometric Cutting Jig Assembly		
Checked :	Assembly drawing		Drawing Number : 036PB_1116_20_PNSDAN002	Rev. : A	Sheet : 2 of 2

C.4.2 Cutting Block Assembly

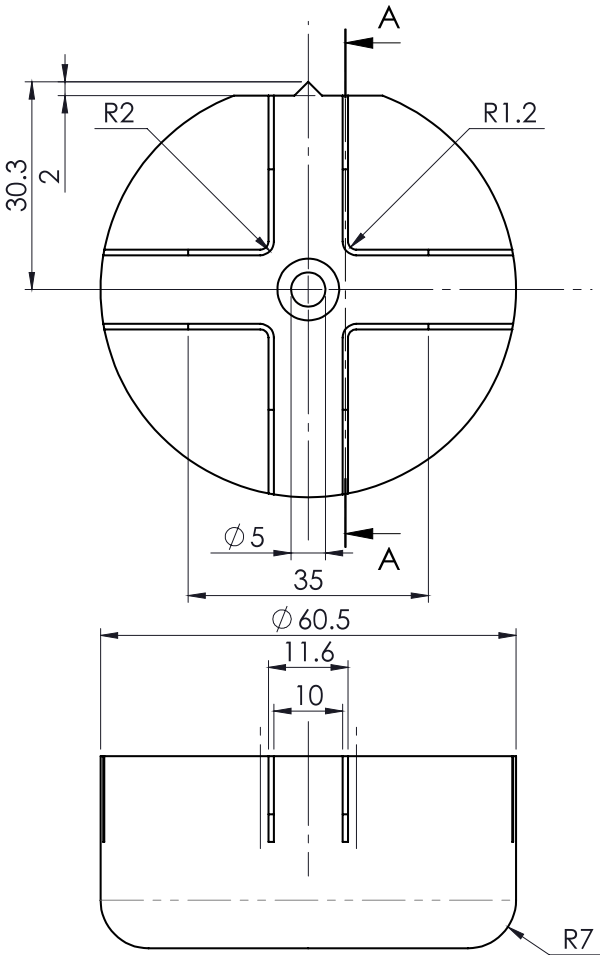
The following drawing shows the assembly of the cutting block and constituent components. The razor blades are not specified using a drawing; however the cutting block was made using FDM methods. The block was shaped to cut out a cruciform specimen.




2	056PB_0528_21_PNSDAN002	Half Razor Blade	Zorrick Disposable Razor Blade	4
1	052PB_0225_21_PNSDAN002	10 mm specimen cutter	See DWG for details, ABS	1
NO.	PART NUMBER	DESCRIPTION	SPECIFICATION	QTY
 Scale: 1:1 on A4		University of Cape Town Department of Mechanical Engineering		
Drawn By: Daniel Pons		All un-toleranced dimensions to adhere to ISO 2768-m	Title: Cruciform Specimen Cutter	
Checked :		Assembly Drawing	Drawing Number : 058PB_0219_22_PNSDAN002	Rev. : A
			Sheet : 1 of 1	



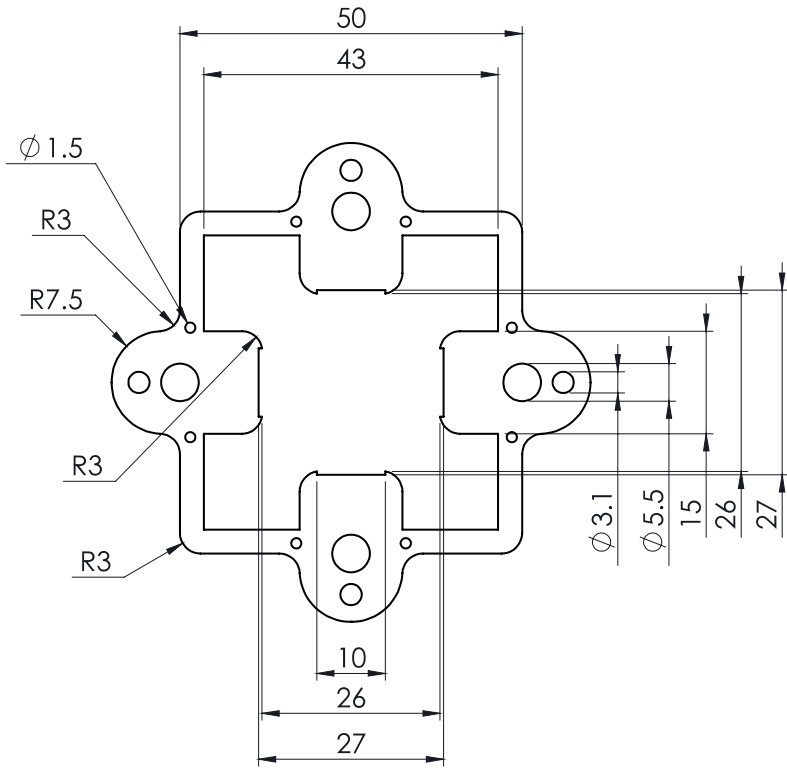
SECTION A-A




		Scale: 1:1 on A4		University of Cape Town Department of Mechanical Engineering		
Drawn By: Daniel Pons		All un-toleranced dimensions to adhere to ISO 2768-m		Title: Cutting Block		
Checked :		Material : ABS		Drawing Number : 055PB_0528_21_PNSDAN002	Rev. : A	Sheet : 1 of 1

C.5 Planar Biaxial Tensile Grip Card

The following drawing shows the card used to help transfer the specimens from the bulge tester to the PBT tester. It also doubled as a mounting grips when applied to the specimen with glue. This was manufactured using laser cutting methods.

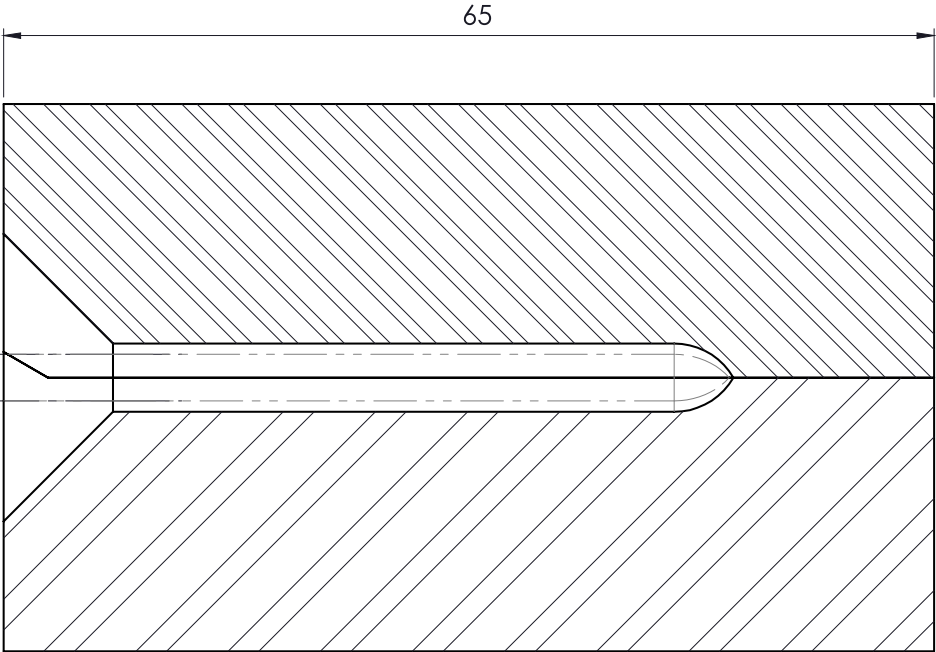
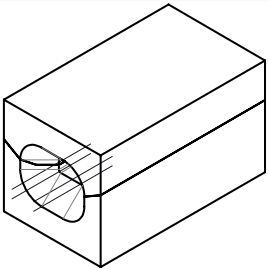


Thickness: 1.2

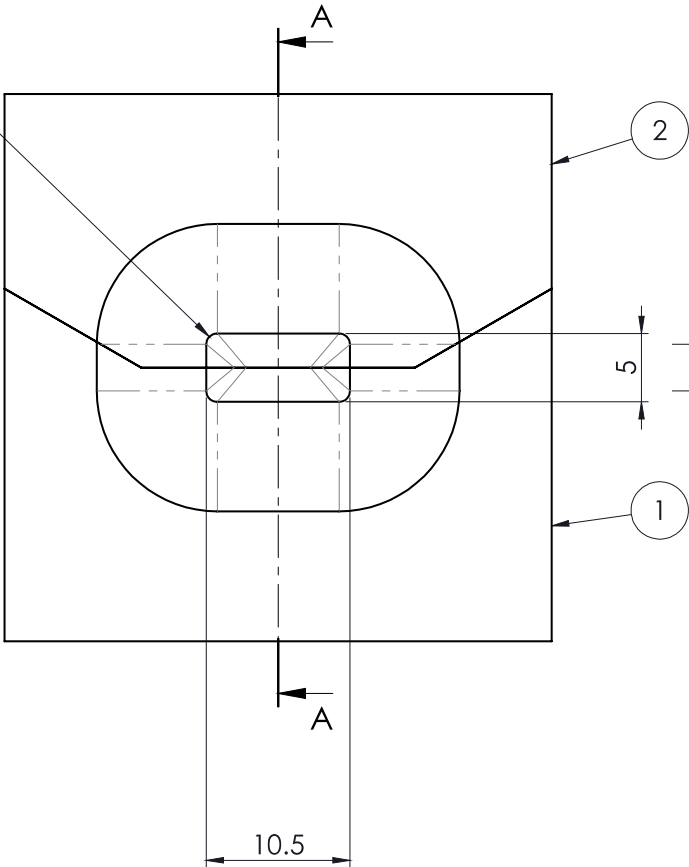
	Scale:	<h1 style="text-align: center;">University of Cape Town</h1> <p style="text-align: center;">Department of Mechanical Engineering</p>			
	1:1 on A4				
Drawn By: Daniel Pons		All un-toleranced dimensions to adhere to ISO 2768-m	Title: <h2 style="text-align: center;">Specimen Transfer Card</h2>		
Checked :	Material : 615 GSM Paper Card	Drawing Number : 052PB_0605_21_PNSDAN002	Rev. : A	Sheet : 1 of 1	

C.6 Wax Mould

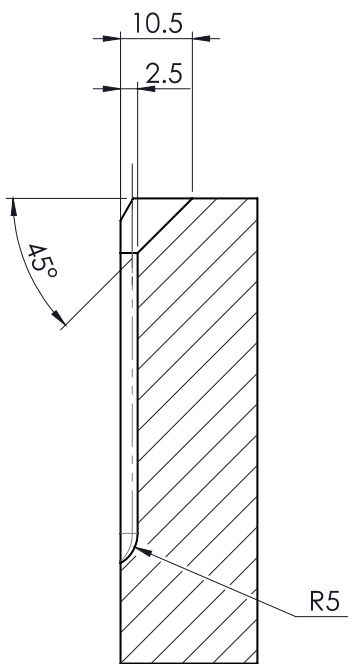
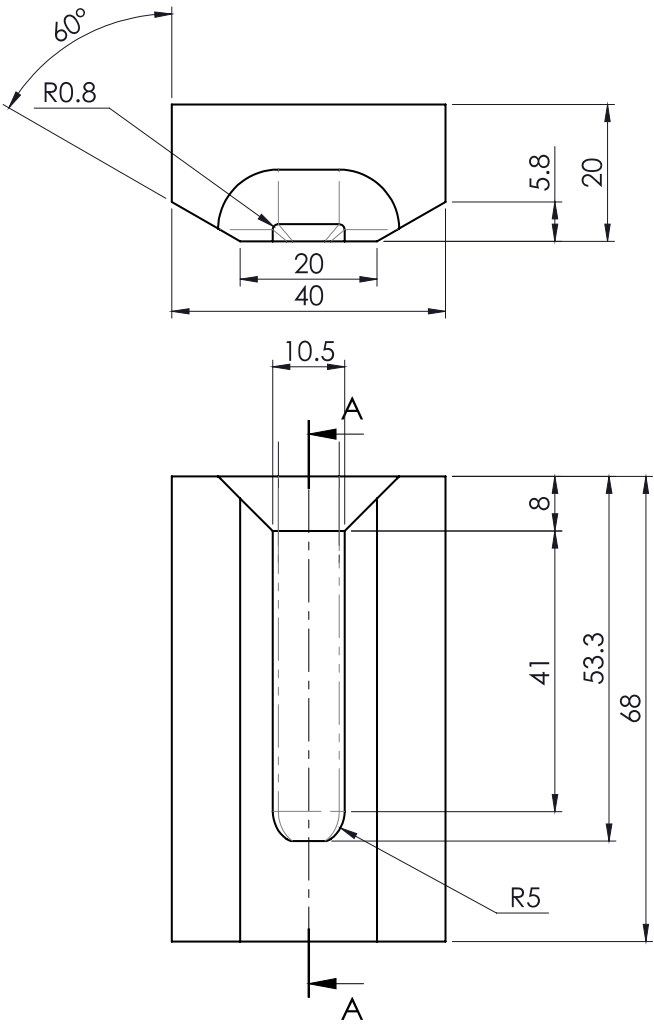
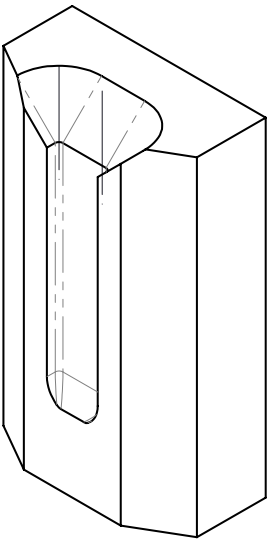
The following drawing shows the wax mould used to help the histological measurement of specimen thickness. This was manufactured using FDM methods.



SECTION A-A

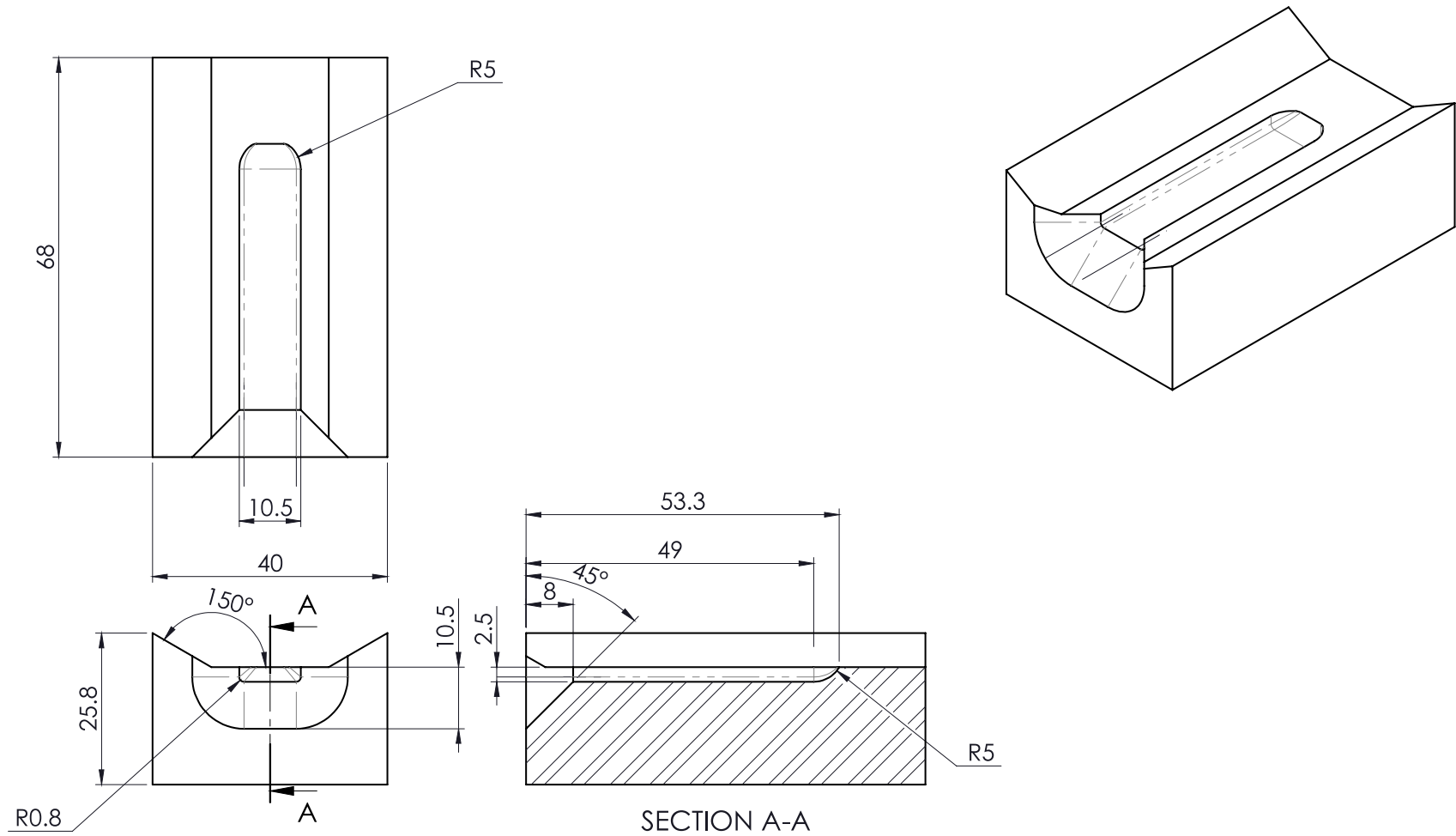



2	045OTH_0330_21_PNSDAN002_REV2	Mould Part A	See DWG for details, ABS	1
1	045OTH_0330_21_PNSDAN002_REV2	Mould Part B	See DWG for details, ABS	1
NO.	PART NUMBER	DESCRIPTION	SPECIFICATION	QTY
		Scale: 2:1 on A4	University of Cape Town Department of Mechanical Engineering	
Drawn By: Daniel Pons		All un-toleranced dimensions to adhere to ISO 2768-m	Title: Wax Mould Assembly	
Checked :		Assembly Drawing	Drawing Number : 045OTH_0330_21_PNSDAN002_REV2	Rev. : A
				Sheet : 1 of 1



SECTION A-A

	Scale: 1:1 on A4	University of Cape Town Department of Mechanical Engineering			
	Drawn By: Daniel Pons	All un-toleranced dimensions to adhere to ISO 2768-m	Title: Mould Part A		
Checked :	Material : ABS	Drawing Number : 0450TH_0330_21_PNSDAN002_ParLA	Rev. : A	Sheet : 1 of 1	



	Scale: 1:1 on A4	University of Cape Town Department of Mechanical Engineering			
	Drawn By: Daniel Pons	All un-toleranced dimensions to adhere to ISO 2768-m	Title: Mould Part B		
Checked :	Material : ABS	Drawing Number : 0450TH_0330_21_PNSDAN002_REV2	Rev. : A	Sheet : 1 of 1	

Appendix D:

Python Code

Direct links to specific code text files in this directory are broken down in this appendix for ease of navigation. A link to the [parent directory](#) for all python code is given as follows:

<https://drive.google.com/drive/folders/1nEMydvYsMQUCr906i0j3tMf1FFmEvZZV?usp=sharing>

D.1 Data Processing

DIC as well as ClipX data export needed to be compiled into usable formats to link load and displacement data for analysis. Import and data-shaping script workflows are presented here. DIC data exports were a list of very large text files of irregular size and length and units beyond user control.

D.1.1 *BTR*

For the MFA-ID algorithm, DIC data needed to be imported, shaped and saved for rapid re-use. The main data used was position and error in position as strain was not used.

The [Data_import3](#) script would handle imports and loads of previously imported data.

https://drive.google.com/file/d/1fkm3c297_-VleUzanSIH_XcG9BAnZVBf/view?usp=sharing

D.1.2 *PBT*

The DIC data for PBT had a very similar data import library to the BTR, just with much more data read in. PBT data also required time synchronisation of DIC displacement data and the ClipX load-cell data.

1. `process1_align_and_trim`: A library with three different variants to allow the synchronisation of DIC data to ClipX data. The [first](#) was the standard, the [second](#) would swap the x & y loads in case of a miswired test. The [last](#) variant was to align specimen data by hand that could not be done otherwise. Efforts were made to make the data processing as painless as possible, but each dataset should be handled individually to avoid a poor synchronisation.

- a. <https://drive.google.com/file/d/1RlBeyjJnTxc7G5xdN054Nczok65GzI3T/view?usp=sharing>
- b. https://drive.google.com/file/d/1U_dcHv99L4U9w-QGUvGdyHTtyoxYvyln/view?usp=sharing

c. <https://drive.google.com/file/d/1Q4Ia46isKfeb70vGF4RHeTUHx1xz0XKc/view?usp=sharing>

2. [process2_reshape](#): a library for shaping the very large temporal DIC dataframes into the same size and shape of *numpy* array such that it could be parsed rapidly and uniformly using standard indices.

<https://drive.google.com/file/d/1drUV2nqyyHuyZjQ8mnvHu5MVhhelTo1N/view?usp=sharing>

D.2 Data Analysis

D.2.1 Basic MFA-ID Algorithm

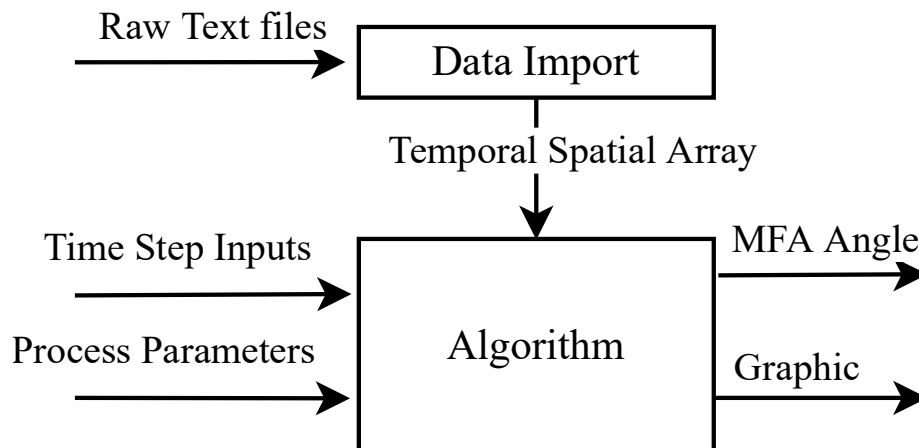


Figure D.2.17: An overview of the algorithm inputs and outputs

1. [trace_ellipse_XY1.4_write_up](#): The MFA-ID Algorithm script.

https://drive.google.com/file/d/1qlEjnOKHHxla_VyUv_CXhkCgy0eDdDD/view?usp=sharing

D.2.2 Multiprocessing MFA-ID Module

1. [trace_ellipse_XY1.4_reverse_param_full_dat](#): an analysis script to efficiently perform MFA-ID with thousands of permutations of input parameters.

https://drive.google.com/file/d/1IEcOMHWP8H-2WcZ6c5yg_FEWkGqwd1kE/view?usp=sharing

2. [Data_stream2_analyser](#): a script to read and process the data-log file of the multiprocessing module.

<https://drive.google.com/file/d/1JgA0fLjPI2RZiKKvJ6bws-Mc5skWzR2y/view?usp=sharing>

D.2.3 PBT Stress-Strain analysis

1. [analyse4_curve_fit](#): The script used to fit exponential curves to the 1:1 extension data.

<https://drive.google.com/file/d/1zCr4T54v-phIrYllhUvJ42cmFI9kZDzO/view?usp=sharing>

D.3 Additional Libraries

1. [email_notify](#): A library to mail you when a multiprocessing algorithm had completed.

<https://drive.google.com/file/d/1KsRHv3TuoaEbLSCW64f7RGfnc6sXYfFK/view?usp=sharing>

2. [polyToparams](#): A library to get elliptical parameters such as radii from the coefficients of the elliptical formula.

<https://drive.google.com/file/d/1-6u32wabXPhrMxCwKDSUnWT1uOPxAOsx/view?usp=sharing>

3. [inkscape_convert](#): A library that uses the command line to run basic operations in the vector image editing software *Inkscape*.

https://drive.google.com/file/d/1Egl_BhgXRwRYm5K7DT8uabZVWRX4LJaO/view?usp=sharing

4. [pdf2emf_convert](#): A library to convert pdf vector images into the MS-Word readable equivalent *.emf. Note that newer versions of MS-Word can now read SVG images which are more flexible with formatting and *matplotlib* plots can be saved directly into this format.

<https://drive.google.com/file/d/1P1nocP5u0JyNU1Gr2JJTrJrkFEBIEvp6/view?usp=sharing>

5. [lib1_data_import_rev2](#): A library with improved importing functionality pertinent to the larger PBT dataframes.

https://drive.google.com/file/d/1Y_ksk8R1I9XnXKtgRwL260Mot9YAuGoB/view?usp=sharing

6. [lib2_data_navigation](#): a library that helps the user easily call data columns and navigate around the dataframe in a logical fashion. Also useful as a reference and guide to how the import and processing codes alter the PBT DIC data.

https://drive.google.com/file/d/1xhyvzMQ3MJZUOIHbfpOr_WJUDpL2ueAN/view?usp=sharing

D.4 Databases

The scripts above all read from the databases listed below. These were typically *.csv, *.npz or *.xlsx format files that were imported using readily available python libraries. These have been presented in the form of direct links or the names and links to the directory. Note that sometimes absolute file paths were used in the code for these files for ease of use. A user would be expected to alter these themselves.

D.4.1 Bulge DIC Data

1. [facet_opt](#): a directory of re-evaluated bulge DIC data at a range of facet sizes for a few specimens.

<https://drive.google.com/drive/folders/1y1n2Dd93OjdN-MtNC1xf4qrXRsmGdSGf?usp=sharing>

2. [original_bulge_dat](#): a directory of DIC data from the original import using 15 px facet size.

<https://drive.google.com/drive/folders/1uTyDHinTZjpmovYvOgfuc7MsgMBU3zzL?usp=sharing>

3. [param_check](#): a directory of multiprocessed data from running the ellipse fitting algorithm on multiple specimens with different parameters.

<https://drive.google.com/drive/folders/1g3N4FCJNvtoNFE7QkNgoUV401Ka5Blh2?usp=sharing>

4. [BULGE_SUMMARY](#): a spreadsheet of the summary of the bulge test parameters and results calculated and recorded.

https://docs.google.com/spreadsheets/d/1vdkY3ZbK8kpbWRL5RUVkKGJujciHWE-_/edit?usp=sharing&ouid=106730535055046894660&rtpof=true&sd=true

D.4.2 Measured Values

1. [width_summary](#): a database of the measured widths of specimen arms for use in area calculation measured in *ImageJ*.

https://drive.google.com/file/d/1Dond5-Ve6z59cjR_dGPEx9vNibVR2lCS/view?usp=sharing

2. [thickness_summary](#): a database of the specimen arm thicknesses measured using *ImageJ*.

https://drive.google.com/file/d/15NzmBJrnq_-1mYJAuMUSJ6JF2AJE7bu9/view?usp=sharing

D.4.3 PBT DIC Data

1. Strain multiplier: a set of databases for the multipliers needed to convert the DIC data into the same units for each specimen to allow ease of comparison. As this changed with each export. One was done for the [15 px export](#) and the second was done for the [59 px export](#).

- a. <https://drive.google.com/file/d/1oSywAqMlFw8Nm2YXNzzjHgZrSCIID2MP/view?usp=sharing>
- b. https://drive.google.com/file/d/1tYK2TY4qMs5fJyPfpbfm_wzjVPqwyRKI/view?usp=sharing

4. [processed_data](#): a directory of all 15 px PBT data used, including full cruciform, region of interest and preconditioning data in .npy format.

<https://drive.google.com/drive/folders/1rcDsWREsDEw6pyFzsENJ6IHCb6iWoWzL?usp=sharing>

5. [processed_data_facet_59](#): a directory of all 59 px PBT data used with full cruciform and region of interest data in .npy format.

<https://drive.google.com/drive/folders/1qQR9B5S7fbX4wp2Vpltl4kUqDlE5ExuF?usp=sharing>

Appendix E:

Modifications to Arduino

Code

Direct links to specific code text files in this directory are broken down in this appendix for ease of navigation. Only small changes were made to the previous version of these codes built by Curry [4]. The code presented in this appendix represents only the snippets that were changed. A link to the [parent directory](https://drive.google.com/drive/folders/1NEUSTe6rhhlWP-JypLyjxhzcOFArr3LE?usp=sharing) for both pressure sensor control and motor Arduino codes for the BTR tester is given as follows:

<https://drive.google.com/drive/folders/1NEUSTe6rhhlWP-JypLyjxhzcOFArr3LE?usp=sharing>

E.1 Max & Min Pressure Triggering

This code helped prevent specimen puncture from negative over-pressure by implementing a negative pressure trigger to terminate deflation. This was needed as there was always some air leakage through the porous membrane.

```
void loop(void){
    TIME = millis() - TestStartTime; TIME = TIME / 1000;
    int16_t adc0;
    adc0 = ads.readADC_SingleEnded(0);
    Voltage = (adc0 * 0.1866) / 1000 - 0.009652; // new voltage calibration
    //Pressure = (Voltage-0.501) * 25 / 3.999; //250mBar Transducer conversion
    Pressure = (Voltage-0.503) * 10 / 3.994; // 100mBar Transducer conversion
    //Send Test pressure reached signal
    if (Pressure > test_pressure_lim & SerialPrintFlag == HIGH & pmaxlimtrig== LOW) {
        //send command to slave (stepper Arduino) to initiate pause and return then end the test
        Wire.beginTransmission(8); // transmit to device #8
        Wire.write(7); // 7 indicates max pressure reached
        Wire.endTransmission(); // stop transmitting
    }
    //Low pressure signal being sent to motor arduino
    else if (Pressure < lower_pressure_lim & SerialPrintFlag == HIGH){
        //send command to slave (stepper arduino) to stop test
        SerialPrintFlag = LOW;
        Serial.println("");
        Serial.print("Specimen returned to zero pressure.");
        Serial.println(" ");
        Wire.beginTransmission(8); // transmit to device #8
        Wire.write(9); // 9 indicates stepper to stop
        Wire.endTransmission(); // stop transmitting
    }
}
```

Figure E.1.18: Code block for additional max and min pressure triggers

E.2 Pressure Profile Control Logic

This code ensured specimens were inflated according to a standardised peak load, held there statically for a while and then deflated to zero. This was needed to ensure the same test criteria with each specimen and to give as much chance of a few good timesteps for DIC to evaluate.

```
// Interrupt function for receiving data between Arduinos
void receiveEvent(int howMany) {
  int x = Wire.read();
  if (x == 7) {
    // '7' is the signal code for test pressure reached, procedure is to hold the stepper then retract.
    stepper.stop();
    Serial.println("x=7");
    pmaxtrip = true;
    stop_button = false;
    start_button = false;
    reverse_button = false;
  }
  if (x == 9) {
    // '9' is the signal code for zero pressure reached,
    pmintrip = true;
    Serial.println("x=9");
    stepper.stop();
    // Setting button flags to prevent further forward movement
    stop_button = true; // also activated as backup
    // start_button = false;
    // reverse_button = false;
  }
  if (x == 3) {
    // '3' is the signal code for max pressure reached, procedure is to stop the stepper,
    // it can only move backwards
    stepper.stop();
    // Setting button flags to prevent further forward movement
    limit_1 = true; // also activated as backup
    stop_button = true; // also activated as backup
    start_button = false;
    reverse_button = false;
  }
}
```

Figure E.2.19: Code block for controlling the inflation profile

E.3 Additional Button Logic

This code ensured that the overpressure signal was received with the same priority as the buttons and would end the test. This helped prevent specimen damage from positive overpressure.

```
void loop(void){
  //Reading button pins
  ...
  // Pressure controlled pulsation.
  else if ((pmaxtrip==true)&&(start_button==false)&&(reverse_button==false)&&(stop_button==false))
  {
    stepper.stop(); // maintain stop
    pmaxtrip = false;
    Serial.println("delay 5s");
    delay(hold time);
    Serial.println("move back1000");
    stepper.begin(TestingSpeed, 8);
    stepper.move(+100000);
  }
}
```

Figure E.3.20: Logic to ensure all circumstances were considered for button events

Appendix F:

Ethics Clearance

Application for Approval of Ethics in Research (EiR) Projects
Faculty of Engineering and the Built Environment, University of Cape Town

ETHICS APPLICATION FORM

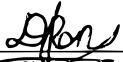
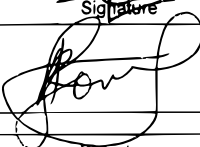

Please Note:

Any person planning to undertake research in the Faculty of Engineering and the Built Environment (EBE) at the University of Cape Town is required to complete this form **before** collecting or analysing data. The objective of submitting this application *prior* to embarking on research is to ensure that the highest ethical standards in research, conducted under the auspices of the EBE Faculty, are met. Please ensure that you have read, and understood the **EBE Ethics in Research Handbook** (available from the UCT EBE Research Ethics website) prior to completing this application form: <http://www.ebe.uct.ac.za/ebe/research/ethics1>

APPLICANT'S DETAILS		
Name of principal researcher, student or external applicant		Daniel Pons
Department		Mechanical Engineering
Preferred email address of applicant:		PNSDAN002@MYUCT.AC.ZA
If Student	Your Degree: e.g., MSc, PhD, etc.	MSc Eng
	Credit Value of Research, e.g., 60/120/180/360 etc.	120 Credits
	Name of Supervisor (if supervised):	Dr. Reuben Govender
If this is a research contract, indicate the source of funding/sponsorship		NRF: Thuthuka Grant Holder's Bursary and UCT 10A Merit
Project Title		Comparison of biaxial material models for pig intestine using commercially available FEM software.

I hereby undertake to carry out my research in such a way that:

- there is no apparent legal objection to the nature or the method of research; and
- the research will not compromise staff or students or the other responsibilities of the University;
- the stated objective will be achieved, and the findings will have a high degree of validity;
- limitations and alternative interpretations will be considered;
- the findings could be subject to peer review and publicly available; and
- I will comply with the conventions of copyright and avoid any practice that would constitute plagiarism

APPLICATION BY	Full name	Signature	Date
Principal Researcher/ Student/External applicant	Daniel Pons		08/07/2019
SUPPORTED BY	Full name	Signature	Date
Supervisor (where applicable)	Dr. Reuben Govender		22 AUG 2019
APPROVED BY	Full name	Signature	Date
HOD (or delegated nominee) Final authority for all applicants who have answered NO to all questions in Section 1, and for all Undergraduate research (Including Honours).			
Chair: Faculty EIR Committee For applicants other than undergraduate students who have answered YES to any of the questions in Section 1.	R Behrens		27 Sep 2019



UNIVERSITY OF CAPE TOWN
Faculty of Health Sciences
Animal Ethics Committee



Room E53-46 Old Main Building
Groota Schuur Hospital
Observatory 7925
Telephone (021) 406 6492
Email: sumayah.ariefdien@uct.ac.za
Website: www.health.uct.ac.za/fhs/research/animalethics/forms

01 April 2019

Dr R Govender
Mechanical Engineering
Upper Campus
UCT

Dear Dr Govender

PROTOCOL TITLE: Mechanical Properties of Membrane Tissues

FHS AEC REF NO: 019/014

Thank you for submitting your request for approval of use of animal material for scientific purposes to the Faculty of Health Sciences (FHS) Animal Ethics Committee (AEC).

I am pleased to inform you that the FHS AEC EXCO has approved your request, which will terminate on **30 April 2022**.

Number of animal material & species: 2Kg -Sheep, Cow, Pig Intestines

Please quote the FHS AEC REF NO (above) in all future correspondence.

Please note that the approval of this protocol imposes the following obligations on the principal Investigator (PI):

1. To submit an annual mandatory progress report. The first annual report for this protocol is due on **28 February 2020**. The forms can be accessed from <http://www.health.uct.ac.za/fhs/research/animalethics/forms>
2. To submit a final mandatory report on the **30 April 2022**, please access the final report form from: <http://www.health.uct.ac.za/fhs/research/animalethics/forms>
3. Ensuring that all study participants perform within the confines of the procedures and experimental design of the protocol as approved, or as amended.

AEC REF# 019/014

4. Ensuring that all study participants comply with all applicable national legislation, UCT policies, FHS AEC policies and standard operating procedures (SOPs) and national standards (SANS 10386: 2008).

My best wishes for a successful research and /or teaching endeavour.

Yours sincerely



PROF PJ COMMERFORD
CHAIR, FHS AEC



Faculty of Health Sciences
Animal Ethics Committee (AEC)

USE OF ANIMAL MATERIAL FOR SCIENTIFIC PURPOSES

<ul style="list-style-type: none"> Current forms to be downloaded from the Administrative Forms web page at http://www.health.uct.ac.za/fhs/research/animalethics/forms This application form is to seek ethics approval for the Use of Animal Material for Scientific Purposes. Please print double-sided where possible. Important: Animals not specifically killed for this study. 	
<p>This application must be typed and one signed completed form submitted to: Mrs Sumayah Ariefdien Animal Research Ethics Committee E 53 Room 48, Old Main Building, Groote Schuur Hospital, Observatory, 7700 Telephone: +27 21 404 6492 An electronic copy of the original application (Word format which is saved as a PDF file) is to be forwarded to fhsanimalresearch@uct.ac.za and sumayah.ariefdien@uct.ac.za</p>	<p>For office use only</p> <p>Application No: 019-014</p> <p>Animal Material: Intestines</p> <p>Species: Sheep, Pig, Cow</p> <p>Source:</p> <p>Date received: 26.08.2019</p> <p>Date approved:</p>

1. TITLE OF APPLICATION	Mechanical Properties of Membrane Tissues
--------------------------------	---

2. DETAILS OF APPLICANT	
Title (e.g. Prof, Dr, Mr, Ms)	Dr
Forenames & Surname	Reuben A. Govender
Qualifications (e.g. PhD)	PhD
Position or appointment	Senior Lecturer
If applicant is a student, please provide name of supervisor	

3. CONTACT DETAILS	APPLICANT	SUPERVISOR (If applicant a student)
Address for correspondence	Mechanical Engineering Library Rd South Upper Campus University of Cape Town Rondebosch 7701	
Telephone number, extension	021 650 4526	
Cell phone number	082 730 2048	
Fax number		
E-mail address	Reuben.govender@uct.ac.za	



FHS029: Application Form: Use of Animal Material (May 2018)

4.1 ANIMAL MATERIAL REQUESTED

Species and Strain	Sheep, cow, pig – Intestines processed into "sausage casings"
Amount of animal material required	Approx. 0.5kg of intestine per student project (2.0kg total)

Describe Animal Material (e.g. tissues) (max 250 words)

Sausage skins (cleaned intestinal membranes) from sheep / pigs / cows will be used for commissioning a newly designed and built bulge / inflation tester. The device measures the mechanical stiffness and strength of thin membranes, and is intended to ultimately assist with characterisation of human membrane tissues and their artificial replacements.

5.1 SOURCE OF ANIMAL MATERIAL

Please indicate the source/supplier of the animal material and where and when it was sourced. Please note that an abattoir registration number is required if the animal material is sourced from an abattoir.

Was material ethically sourced? Please explain.

Intestines will be purchased as "natural sausage casings" from Freddy Hirsch Group (www.freddyhirsch.co.za), who are suppliers of sausage casings, spices and butcher's equipment in wholesale quantities to retail butchers and the meat processing industry. The Freddy Hirsch Group is supplied by several abattoirs, as they sell both halaal-certified products and non-halaal products.

5.2 ANIMALS KILLED

Briefly explain, if known, how and why animals were killed.

This study will not use tissue from any animal that was not destined for slaughter at a commercial abattoir.

6. STUDY PARTICIPANTS:

Name	Department	Role
Dr Reuben Govender	Mechanical Engineering	Principal Investigator
Jonathan Caine	Mechanical Engineering	PG Student (Lab Work Involves handling specimens)
Daniel Pons	Mechanical Engineering	PG Student (Lab Work Involves handling specimens)
Andrew Curry	Mechanical Engineering	Research Assistant
Deharen Pillay	Mechanical Engineering	UG Student (Lab Work involves handling specimens)

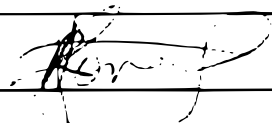
UNIVERSITY OF CAPE TOWN UNIVERSITEIT VAN KAAPSTAD		FHS029: Application Form: Use of Animal Material (May 2018)	
SECTION OF STUDY			
Period the application is required (not less than 1 year)		Years	2
May 2019		End date	July 2021
FOSE (select category)			
<input checked="" type="checkbox"/> X		Teaching/training	Other (specify)

9. Briefly describe what you will be doing
 If a hypothesis is being tested (explanatory research) please state what it is.

This project is investigating different ways of quantifying the mechanical properties (stiffness, failure strain and stresses etc) of biological membrane tissues. The PI's PG students in Mechanical Engineering have been designing and building the experimental apparatus (bulge tester and planar biaxial tensile tester) to perform these experiments. To date, the early commissioning work on the apparatus has been completed with engineering surrogate materials (latex and silicon elastomers). Further improvements to the apparatus specifically the imaging system used for strain measurements and the gripping system for delicate specimens, require that specimens are prepared from biological tissues. For this level of commissioning work, animal intestines that have been processed into "natural sausage casing" are an ideal material – they are of similar composition / properties to the ultimate material of interest, can be sourced inexpensively in suitable quantities and specimens can easily be prepared.

The desired outcome of this phase of the project is a calibrated testing apparatus and mature testing protocol, such the investigations of human membrane tissues or material destined for human clinical applications (e.g. artificial skin cultured for burn treatment) may proceed. This will clearly require a further application to the appropriate ethics committee.

10. SIGNATURES

Applicant Signature:  Date 26 MARCH 2019

NOTE: Please note that an Annual or Final Report is required in order to maintain AEC approval.